UNIVERSITÉ DE STRASBOURG

École doctorale de Physique - Chimie Physique (ED 182)

THÈSE

présentée et soutenue publiquement le 22 mai 2015

pour l'obtention du grade de

DOCTEUR DE L'UNIVERSITÉ DE STRASBOURG

Spécialité : Physique Subatomique pour la Santé

présentée par

Harold BARQUERO

Micro-tomographie par rayons X à angle limité: dérivation d'une information anatomique a priori pour la Tomographie Optique par Luminescence

Limited angular range X-ray micro-Computerized Tomography: derivation of anatomical information as a prior for Optical Luminescence Tomography

Composition du jury

Rapporteurs :	Prof. Dr. Hans-Peter MEINZER	DKFZ, Heidelberg, Allemagne
	Dr. Dimitris VISVIKIS	LaTIM, Brest, France
Examinateurs :	Dr. Yannick BOURSIER	CPPM - Marseille, France
	Prof. Dr. Fabrice HEITZ	ICube, Strasbourg, France
Directeur de thèse :	Dr. David BRASSE	IPHC, Strasbourg, France

Remerciements

A l'issue de ce travail de doctorat, je tiens à remercier les différents acteurs qui ont contribué à sa mise en place, à son déroulement et à son achèvement.

Je tiens, en particulier, à remercier les membres du jury, Messieurs Yannick BOURSIER, Fabrice HEITZ, Hans-Peter MEINZER, Dimitris VISVIKIS, pour avoir accepté de rapporter et d'examiner mon travail et pour leurs conseils avisés.

Je suis vivement reconnaissant envers Monsieur David BRASSE, mon directeur de thèse, pour son soutien et sa confiance tout au long de ce travail.

Mes remerciements vont également à l'entreprise Biospace Lab, pour cette expérience riche et formatrice. Je tiens à remercier tout particulièrement Monsieur Serge MAITREJEAN pour la genèse du projet.

L'accueil chaleureux et le soutien manifestés par l'ensemble des membres du groupe ImaBio de l'IPHC a été déterminant dans le développement, la maturation et l'achèvement de ce projet ainsi que de tout ce qui l'a accompagné, notamment les différents aspects de la vie collective du groupe. Je les en remercie vivement.

Je souhaite également remercier le personnel permanent de l'Institut Pluridisciplinaire Hubert Curien, pour son accueil et son soutien pour mon doctorat ainsi que dans les divers projets nés et menés à bien au cours de cette période, notamment mon implication auprès de la communauté des doctorants du laboratoire.

Enfin, j'adresse mes remerciements aux personnels du service CIFRE de l'Association Nationale de la Recherche Technologique (ANRT) pour la mise en place et le suivi de la Convention Industrielle de Formation par la Recherche, de l'Ecole Doctorale 182 – Physique, Chimie Physique – de l'Université de Strasbourg ainsi que des différents services de l'Université de Strasbourg avec lesquel j'ai pu interagir pour les aspects administratifs attenant au déroulement de mon projet.

Aucun des dieux ne philosophe ni ne désire devenir savant, car il l'est; et en général, si l'on est savant on ne philosophe pas; les ignorants non plus ne philosophent pas et ne désirent pas devenir savants; car l'ignorance a précisément ceci de fâcheux que, n'ayant ni beauté, ni bonté, ni science, on s'en croit suffisamment pourvu. Or, quand on ne croit pas manquer d'une chose, on ne la désire pas.

Platon, Le Banquet, XXIII

Table of Contents

2 Optical Luminescence Tomography

Conclusion

Chapitre 1

Résumé détaillé en français

Ce chapitre en français constitue un résumé détaillé du matériel présenté dans les chapitres suivants en anglais. Ce travail propose une approche d'imagerie multimodale associant la tomographie par rayons X d'une part et l'imagerie optique de source luminescentes d'autre part. L'idée sous-jacente est d'exploiter l'information contenue dans les images tomographiques obtenues avec la première modalité afin d'injecter une connaissance *a priori* dans le processus de reconstruction de la seconde modalité. Le couplage de ces deux modalités d'imagerie impose de considérer des problématiques pratiques de disposition spatiale des instruments. Dans ce travail, un appareil d'imagerie optique en cours de développement par la société Biospace Lab, le Photon IMAGER Optima, a été étudié. Afin de répondre aux contraintes imposées par l'appareil d'imagerie optique, les choix de conception ont conduit à limiter l'intervalle angulaire d'acquisition du micro-tomographe par rayons X. Il en résulte une problématique de reconstruction d'image à partir d'une information limitée – l'information complète étant donnée par un intervalle angulaire complet, c'est-à-dire une acquisition réalisée avec un échantillonnage suffisant sur 360°. Un algorithme itératif régularisé a été implémenté et son application à la problématique considérée a été méthodiquement étudiée afin de caractériser les performances de l'algorithme dans ce cas donné. Une fois des images tomographiques reconstruites, il s'est agi d'interpréter ces images en termes anatomiques, afin de fournir une information pour la tomographie optique de sources luminescentes. A cette fin, une chaîne de segmentation automatique a été implémenté, comprenant une première phase de segmentation des tissus à fort contraste –le squelette, l'enveloppe de l'animal et ses poumons – et une seconde phase visant à estimer automatiquement l'emplacement et le contour de certains tissus à faible contraste – coeur, foie, reins, rate. L'intérêt est double puisque d'une part il est généralement difficile de distinguer les tissus dits "à faible contraste" dans une image micro-CT standard, d'autre part la réduction de l'intervalle angulaire dégrade l'image reconstruite. Plusieurs techniques de recalage d'image ont été implémentées et mises en oeuvre afin d'arriver à cette fin. Le résultat final, c'est-à-dire l'estimation des contours des tissus à faible contraste, est en fait le produit du recalage d'un atlas statistique des tissus de la souris. Aucun atlas statistique des tissus de la souris, corps entier, n'étant disponible ni dans le domaine public ni dans le domaine privé, la construction de ce modèle a constitué une partie de notre travail. Cette thèse est composée de cinq chapitre – incluant ce résumé détaillé. Dans cette partie en français, quatre sections remplacent les chapitres correspondants de la partie en anglais. La tomographie optique de source luminescentes est présentée dans le premier chapitre, et le besoin d'un couplage multimodal y est mis en évidence. La seconde section contient la description de l'algorithme de reconstruction implémenté pour la reconstruction tomographique à angle limité, ainsi que l'évaluation des résultats obtenus dans le contexte étudié. La troisième et la quatrième sections contiennent, respectivement, la description de la procédure de segmentation des tissus à fort contraste et de la procédure de segmentation des tissus à faible contraste. La quatrième section contient, en outre, la description du concept de l'atlas statistique et la procédure mise en oeuvre pour sa construction. Les résultats de la segmentation des tissus à fort et faible contraste sont présentés dans les chapitres correspondants. La cinquième section de ce résumé constitue la conclusion de ce travail.

1.1 Tomographie optique de sources luminescentes

La luminescence regroupe les phénomènes physiques conduisant à l'émission de photons optiques par un phénomène autre que thermique. Les trois principales techniques d'imagerie corps entier du petit animal par luminescence sont l'imagerie par bioluminescence, l'imagerie par fluorescence et l'imagerie par luminescence Cerenkov. Introduites respectivement dans ce contexte en 1995 [Contag et al., 1995], 2000 [Yang et al., 2000] et 2009 [Robertson et al., 2009], ces techniques sont purement fonctionnelles. En deux dimensions, elles permettent de localiser approximativement une zone de luminescence, et délivrent une information sur l'intensité du signal qui peut être relativisée connaissant l'intensité injectée [Ntziachristos, 2006]. En effet, les photons optiques évoluant dans la matière sont sujets à deux principales interactions : la diffusion et l'absorption. L'absorption est très importante par rapport à la diffusion sauf dans la fenêtre optique. Plus récemment, la tomographie optique de sources luminescentes a été introduite : il s'agit de reconstruire la distribution de la source de luminescence à partir des photons optiques détectés à la surface de l'animal. Cette modalité fait émerger plusieurs problématiques relatives à la reconstruction d'image. En effet, la réalisation d'une reconstruction tomographique suppose un modèle physique des interactions entre le vecteur d'information et les matériaux observés. La probabilité de ces interactions est typiquement représentée au moyen de coefficients de diffusion et d'absorption. La reconstruction d'image passe typiquement par la résolution d'une équation de diffusion dont la forme brute est l'équation de Boltzmann – formalisée en Section 2.4.2. Dans cette équation et dans ses approximations, les coefficients optiques en question entrent en jeu. Or, dans le cas de l'imagerie optique, l'acquisition optique seule n'est pas apte à fournir cette information. Trois approches sont possibles étant donné cet énoncé : la première approche, triviale, consiste à reconstruire une image même si les coefficients optiques sont inconnus ; l'hypothèse est faite que les photons optiques interragiront avec tous les tissus de la même manière. Cela revient à attribuer les même coefficients optiques à l'ensemble des tissus de l'animal – généralement, l'intérieur de l'enveloppe est considéré, cette dernière pouvant être estimée au moyen de techniques optiques telles que la projection de lumière structurée. Cette approche aboutit à des erreurs importantes en termes de localisation et de quantification – ces deux caractéristiques étant étroitement liées. Deux approches alternatives consistent à considérer que les tissus sont hétérogènes et que, par conséquent, les coefficients optiques sont eux-mêmes hétérogènes dans les tissus. Dans ce cadre, il a été proposé i) d'attribuer des coefficients optiques distincts à différentes régions définies au préalable, ii) d'exploiter l'information obtenue en filtrant le signal sur plusieurs intervalles distincts de longueur d'onde – il s'agit d'imagerie multispectrale.

Dans cette thèse, le choix est fait d'attribuer des coefficients optiques à des régions définies au préalable. Il s'agit donc d'abord de définir les régions puis de leur attribuer des coefficients optiques réalistes. La détermination des coefficients optiques est hors du champ de ce travail, il est possible, par exemple, de se baser sur des données tabulées ou sur des modèles semi-empiriques tels que celui proposé par Alexandrakis et al. [Alexandrakis et al., 2005]. L'objectif général de ce travail est donc la définition de régions de propriétés optiques distinctes. Deux questions se posent : la première, jusqu'à quel degré d'inhomogénéité faut-il descendre. La seconde : comment déterminer ces régions. Dans un contexte d'imagerie corps entier, il est assez commode de distinguer des régions sur la base de leur signification anatomique – il s'agit donc de distinguer les différents tissus. La détermination de ces régions passe typiquement par le couplage de la modalité de tomographie par luminescence avec une modalité d'imagerie apte à délivrer une information morphologique. Supposant qu'une telle modalité a été choisie, il s'agit ensuite d'appliquer des méthodes de segmentation afin de déterminer, à partir de l'image morphologique, les différentes régions d'intérêt. L'application d'une procédure de recalage peut s'avérer nécessaire afin d'exprimer les images morphologiques – et donc les contours des régions qui en sont extraites – dans le référentiel des images optiques.

Dans ce travail, la tomographie par rayons X a été choisie pour sa capacité à délivrer des images caractérisées par un fort contraste entre le squelette, les poumons, l'enveloppe et les tissus qui les environnent directement. Il s'agit donc de considérer l'association d'un système d'imagerie optique et d'un micro-tomographe par rayons X. Le premier – présenté en Section 1.1.1 – est basé sur un système d'imagerie en cours de développement, le PhotonIMAGER Optima, développé par la société Biospace Lab. Le second – présenté en Section 1.2.1 est basé sur un système d'imagerie existant, développé à l'IPHC.

1.1.1 PhotonIMAGER Optima

Le PhotonIMAGER Optima est un système d'imagerie optique par luminescence. Le système est constitué d'une boîte noire, d'un module d'illumination et d'un module de détection, d'un pico-projecteur ainsi que les alimentations, la connectique et les logiciels associés.

Le module de détection est composé d'éléments assurant les fonctions de filtrage, de grossissement et de détection proprement dite. Un ensemble de dix filtres permet de sélectionner des bandes de longueur d'onde, sur une gamme totale de 370 à $900\ \mathrm{nm}$. Un objectif photographique de longueur focale $50\ \mathrm{mm}$ et d'ouverture $f/1.2-16$ assure le grossissement de l'image optique. Enfin, les photons sont détectés au moyen i) d'un convertisseur photon/électron, ii) d'une plaque de phosphore qui réalise la conversion électron/photon, iii) une caméra CCD composée de pixels de côté $2.5\mu\mathrm{m}$, pour une surface totale de $25 \times 25\ \mathrm{mm}^2$, associée à une galette de micro-canaux refroidie. Un cryostat refroidit la galette de micro-canaux pendant le fonctionnement de l'appareil.

Le module d'illumination, utilisé pour les études de fluorescence, est composé d'éléments assurant la production de photons, le filtrage de la longueur d'onde du signal d'excitation et le guidage des photons. Une lampe halogène au Xénon, d'une puissance de $100\ \mathrm{W}$, est utilisée pour la production des photons. Le filtrage est réalisé par un filtre linéaire d'une gamme de longueur d'onde de 400 à $760\ \mathrm{nm}$. Un ensemble de réseaux de fibres optiques permet de guider le signal d'excitation et de le diriger vers l'objet selon un montage d'épi-illumination.

Distinct du module d'illumination, le pico-projecteur permet de projeter des motifs de lumière structurée sur l'objet.

Une plateforme élévatrice permet d'élever certains de ces composants. Les dimensions de la boîte noire sont $50\ cm \times 40\ cm \times 70\ cm$. Celle-ci contient l'objectif photographique, la plateforme, le pico-projecteur ainsi que l'interface de sortie du système d'illumination.

Deux modules supplémentaires peuvent être placés dans le champ de vue. Le premier est une macro-lentille installée dans le champ de vue pour une magnification supplémentaire, Le second est le module "quatre vues", composé de miroirs agencés de manière à acquérir les photons issus de la luminescence selon quatre angles de vue – au dessus, en dessous et sur chacun des côtés de l'objet. Le module "quatre vues" est utilisé, en particulier, pour la tomographie par luminescence.

L'association d'une modalité de tomographie par rayons X au système existant suppose l'ajout d'instruments spécifiques dans le système existant. Partant de là, quatre approches sont possibles. La première consiste à ne pas modifier le système d'imagerie optique et à construire le système micro-CT à côté ou à l'extérieur de la boîte noire – dans la continuité du champ de vue de l'imageur optique, par exemple. La seconde consiste à modifier le système d'imagerie optique et d'adapter la géométrie du système de tomographie par rayons X afin d'intégrer les deux dans la boîte noire. La troisième consiste à modifier le système d'imagerie optique pour répondre aux contraintes imposées par la mise en place et le fonctionnement d'un système micro-CT dans le système. La quatrième approche consiste à adapter le système de tomographie par rayons X au système existant pour qu'il réponde aux contraintes imposées par les éléments contenus dans la boîte noire, sans modifier ceux-ci.

Ce travail de thèse propose une solution développée à partir de la quatrième approche, choisie par Biospace Lab. L'objectif initial de cette thèse était d'intégrer au PhotonIMAGER Optima un tomographe par rayons X basé sur un système existant – un système micro-CT développé à l'IPHC, moyennant des modifications de la géométrie d'acquisition afin de respecter l'agencement des instruments d'imagerie optique du PhotonIMAGER Optima et de s'affranchir de toute interférence matérielle. Le système existant est un micro-CT à géométrie conique. Les contraintes expliquées ont conduit à réduire l'intervalle angulaire de l'ensemble source-détecteur lors de l'acquisition, passant ainsi de 360° à 90°. Géométrie d'acquisition et reconstruction d'image étant intimement liées en tomographie, la modification de la géométrie d'acquisition impose en fait de considérer l'impact de la nouvelle géométrie en termes de reconstruction d'image. Les questions suivantes sont soulevées par ce choix. Quels critères permettent de juger si une image est exploitable dans le contexte multimodal considéré ? Les images reconstruites au moyen des algorithmes de reconstruction d'image utilisés pour le micro-CT de manière standard répondent-elles à ces critères ? Supposant qu'elles n'y répondent pas, est-il possible d'y répondre au moyen d'autres algorithmes, et avec quelles performances ? Cette problématique est traitée dans la section suivante.

1.1.2 Derivation d'une information *a priori* sur les contours des tissus

La problématique ainsi posée doit être considérée dans une perspective plus large que la seule reconstruction tomographique à partir de la modalité par rayons X. Il faut en effet garder à l'esprit que l'objectif final est de fournir à l'algorithme de tomographie par luminescence une information sur les contours des différents tissus de l'animal. De manière générale, un contour peut être défini dans une image i) manuellement, ou ii) sur la base de critères quantitatifs permettant de distinguer des régions dans l'image. Le contourage manuel n'est pas considéré comme une approche viable en contexte préclinique, pour le temps de traitement requis, son caractère fastidieux et son manque de reproductibilité. La définition automatique de contours est donc à considérer. Cependant, dans ce travail, on cherche à déterminer le contour de tissus tels que le foie, le coeur ou les reins. Or, ces tissus font partie de la catégorie des tissus "à faible contraste" en tomographie par rayons X. En d'autres termes, le contraste de ces tissus par rapport aux tissus qui les entourent est, en général, insuffisant pour une distinction visuelle ou automatique. Il est possible d'augmenter le contraste entre ces tissus et ceux qui les entourent par l'injection d'agents de contraste, mais cette utilisation du micro-CT tombe hors du champ des examens "standard". Elle est donc rejetée dans notre cas. Les tissus à faible contraste sont à distinguer des tissus "à fort contraste" – principalement le squelette, les poumons et l'enveloppe de l'animal – qui peuvent, eux, être distingués visuellement ou automatiquement. En principe, il est donc possible, admettant que les images reconstruites par le tomographe par rayons X soient exemptes d'artefacts, de distinguer automatiquement ces tissus de ceux qui les entourent – on parle d'une procédure de "segmentation". Dans des travaux récents visant à pallier l'impossibilité de distinguer les tissus "à faible contraste", plusieurs équipes ont proposé des procédures de segmentation couplée au recalage d'un modèle numérique définissant les contours des différents tissus – on parle d'un "atlas anatomique".

Une procédure de recalage détermine un ensemble de transformations rigides ou non-rigides, à l'échelle globale ou locale, mettant en relation deux objets dont on considère soit qu'ils sont identiques, soit qu'ils représentent deux instances d'un groupe d'objets présentant certaines caractéristiques morphologiques communes. L'hypothèse est faite que l'application de cet ensemble de transformation à l'une des instances, le *modèle*, a pour résultat l'autre instance, la *cible*. Elle permet, par conséquent, d'établir une correspondance entre des éléments communs aux deux objets – typiquement, une correspondance "un pour un" des points caractéristiques, ou de manière plus générale, une correspondance pondérée entre les points de deux distributions correspondantes permettant de représenter chacune des surfaces à recaler de manière discrète. En tomographie par rayons X, le recalage est généralement basé sur des informations dérivées des contours des tissus à fort contraste segmentés dans les images tomographiques. En vue du recalage d'un atlas anatomique, il s'agit donc en premier lieu de segmenter les tissus à fort contraste – c'est-à-dire d'identifier les régions correspondant à ces tissus – et de dériver une représentation de ces tissus sous une forme qui permette le recalage – par exemple, une approximation discrète de la surface sous la forme d'un maillage triangulaire. En second lieu, un atlas approprié doit être choisi – et, le cas échéant, constitué – ainsi qu'une procédure de recalage adaptée. Plusieurs approches existent qui permettent de mener à bien ces deux étapes. Concernant les tissus à fort contraste, des méthodes de segmentation dites "de bas niveau" – basées sur un critère quantitatif tel qu'un seuil ou encore le gradient de l'image – permettent d'identifier relativement aisément les tissus en question. Des méthodes dites "de haut niveau" – intégrant une information a priori – peuvent être utilisées pour raffiner la segmentation ainsi obtenue. Le choix de l'atlas et de la procédure de recalage – et, le cas échéant, leur implémentation – sont étroitement liés. On distingue deux catégories d'atlas : les atlas déterministes tels que MOBY [Segars et al., 2004] ou Digimouse [Dogdas et al., 2007] – basés sur la segmentation manuelle d'un seul individu à partir d'une ou plusieurs modalités d'imagerie – et les atlas statistiques – basés sur la segmentation d'images d'un groupe d'individus issu de la population considérée, obtenues au moyen d'une ou plusieurs modalités d'imagerie. Chaque catégorie présente des avantages et des inconvénients par rapport à l'autre. Dans ce travail c'est l'approche statistique qui a été choisie. Ce choix a été motivé par la capacité théorique d'un tel atlas à représenter au moyen d'un modèle statistique des variations morphologiques au sein d'une population. Ces variations peuvent en effet être importantes et il est assez intuitif que l'utilisation d'un atlas constitué à partir d'un seul individu ne permet pas de prendre en compte ces variations morphologiques. Or, il n'existe actuellement aucun atlas statistique des tissus de la souris ni commercial, ni public. Aussi, il est vraisemblablement impératif, pour adopter une telle approche, de développer soi-même l'atlas.

1.2 Reconstruction d'image pour le micro-CT à angle limité

La première étape de ce travail consiste à reconstruire une image tomographique à partir d'acquisitions réalisées avec un système dont la géométrie d'acquisition est pénalisée par rapport à un micro-CT standard. Les algorithmes de reconstructions sont en effet étroitement liés au matériel utilisé puisqu'ils se basent sur un échantillonnage spatial et angulaire des mesures. Il s'agit donc de décrire dans un premier temps la géométrie sur laquelle le système développé est basé. Dans un second temps, il s'agit de décrire la géométrie utilisée et de caractériser le résultat obtenu par l'utilisation des algorithmes dédiés au micro-CT dans le cas de cette géométrie pénalisée. La troisième étape consiste à développer un algorithme de reconstruction qui permette de compenser la pénalisation induite par la géométrie d'acquisition, à l'étape de la reconstruction. Finalement, il s'agit d'évaluer les performances de cet algorithme en comparant les résultats obtenus dans le cas du micro-CT à angle limité, à ceux obtenus avec un micro-CT complet et un algorithme de référence. Les distorsions induites par la géométrie d'acquisition choisie imposent de considérer la fidélité de l'image à l'objet observé de manière plus générale qu'en considérant seulement des critères quantitatifs tels que la résolution ou le contraste.

1.2.1 Micro-CT

Dans ce travail, la modalité de tomographie par rayons X est basée sur un système micro-CT existant. Le micro-CT a été introduit au début des années 1980 par Elliot et Dover [Elliott and Dover, 1982].

Aujourd'hui, une grande variété de protocoles précliniques impliquent cette modalité d'imagerie. Celle-ci permet notamment d'obtenir des images caractérisées par un fort contraste entre le squelette, les poumons, et les tissus environnants, avec une résolution de l'ordre de 50 μm.

Description du matériel

Le système est constitué i) d'une source de rayons X à flux conique Hamamatsu L9181-02 ainsi que ii) d'un détecteur plan Hamamatsu C7942-CA22. Ces deux éléments sont solidaires et fixés sur une structure rotative. La distance source-détecteur est, de fait, fixée à 228 mm. Le rayon de rotation de la source quant à lui est fixé à 172 mm. La rotation de la structure ainsi que le fonctionnement de la source et du capteur sont contrôlés par le programme d'acquisition. Les données sont envoyées sur un serveur de reconstruction équipé d'une carte GPU.

La source de rayons X produit des rayons de 30 à 130 keV. Deux filtres permettent de durcir le spectre – 200 μm de Beryllium et 0.5 mm d'Aluminium. La taille de la tache focale dépend des paramètres de puissance de la source et vaut au minimum 5 μm et au maximum 40 μm, à 4 W et 39 W, respectivement.

Le détecteur est composé d'une plaque de matériaux scintillant couplé à une matrice de photodiodes de technologie CMOS. Un filtre de 1 mm d'Aluminium recouvre en outre la plaque scintillante. Celle-ci est composée d'iodure de Césium dopé au Thallium – CsI(Tl). La matrice comporte 2400×2400 pixels de taille 50 μm. Trois arrangements des pixels sont possibles, soit 1×1, 2×2 ou 4×4. La conversion analogique/numérique est intégrée au capteur. La sortie numérique est encodée sur 12 bits. La gamme dynamique est 2×10^3 et la moyenne quadratique du bruit est de 1100 électrons.

L'acquisition consiste en la mesure de 768 images radiologiques – ou *projections* – sur 360°. Le temps d'acquisition est fixé à 470 ms par projection pour un temps total de 6 minutes. Pendant l'acquisition, l'animal est placé dans le champ de vue sur un support prévu à cet usage. L'anesthésie est assurée par un mélange gazeux de 2% d'isoflurane dans l'air.

Algorithmes de reconstruction

Différents algorithmes peuvent être utilisés pour la reconstruction de l'image. Ces algorithmes peuvent être classés en deux catégories principales, i) les algorithmes analytiques et ii) les algorithmes itératifs. Les algorithmes itératifs se déclinent eux même en deux catégories que sont i) les algorithmes algébriques et ii) les algorithmes statistiques.

Chaque catégorie d'algorithme présente des avantages et des inconvénients par rapport aux autres. Les algorithmes analytiques consistent comme leur nom l'indique en une résolution analytique du problème de reconstruction. L'algorithme analytique de référence pour une géométrie d'acquisition à rayons parallèles est l'algorithme de filtrage/rétroprojection, FBP (Filtered BackProjection). Il exploite le théorème dit "de la coupe centrale" qui permet d'estimer la transformée de Fourier de l'image à partir des transformées de Fourier des projections. Dans sa formulation théorique continue, FBP permet de calculer exactement l'image correspondant aux mesures. Dans le cas de la géométrie à flux conique, l'algorithme *Feldkamp, Davis and Kress* (FDK, [Feldkamp et al., 1984]) est couramment utilisé et considéré comme l'algorithme de référence. La solution approximative calculée par cet algorithme est considérée quasi-exacte – et largement acceptée dans la communauté comme vérité terrain et comme base de comparaison pour l'évaluation d'autres algorithmes. En l'occurence, l'algorithme analytique FDK est utilisé en routine dans le cas du système étudié. Cet algorithme analytique est une extension de l'algorithme FBP – basé sur le théorème de la coupe centrale de Fourier – pour la géométrie d'acquisition à flux conique. Les images radiologiques collectées à chaque angle sont prétraitées puis utilisées en ligne pour la reconstruction de l'image. De fait, celle-ci est simultanée à l'acquisition à l'issue de laquelle l'utilisateur dispose immédiatement de l'image reconstruite. Une telle reconstruction "à la volée" n'est pas possible avec les algorithmes itératifs qui nécessitent de collecter l'ensemble des projections avant la première itération.

Différents facteurs tels que le bruit photonique, le courant de fuite du détecteur, les mouvements de l'animal et la précision de la calibration du micro-CT peuvent aboutir à des erreurs numériques dont l'impact est plus ou moins négligeable.

Les algorithmes itératifs constituent des approches radicalement différentes au problème de reconstruction. Comme leur nom l'indiquent, les algorithmes algébriques approchent le problème de reconstruction au moyen d'un formalisme algébrique. L'ensemble des mesures et l'image à estimer sont des vecteurs représentant le même objet dans des bases différentes – la base des mesures d'une part et la base de l'image d'autre part – et une matrice de projection permettant d'associer à un vecteur exprimé dans la base de l'image, un vecteur exprimé dans la base des mesures. Formellement, le problème est exprimé comme suit :

$$\tilde{g} = Pf \tag{1.1}$$

avec $\tilde{g}$ le vecteur des mesures, P la matrice de projection et f le vecteur de l'image. En théorie, faisant l'hypothèse que la matrice de projection est inversible, une inversion formelle de la matrice permet d'exprimer un vecteur de la base de l'image à partir d'un vecteur quelconque exprimé dans la base des mesures. On calculerait alors

$$f = P^{-1}\tilde{g} \tag{1.2}$$

En pratique, l'hypothèse d'inversibilité de la matrice n'est pas forcément valide et de surcroit les dimensions du problème rendent prohibitif le temps d'inversion formelle. Par conséquent, l'inversion numérique des matrices de projections est généralement préférée, par exemple au moyen de la méthode de Kaczmarz. C'est ce que fait l'algorithme ART qui à l'itération $k+1$ calcule :

$$f^{k+1} = f^k + \lambda P^b \frac{Pf^k - g}{\|P\|} \tag{1.3}$$

avec P^b la matrice de *rétroprojection* et λ un facteur de *relaxation*. Les algorithmes algébriques sont généralement plus sensibles au bruit des projections.

Les algorithmes statistiques quant à eux trouvent leur origine dans les tomographies d'émission. L'expression du problème sous forme statistique dans un formalisme Bayesien permet de rechercher des solutions qui maximisent la vraissemblance de l'image au vu des mesures collectées.

Différentes informations *a priori* peuvent être injectées dans les algorithmes itératifs afin de réduire le domaine des solutions possibles pour ne garder que les plus vraissemblables – selon des critères subjectifs. Il peut s'agir, par exemple, d'une contrainte de positivité de l'image, de limites spatiales imposées, ou encore de la "douceur" ou de la "rugosité" d'une image. Une *régularisation* permet en effet de renforcer certaines caractéristiques de l'image estimée dans le cas des algorithmes itératifs. La minimisation d'une fonctionnelle basée sur un caractère quantitatif lié à ces caractéristiques qualitatives permet typiquement de réaliser cette régularisation.

1.2.2 Reconstruction tomographique à angle limité

Limiter l'intervalle angulaire de l'acquisition en tomographie par rayons X revient

- du point de vue analytique, à réduire le nombre de coefficients de Fourier disponibles dans une certaine région de l'image ;
- du point de vue algébrique, à réduire le nombre d'équations du système à inverser ;

- du point de vue statistique, à réduire le nombre de mesures permettant de calculer l'image vraisemblable.

En dessous d'un certain seuil, le nombre de mesures ne suffit pas à estimer l'image dans une marge d'erreur acceptable par rapport à l'image quasi-exacte obtenue avec FDK pour une acquisition sur 360°. En fait, la réduction du nombre de mesures peut même compromettre la convergence de l'algorithme dans le cas itératif – en effet une infinité de solution peut correspondre aux mesures collectées – voire causer sa divergence. La distribution des mesures sur l'intervalle angulaire complet conduit à différentes occurences d'un problème aux données limitées. Dans notre cas, il s'agit d'un problème d'angle limité, c'est-à-dire que l'échantillonnage angulaire est suffisant sur l'intervalle angulaire couvert par l'acquisition, par contre celui-ci est tronqué – c'est à dire qu'une zone plus ou moins grande de l'intervalle angulaire $[0; 2\pi]$ ne comporte aucune mesure. L'intervalle angulaire *mesuré* est donc réduit à $[0; \omega]$, et l'intervalle angulaire *manquant* est $\bar{\omega} = 2\pi - \omega$. Les contraintes géométriques citées précédemment ont conduit, dans le cas précis de l'appareil étudié, à la conception d'un système micro-CT caractérisé par un débattement angulaire de $\frac{\pi}{2}$.

Etat de l'art

La problématique de la reconstruction tomographique à angle limité a suscité de nombreux travaux et diverses stratégies ont été proposées pour compenser le "manque d'information" qui résulte de la réduction de l'intervalle angulaire d'acquisition. On parle de manque d'information en partant du principe qu'une couverture et un échantillonnage angulaires minimums sont requis pour estimer l'image sans introduire d'artefacts. Dans ce travail, c'est la couverture angulaire qui est limitée – tandis que l'échantillonnage est gardé identique à une acquisition micro-CT standard. Dans le cas de la géométrie d'acquisition à flux conique, la couverture angulaire doit contenir l'intervalle $[0; \pi + \frac{\beta}{2}]$ où β est l'angle du cône. Or, on l'a vu, dans notre cas la couverture angulaire est l'intervalle $[0; \frac{\pi}{2}]$. L'application directe d'algorithmes développés pour une acquisition standard, tel que l'algorithme FDK, résulte en une image corrompue de nombreux artefacts. La réalisation d'une analyse qualitative et l'analyse quantitative de l'image s'en trouvent fortement impactées.

Les différentes stratégies proposées pour résoudre ce problème de données limitées peuvent être classées en trois catégories : i) les méthodes basées sur des transformées ; ii) les méthodes de "récupération" du sinogramme ; iii) les méthodes itératives.

Les méthodes basées sur des transformées travaillent dans un domaine réciproque au domaine spatial telles que la transformée de Fourier. Ces méthodes exploitent une formulation analytique du problème de reconstruction ; elles sont généralement désignées comme des méthodes de "convolution-rétroprojection" du fait du procédé utilisé. Couramment utilisées en reconstruction d'image pour des cas où la couverture angulaire est complète, certaines applications ont été reportées dans le cas de la reconstruction à angle limité – notamment pour la tomosynthèse numérique (DBT pour *Digital Breast Tomosynthesis*, [Dobbins and Godfrey, 2003]). Ces méthodes ont l'avantage de permettre une reconstruction d'image rapide ; les résultats sont généralement entachés d'artefacts ; pour cette raison, un couplage avec une méthode de restauration – par exemple dans le domaine des ondelettes – est parfois mis en oeuvre. L'injection d'une information *a priori* dans ces algorithmes de reconstruction est malaisée, sauf par exemple en imposant un support au sinogramme.

Les méthodes de récupération du sinogramme travaillent dans le domaine du sinogramme, c'est à dire de l'image transformée par la transformée de Radon. Dans le cas d'une acquisition à angle limité, le sinogramme est incomplet, c'est à dire qu'une bande – correspondant à l'intervalle angulaire non couvert – en est inconnue. Ces méthodes consistent typiquement à estimer la bande inconnue à partir de la partie connue du sinogramme, avant de réaliser une reconstruction standard par convolution-rétroprojection. Diverses approches d'interpolation ont été proposées, basées par exemple sur des conditions de consistence telles que celle de Helgason-Ludwig, ou sur la représentation du sinogramme connu par des sinusoïdes. En revanche, la plupart de ces méthodes ont été appliquées en géométrie à rayons parallèles et à des cas où la partie manquante du sinogramme est inférieure à 38% du sinogramme complet – à comparer à 44% dans notre cas. Les résultats reportés issus de la simulation utilisant des objets test numériques ne laissent pas supposer de résultats satisfaisants dans notre cas.

Les méthodes itératives travaillent directement dans le domaine de l'image. Elles sont typiquement basées sur une formulation algébrique ou statistique du problème de reconstruction. L'algorithme actualise l'image estimée à chaque itération, localement, par addition ou multiplication selon une formule déterminée par l'approche choisie. Une information *a priori* peut être injectée assez commodément dans le processus de reconstruction, soit directement dans la boucle itérative comme dans le cas de Maximum A Posteriori (MAP), ou dans une boucle itérative secondaire, comme c'est le cas dans l'algorithme Adaptive Steepest Descent - Projection Onto Convex Sets (ASD-POCS) [Sidky et al., 2009a]. Ces méthodes ont été proposées commes des alternatives viables aux algorithmes de reconstruction analytiques dans le cas de données manquantes. Des résultats très encourageants ont été rapportés à partir de simulation d'acquisition utilisant des objets test numériques. C'est le cas par exemple des travaux rapportés sur la minimisation de la norme Variation Totale (TV, pour *Total Variation*) pour régulariser la reconstruction.

Chaque voxel étant identifié par $f_{i,j,k}$, où i, j et k sont les indices dans les trois dimensions du repère cartésien discret, l'image de la magnitude du gradient (GMI pour *Gradient Magnitude Image*) de f est :

$$\nabla f_{i,j,k} = \sqrt{(\triangle_{i,j,k}^{i+1,j,k} f)^2 + (\triangle_{i,j,k}^{i,j+1,k} f)^2 + (\triangle_{i,j,k}^{i,j,k+1} f)^2} \tag{1.4}$$

avec $\triangle_{i,j,k}^{i',j',k'}$ l'opérateur discret du gradient :

$$\triangle_{i,j,k}^{i',j',k'} f = f_{i',j',k'} - f_{i,j,k} \tag{1.5}$$

et la norme TV de f – la norme ℓ_1 de la GMI de f est :

$$||f||_{TV} = \sum_{i,j,k} |\nabla f_{i,j,k}|. \tag{1.6}$$

La régularisation utilisant la TV a ses défenseurs et ses détracteurs au sein de la communauté. Elle est communément utilisée pour la restauration et le débruitage d'images. Récemment, elle a servi d'illustration à la théorie mathématique de l'échantillonnage comprimé (CS, pour *Compressed Sensing*) et a été appliquée à la reconstruction tomographique. Son usage est rapporté depuis pour différentes problématiques : acquisitions CT à faible échantillonnage angulaire, acquisitions CT à faible flux et donc bruitées, et enfin la tomosynthèse mammaire numérique (DBT pour *Digital Breast Tomosynthesis*) – problématique très proche du micro-CT à angle limité. Les résultats très prometteurs rapportés dans la littérature – par exemple dans [Sidky et al., 2009a] nous ont encouragé à implémenter un algorithme itératif régularisé minimisant la norme TV et à l'appliquer au système considéré.

Implémentation de l'algorithme ASD-POCS

Le problème d'optimisation à résoudre est le suivant : trouver la solution qui minimise la distance entre la projection de l'image estimée et les données mesurée ainsi que la norme TV de l'image, et respecte une contrainte de positivité. Formellement, l'optimum est défini ainsi :

$$f^* = \underset{f}{\operatorname{argmin}} ||f||_{TV}, \text{sujet aux contraintes } ||Pf - \tilde{g}||_{\ell_2}^2 \leq \kappa, f \geq 0 \tag{1.7}$$

where P denotes the projection matrix, $\tilde{g}$ denotes the projection data and κ is a small positive real number – the size of the error term.

L'algorithme Adaptive Steepest Descent - Projection Onto Convex Sets (ASD-POCS) – que l'on pourrait traduire par "Descente du gradient adaptative - projection sur des ensembles convexes" – a été proposé par Sidky *et al.* en 2009 [Sidky et al., 2009a]. Cet algorithme comporte une boucle itérative principale, elle-même composée i) d'une itération de l'algorithme Algebraic Reconstruction Techniques (ART), ii) une étape de "renforcement" de la positivité et iii) une boucle itérative de descente du gradient utilisant comme fonctionnelle la norme TV de l'image.

L'algorithme peut être exprimé formellement de la manière suivante : La boucle itérative principale est repérée par l'indice $k \in \mathbb{N}$ tel que $1 \leq k < K$, et la boucle de la descente du gradient est repérée par l'indice $l \in \mathbb{N}$ tel que $1 \leq l < L$ La formule d'actualisation de l'étape ART est :

$$f^{k+1} = f^k + r\frac{P^b(\tilde{g} - Pf)}{\|P\|} \tag{1.8}$$

avec $r \in \mathbb{R}^{+*}$ le facteur de relaxation de l'ART et P^b l'opérateur de rétroprojection. La seconde boucle itérative peut être formalisée comme suit :

$$f^{l+1,k+1} = w \times |\bar{f}^{k+1} - f^{k+1}| \times \left[\frac{\partial\|f\|_{TV}}{\partial f^{l,k+1}}\right]_{i,j,k} \tag{1.9}$$

où $w \in \mathbb{R}^{+*}$ est le facteur de relaxation pondérant la descente du gradient et

$$\bar{f}_{i,j,k} = \begin{cases} f_{i,j,k} & \text{si } f_{i,j,k} \geq 0 \\ 0 & \text{sinon.} \end{cases} \tag{1.10}$$

L'expression discrète de $\partial\|f\|_{TV}/\partial f^{l,k+1}$ en Equation 3.37 est celle dans [Persson et al., 2001], corrigée.

Les étapes i) et ii) correspondent à la projection sur des ensembles convexes (POCS). En fait, ART permet de conformer l'image aux mesures à chaque itération de la boucle principale, en calculant un terme correctif à apporter à l'estimation actuelle, défini comme la différence entre la projection simulée de l'estimation actuelle et des mesures effectivement collectées. Le "renforcement" de la positivité correspond à l'injection d'une information *a priori* dans l'algorithme – qui correspond à la définition physique du coefficient d'atténuation : celui-ci peut être considéré nul, mais pas négatif. Il s'agit bien d'une projection sur des ensembles convexes où la solution est projetée sur différents hyperplans convexes renforçant la conformité à chacune des mesures et finalement sur un hyperplan correspondant aux solutions positives. L'objectif est d'approcher itérativement le point de l'espace des solutions qui correspond à l'objet observé. Les mesures, incomplètes, peuvent en fait correspondre à une infinité de solutions. Les deux premières étape seules ne suffisent pas en pratique à converger vers une solution stable. Ceci est illustré dans l'article [Sidky et al., 2009a], dans lequel il est rendu évident que la convergence de l'algorithme ART est peu probable dans un cas aussi pénalisé que le notre. La minimisation de la norme TV par la descente du gradient est proposée comme une manière de restreindre le domaine des solutions possibles. Diverses applications de l'algorithme ASD-POCS ont été rapportées dans la littérature, incluant une application très similaire à la notre présentée dans une étude par simulation [Sidky et al., 2009a].

Plusieurs paramètres permettent de réguler le fonctionnement de l'algorithme. Mises de côté les caractéristiques données telles que le nombre de voxels utilisés pour représenter l'image et le nombre de pixels utilisés pour les mesures, le nombre d'itérations des boucles principale et secondaire, ainsi que des "facteurs de relaxation" pondérant l'actualisation additive dans les algorithme ART et de descente du gradient doivent être choisis et spécifiés par l'utilisateur au préalable. En d'autres termes, contrairement à un algorithme analytique tel que FDK où la valeur des paramètres peut être déterminée de manière unique pour des caractéristiques données de l'image et des mesures, il existe un certain nombre de paramètres "libres" influençant les résultats. Ces paramètres libres constituent l'un des points faibles de l'algorithme, le choix de ces paramètres n'étant pas dicté par les caractéristiques propres de l'image et des mesures. La convergence de l'algorithme n'a – en outre et par conséquent – pas été prouvée – à la différence d'autres algorithmes basés sur la minimisation de la norme TV [Defrise et al., 2011].

L'algorithme a été implémenté par l'auteur sous la forme d'un programme C++ sur une unité centrales de traitement (CPU pour *Central Processing Unit*) (intel core i7 980 at 3.33 GHz) dont certaines tâches sont parallélisées sur carte graphique (GPU pour *Graphical Processing Unit*, NVIDIA GTX 580) en langage de programmation CUDA. Les possibilités actuelles d'implémentation sur architecture parallèles permettent, au moyen d'un serveur de reconstruction équipé d'une carte graphique, de reconstruire une image dans un temps équivalent au traitement sur de multiples CPU par une grappe de serveurs.

Evaluation de l'algorithme

L'algorithme implémenté a été appliqué à la géométrie d'acquisition considérée dans ce travail. Une évaluation méthodique des résultats en fonction du choix des paramètres libres s'est avérée nécessaire. A cette fin, plusieurs ensembles de données simulées et issues d'acquisitions précliniques ont été utilisés. Plusieurs options existent pour la simulation, en fonction de la représentation de l'objet choisie – analytique, discrète – et du principe de simulation – analytique ou par tirages aléatoires. L'étude est composée de deux volets, le premier se concentrant sur la tranche centrale du système d'acquisition – donc en deux dimensions, le second considérant la géométrie conique à l'étude en trois dimensions.

Etude dans la tranche centrale Dans notre cas, les données simulées ont été obtenues par simulation analytique pour un objet représenté de manière analytique ainsi que pour le même objet représenté de manière discrète. Les données précliniques ont été acquises au moyen du système micro-CT défini à la section 1.2.1. Dans ces différents cas, un nombre identique de 768 projections a été acquis sur la couverture angulaire complète – l'intervalle $[0; 2\pi]$. Plusieurs couvertures angulaires ont ensuite été choisies, en conservant le même échantillonnage angulaire : π, $\pi/1.2$, $\pi/1.5$, $\pi/2$, correspondant respectivement à 384, 320, 256, 192 projections. Les projections comprises dans ces différents intervalles angulaires ont été utilisées afin de reconstruire une image à partir des différents ensembles de données. Les projections simulées sont composées de 2048×2350 pixels de côté 50 μm, et réarrangées en 512×578 pixels de côté 200 μm avant l'extraction de la ligne centrale. Les images reconstruites sont composées de voxels cubiques de côté 400 μm – soit 128×128 voxels pour les données simulées, et 120×90 pour les données précliniques.

L'étude a consisté à comparer les images estimées pour 1000 itérations de la boucle itérative principale avec différents jeux de paramètres selon un critère quantitatif, en l'occurence une mesure de distance entre l'image estimée et une image de référence. Le critère quantitatif est défini par :

$$M_{re}(f, f_{ref}) = \|f - f_{\mathrm{ref}}\| / \|f_{\mathrm{ref}}\| \tag{1.11}$$

L'objectif était à la fois d'observer l'impact des différents paramètres sur l'image reconstruite, et de déterminer, dans chaque configuration, l'image optimale qui pourrait être obtenue. L'observation de l'image optimale obtenue pour chaque intervalle angulaire permet de procéder à l'analyse qualitative.

Etude en trois dimensions L'étude de l'algorithme en trois dimensions a été réalisée au moyen de données précliniques, obtenues au moyen d'une acqusition standard d'une souris. Une image tomographique "de référence" a été reconstruite en utilisant l'algorithme FDK. Les projections correspondant à une couverture angulaire de $\pi/2$ ont ensuite été isolées afin de comparer les résultats à l'image de référence. De même que pour l'étude dans la tranche centrale, différents jeux de paramètres ont été confrontés pour un nombre d'itérations fixe de la boucle itérative principale. Une fois la reconstruction optimale obtenue, une analyse quantitative de cette image a été réalisée, utilisant l'information extraite de l'image de référence. A cette fin, divers tissus – squelette, poumons, foie, coeur, rate, reins – ont été segmentés de manière semi-automatique et manuelle à partir de l'image reconstruite avec FDK utilisant l'ensemble des données d'une acquisition standard, et à partir d'une acquisition du même animal dans la même position, auquel un agent de contraste iodé (Iomeron) a été injecté. L'objectif de cette étude quantitative était de comparer la valeur moyenne du coefficient d'atténuation obtenue au sein de différents tissus, entre l'image estimée et l'image de référence, ainsi que le contraste entre les tissus.

Le protocole d'acquisition est le suivant : i) anesthésie d'une souris de type naturel par mélange gazeux d'air et 2% d'isoflurane ; ii) placement de l'animal sur le support prévu au centre du champ de vue du micro-CT ; iii) acquisition de 768 projections sur $360°$ – paramètres de puissance $40\ \mathrm{kV}, 200\ \mu\mathrm{A}$, temps d'intégration $470\ \mathrm{ms}$ et pixels en binning 1×1 soit 2048×2350 pixels de côté $50\mu\mathrm{m}$. iv) réarrangement des projections sur une grille de pixels de côté $200\ \mu\mathrm{m}$. Le protocole de segmentation est identique à celui décrit en Section 1.4.2 après reconstruction standard par l'algorithme FDK.

La reconstruction d'image a ensuite été effectuée à partir des projections acquises sur $90°$ avec 100 itérations de l'algorithme ASD-POCS sur une grille de voxels cubiques de côté $400\ \mu\mathrm{m}$ centrée sur l'abdomen de l'animal. Les paramètres ont été déterminés de manière identique à celle utilisée pour la tranche centrale 1.2.2 au moyen d'une étude basée sur la simulation de projections utilisant un fantôme anatomiquement réaliste, généré à partir de l'atlas anatomique Digimouse [Dogdas et al., 2007].

Résultats

Les résultats de l'étude dans la tranche centrale sont présentés en Figure 3.14, pour les différents types de données et pour différents intervalles angulaires. La valeur de M_{re} en fonction de l'intervalle angulaire est représentée dans le graphique en Figure 3.12. La valeur de la norme TV normalisée par la TV de l'image de référence en fonction de la valeur de M_{re} est représentée dans le graphique en Figure 3.13. Les tableaux 3.6, 3.7 et 3.8 contiennent les valeurs des paramètres correspondant aux images optimales déterminées ainsi que la valeur de M_{re} et de la norme TV à l'issue des 1000 itérations, pour chaque jeu de données.

Concernant l'étude en trois dimensions, les tableaux 3.9 et 3.10 contiennent la valeur des contrastes entre les différents tissus étudiés. La Figure 3.16 représente le coefficient d'atténuation moyen calculé pour les différents tissus étudiés, dans l'image de référence et dans l'image tomographique à angle limité.

La Figure 3.15 représente le temps d'exécution pour une itération de l'algorithme ASD-POCS, sur un CPU et avec l'implémentation GPU réalisée, respectivement, en fonction de différents couples taille de pixel / taille de voxel pour un objet de taille $51.2 \times 51.2 \times 51.2\ \mathrm{mm}^3$ et des projections de taille $102.4 \times 102.4\ \mathrm{mm}^2$.

Discussion

L'étude dans la tranche centrale met en évidence un phénomène dénommé *inverse crime*, observable pour les données simulées à partir du fantôme discret. Le fait d'utiliser pour la simulation le même opérateur de projection que dans l'algorithme de reconstruction a pour effet de permettre une reconstruction quasi-exacte même avec très peu de mesures. En revanche, une telle reconstruction ne peut pas être attendue de données plus réalistes telles que celles simulées avec un fantôme analytique ou de surcroît des données précliniques. Dans ce cas, la régularisation par la minimisation de la norme TV a un effet "aggravant" – dans le sens où l'algorithme ne diverge pas, contrairement à l'ART seul. Ce phénomène peut être observé dans les résultats présentés dans [Sidky et al., 2009a]. Revenant à notre travail, les images reconstruites sont globalement lisses – en particulier celles issues des données précliniques, desquelles on pourrait attendre un bruit plus important de fait des statistiques d'émission et de comptage. La minimisation de la norme TV a été introduite en traitement d'image pour des tâches de débruitage ; ainsi l'observation d'image lisses n'a rien de surprenant. D'autre part, mis à part l'*inverse crime*, il peut être observé que la réduction de l'intervalle angulaire, quelle que soit la source des données, aboutit à la dégradation de l'image, mise en évidence qualitativement, pour un nombre d'itérations égales, par l'apparition d'artefacts localisés, et quantitativement par une distance plus importante entre l'image estimée et l'image de référence. Les artefacts observés rendent floues les frontières entre les structures de l'objet, ainsi que la frontière entre l'objet et l'air. Les frontières nettes sont celles auxquelles une ligne de réponse a été tangente au cours de l'acquisition. Les autres sont plus ou moins lissées, en fonction de la taille de la structure considérée. L'analyse qualitative des résultats permet, enfin, d'observer que malgré les artefacts localisés et rendant floues les frontières entre certaines structures à fort contraste demeurent visibles dans l'image reconstruite – malgré une apparente distorsion due aux fluctuations d'intensité et de manière primordiale aux artefacts lissant les frontières. Dans les images issues des données précliniques, ces structures à fort contraste sont typiquement des structures osseuses. Cette observation encourage à considérer la distinction automatique des structures à fort contraste.

En ce qui concerne l'étude en trois dimensions, on peut observer, outre que les observations faites dans l'étude dans la tranche centrale tiennent, que le contraste entre le squelette, les poumons et les tissus adjacents est globalement diminué, – il demeure en revanche significativement supérieur aux contraste des autres tissus entre eux. Cette observation i) confirme l'observation qualitative faite dans l'étude de la tranche centrale et ii) encourage à considérer la segmentation automatique des tissus à fort contrastes.

De manière générale concernant l'utilisation de l'algorithme, nous soulignons la difficulté du choix des paramètres. Comme on l'a vu, le fonctionnement du programme peut être réglé par différents paramètres, et aucune règle n'a été publiée à ce jour qui permettrait de déterminer, pour une acquisition donnée, les paramètres à utiliser. Dans l'étude réalisée, une image "optimale" correspondant à un jeu de paramètres "optimal" a été désignée, sur la base de la comparaison avec une image de référence. En revanche, pour une acquisition réellement pénalisée pour laquelle aucune vérité terrain ne peut être déterminée, cette comparaison est impossible. La simulation permet d'apporter une réponse à cette problématique – on peut imaginer par exemple la recherche d'un jeu de paramètres optimal au moyen d'un objet test présentant des caractéristiques similaires à celles attendues dans l'objet observé – par exemple, un modèle numérique anatomiquement réaliste tel que MOBY [Segars et al., 2004] ou Digimouse [Dogdas et al., 2007]. Le point faible de cette approche est qu'elle ne permet pas de déterminer le jeu de paramètre optimal avec certitude pour l'objet réellement observé. Elle a néanmoins l'avantage de baser le choix sur une étude préalable. En ce qui concerne la détermination même du jeu de paramètres optimal, une recherche exhaustive sur l'ensemble des paramètres a été réalisée. L'utilisation d'algorithmes d'optimisation paramétrique tels que les algorithmes génétiques serait une alternative à cette approche. Le nombre d'itérations de la boucle principale a, quant à lui, été choisi de manière arbitraire, faute d'un critère de convergence robuste.

Enfin concernant le temps de reconstruction, on peut observer que l'implémentation sur GPU réduit drastiquement le temps de reconstruction. Celui-ci reste néanmoins prohibitif pour un nombre élevé d'itérations tel que celui utilisé dans les études présentées. La programmation multi-GPU offre une perspective de réduction proportionnelle du temps de reconstruction pour un nombre plus important de voxels et de pixels. Quoi qu'il en soit, le temps de reconstruction peut s'avérer un critère de choix ou de rejet décisif par rapport à l'applicabilité de l'algorithme dans un contexte préclinique.

1.3 Segmentation des tissus à fort contraste

Ce travail traite de l'obtention d'une information anatomique à partir d'images tomographiques, en vue de l'injection de cette information dans un algorithme de reconstruction d'image pour la tomographie optique par luminescence. Les images micro-CT sont caractérisées par un contraste relativement important entre le squelette, les poumons, et les tissus adjacents – ainsi qu'entre les tissus et l'air qui les entoure. Ces tissus, typiquement regroupés sous l'appellation "tissus à fort contraste", peuvent généralement être aisément distingués à l'oeil nu autant que par des méthodes informatisées basées sur un critère quantitatif de distinction. A l'inverse, les autres tissus sont rassemblés sous l'appellation "tissus à faible contraste", le contraste qu'ils présentent entre eux étant typiquement insuffisant pour les distinguer à l'oeil nu autant qu'au moyen de méthodes informatisées basées sur un critère quantitatif de distinction. On trouve dans la littérature différentes propositions visant à compenser ce manque d'information par l'intermédiaire d'un modèle numérique des tissus – ou "atlas anatomique". Il s'agit dès lors d'associer à l'image reconstruite une configuration de l'atlas anatomique ; cette configuration est déterminée par une procédure de "recalage", basée sur des éléments significatifs dont on considère qu'ils sont communs à l'objet observé et à l'atlas anatomique, désignés par le terme "amers". Les images tomographiques considérées dans ce travail sont, de surcroît, dégradées par une couverture angulaire d'acquisition réduite afin de satisfaire aux choix de conception du PhotonIMAGER Optima, appareil d'imagerie optique par luminescence du petit animal, corps entier. On a vu dans la section précédente que le contraste entre le squelette, les poumons et les tissus adjacents restait largement supérieur au contraste entres les autres tissus même dans le cas du micro-CT à angle limité. C'est ce constat qui nous a conduit à considérer la mise en place d'une procédure standardisée qui permettrait i) d'identifier automatiquement les tissus à fort contraste dans les images tomographiques, ii) d'en générer une représentation qui permette d'envisager commodément le recalage d'un modèle anatomique.

La représentation choisie dans ce travail est celles des maillages surfaciques à base triangulaire. Cette représentation très commode consiste à représenter le domaine d'intérêt comme l'intérieur d'une surface dont le maillage constitue une approximation plane par morceaux et dont l'élément de base est le triangle. Par conséquent, les procédures de recalage utilisées dans ce travail sont toutes basées sur des amers géométriques – en l'occurence les points correspondant aux sommets du maillage. L'un des avantages de ces procédures est leur versatilité par rapport à la diversité des sujets observables.

1.3.1 Procédé, méthode

La segmentation des tissus à fort contraste a été réalisée de manière entièrement automatique. Plusieurs fonctionnalités ont été articulées à cette fin. La première consiste en la distinction "de bas niveau" des tissus entre eux, c'est à dire basée sur un critère quantitatif seulement. La seconde est l'injection d'une information "de haut niveau", qui permet d'attribuer aux différentes régions de l'image une signification anatomique. En l'occurence, le squelette et l'enveloppe sont d'abord segmentés par la distinction de bas niveau. Dans un second temps, la région de la cage thoracique est déterminée par l'injection de l'information de haut niveau. Enfin, les poumons sont segmentés par distinction "de bas niveau" intégrant l'information de leur localisation dans la cage thoracique.

La distinction des tissus proprement dite est basée sur le critère quantitatif de la valeur du coefficient d'atténuation. Une méthode utilisant le principe du grossissement de régions a été implémentée. Elle consiste i) à spécifier une valeur du coefficient d'atténuation qui sera utilisée pour la recherche de "graines" ; ii) à rechercher les graines associées – c'est à dire tous les voxels dont la valeur est égale à celle spécifiée ; iii) à faire grandir une région autour des voxels ainsi déterminés, la croissance s'arrêtant lorsqu'un seuil inférieur et un seuil supérieur – spécifiés par l'utilisateur – ont été atteints. La région déterminée à l'issue de cette procédure est ensuite "pavée" au moyen de l'algorithme Marching

Cubes [Lorensen and Cline, 1987] dont le résultat est un maillage surfacique triangulaire de la surface entourant la région.

L'injection d'une information "de haut niveau" est mise en oeuvre par une procédure de recalage. Dans un premier temps, un "modèle" du squelette est créé en amont – et destiné à servir par la suite dans toutes les occurences de la segmentation – comme suit : i) un squelette est identifié par distinction de bas niveau dans une image tomographique obtenue par acquisition et reconstruction standard ; ii) un maillage de ce squelette est généré en utilisant l'algorithme Marching Cubes ; iii) le maillage du modèle est segmenté manuellement, distinguant chacune des pattes avant et arrière, le crâne, la cage thoracique, la colonne vertébrale, le pelvis et la queue. Dans un second temps, la procédure suivante est appliquée à l'image micro-CT considérée : i) le squelette est identifié par distinction de bas niveau dans l'image reconstruite ; ii) un maillage de ce squelette est généré en utilisant l'algorithme Marching Cubes – il s'agit du maillage "cible" ; iii) le maillage modèle est recalé de manière rigide sur le maillage cible au moyen de l'algorithme de recherche itérative du point le plus proche (ICP pour *Iterative Closest Point*, [Besl and McKay, 1992]) ; iv) le maillage modèle est recalé de manière non-rigide sur le maillage cible au moyen de l'algorithme d'appariement robuste de points (RPM pour *Robust Point Matching*, [Chui and Rangarajan, 2003]) ; v) dans le cas du micro-CT, la "boîte inclusive minimale" – *minimal bounding box/ enclosing box* – contenant la cage thoracique est utilisée pour restreindre la recherche des poumons ; dans le cas du micro-CT à angle limité, la "coquille convexe" – *convex hull* – de la cage thoracique a été déterminée et utilisée comme domaine de recherche pour les poumons.

Les valeurs utilisées pour la recherche de graine et le seuillage, pour les distinctions de bas niveau, sont reportées dans le tableau 4.2. Les images sont, au préalable, i) réarrangées pour obtenir des voxels de 400 μm et ii) filtrées afin de s'affranchir du bruit et de petits éléments de forte intensité assimilables au squelette. Le filtrage a l'inconvénient de réduire la résolution spatiale des images, néanmoins l'observation des résultats de la segmentation pour des images filtrées et non filtrées indique qu'il permet effectivement de s'affranchir d'éléments étrangers au squelette et que la perte de résolution n'est pas préjudiciable à l'échelle spatiale utilisée.

1.3.2 Application à des images micro-CT

Le protocole d'acquisition est celui présenté dans la section 1.2.2 pour l'étude en trois dimensions. Plusieurs jeux de données ont été collectés, de différentes souris. Dix d'entre eux ont été utilisés pour l'évaluation. Dans ce qui suit on considère que le résultat de l'étape de distinction de bas niveau pour le squelette et l'enveloppe constitue la vérité terrain. Aussi, aucune segmentation manuelle n'a été utilisée comme référence pour réaliser la comparaison. De même, le résultat de la segmentation des poumons utilisant l'information de haut niveau est considérée comme la vérité terrain.

L'un des points critiques de la segmentation est l'injection de l'information de haut niveau. En effet, le succès de la segmentation des poumons repose sur le succès de cette étape. L'évaluation a donc porté en priorité sur la segmentation du squelette en sous-parties, qui constitue le prérequis à l'injection de cette information de haut niveau. L'évaluation a été menée de manière qualitative, par la confrontation des observations de huit observateurs humains. Une échelle de notation qualitative a été définie pour caractériser les observations qualitatives. Elle est reportée dans la table 4.4. Chacun des observateurs a attribué une note à chacun des éléments du squelette pour chaque animal – i) le crâne, ii,iii) chaque patte avant dans son intégralité, iv,v) chaque patte arrière dans son intégralité, vi) la queue, vii) la cage thoracique, viii) la colonne vertébrale et le pelvis considérés comme un élément unique, ix) la colonne vertébrale, la cage thoracique et le pelvis considérés comme un élément unique – sans contrainte de temps à respecter ; un livret était mis à leur disposition, contenant des planches anatomiques du squelette. Les résultats de l'évaluation par les autres évaluateurs n'ont pas été communiqué à l'évaluateur durant l'évaluation, et l'attribution d'une note à chaque partie du squelette est définitive, non modifiable par la suite. Seul l'attribution des labels à chaque élément du squelette a été évaluée – et non la morphologie des éléments observés, par exemple une partie du crâne absente de l'image ne doit pas dégrader la note attribuée au crâne.

La représentation de chaque squelette, enveloppe et poumons ainsi que les résultats de l'évaluation qualitative sont représentés en Annexe C. La Figure 4.13 représente les résultats de l'analyse qualitative de la segmentation du squelette pour un individu.

Les résultats des segmentations ainsi réalisées ont été utilisés pour l'évaluation de l'application de l'approche au micro-CT à angle limité.

1.3.3 Application à des images micro-CT à angle limité

La procédure de segmentation automatique a été appliquée à des images micro-CT à angle limité. La reconstruction a été réalisée suivant la procédure indiquée en section 1.2.2 avec 100 itérations d'ASD-POCS et le jeu de paramètres déterminé par l'optimisation par simulation. Les jeux de données de 4 individus utilisés pour la segmentation des images micro-CT ont été restreints aux projections correspondant à la couverture angulaire de $\pi/2$ – soit 192 projections. Une fois les images reconstruites, la même procédure de segmentation leur a été appliquée, avec des valeurs de seuil appropriées.

Les surfaces générées des poumons et squelettes segmentés sont représentés en Figure 4.14 et Figure 4.15, respectivement. Un code couleur défini aux equations, 4.5 et 4.6 dans la partie en anglais de ce manuscrit, permet de représenter la distance entre la surface de référence issues de la segmentation des images micro-CT et la surface issue de la segmentation des images micro-CT à angle limité.

L'analyse des résultats a été effectuée au moyen de mesures de similarité entre les surfaces déterminées par la segmentation des images micro-CT et les surfaces déterminées par la segmentation des images micro-CT à angle limité. Trois mesures ont été utilisées : le coefficient de Dice D, le rapport des volumes $\mathrm{R_v}$, et la distance réciproque moyenne $\mathrm{A_{SD}}$ entre les surfaces. Elles sont définies comme suit :

$$\mathrm{D} = 2 \times \frac{|S_r \cap S_m|}{|S_r| + |S_m|} \tag{1.12}$$

$$\mathrm{R_v} = \frac{V_r}{V_m} \tag{1.13}$$

$$\mathrm{A_{SD}} = \frac{1}{2}\left[\frac{1}{n_r}\sum_{i=1}^{n_r} d_i + \frac{1}{n_m}\sum_{j=1}^{n_m} d_j\right] \tag{1.14}$$

Ces trois mesures sont complémentaires et compensent l'absence d'une mesure qui pourrait rendre compte tout à la fois du recouvrement des surfaces, de leur distance réciproque et du volume estimé, globalement et localement. Elles fournissent une mesure globale, qui doit nécessairement être complétée par une analyse qualitative permettant d'expliquer les valeurs obtenues par des différences morphologiques locales et/ou globales. Les résultats de la comparaison sont reportés dans les tableaux 4.5, 4.6, 4.7 pour l'enveloppe, le squelette et les poumons, respectivement. Les valeurs du coefficient de Dice sont supérieures ou égales à 0.75 dans tous les cas. Le rapport des volumes indique une légère surestimation pour l'enveloppe – entre 1.02 et 1.10, une surestimation relativement importante pour les poumons – entre 1.22 et 1.46, et une sous-estimation pour le squelette – entre 0.7 et 0.76. Enfin, les distances sont comprises entre entre 0.47 et 0.62 mm pour l'enveloppe, 0.23 et 0.39 mm pour le squelette, et entre 0.51 et 0.67 mm pour les poumons ; les écarts-type sont du même ordre de grandeur.

1.3.4 Discussion

Concernant la segmentation des images micro-CT, il a été mentionné que les surfaces extraites seraient considérées comme la vérité terrain. En pratique, ce choix pourrait être consolidé par la comparaison avec des segmentations manuelles. Il serait rigoureux de comparer les surfaces représentant les poumons aux surfaces qui auraient été obtenues par spécification manuelle d'une graine dans la région des poumons. De même il serait rigoureux de comparer le résultat de la segmentation des squelettes et de l'enveloppe à une segmentation manuelle. En revanche ces segmentations sont coûteuses en temps, fastidieuses et peu reproductibles ; le bénéfice d'une telle opération est donc discutable.

Les valeurs obtenues pour le coefficient de Dice indiquent une bonne adéquation entre les surfaces en termes de recouvrement. Les rapports de volumes indiquent néanmoins que les volumes inclus dans les surfaces extraites des images micro-CT à angle limité sont parfois surestimés – enveloppe et poumons – et parfois sous-estimés – squelette. L'observation des représentations de ces surfaces permet de dégager certaines causes de ces sur- et sous-estimations. En effet, l'observation des surfaces des squelettes met en évidence certaines parties manquantes, telles que le sommet du crâne – et, de manière générale, les régions oblongues auxquelles aucune ligne de réponse n'est tangente au cours de l'acquisition. L'observation des images tomographiques permet d'expliquer l'absence de certaines de ces parties : du fait de l'absence de certaines lignes de réponse – le manque d'information – les reconstructions sont, on l'a vu, caractérisées par un artefact qui lisse les frontières entre les structures. Il en résulte une sous-estimation du volume du squelette, puisque celui-ci se trouve amputé de certaines parties. Le recouvrement semble, par ailleurs, être adéquat pour les parties correctement reconstruites, hormis une légère distorsion suivant la direction des lignes de réponse inconnues.

A l'inverse, pour les poumons et l'enveloppe, l'artefact lissant les structures a pour effet d'accroitre l'étendue spatiale des régions segmentées. Il en résulte une sur-estimation du volume ; l'observation des surfaces et des valeurs du coefficient de Dice indique par ailleurs que le domaine de référence est en grande partie contenu dans le domaine extrait par segmentation de l'image micro-CT.

Les valeurs de la distance réciproque entre les surfaces et leurs écarts type peuvent être expliquées de la même manière : la distance réciproque moyenne est relativement faible par rapport à la taille des voxels utilisés pour la reconstruction – 400μm, ce qui indique que les surfaces sont globalement proches. C'est le cas notamment dans toutes les régions auxquelles une ligne de réponse a été tangente pendant l'acquisition. Les écarts type du même ordre de grandeur que les moyennes, en revanche, sont révélateurs de la différence induite par l'artefact lissant les frontières : ainsi dans le cas du squelette la distance entre un point au sommet du crâne dans la surface de référence et la surface réciproque est nettement plus élevée que la distance entre un point d'une patte par rapport à la surface réciproque. Dans le cas de l'enveloppe et des poumons, la distance est plus élevée sur les limites de la zone de distorsion.

Le temps de traitement moyen requis pour réaliser la segmentation est de 40 minutes, dont 10 pour le filtrage Gaussien et 25 pour le recalage non-rigide. Ce temps de traitement pourrait être grandement réduit par l'optimisation des programmes et notamment l'implémentation sur GPU de l'algorithme RPM de recalage non-rigide et de l'opération de filtrage gaussien. Les programmes compilés, pour l'instant appelés par un script bash qui permet de prototyper le processus et de gérer les données de manière flexible, pourraient-être réagencés et intégrés dans un super-programme compilé. Cette approche aurait en outre l'avantage de réduire les transferts de mémoire entre ROM et RAM.

1.4 Segmentation automatique des tissus à faible contraste utilisant un atlas statistique

Les modèles numériques des tissus biologique peuvent être distingués de manière schématique en deux grandes catégories, i) les modèles déterministes générés à partir d'une unique observation et représentation de l'ensemble tissus – une unique observation signifie ici l'ensemble des observations faites d'un seul individu, éventuellement obtenue à partir de différentes modalités d'imagerie – et ii) les modèles statistiques générés à partir d'un ensemble d'observations des tissus. La première catégorie suppose la segmentation d'images d'un individu et le rassemblement des informations ainsi collectées dans un objet commun, l'atlas anatomique. Dans ce modèle, typiquement, le contour de chaque tissu est décrit de manière discrète – au moyen d'une grille de voxels ou d'un maillage surfacique par exemple, paramétrique – par exemple au moyen de NURBS (Non Uniform rational B-Splines) – ou implicite, par exemple au moyen de cartes de distance signées (SDF pour *Signed Distance Function*). Certains atlas comprennent un module de modélisation de phénomènes physiologiques tels que la déformation de la cage thoracique au cours des phases d'inspiration et d'expiration ou le battement du coeur, ou encore des modèles cinétiques de distributions de traceurs. Ces modules de simulation ne sont pas considérés dans notre travail, dont l'objectif est de représenter les tissus à un instant donné, négligeant les déformations subies par les tissus au cours de l'acquisition. Le recalage de tels modèles implique donc d'avoir recours à l'établissement de correspondance entre les points ; l'absence de contraintes peut mener à des résultats aberrants. Des méthodes de recalage incluant des contraintes explicites censées garantir le réalisme des déformations ont été proposées, par exemple dans [Baiker et al., 2010] où les déformations rigides des parties principales du squelette sont régies par un système de liaisons mécaniques.

Les atlas statistiques, quant à eux, modélisent le contour des tissus de manière statistique. En d'autres termes, ils encapsulent une représentation explicite des variations morphologiques au sein d'une population, qui se ramène à une combinaison linéaire de vecteurs de variation ajoutés ou soustraits au contour moyen de l'objet sur la population considérée. Le recalage de ces modèles peut mobiliser différentes techniques de recalage rigide et non-rigide, mais comprend aussi forcément une phase d'estimation itérative des coefficients pondérant les principaux modes de variation morphologique.

Dans ce travail, la segmentation des tissus à faible contraste a été réalisée au moyen d'un atlas statistique. L'atlas statistique est un modèle numérique rassemblant une description statistique des contours des différents tissus de l'animal. Ce modèle complexe exploite l'interdépendance de certaines des caractéristiques morphologiques des tissus à fort contraste d'une part, et à faible contraste d'autre part. Deux modèles statistiques de la forme reliés par un modèle conditionnel Gaussien permettent d'estimer les contours des tissus à faible contraste à partir des contours des tissus à fort contraste identifiés dans les images tomographiques par la méthode présentée en section 1.3. Il ne s'agit donc pas rigoureusement de segmentation puisque les régions sont délimitées sans considération des critères quantitatifs dans l'image.

1.4.1 Atlas statistique : description du concept

Le contour d'un tissu est la surface qui délimite l'intérieur et l'extérieur de ce tissu. La description de ce contour peut être considérée comme une observation des caractéristiques morphologiques de ce tissu. La collecte d'un ensemble d'observation des caractéristiques morphologiques du même tissu, dans des individus différents, permet de traiter cette information par des méthodes statistiques. Les méthodes introduites en morphométrie géométrique permettent, notamment, de décrire par un nombre réduit de vecteurs propres l'ensemble des variations statistiques du contour d'un élément, au sein d'un échantillon [Bookstein, 1989]. Le modèle statistique ainsi obtenu représente la forme de l'élément observé ; il est dénommé "modèle statistique de la forme" (SSM pour *Statistical Shape Model*). Cette méthode est particulièrement intéressante dans le cas des données issues de l'imagerie biomédicales, où le contour d'un tissu est courramment représenté par un grand nombre de points - par exemple, les sommets du maillage triangulaire qui constitue l'approximation de la surface.

La construction d'un SSM suppose que le contour d'une instance quelconque d'un élément peut être représentée par un vecteur f. Celui-ci peut être exprimé comme :

$$f = \bar{f} + Vb \tag{1.15}$$

où $\bar{f}$ est le contour moyen de l'instance sur la population, V est une matrice contenant les modes de variation et b est un vecteur pondérant chacun des modes de variation.

La question de la relation entre les deux modèles statistiques de la forme est bien entendue capitale, car deux modèles statistiques des tissus à fort contraste d'une part, et des tissus à faible contraste d'autre part, peuvent être générés de manière indépendante ; ils doivent être mis en relation une fois cette étape terminée. Le modèle conditionnel gaussien (CGM, pour *Conditional Gaussian Model*) a été proposé pour représenter la corrélation entre le contours de vertèbres en radiographie [Iglesias and de Bruijne, 2007]. Il a été proposé comme une approche viable pour mettre en relation deux modèles statistiques de la forme dans le cas d'un atlas statistique du petit animal [Wang et al., 2012b]. Il utilise un modèle statistique de corrélation des coefficients associés à chacun des vecteurs propres représentant les variations morphologiques dans chaque SSM.

Il est possible de générer un SSM dès que plusieurs observations des caractéristiques morphologiques d'un même élément sont disponibles. Typiquement, les résultats d'une procédure de segmentation couplée à un recalage permettent d'identifier un tissu, et d'estimer la position d'un ensemble de points – supposés observables chez chaque individu de la population considérée – dans chaque instance de l'élément observé. Dans notre cas, une procédure de segmentation automatique des tissus à fort contraste permet d'effectuer cette étape pour cette catégorie de tissus. Pour les tissus à faible contraste, une phase de segmentation manuelle/interactive est nécessaire en amont de la création de l'atlas – afin de permettre, par la suite, l'estimation automatique de la configuration et des contours de ces tissus.

1.4.2 Construction de l'atlas statistique

La construction de l'atlas statistique consiste donc en deux étapes : i) la génération d'un SSM pour les tissus à fort contraste et les tissus à faible contraste, respectivement, ii) la construction du CGM.

Construction des modèles statistiques de la forme

Le principe de construction standardisé des SSM est le suivant : i) collecte des représentations de plusieurs instances d'un élément d'intérêt ; ii) recalage rigide et non-rigide d'une instance – le modèle – sur chacune des instances collectées ; à l'issue de cette étape, la position de chaque point composant le modèle a été estimée dans chacune des instances – il s'agit des observations. iii) suppression des variables d'orientation, translation, homotétie par analyse procrustéenne généralisée (GPA pour *Generalized Procrustes Analysis*, [Bookstein, 1997a]). iv) Analyse des composantes principales (PCA pour Principal Component Analysis, [Abdi and Williams, 2010]) de l'ensemble des observations ; v) réduction du modèle aux vecteurs propres représentant 95% de la variance.

Collecte des données La segmentation des tissus à faible contraste a nécessité la mise en place d'un protocole dédié, qui a en fait déterminé le déroulement des acquisitions précédemment citées. Un échantillon de 30 souris de souche ICR+ a été constitué et chaque individu a été le sujet d'une série d'examens tomographiques, corps entier. Chaque animal a été l'objet de plusieurs acquisitions, afin d'avoir, pour chacun, un ensemble d'images standard – permettant de segmenter squelette, poumons et enveloppe – ainsi qu'un ensemble d'images caractérisées par une absorption plus importante des tissus à faible contraste, obtenue par injection intraveineuse d'un agent de contraste iodé. Les acquisitions standard, au nombre de deux, ont été centrées sur la partie antérieure et la partie postérieure de l'animal. Les acqusitions utilisant l'agent de contraste ont été centrées sur la région abdominale, afin d'extraire une description du contour des tissus abdominaux inclus dans l'atlas statistique. Sur les ensembles d'images de chacun des 30 animaux considérés, seuls 12 se sont avérées utilisables pour les tâches de segmentation. Certaines caractéristiques telles que l'âge lors de l'acquisition, le sexe, la masse des animaux utilisés pour la constitution de l'échantillon sont décrites en Annexe H. Ils ont été utilisés pour la construction de l'atlas statistique.

Segmentation des tissus à fort contraste La segmentation des tissus à fort contraste a été réalisée de manière automatique par la méthode présentée en Section 1.3. Le recalage du maillage modèle fait partie du processus de segmentation puisqu'à l'étape de segmentation du squelette en sous partie il est déjà recalé sur le maillage cible extrait de l'image tomographique.

Segmentation des tissus à faible contraste La segmentation a été réalisée de manière manuelle ou interactive, selon les tissus. Les contours du coeur, du foie et de la rate ont été définis manuellement dans les images au moyen du logiciel ITKsnap. Les fonctionnalités de grossissement de régions de ce logiciel ont été utilisées pour finaliser la segmentation et générer une description lisse des tissus. Quant aux reins, ils ont été segmentés de manière interactive par la définition manuelle d'une région d'intérêt parallèlépipédique contenant les deux reins. Ensuite, la procédure de distinction sur critère quantitatif associée au grossissement de région, décrite en Section 1.3, a été appliquée.

Le correspondance entre les maillages modèles – issus du même individu que les maillage modèles des tissus à fort contraste – et chaque instance de chaque tissu a été établie par recalage rigide et non-rigide : i) le maillage modèle est recalé de manière rigide sur le maillage cible au moyen de l'algorithme ICP ; ii) le maillage modèle est recalé de manière non-rigide sur le maillage cible au moyen de l'algorithme RPM ;

Génération des modèles statistiques de la forme Une fois les maillages générés, les opérations suivantes ont été mises en oeuvre : i) les maillages représentant les tissus à fort contraste, d'une part, et les tissus à faible contraste, d'autre part, de chaque individu ont été concaténés ; ii) la procédure décrite en Section 1.4.2 a été appliquée à chacun des deux groupes de tissus.

Huit modes de variation ont permis de modéliser plus de 95% des variations morphologiques de chaque groupe de tissus. Les résultats sont représentés en Figure 5.6 et 5.7 pour les tissus à fort contraste et les tissus à faible contraste, respectivement.

Construction du Modèle Conditionnel Gaussien

L'utilisation d'un modèle conditionnel Gaussien repose sur l'hypothèse que les vecteurs de paramètres de la forme de chaque groupe de tissus suivent des distributions de probabilité Gaussiennes multivariées. La construction du CGM consiste en la réalisation des opérations suivantes : i) calcul des vecteurs de la forme de chacune des instances, pour chaque groupe de tissus ; ii) calcul des matrices moyennes et de covariance des vecteurs de la forme de chaque instance ; iii) calcul de la moyenne conditionnelle et de la matrice de covariance conditionnelle. Une fois ces opérations réalisées, il est possible de réaliser un tirage aléatoire suivant la loi de probabilité Gaussienne multivariée décrivant les variations statistiques des vecteurs de la forme sur l'échantillon définie dans l'Equation 5.15.

La moyenne conditionnelle, la matrice de covariance et la densité de probabilité conditionnelle sont formalisées dans la Section 5.3 de ce document.

1.4.3 Recalage de l'atlas statistique

Le recalage de l'atlas statistique a été effectué en utilisant deux méthodes distinctes.

La première, désignée "recalage SSM" consiste en la réalisation des opérations suivantes : i) segmentation automatique des tissus à fort contraste de l'animal sujet de l'examen – à l'issue de cette étape, les maillages de la cible sont concaténés pour former un maillage des tissus à fort contraste ; ii) initiation de la procédure recalage par recalage rigide de la cible sur le modèle – l'atlas – et application de la méthode GPA ; iii) estimation itérative des paramètres de la forme de la cible par inversion de l'équation 1.15, pour les tissus à fort contraste ; iv) génération du modèle conditionnel gaussien : estimation des contours moyens des tissus à fort contraste ; v) de manière optionnelle : génération de cartes de probabilité de présence des tissus à faible contraste par tirage aléatoire d'un ensemble de vecteurs de la forme ; vi) déconcaténation des contours des tissus à faible contraste d'une part et à fort contraste, d'autre part ;

La seconde, désignée "recalage TPS" consiste en la réalisation des opérations suivantes : i, ii et iii) pareil que pour la méthode "recalage SSM" ; iv) estimation d'un champ de déformation par les splines de plaque mince (TPS pour *Thin Plate Splines*, [Bookstein, 1989]) en trois dimensions, et application des déformations locales au SSM des tissus à faible contraste ; v, vi) pareil que pour la méthode "recalage SSM" ;

1.4.4 Estimation des contours des tissus à faible contraste dans des images tomographiques

L'application à des données tomographiques et la comparaison au résultat d'une segmentation manuelle constitue l'indicateur le plus commode de la qualité de l'atlas anatomique statistique. Elle constitue, en outre, la manière obligatoire d'évaluer les performances de l'atlas dans l'application particulière à l'étude.

Description des données

Des acquisitions de quatre individus ont été collectées afin de réaliser l'étude, suivant le protocole décrit en Section 1.4.2, excepté le fait que les deux acquisitions standard centrées sur les parties antérieure et postérieure ont été remplacées par une seule acquisition centrée sur l'abdomen. Les images tomographiques correspondant à chaque acquisition ont été obtenues au moyen de l'algorithme FDK. Certaines caractéristiques telles que l'âge lors de l'acquisition, le sexe, la masse des animaux utilisés pour la constitution du groupe d'évaluation sont décrites en Annexe H.

Pour chaque animal, les données de l'acquisition standard centrée sur l'abdomen ont servi à la reconstruction tomographique à angle limité, une fois le jeu de projections réduit à un intervalle angulaire de 90°. La procédure de segmentation a ensuite été appliquée, pour chaque animal, aux images correspondant à cette acquisition, i) pour le jeu de projecitons complet acquis sur 360° et ii) pour le jeu de projections réduit à l'intervalle angulaire de 90°.

Evaluation

L'évaluation a été réalisée i) de manière qualitative par l'examen visuel des images, régions définies automatiquement et cartes de probabilité, comparés aux résultats de la segmentation manuelle des tissus à faible contraste ; ii) de manière quantitative utilisant les mesures décrites en Section 1.3.3.

Résultats

Les résultats visuels de la segmentation et de l'estimation des contours des tissus sont représentés en Annexe F pour un animal, sous la forme du contour moyen obtenu grâce au modèle Gaussien conditionnel ainsi que des cartes de probabilité, superposés sur les images tomographiques standard. Les résultats de l'analyse quantitative sont quant à eux synthétisés en Figures 5.8 et 5.9.

L'observation visuelle de la superposition des tissus estimés et des images tomographiques permet de tirer les appréciations suivantes :

- la position des tissus à faible contraste est, de manière générale, estimée correctement dans l'abdomen et dans une configuration correcte les uns par rapport aux autres ;
- les contours estimés présentent des différences plus ou moins importantes avec la référence issue de la segmentation manuelle ; des différences importantes sont observables pour le foie et la rate ;
- la représentation sous forme de cartes de probabilité permet d'indiquer une région où il est probable de trouver les tissus ; cette représentation a l'avantage de ne pas imposer un contour unique pour le tissu estimé mais permet au contraire d'intégrer une notion d'incertitude inhérente à la problématique de segmentation ;

Nous avons choisi, pour chaque mesure de similarité et chaque type de recalage, dans les deux configurations d'acquisition, de présenter la répartition des résultats par rapport i) à la médiane pour le coefficient de Dice et la distance réciproque, et ii) à la valeur 1 pour le rapport des volumes.

Images micro-CT Les volumes des organes sont sous-estimés de manière générale. Les rapports de volume R_v valent entre 0.55 et 0.82 avec le "recalage TPS" et entre 0.42 et 0.87 pour le "recalage SSM".

Les coefficients de Dice, dans le cas du "recalage TPS", valent entre 0.55 et 0.68 sauf pour la rate – 0.23. Les valeurs sont supérieures à la médiane de 0.65 pour le foie et les reins et inférieures à la médiane pour le coeur et la rate. Dans le cas du "recalage SSM", ils valent entre 0.4 et 0.7, sauf pour la rate – 0.34. Les valeurs sont supérieures à la médiane de 0.6 pour le coeur, le foie et le rein gauche, et inférieures à la médiane pour la rate et le rein droit.

La distance réciproque moyenne est inférieure à 1.2 mm sauf pour le foie où elle vaut 1.6 mm. Dans le cas du "recalage TPS", les valeurs sont supérieures à la médiane de 1.13 mm pour la rate et les reins et inférieurs à la médiane pour le coeur et le foie ; Dans le cas du "recalage SSM", ils sont supérieurs à la médiane de 1.04 mm pour le coeur, la rate et le rein gauche et inférieurs à la médiane pour le foie et le rein droit.

Images micro-CT à angle limité Les volumes des organes sont sous-estimés avec le "recalage TPS" sauf pour le foie (1.5). Avec le "recalage SSM", le volume est sous-estimé pour le coeur et le rein gauche (0.65) tandis qu'il est suresitmé pour tous les autres organes (entre 1.35 et 1.62).

Les coefficients de Dice sont entre 0.45 et 0.75 pour tous les organes avec le "recalage TPS". Les valeurs sont supérieures à la médiane de 0.73 pour le foie et les reins, et inférieures à la médiane pour la rate et le coeur. Avec le "recalage SSM" ils sont entre 0.55 et 0.8 sauf pour la rate – 0.28. Les valeurs sont supérieures à la médiane de 0.78 pour le coeur, le foie et le rein gauche, et inférieures à la médiane pour la rate et le rein droit.

Les distances sont inférieures à 1 mm pour tous les tissus avec le "recalage TPS", sauf pour le foie (1.5 mm). Les valeurs sont supérieures à la médiane de 0.86 mm pour le coeur, la rate et le rein droit et inférieures à la médiane pour le foie et le rein gauche.

Avec le "recalage SSM", elles sont inférieures à 0.65 mm pour le coeur et le rein gauche, supérieures à 1.38 mm pour le foie, la rate et le rein droit. La valeur est supérieure à la médiane de 1.38 mm pour le coeur, le foie et le rein gauche, tandis qu'elle est inférieure à la médiane pour la rate et le rein droit.

Temps de calcul Le temps de calcul est i) de 20 minutes pour le "recalage SSM", et ii) de 40 minutes pour le "recalage TPS", dont 20 minutes pour l'application des transformations aux cartes de probabilité. Le recalage non-rigide par l'algorithme RPM représente 85% des 20 minutes communes aux deux procédures.

1.4.5 Discussion

Outre une discussion des résultats obtenus, dans l'absolu, ceux-ci ont aussi été confrontés aux travaux existants, dans le but de situer le travail réalisé par rapport à l'état de l'art. Il s'avère que notre travail ne constitue pas l'implémentation d'un travail déjà publié, aussi la comparaison est souvent purement indicative.

Analyse quantitative et qualitative

La confrontation des résultats quantitatifs et de l'observation visuelle des surfaces estimées – ainsi que la superposition des cartes de probabilité sur les images tomographiques – nous permet de développer l'analyse suivante : i) l'usage complémentaire des trois mesures choisies donne des indications sur le niveau de différences locales entre surfaces estimées automatiquement par la méthode développée et surfaces déterminées par segmentation manuelle ; ii) ces différences locales sont de manière générale assez élevées ; les résultats dépendent des tissus considérés et aucune tendance ne nous semble se dégager pour un tissu particulier ni pour l'ensemble des tissus.

Il convient de rappeler i) le caractère subjectif et non-reproductible des méthodes de segmentation manuelle ; ii) le fait qu'à l'échelle globale, les tissus sont estimés dans une configuration correcte les uns par rapport aux autres et par rapport à la morphologie de l'animal.

Comparaison à des travaux existants

Notre travail est issu de la combinaison de différentes approches reportées dans la littérature, et le fruit de certains choix. Les principaux articles traitant de segmentation corps entier par recalage d'un atlas anatomique sont i) [Baiker et al., 2010] et ii) [Wang et al., 2012b]. D'autres articles reportent des approches dont l'objectif est bien la segmentation automatique d'images tomographiques mais dont la mise en oeuvre n'est soit pas aussi complète, soit pas aussi proche en termes d'application. Dans [Baiker et al., 2010], l'atlas MOBY est déformé en utilisant un modèle de liaisons mécaniques. Dans un premier temps, les tissus à fort contraste sont segmentés par une méthode de distinction de bas niveau. Dans un second temps, un squelette articulé de MOBY – généré en amont – est recalé sur le squelette segmenté. Les poumons sont recalés de manière rigide et l'enveloppe est recalée de manière non-rigide. La configuration des tissus à l'intérieur de l'abdomen est estimée par l'application du champ de déformation dérivé de la configuration du squelette et de l'enveloppe, à la configuration initiale de l'atlas.

La procédure développée dans notre travail est plus proche de celle proposée dans [Wang et al., 2012b]. Dans ce travail, un atlas statistique est constitué à partir de 45 individus, et recalé sur des images micro-CT. Les procédures de génération de l'atlas et de son recalage développées dans notre travail sont celles définies dans cet article.

Les procédures utilisées dans ces deux travaux sont constituées de plusieurs étapes dont chacune a fait l'objet de nombreux travaux : distinction de bas niveau, recalage rigide, recalage non-rigide. Ainsi, le résultat final consiste en l'articulation de plusieurs techniques dont l'implémentation même pourrait être l'objet d'une comparaison à une implémentation de référence, essayée sur des données de référence. Malheureusement, une telle implémentation de référence et de telles données de référence n'existent pas actuellement dans la communauté. De plus, certaines des méthodes utilisées – telles que la méthode

RPM pour le recalage non-rigide – reposent sur des paramètres dont le choix est souvent arbitraire, et dont la valeur est rarement publiée. Ainsi, à chaque niveau de l'implémentation, des différences d'implémentation ou de choix de paramètres peuvent se propager pour conduire en définitive à des résultats qu'il est difficile de comparer à une référence inexistante. L'une des barrières majeures pour la comparaison aux travaux existants repose sur le choix des mesures de similarité ; leur application systématique aux mêmes tissus ou groupes de tissus est loin de caractériser les articles mentionnés. De plus, le nombre d'individus utilisés pour l'évaluation des méthodes est très variable et la question se pose de la valeur des évaluations qui en sont issues, surtout au vu des barres d'erreur montrées par exemple dans [Wang et al., 2012b] et [Baiker et al., 2010]. Enfin, la représentation des résultats laisse souvent à désirer, les graphiques constituant un bon outil de synthèse mais ne permettant pas, en général, de déterminer précisément une valeur.

Les tableaux 5.9, 5.10 et 5.11 contiennent une synthèse des résultats quantitatifs présentés dans différentes publications visant à segmenter des images tomographiques de manière automatique. De manière générale, notre implémentation appliquée à des images tomographiques à angle limité donne des résultats cohérents comparés à la littérature, avec des mesures quantitatives du même ordre de grandeur. Notre travail constituant la première application d'une telle approche de segmentation automatique à des images tomographiques à angle limité, il faut se contenter de cette comparaison avec des approches et des applications différentes.

Points critiques et proposition de voies d'amélioration

Plusieurs points critiques de l'approche ont été identifiés. Cette section recense ces points critiques et propose des voies d'améliorations pour chacun d'eux.

Protocole expérimental Le protocole expérimental comporte plusieurs points critiques, en particulier : Le choix d'un agent de contraste ; dans ce travail, c'est Iomeron qui a été choisi ; des options alternatives existent avec des agents de contraste caractérisés par des temps de métabolisation différents, une persistance dans les tissus plus ou moins longue, ainsi qu'une aisance d'utilisation plus ou moins importante. Le choix est forcément un compromis entre les exigences de contraste dans l'image tomographique, de complexité du protocole expérimental, de la toxicité pour l'animal, de la possibilité de réaliser à la suite les acquisitions standard, l'injection du produit et l'acquisition avec agent de contraste – à condition que celui-ci se soit fixé sur les tissus d'intérêt assez rapidement, etc.

Constitution de l'échantillon : nombre d'individus, sexe / poids / âge de l'individu La composition de l'échantillon joue un rôle crucial dans le développement d'un atlas statistique. Les différences morphologiques induites, en particulier, par le sexe, le poids et l'âge de l'individu, et la combinaison de ces paramètres, ont un impact certain sur le réalisme du modèle et sa capacité à représenter une population. En outre, le nombre d'individus impliqués dans la construction du modèle statistique est un critère décisif sur la capacité du modèle à représenter des variations au sein de la population. La question se pose en fait du nombre minimal d'individus requis pour obtenir un modèle réaliste. En pratique, plus nombreux sont les individus, plus réaliste sera le modèle. Dans notre travail, douze individus ont été utilisés et au vu des résultats ce nombre est trop faible. Dans [Wang et al., 2012b], article de référence pour notre travail, et dont les performances sont meilleures de manière générale même pour l'application au micro-CT standard, 45 individus ont été utilisés. En statistique, un échantillon de moins de 30 individus est généralement considéré comme un échantillon de petite taille. L'utilisation de modèles Gaussiens n'est pas atypique pour des échantillons de petites taille, mais la question de sa pertinence est d'autant plus importante que le nombre de paramètres est grand par rapport à la taille de l'échantillon. Si l'on se base sur l'observation empirique de Meinzer et al. qui suggère qu'un modèle constitué d'au moins 12 composantes principales décrivant plus de 95% de la variance est généralement satisfaisant, et qu'on considère le nombre d'individus N_i grand par rapport au nombre de composantes N_c dès lors qu'il le dépasse d'un ordre de magnitude. Un nombre de 120 individus semble indiqué pour l'obtention d'un modèle convenable, ce nombre pouvant être ajusté par dichotomie admettant que moins de 12 composantes principales suffisent effectivement à décrire 95% des variations morphologiques. Notre travail se situe donc loin de ce cas idéal, et les résultats obtenus – comparés par exemple à ceux reportés dans [Wang et al., 2012b] – indiquent effectivement la sensibilité du modèle par rapport à la taille de l'échantillon.

Segmentation manuelle L'étape obligatoire de segmentation manuelle des images tomographiques pour la construction du modèle – ainsi que pour la constitution d'une vérité terrain pour l'évaluation des contours estimés – constitue l'un des points critiques de l'approche. En effet, la segmentation manuelle est reconnue comme un procédé fastidieux, peu reproductible, et subjectif. Par conséquent, le modèle développé intègre une part de subjectivité qui ajoute une part d'incertitude sur les contours estimés des tissus. Des procédures automatiques et standardisées telles que celles reportées en [Wang et al., 2012b] et [Baiker et al., 2010] constituent des options intéressantes pour un pré-traitement automatique des images qui pourrait précéder une procédure de segmentation manuelle dans laquelle les contours estimés automatiquement pourraient être raffinés par des opérations manuelles interactives. La question de leur implémentation et de leur validation subsiste et reste l'une des principales barrières. A ce jour, aucune solution logicielle publique ou commerciale ne permet de réaliser automatiquement la segmentation automatique d'une image micro-CT.

Méthodes de recalage : stabilité / implémentation GPU La stabilité et l'implémentation des méthodes de recalage est un autre point critique de l'approche. En effet, comme mentionné dans la Section 1.4.5, l'utilisation de certaines des méthodes de recalage utilisées reposent sur le choix de paramètres. Ces paramètres ne sont généralement pas communiqués par les auteurs des travaux qui intègrent ces méthodes comme une étape d'un flux de travail plus important. Pourtant, le choix des paramètres peut affecter sensiblement les résultats mais cette problématique est loin d'être triviale. Aucune méthode n'a été proposée, à notre connaissance, pour guider le choix des paramètres d'un algorithme tel que TPS-RPM.

En termes d'implémentation, notre travail repose sur des implémentations CPU, or le temps d'exécution est pour l'instant prohibitif, et largement supérieur à celui reporté par [Wang et al., 2012b]. Il convient donc d'explorer les voies d'amélioration qui permettraient de réduire le temps d'exécution des mêmes tâches. Une implémentation GPU de l'algorithme RPM a été proposée, et la parallélisation des opérations d'algèbre linéaire telles que l'inversion des matrices peuvent également être implémentées sur carte graphique.

1.5 Conclusion

Ce travail, réalisé à l'IPHC – CNRS UMR 7178 – en collaboration avec l'entreprise Biospace Lab dans le cadre d'une Convention Industrielle de Formation par la Recherche, a consisté en l'investigation des techniques i) de reconstruction d'image en tomographie à angle limité pour un dispositif caractérisé par une couverture angulaire de 90° seulement comparé à 360° pour un micro-CT standard, et ii) des techniques de segmentation automatique d'images tomographiques par des méthodes de haut niveau, intégrant une distinction de bas niveau et exploitant une information anatomique *a priori*. L'objectif de l'articulation de ces techniques était de fournir une information *a priori* à injecter dans un algorithme de reconstruction de tomographie optique par luminescence, basé sur un système de micro-tomographie par rayons X prenant en compte des contraintes de conception liées à la configuration des instruments dans un appareil d'imagerie par luminescence existant, le PhotonIMAGER Optima.

Le premier axe, cas particulier d'un problème de reconstruction à données limitées, a été mené à bien par l'implémentation et l'étude d'un algorithme de reconstruction itératif régularisé, basé sur la formulation algébrique du problème de reconstruction tomographique associée à la minimisation d'une fonctionnelle, la norme Variation Totale de l'image. Notre application a constitué la première application publiée du micro-CT à angle limité et de l'utilisation de l'algorithme ASD-POCS dans ce contexte.

Les résultats obtenus ont confirmé la possibilité d'analyser automatiquement les images, principalement car les images obtenues sont très similaires à des images micro-CT standard, hormis un artefact causant le lissage des frontières entre des régions d'absorption différente, causé par le manque d'information. En effet, certains tissus – le squelette, les poumons et l'enveloppe – ressortent avec un fort contraste par rapport aux tissus environnants. Ce constat nous a conduits à considérer l'identification automatique de ces tissus, l'approximation de leur contour par des maillages surfaciques et l'utilisation de cette représentation discrète pour le guidage d'une procédure de recalage d'un atlas anatomique. Plusieurs options existent lorsqu'il s'agit de modéliser l'anatomie d'un individu. L'approche consistant en la combinaison de modèles statistiques de la forme (SSM) a retenu notre attention du fait de sa capacité à encapsuler les variations morphologiques au sein d'une population, et des résultats significativement plus précis reportés dans la littérature comparé à l'utilisation d'atlas basés sur la représentation d'un unique individu. Un atlas anatomique statistique du petit animal pour le micro-CT doit consister en l'articulation de deux modèles statistiques de la forme, l'un pour les tissus à fort contraste, distinguables par des méthodes de bas niveau, et l'autre pour les tissus à faible contraste, correspondant à ce qui est inconnu et doit être estimé. L'articulation entre les deux modèles statistiques de la forme repose sur l'hypothèse que les vecteurs de la forme représentant les instance de chaque classe de tissus suivent des distributions Gaussiennes multivariées. L'expression conditionnelle des vecteurs de la forme des tissus à faible contraste connaissant les vecteurs de la forme des tissus à fort contraste aboutit en l'expression d'une distribution de probabilité conditionnelle qui permet d'estimer une configuration de la première classe de tissus en fonction de la seconde. Aucun atlas statistique public ou commercial du petit animal n'existant actuellement, l'utilisation d'un tel atlas supposait que nous le construisions. Nous avons donc, à cette fin, établi un protocole expérimental visant à réaliser l'acquisition de plusieurs images tomographiques de chaque animal ; les images ont été segmentées manuellement et de manière interactive ; l'analyse statistique a été appliquée aux contours estimés.

L'atlas statistique ainsi construit a été utilisé pour l'estimation automatique des tissus à faible contraste dans des images micro-CT standard et à angle limité. Notre travail constitue à notre connaissance la première application d'une telle technique au micro-CT à angle limité et la comparaison à des travaux d'objectif similaire reportés dans la littérature nous a permis de situer notre travail par rapport à ceux-ci et de considérer le fait que les résultats obtenus sont relativement bons malgré plusieurs inconvénients et point critiques – découlant de contraites pratiques – dans la mise en oeuvre de la démarche adoptée. L'analyse des résultats et l'observation rétrospective de l'approche développée nous ont permis d'identifier les principaux points critiques et de formuler des voies d'amélioration pour chacun d'entre eux. L'injection proprement dite de l'information anatomique dans un algorithme de reconstruction en tomographie optique par luminescence est l'application immédiate de notre travail, et constitue une extension prometteuse à ce travail.

Introduction

Since the dawn of medicine, animals and especially vertebrates have been used by human investigators as models of their anatomy and physiology [Franco, 2013]. The first mentions of the formal study of human and animal diseases through the observation of nature – counterbalancing the explanations based on the actions of the gods – date back to ancient Greece, around 500 BC. The early reports made by Anaxagoras[1] and writings from the *Hippocratic Corpus*[2] denote the beginning of a new approach of the study of diseases, based on their observation and classification, including the fact that they affect vegetables, animals or humans differently [Jouanna et al., 2012]. The observation that the diseases affecting human were closer to these affecting animals than these affecting vegetables followed shortly. These authors have been attributed the first observation of the interior of the animals, by dissection. The first dissections of human cadavers were reported only during the third century before our era[3]. Until this time, consequently, human anatomy was mostly known by analogy to animals. The dissection of human cadaver, however, remained marginal: in the first century of our era, Galenus[4] performed vivisections of animals, including primates, to bypass the prohibition of the dissection of human cadavers by the law of the Roman empire. The observation of living and dead animals lead, nevertheless, to important discoveries before this time [Jouanna et al., 2012]. Since then, major discoveries have been made possible by the methodic study of living animals, including the study of blood transport and heart motion by Harvey[5] – as well as the discovery of vaccination by Pasteur[6] in the nineteenth century.

Today, along with the evolution of the ethical standpoints, biomedical research still makes use of various animal species [Franco, 2013]. The place of the experiments on animals in the development of medical purpose molecules and medical treatments, was formalized in during the twentieth century, for example in the *Nuremberg Code*[7] [Allied Control Council, 1949] as well as in the declaration of Helsinki of the World Medical Association[8] [World Medical Association, 1964]. Current experiments on animals are realized mainly for i) fundamental biology studies, ii) Research and Development (R&D) studies on human, veterinary and dentistry medicine, iii) production and quality control for products for

---

[1] Anaxagoras (510–428 BC) was a pre-socratic philosopher of Classical Greece.

[2] The Hippocratic Corpus – or *Corpus Hippocraticum* in Latin, collects writings related to Hippocrates' School of medicine.

[3] These first dissections of human bodies were performed by the Greek anatomists Herophilus of Chalcedon (c.330–c.260 BC) and Erasistratus of Iulis on Ceos (c. 315–240 BC), seen as the most important Alexandrian physicians [Serageldin, 2013].

[4] Claudius Galenus (129–216) was a Greek physician of the Roman empire.

[5] The British physician William Harvey (1578–1657) also used animal dissections for his research.

[6] The french scientist Louis Pasteur (1822-1895) has been a pioneer of the research on infectious diseases.

[7] The Nuremberg Code refers to the judgement of the Doctor's trial held from December 9th, 1946 to August 20th, 1947, within the subsequent Trials of War Criminals before the Nuremberg Military Tribunals, held from 1946 to 1949. It draws ten ethics principles to be observed by physicians in their research. Specifically, Article 3 states that experiments on human beings "should be so designed and based on the results of animal experimentation and a knowledge of the natural history of the disease or other problem under study that the anticipated results justify the performance of the experiment."

[8] Article 12 of the Helsinki declaration states that "Medical research involving human subjects must conform to generally accepted scientific principles, be based on a thorough knowledge of the scientific literature, other relevant sources of information, and adequate laboratory and, as appropriate, animal experimentation. The welfare of animals used for research must be respected."

human medicine and dentistry and iv) toxicological and other safety evaluations[9]. The animal species that is the most used to research ends in the member states of European Union – in terms of the number of individuals – is the mouse[10]. Mice and human are both eutherian mammals[11]; despite considerable physiological, morphological and metabolic differences[12], human and mice have about 30000 protein coding genes and present "eighty percent of one-to-one corresponding counterparts in the other's genome" [Emes et al., 2003]. Moreover, from the same source, "in genomic alignments, 40% of nucleotides are identical". The advent of genetic engineering has made possible, since the last quarter of the twentieth century, to engineer the genotype – and thus, the phenotype – of mice[13], allowing the production of genetically modified mice and thus various disease models. Their fast breeding – gestation time of three weeks [Hartwell et al., 2010] – and the relative ease of housing and care compared to other mammal species, constitute another advantage of using mice for biomedical experiments.

As mentioned at the beginning of this introduction, the interior of the body of animals has been observed invasively – by vivisection or dissection – for ages. The advent of the microscope made it possible to observe phenomena at the celullar scale as well, and to correlate information collected at the macroscopic and microscopic scales. The description, representation and anotation of the observations has played a key role in the history of biology and medicine, from the treatises of anatomy of the Renaissance [14] to the discovery of microorganisms using the microscope[15]. *In vivo biomedical imaging*[16] has brought out another revolution in the fields of diagnosis and research in medicine and biology.

This field of study, standing at the crossroads between medicine, biology, engineering and physics, aims at providing a representation of the interior of the body of living subjects. As such, it constitutes a non-invasive alternative to vivisection. It can be used either to support diagnosis and help the physician understanding the patient's disease - and, further, finding the best remedy to it - or to observe organic phenomena through experimental protocols and formulate conjectures about it. In 1896, one year after

---

[9] These applications represent, respectively, 46.1%, 18.8%, 10.97% and 3.5% of the experiments in the member states of the European Union. All the data about the use of animals for experiments in the member states of the European Union come from – or are calculated after [European Commission, 2013]

[10] The total number of animals used for experimental and other scientific purpose was estimated to 11.5 millions, for year 2011, in the member states of the European Union. Over that number 91% are used for studies of human diseases, among which 18.5% for cancer, 22.2% for mental and nervous disorders and 8.7% for cardiovascular diseases. As for the number of mice used for experiments, it was estimated 61% of the total number of animals in the European member states, which corresponds to 7 million in 2011.

[11] *Eutheria*, from the ancient Greek $\epsilon\upsilon$ – *eu* – "true" and $\theta\eta\rho\iota o\nu$ – *therion* – "beast", is one of the two mammalian clades – the other being *metatheria*. Human and mice belong, respectively to the *archonta* and *anagalida* clades which differentiated between 65 and 110 million years ago [Emes et al., 2003]. A clade, from the ancient Greek $\kappa\lambda\alpha\delta o\varsigma$ – *klados* – "branch" also called *monophylum*, from the ancient Greek $\mu o\nu o$ – *mono* – "only" and $\phi\upsilon\lambda o\nu$ – *phylon* – "tribe", is a group consisting in an ancestral species and all its descendants.

[12] The ratio of mass between human and mice is 2360 times – for a mean human body mass in Europe of 70.8kg [Walpole et al., 2012] and a mean mass of the adult mouse estimated to 30g.

[13] In 1962, the British physicist Maurice Hugh Frederik Wilkins (1916–2004), the British biologist Francis Harry Compton Crick (1916–2004) and the American biochemist James Dewey Watson (born 1928) shared the Nobel prize of Physiology – one third each – "for their discoveries concerning the molecular structure of nucleic acids and its significance for information transfer in living material". Watson and Crick had reported previously, in 1953, the structure of the Deoxyribose Nucleic Acid (DNA) which encodes the genetic material of an organism, the genome [Watson and Crick, 1953]. In 1972, the first genetically modified organism (GMO), a virus, was engineered [Jackson et al., 1972], followed shortly by the first genetically modified mouse in 1974 [Jaenisch and Mintz, 1974].

[14] See, for example, the treatises of Ambroise Paré (1510–1590), Vesalius (1514–1564) and Leonardo Da Vinci (1452–1519).

[15] The Dutch scientist Antonie Philips van Leeuwenhoek (1632–1723) made significant discoveries including the vacuole of the cell and bacteriae, using homemade microscopes.

[16] The word *biomedical* comes from the ancient Greek $\beta\iota o$ – *bio-* – meaning "organic life" in modern science, and from the Latin *mederi* "to heal, give medical attention, cure". The word *imaging* finds its origin in the Latin *imagino* "copy, statue, picture", figuratively "idea, appearance" [www.etymonline.com, 2015]. The term *biomedical research* refers, in this thesis, to fundamental biology studies as well as any direct or indirect research focusing on the development of techniques, instruments and molecules for medicine.

the discovery of X-rays by Roentgen [17], the first services of radiology were created, coinciding with the birth of medical imaging. Several discoveries have punctuated the development of this pluri-disciplinary domain, including the radioactivity[18] as well as major technical inventions such as the digital acquisitions and processing of images. Since the advent of radiology, tremendous progress and the combined efforts of clinicians, physicists, biologists, chemists as well as engineers in various fields including computer science and electronics, have lead to the conception of a variety of imaging modalities and techniques. These modalities can typically provide a *morphological* or *functional* information. While some modalities deliver exclusively a morphological or functional information, some are also able to deliver a combined information. Morphological modalities deliver information about the physical structure and specific properties of biological tissues. Functional modalities provide information about the function of the organs or their subcomponents. The performance of any imaging modality is mainly characterized by the *sensitivity*, the achievable *resolution* and *contrast* – these two features of an imaging system are interdependant. The advent of *molecular imaging* has paved the way to the retrieval of information at the molecular scale – of cellular or biochemical nature – from macroscopic experiments.

Today, there is a wide choice of such imaging modalities and techniques. Most of these modalities, first developed for human imaging, have been adapted for small animal, at the expense of considerable developments in instrumentation. In some cases, *in vitro* experiments can also be carried out, using cellular cultures, but this approach reaches its limits when processes must be studied at the scale of the organism – which is the logical following of *in vitro* experiments. In this thesis, biomedical imaging systems designate *clinical* and *preclinical* imaging systems. As explained, a clinical biomedical image is typically intended to be used as a support for diagnostic for the physician[19]: it brings supplementary information in the form of clinical signs which can be combined to external clinical signs, observable without imaging, and the symptoms. . The role of a preclinical biomedical image is similar, except that the subject under observation is an animal. According to this definition, the biomedical image is not expected to be self-sufficient, since the physicians typically *interpretes* it by mobilizing their medical knowledge, along with the interpretation of other clinical signs and symptoms, to formulate a diagnosis.

A modern biomedical imaging system delivers a representation either i) of biological tissues based on their physical properties, or ii) of the distribution of a molecular probe[20] in these biological tissues. The advent of the digital revolution[21] in the second half of the twentieth century, including the development of Computer Science, have open a wide range of possibilities in the field of *digital biomedical imaging*. The automatic interpretation of images has been allowed by *computer vision* techniques which aim is, according to J.D. Prince, "to extract useful information from images" [Prince, 2012]. The use of computer vision techniques, in this thesis, addresses the need for automation of the image processing tasks to yield

---

[17] The German physicist Wilhelm Conrad Roentgen (1845–1923) was awarded the Nobel Prize in 1901 for the discovery of X-rays, "in recognition of the extraordinary services he has rendered by the discovery of the remarkable rays subsequently named after him" [www.nobelprize.org, 2015].

[18] Radioactivity was discovered by the French scientist Henri Becquerel (1852–1908). The phenomenon was immediately investigated by the French scientists Pierre Curie (1859–1906) and the Polish – and naturalized-French– Physicist Marie Skłodowska Curie (1867–1934). The three of them earned the 1903 Nobel Prize in Physics, respectively half for Becquerel "in recognition of the extraordinary services he has rendered by his discovery of spontaneous radioactivity", and quarter to each for Pierre and Marie Curie "in recognition of the extraordinary services they have rendered by their joint researches on the radiation phenomena discovered by Professor Henri Becquerel" [www.nobelprize.org, 2015].

[19] Clinical biomedical imaging is also extensively used for treatment planning – e.g. prior to surgery or radiation therapy – quality insurance and treatment follow-up. Interventional imaging is also developed to support the surgeon in his task.

[20] A *molecular probe* – called simply a *probe* in this thesis – refers to a molecule used to study a molecule or structure of interest. Probes are typically made of a *ligand*, able to react with the molecule or structure of interest, and a reporting component – for example, the florescent dye, quantum dot, or a radioactive element.

[21] The digital revolution coincides with the spread of the digital processing of data. This spread was highly facilitated by the invention of the transistor, in 1947, by William Bradford Shockley (1910–1989), John Bardeen (1908–1991) and Walter Houser Brattain (1902–1987). These three American physicists earned the 1956 Nobel prize in Physics for their invention.

a comprehensive anatomical interpretation of a whole-body morphological image. This task could not be performed without *image processing* and *information retrieval* techniques, including *machine learning* techniques.

Current trends in biomedical research have created the need for efficient quantitative imaging techniques[22], especially for preclinical biomedical studies. Optical luminescence imaging[23] belongs to the range of applicable techniques for such studies. Factually, it has become the most used single-modality for *in vivo* imaging protocols carried out in biomedical research[24]. While several advantages are claimed to explain the spread of optical imaging, this approach remains limited in practice by the current impossibility to achieve an absolute quantification of a luminescent probe distribution within living tissues. This is mainly due to the highly diffusive and absorptive behavior of biological tissues for photons in the wavelength range of visible light. Another drawback is that optical images do not carry morphological information precise enough to localize accurately the tissue where the photons were emitted, in three dimensions. Recent works have reported efforts to make optical imaging a quantitative imaging technique, through an approach called *optical luminescence tomography*.

In [Kak and Slaney, 1988], Kak and Slaney state that "tomography[25] refers to the cross-sectional imaging of an object from either transmission or reflection data collected from many different directions". *Computerized tomography*, which theoretical bases were introduced by Radon[26] in 1917 and which was put in practice in the first Computed Tomography (CT) scanner using X-rays, by Hounsfield[27] in 1972 – refers to the computation and representation of the distribtion of the X-ray lineic attenuation coefficient. The development of X-ray CT was accompanied by the development *nuclear emission tomographies*, which refers either to Single Photon Emission Computed Tomography (SPECT) or Positron Emission Tomography (PET)[28], in which the distribution of the activity of a gamma or positron emmiting isotope in tissues, respectively, is computed and represented. When it comes to *optical luminescence tomography*[29], the aim is to estimate the distribution of a luminescent source within the biological tissues. It is noteworthy that luminescence imaging delivers an intrinsically functional information. Due to the complexity of the models for the transport of visible photons in biological tissues, the strong absorption

---

[22] From the side of the pharmaceutical industry, according to [EFPIA, 2013], "only one to two of every 10000 substances synthetized in laboratories will successfully pass all stages of development required to become a marketable medicine". Preclinical testing of the substances is an early stage of the R&D process; it is typically involved in a massive screening of newly-engineered molecules.

[23] *Optical luminescence imaging* refers to the imaging of a luminescent source inside the tissues. It has to be distinguished from *diffuse optical tomography* which refers to a kind of transmission imaging used as a morphological imaging modality.

[24] In [Comley, 2011] John Comley reviews the HTStec survey *In Vivo Preclinical Imaging Trends 2011* "based on 76 responses from University Research Labs, Pharma and Biotech, mainly in North America and Europe" [http://www.htstec.com/,]. From his review, 47% of the survey respondents use primarily optical luminescence imaging – to be compared to 20% for Positron Emission Tomography (PET) and 23% for Magnetic Resonance Imaging (MRI).

[25] from the ancient Greek *τομος*, *tomos*, "slice", "section", and *-γραφια*, *-graphia*, "description of". As the prefix denotes, the first tomographic systems yielded the description of an object as a stack of slices. The term was reported for the first time by the German manufacturer Gustav Grossman (1878-1957) in reference to conventional tomography. It was later adopted internationally in 1962 at a comitee of the International Comitee of Radiological Units and Measurements (ICRU) [European Society of Radiology, 2013]. The concept of *conventional tomography* are briefly explained in Chapter 3.

[26] The Austrian mathematician Johann Karl August Radon (1887–1956) is the inventor of the *Radon transform*.

[27] The British engineer Sir Godfrey Newbold Hounsfield (1919–2004) was awarded the 1979 Nobel prize in Physiology or Medicine, "for the development of computer assisted tomography" [www.nobelprize.org, 2015], along with the South-African physicist Allan McLeod Cormack (1924–1998).

[28] The introduction of SPECT dates back to 1962 [Jaszczak, 2006]. As for PET, early attempts were reported as soon as 1963 and the first human tomographic images were reported in 1972 [Townsend, 2008].

[29] The meaning of *tomography* has been extended in this case, indeed it is not correct if we consider the etymology since the cross-sectional information can be derived in the case of optical luminescence tomography, but is not the raw output of reconstruction algorithm. It constitutes an extension of its meaning which could be stated as "the estimation of a tri-dimensional distribution of a radiation-emitting probe from two-dimensional measurements". This could be used to qualify the nuclear emission tomographies as well, adding that these aim at delivering a cross-sectional information.

of photons in these tissues, the small amount of collected measurements and the fact that in practice the optical scattering and absorption coefficients are unknown, luminescence tomography is a severly ill-posed problem[30]. Logically, ongoing developments aim at increasing the practical applicability of the physical models, collecting more data and estimating the optical properties of the tissues.

Jointly to the research ongoing at the instrumentation side as well as in the development of more efficient formulations of the reconstruction problem, two main – and complementary – approaches have been proposed to inject additional information in the reconstruction problem. They are i) multi-spectral measurements and ii) the use of anatomical priors. Multi-spectral measurements, indeed, give the possibility to re-write the inverse problem of the tomographic reconstruction, by multiplying the number of measurements by the number of considered wavelength ranges. As for the use of anatomical priors, the aim is to assign optical properties to regions identified *a priori*. Both approaches are highly complementary and contribute to reduce the region of the possible solutions.

The derivation of anatomical priors can be achieved in various complementary ways, including mainly i) the combination of optical luminescence modality with a mostly morphological imaging modality, leading to a *multimodality context*; ii) the use of a numerical model of the tissues. Using multimodality implies that the images must be expressed in the same reference frame. Moreover, a *segmentation*[31] of the morphological image is typically needed to obtain anatomical priors, since no robust relations are known between the physical properties estimated by morphological modalities such as X-ray CT and MRI[32], and the optical properties of the tissues. Therefore, regions of the images must be defined and optical properties must be attributed to them. The development of numerical models of the tissues, encapsulating an anatomical information, has been reported. But still, correspondence between the structures of the subject that are distinguishable in the morphological images and their counterparts in the anatomical model must be estimated. This is typically achieved through a *registration*[33] process.

Rigid image registration has been investigated since the 1980s for object recognition [Chin and Dyer, 1986]. It is typically used to register images of the same individual acquired using different imaging modalities therefore in different reference frames. Affine registration can account for anisotropic scaling of one of these image with respect to another. The performance of rigid and affine image registration, however, reach practical limits when the objects to be registered together present considerable differences in posture and morphology, as it is typically the case with macroscopic organisms and organs. Non-rigid registration was reported in the early 1970s [Fischler and Elschlager, 1973, Goshtasby et al., 2003] and has been, since then, widely used in biomedical imaging. Registrating precisely the images of the same individual from weekly acquisitions, for example, had become possible. A wide range of such approaches

---

[30] A mathematical model of a physical phenomenon is said to be well-posed if i) a solution exists, ii) this solution is unique and iii) the solution must depend continuously on the data [Mandelbrojt and Schwartz, 1965]. These conditions were formalized by the French mathematician Jacques Hadamard (1865–1963).

[31] *Segmentation* refers to the action of identifying regions in an image. In the case of biomedical images, it is generally sought to identify meaningful regions from the anatomical standpoint.

[32] Magnetic Resonance Imaging (MRI) – invented in 1972 after discovery of its principles in the 1950s – is a tomographic technique "in the sense that it produces a cross-section of the object" [Kak and Slaney, 1988]. MRI produces images of the subject, by exploiting the property of nuclei having an odd number of nucleons – protons and neutrons – and thus characterized by a *magnetic moment*. The hydrogen nucleus is made of one proton; its magnetic properties and the structural properties of the tissues which contain it – mostly soft tissues such as adipose, brain or muscle tissues – make it suitable to MRI. On the contrary, cortical bone – made of less than 3.4% hydrogen in mass, to be compared with blood, muscle, adipose or brain with respectively 10.2%,10.2%, 11.4% and 10.7% – cannot be practically observed [National Institute of Standards and Technology, 2015].

[33] *Registration* refers to the estimation of a *transform* which associates corresponding elements in two or more images. Registration approaches are qualified of global and local approaches depending wether they solve the problem with a global transformation or a local transformation. In this work, registration refers to the registration of point sets – as opposed to other geometric registration methods or iconic registration methods. Geometric registration methods typically address the registration of geometrical primitives derived from the image, wile iconic registration methods typically work directly with the image intensities.

have been proposed and applied in various contexts. The non-rigid registration of statistical models of the *shape*[34] was introduced in 1992 by Cootes and Taylor [Cootes et al., 1995]. The advent of geometric morphometrics[35] in the 1990s [Bookstein, 1989] has brought tools applicable in a biomedical imaging context to model the shape of organs. Numerous applications of such models have been reported for biomedical imaging [Heimann and Meinzer, 2009]. Recently, this approach was applied to small animal whole-body segmentation [Wang et al., 2012b]. The introduction of these methods has brought promising perspectives towards their fully automatic anatomical interpretation.

This work focuses on an luminescence imaging system commercialized by the French company Biospace Lab, the PhotonIMAGER$^{\mathrm{TM}}$ Optima. The aim of this work is to obtain a prior anatomical information for optical luminescence tomography, using cone beam X-ray micro-Computerized Tomography. Since the aim was to integrate such a device in the luminescence imaging system, it was mandatory to cope with geometrical constraints. It was chosen, consequently, to reduce the angular range of the micro-CT system. The first chapter of this document contains an overview of optical luminescence imaging principles and applications – with an emphasis put on the tomographic reconstruction problem – as well as the description of the X-ray micro-CT system considered in this work. The integration of a X-ray tomographic modality in PhotonIMAGER$^{\mathrm{TM}}$ Optima lead to the implementation of a dedicated tomographic reconstruction algorithm which is described in the second chapter of this thesis. The algorithm performance was studied in the central slice on various datasets, as well as in three dimensions on preclinical data. These studies are described in the second chapter as well. The third chapter focuses on the development of an automatic segmentation workflow for *high contrast tissues*. In the fourth chapter, the construction of a *statistical atlas* of the mouse made of two distinct *statistical shape models* of the tissues, is explained[36]. The statistical atlas was registered on tomographic images reconstructed from the preclinical acquisitions using data from a full scan, as well as with the geometrical constraints – on images reconstructed with the algorithm presented in the second chapter, from data collected over a reduced angular range. Registrating the atlas on tomographic images allowed to automatically delineate the organs represented in the atlas, an thus to automatically segment the tomographic images. The results of the automatic segmentation and their quantitative study are presented in the fourth chapter as well, preceding the general conclusion.

---

[34] In common language, the *shape* of an object designates its outline. In [Bookstein, 1997a], Bookstein notes that "in ordinary language, the shape of an object is described by words or quantities that do not vary when the object is moved, rotated, enlarged or reduced". In other words, the shape of a set of points is defined as "the equivalence class of the same cardinality, under the operation of the similarity group". In this work, we adopt this meaning of the shape – it is, indeed typically adopted in geometric morphometrics.

[35] morphometrics – from the greek $\mu o\rho\phi\eta$ – *morphé* – "shape" and $\mu\epsilon\tau\rho\iota\alpha$ – *-metrìa* – "a measuring of" is at the crossroads of statistics and biology, and studies the morphological variations within organisms, often in a functional or evolutionary perspective.

[36] Throughout this document, statistical atlas refers to a combination of statistical models of the shape – or *statistical shape models*.

Chapter 2

Optical Luminescence Tomography

Contents

As mentioned in the Introduction of this thesis, optical luminescence imaging techniques belongs to the class of intrinsically functional molecular imaging techniques. Three main processes of *luminescence*[37] are used for *in vivo* optical luminescence imaging. All of them are characterized by the emission of photons in the visible – or optical – region or in the near infra-red region of the electromagnetic radiation spectrum[38].

Fluorescence denotes the emission of a photon by a transition between an excited electronic state – reached by photon absorption – and the ground state of a molecule called *fluorophore* – as well as *dye* and *fluorochrome*. This phenomenon is therefore related to energy level transitions in the electronic molecular orbitals of the fluorophore. The ground state of a fluorophore is typically characterized by a singlet state in which all the electrons are *spin-paired*. Once brought to an excited singlet state[39] – in which electrons are paired between the excited orbital and the ground state orbital – the molecules typically return to the ground state through a *deexcitation*. This transition involved in fluorescence is

---

[37] The term *luminescence* was introduced by the German physicist Gustav Heinrich Wiedemann (1826–1899) – from the Latin *lumen*, "light", and *-escentia*, "process or state of being" [www.etymonline.com, 2015], to refer to the phenomenon of light emission from a substance by any cause except temperature, as opposed to *incandescence* – from Latin *incandescere*, "become warm, glow, kindle" – which results from the heating of the substance.

[38] The corresponding wavelength ranges are, respectively, 380 to 750 nm for the visible region, and 750 to 3000 nm for the near infra-red region [Bruno and Svoronos, 2005], and the frequency ranges are 6.67×10^8 to 4.0×10^8 MHz and 4.0×10^8 to 1.0×10^8 MHz, the frequency being calculated as $f = c/\lambda$ with $c = 2.99792458 \times 10^8$ $\mathrm{m.s}^{-1}$ the speed of light in vacuum and λ denotes the wavelength in inverse length unit.

[39] The transitions involved in the excitation process typically occur in 10^{-15} s [Lakowicz, 2006].

said to be *spin-allowed*[40] and results in the emission of a photon[41]. A fluorophore is characterized by an *absorption spectrum* and an *emission spectrum*. The shift between the mean values of these spectra is called the *Stokes shift*[42]. The emission wavelength is typically greater than the absorption wavelength – conversely, the energy $h\nu_e$ of the emitted photon is smaller than the energy $h\nu_a$ of the absorbed photon, where $h = 6.62606957 \times 10^{-34} J.s^{-1}$ is the Planck constant.

Bioluminescence refers to a specific case of *chemiluminescence*[43] occuring in living organisms. In the case of bioluminescence, an enzyme catalyzes the reaction of its specific substrate and other compounds such as molecular oxygen or ATP[44], under certain biochemical conditions, which results in the formation of an excited molecule[45]. In the case of bioluminescence the enzyme is typically called a *luciferase* and its substrate a *luciferin*[46]. Practically, the enzyme is produced by a cell of the subject through expression of the gene responsible for its creation – this gene must be encoded in the cell DNA[47]. The gene responsible for the creation of a luciferase is typically called a *lux* gene.

Cerenkov luminescence – or *Cerenkov effect*[48] – refers to the emission of photons – refered to as *Cerenkov radiation* – caused by charged particles - typically issued from α or β radioactive decays[49] - traveling through matter under certain conditions. Let n be the refractive index of a dielectric medium

---

[40] The transition is *allowed* as opposed to the *forbidden* transition between a triplet excited state and the ground state, which results in phosphorescence.

[41] Typical lifetime of excited fluorophores is of the order of 10 ns for a deexcitation rate of 10^8 s^{-1} [Lakowicz, 2006]. As for phosphorescence, the lifetime is of the order of the millisecond to the second for a deexcitation rate of 10^3 s^{-1} to 1 s^{-1} [Lakowicz, 2006].

[42] The British physicist George Gabriel Stokes (1819–1903) observed and reported this shift of the spectra. The term fluorescence was introduced by him in 1852.

[43] Chemiluminescence designates light production through a chemical reaction which produces a molecule in singlet excited state. The excited molecule returns to its ground state through the same process as for fluorescence.

[44] *Adenosine Triphosphate* is responsible for the transport of chemical energy in cells and thus is involved in the metabolism.

[45] An enzym is a molecule involved in chemical reactions as a catalyzer – a typical enzymatic reaction involves at least the enzyme and one or more substrate. For example, the reaction between the firefly luciferin, adenosine triphosphate bound to a magnesium ion Mg^{2+} (MgATP) and oxygen gets catalyzed by firefly luciferase, which yields electronically excited oxyluciferin molecules. The reaction is the following:

$$\mathrm{MgATP} + \mathrm{luciferin} + \mathrm{O}_2 \xrightarrow{\mathrm{luciferase}} \mathrm{AMP} + \mathrm{PP}_i + \mathrm{oxyluciferin} + \mathrm{CO}_2 + h\nu \tag{2.1}$$

where $h\nu$ represents the emitted photon.

[46] These terms were introduced in 1885 by the German biologist Emil Du Bois-Reymond (1818–1896)[Roura et al., 2013]. *Lucifer* means, in Latin, *the light bringer*.

[47] The *Deoxyribonucleic Acid* molecule.

[48] This phenomenon was named after the Russian physicist Pavel Alekseievitch Cerenkov (1904–1990). He was awarded a Nobel Prize in 1958 jointly with Ilia Mikhailovitch Frank (1908–1990) and Igor Ievgenievitvh Tamm (1895–1971) – one third each, "for the discovery and the interpretation of the Cherenkov effect" [www.nobelprize.org, 2015]. Cerenkov radiation was first reported by Marie Curie before Cerenkov started to characterize it in 1934 [Jelley, 1958].

[49] *Alpha decay* refers to the decay of a typically heavy nucleus by emission of a He^{2+} ion – α particle:

$${}^A_Z X \rightarrow {}^{A-4}_{Z-2} X' + {}^4_2\,\mathrm{He}^{2+}.$$

Beta decay refers either to a i) *beta minus* decay, characterized by the emission of an electron e^- and an antineutrino $\bar{\nu_\mathrm{e}}$ by conversion of a neutron in a proton:

$${}^A_Z X \rightarrow {}^{A}_{Z+1} X + \mathrm{e}^- + \bar{\nu_\mathrm{e}}$$

or to ii) a *beta plus* decay, characterized by the emission of a positron e^+ – the anti-particle of the electron – and a neutrino ν_e by conversion of a proton in a neutron:

$${}^A_Z X \rightarrow {}^{A}_{Z-1} X + \mathrm{e}^+ + \nu_\mathrm{e}.$$

In the precedent equations, Z is the atomic number – proton number, A is the number of nucleons – protons and neutrons. The mass of the alpha particle is 6.44656×10^{-27} kg. The mass of the electron and positron is $9.10938291 \times 10^{-31}$ kg. A charged atom or particle X^{k+} bears a total charge $k \times e$ where $e = 1.602176565 \times 10^{-19}\ C$ is the elementary charge – conversely, X^{k-} bears a total charge $-k \times e$.

under consideration. Cerenkov radiation is generated when the particle verifies – following the notation of the special relativity:

$$\beta > \frac{1}{n} \tag{2.2}$$

with

$$\beta = \frac{v}{c} \tag{2.3}$$

where v is the particle velocity and $c = 2.99792 \times 10^8$ m.s^{-1} is the speed of light in vacuum [Jelley, 1958]. For example, in water at $20°C$ and 1 atm, the refractive index is 1.33 at 589 nm [Halliday et al., 2010] so the minimum value of β for Cerenkov emission is

$$[\beta_{min}]^{\mathrm{H_2O}}_{T=20°\mathrm{C},P=1\ \mathrm{atm},\lambda=589\ \mathrm{nm}} = 0.752. \tag{2.4}$$

The charged particle temporarily and locally polarizes the medium along its path. Polarized molecules then return to their initial state; this process causes each polarized element to emit an electromagnetic pulse. For non-relativistic particles[50] in these conditions, local polarization of the medium and subsequent relaxation to the initial state results in a coherent cone-shaped electromagnetic wavefront. The semi-vertical angle of the cone is defined by the relation

$$\cos\theta = \frac{1}{\beta n} \tag{2.5}$$

while its apex and axis coincide respectively with the particle location and particle track. The electric and magnetic vectors are everywhere orthogonal and tangential to the cone surface, respectively.

The Frank-Tamm formula [Frank and Tamm, 1937] gives the number $N(\lambda_1, \lambda_2, l, \beta, n)$ of photons emitted by the transport of a charged particle characterized by its velocity $v = \beta c$ over the path length l in a medium of refractive index n, between two wavelengths λ_1 and λ_2:

$$N(\lambda_1, \lambda_2, l, \beta, n) = 2\pi\alpha \left(\frac{l}{\lambda_2} - \frac{l}{\lambda_1}\right)\left(1 - \frac{1}{\beta^2 n^2}\right) \tag{2.6}$$

where α is the fine structure constant $\alpha = 7.2973525698 \times 10^{-3}$ without unit. From this formula, Frank and Tamm calculate that 10 photons between 400 and 600 nm are emitted by one electron of 500 keV in water on a 1 mm path length. The derivation of Equation 2.6 with respect to λ gives:

$$\left[\frac{dN(\lambda)}{d\lambda}\right]_{\beta,n} = -2\pi\alpha\frac{l}{\lambda^2}\left(1 - \frac{1}{\beta^2 n^2}\right) \propto \frac{1}{\lambda^2}. \tag{2.7}$$

In materials with refractive index greater than 1, the radiation occurs in the visible and near visible regions of the electromagnetic spectrum[51]. Thus photons are mainly emitted in the blue region of the visible spectrum. Moreover, the velocity of a charged particle can be calculated as:

$$v = c \times \sqrt{1 - \frac{E_0^2}{(E + E_0)^2}} \tag{2.8}$$

which makes it possible to determine the threshold values for Cerenkov radiation in a given material. In water, considering a refractive index of 1.33 the minimum energy for Cerenkov radiation emission from β particles and α particles are 0.2639 MeV and 1.8679 MeV, respectively.

---

[50] A particle is considered to be *relativistic* when $\beta \approx 1$.

[51] In fact, $n = 1$ in vacuum and in any material n satisfies $n \geq 1$.

2.1 Light transport in biological tissues

Photons traveling in biological tissues undergo various phenomena, including *reflection* and *refraction*, *absorption* and *scattering*. Interaction of visible photons and tissues are determined by the *optical properties* of these tissues.

Reflection and refraction occur when visible photons encounter a boundary between two tissues with different refractive indices. For example, the skin of the subject is responsible for the reflexion of the excitation signal. Consequently in fluorescence the intensity of excitation arriving to the fluorophore is reduced compared to the excitation signal before encountering the skin. Conversely in the case of refraction the photon goes through the boundary but its trajectory changes. Internal reflection also occurs within the body at interfaces between media of different refractive index.

Absorption of photons in the visible spectrum is caused by chromophores[52] in biomolecules such as water or hemoglobin[53]. The absorption coefficient of hemoglobin and deoxyhemoglobin are represented in Figure 2.1. Luminescence imaging is severely limited in the near-UV and visible spectrum, because the absorption coefficient decreases when the wavelength increases. The absorption is very strong below 460 nm and remains important up to 650 nm. Beyond 900 nm the water is a strong light filter for IR. Luminescence imaging in these wavelength region requires for strong illumination signal, and possibly strong emission. The wavelength range between 650 nm and 900 nm, where scattering is generally greater than absorption in the biological tissues, is commonly refered to as the *optical window*. Moreover, light absorption by the tissues may result in fluorescence from the tissues which contain endogeneous fluorophores[54].

Scattering of photons comes from the turbid nature of the biological tissues – more precisely, from the mismatch of refractive index between the various cellular components and other elements[55]. The photons arriving to the detector can be classified in i) *coherent* or *ballistic* photons which have travelled in straight line from their emission point to the detector, ii) *serpentile* photons which have been subject to few interactions and which trajectory is close to a straight line, and iii) *scattered* photons which have complex paths because of multiple scattering. In biological tissues, most of the emitted photons undergo multiple scattering due to microscopic heterogeneities of the tissues. Therefore, a directional beam tends to spread and loses its directionality.

Figure 2.2 and 2.3 show, respectively the reduced scattering coefficient μ_s' and absorption coefficients μ_a, for various biological tissues. The reduced scattering coefficient μ_s' is calculated as:

$$\mu_s' = (1-g)\mu_s \tag{2.9}$$

where μ_s is the scattering coefficient in inverse length unit and g without unit is called the *anisotropy factor*, calculated as the mean cosine of scattering angle[56] [Patterson et al., 1991]. The values were calculated following the semi-empirical method proposed in [Alexandrakis et al., 2005] and based on tabulated data. From this figures, it can be observed that the dependency of these coefficients to the wavelength is globally similar between the various biological tissues. The global behaviour is, in fact,

---

[52] Chromophores are molecules or groups of atoms part of a molecule and responsible for light absorption of certain wavelength, while other wavelengths are reflected or transmitted. The absorption is due to the resonance induced by photons at certain wavelengths in the electron cloud of these groups of atoms.

[53] Hemoglobin, abbreviated Hb, is the metalloprotein containing four *hemes* – a heme is a chemical structure enclosing a metallic atom – of iron. Hb is found in the red blood cells of vertebrates. It is either saturated with oxygen, or desaturated (deoxyhemoglobin). The oxygen saturation affects the optical properties of Hb.

[54] This process is called *auto-fluorescence*.

[55] Animals are part of the *Eukarya* taxon. The eukariotic cell is made of several elements: nucleus, mitochondria, endoplasmic reticulum, golgi appartus, fibers, as well as membranes – for plasma and nucleus [Schleif, 1993].

[56] Scattering is typically highly forward directed in biological tissues, but multiple scattering causes a complete loss of directionality in thick samples [Golzio et al., 2004].

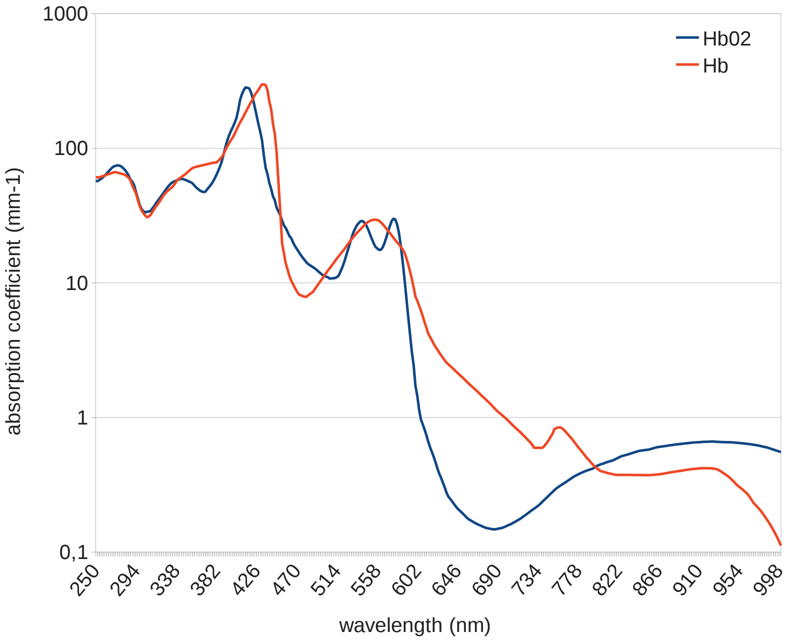

Figure 2.1: Absorption coefficient of oxy-hemoglobin and deoxy-hemoglobin with respect to the wavelength, calculated using the data tabulated in `http://omlc.org/spectra/hemoglobin/summary.html`. Ordinates are in logarithmic scale.

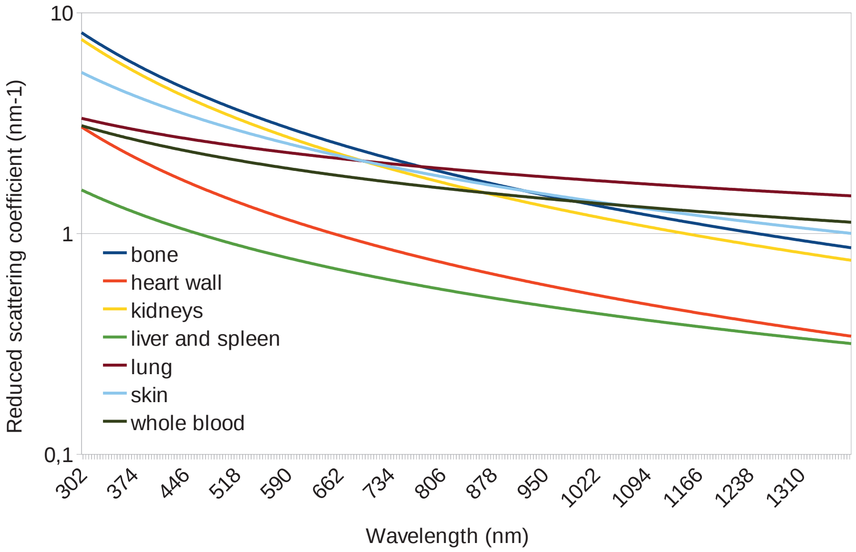

Figure 2.2: Reduced scattering coefficient for optical photons in biological tissues, calculated as proposed in [Alexandrakis et al., 2005]. Ordinates are in logarithmic scale.

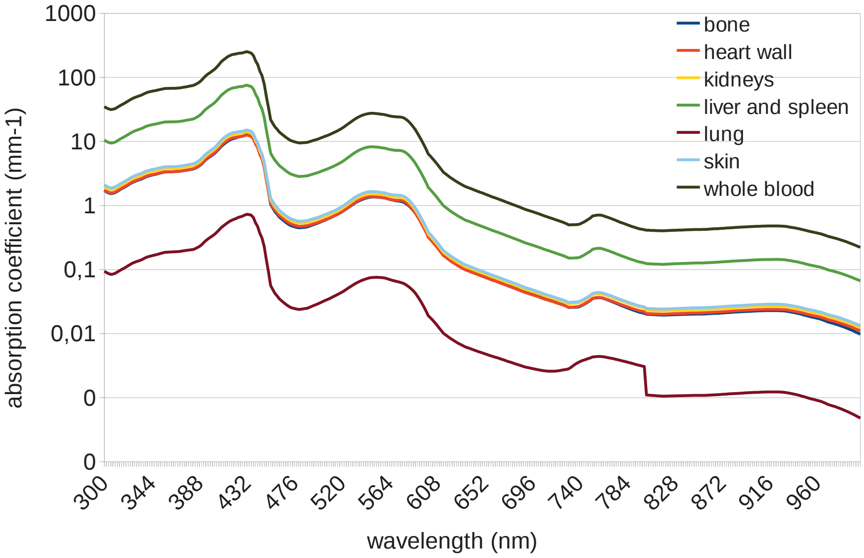

Figure 2.3: Absorption coefficients for optical photons in biological tissues, calculated as proposed in [Alexandrakis et al., 2005]. Ordinates are in logarithmic scale.

closely related to the respective percentage of blood and water in the tissue composition. Indeed, the reduced scattering coefficient tends to decrease as the wavelength increases. In some tissues, the decrease rate is lower than in others, such as in the lungs compared to the bone. As for the absorption coefficient, the tendency is the same for all the tissues, but it is not characterized by a global decrease. In the wavelength range of optical photons, absorption is mainly related to the presence of chromophores such as hemoglobin in the tissues. Figure 2.4 displays the absorption coefficient and reduced scattering coefficient of blood, with respect to the wavelength.

2.2 Use of Luminescence Imaging for *in vivo* experiments

Bioluminescence imaging[57] was observed for the first time in the mouse inoculated with a bacteria expressing a luciferase, twenty years ago [Contag et al., 1995]. Since then, it has been extensively used in the *reporter gene strategy*, that is to say to report the expression of a *reporter gene*[58]. As explained in the Introduction, techniques of genetic engineering developed in the last quarter of the twentieth century have enabled the insertion of a *lux* gene into mammalian cells. Table 2.1 reports common luciferases used for bioluminescence imaging – various other organisms produce naturally such enzymes, including bacteria, plancton, insects and fishes [Hagelshuher et al., 2009]. The advantages of bioluminescence are that i) it is characterized by the absence of background signal and thus an extremely

---

[57] In some papers the terms luminescence imaging and bioluminescence imaging are mixed up. In this thesis, luminescence imaging refers to bioluminescence imaging, fluorescence imaging and Cerenkov luminescence imaging.

[58] A reporter gene is "a gene with a readily measurable phenotype, that can be distinguished easily over a background of endogeneous proteins", according to [Naylor, 1999]. *Endogeneous* refers to something originated in the organism, as opposed to *exogeneous* which refers to something originated outside this organism. Moreover, from the same source, "specific response elements have been fused to genes encoding reporter proteins. Activation of appropriate signal transduction pathways then alters the expression of the reporter gene, providing a simple method for monitoring their effect on gene expression."

Figure 2.4: Absorption coefficient and reduced scattering coefficient of optical photons in blood, calculated as proposed in [Alexandrakis et al., 2005]. Ordinates are in logarithmic scale.

source	emission wavelength	reference
Photinus Pyralis	$550 - 580\ nm$ range	[Golzio et al., 2004]
Renilla Reniformis	$450 - 480\ nm$ range	[Golzio et al., 2004]
Gaussia Princeps	peak at $480\ nm$	[Remy and Michnick, 2006]

Table 2.1: Commonly used luciferases with emission wavelength and reference. *Photinus pyralis*, *Renilla reniformis* and *Gaussia Princeps* refer to, respectively, the North-American firefly, a sea pansy, and a mesopelagic copepod.

high sensitivity, and ii) there is no need for illumination, which can be responsible for physiological perturbation under certain conditions [Bloquel et al., 2006]. As for the drawbacks, i) bioluminescence requires the injection of an exogeneous substrate, ii) it is restricted to intra-cellular targets and iii) anesthesia has been reported to possibly alter luminescent signal intensity, by affecting the host and tumor physiology [Hagelshuher et al., 2009].

Fluorescence was discovered in 1852 by Stokes but its potential for diagnostic purpose was considered for the first time 1911 by Stuebel [Andersson-Engels et al., 1997]. Since then, various clinical applications of fluorescence *in vivo* have been developed [Andersson-Engels et al., 1997]. The development of the fluorescence microscope[59], along with the development of the synthetic dye industry[60] have gone along the development of various applications in biology studies. In 2000, Yang *et al.* report the first whole-

---

[59] Between 1911 and 1913 by two companies, Carl Zeiss and Carl Reichert [Masters, 2010].

[60] This development started in 1856 on the initiative of William Perkin (1838–1907) [Masters, 2010].

name	type	source	λ_{ex}	λ_{em}	ref.
GFP	P	*Aequorea victoria*	488	507	[Golzio et al., 2004]
DsRed	P	*Discosoma Striata*	558	583	[Golzio et al., 2004]
HcRed	P	*Heteracis Crispa*	600	640	[Golzio et al., 2004]
ICG	M	chem. synth.	780	820	[Malicka et al., 2003]
Azurite	P	chem. synth. (from GFP)	383	447	[Subach et al., 2011]
peptide coated CdTe/CdS/ZnS	QD	chem. synth.	760	875	[Michalet et al., 2005]

Table 2.2: Non-exhaustive list of fluorophores, their source, maximum excitation and emission wavelengths, operation mode if any, and reference.
Aequorea victoria is a jelly fish; *discosoma striata* is a coral commonly known as the mushroom coral; *heteractis crispa* is a sebae anemone.
- chem. synth. = chemical synthesis
- P = protein
- M = molecule
- QD = quantum dot

body visualization of Green Fluorescent Protein[61] (GFP) expressed by tumors and metastases in a living mouse [Yang et al., 2000], after previous work of Chishima *et al.* for *transfection*[62] of the GFP gene of the jellyfish *Aequoria victoria* in tumor cells *in vitro* [Chishima et al., 1997]. GFP had previously been produced in genetically modified mice, in 1995 [Ikawa et al., 1995]. Apart from the use of fluorescence in a reporter gene strategy – which is to say, *indirect* fluorescence imaging [Ntziachristos, 2006] – engineered fluorescent probes can be administrated to the living animal – this is called *direct* fluorescence imaging. Probes used in direct fluorescent imaging can be further classified in *active* probes and *activatable probes* [Ntziachristos, 2006]. Active probes are generally attached to a target-specific *ligand* in a similar manner as in nuclear emission tomographies. The activatable probes[63] are molecules engineered to carry *quenched* fluorophores[64], which can typically be freed by enzymatic reactions. The main difference between images obtained with active and activatable probes is the important background signal in the case of active probes, caused by the fact that the fluorophore can emit light throughout its transport in the organism, whereas activated optical switches reveal the occurence of a specific reaction – in specific conditions, and will not emit light until they have been freed by this reaction. Various fluorophores used for *in vivo* imaging are reported in Table 2.2; the various physiological and biochemical reactions between these fluorophores and these organisms are beyond the scope of this thesis. Reviews of various proteins and their characteristics can be found in [Shaner et al., 2005]. Alternatives to proteins include *quantum dots* – semiconductor nanocristals [Jamieson et al., 2007], as well as other molecules such as indocyanine green (ICG) [Malicka et al., 2003]. Fluorescence is generally characterized a strong signal, and acquisitions are characterized by a persistent background caused by auto-fluorescence of tissues.

Cerenkov luminescence imaging (CLI) is being developed since the proof of concept of its applicability for observation and quantification of activity in microfluidic chips used in the synthesis of ^{18}F-based compounds [Cho et al., 2009]. In 2009, Robertson *et al.* have shown that CLI could be used *in vivo*

---

[61] The Green Fluorescent Protein was discovered in 1962 by Shimomura *et al.* [Shimomura and Saiga, 1962]. The Japanese biologist Osamu Shimomura (born 1928), the American biologist Martin Chalfie (born 1947) and the American biochemist Roger Tsien (born 1952) earned each one third of the 2008 Nobel prize of Chemistry "for the discovery and development of the green fluorescent protein, GFP" [www.nobelprize.org, 2015].

[62] *Transfection* refers to a technique of genetic engineering which consists in introducing nucleic acids into cells.

[63] Activatable probes are known as *molecular beacons*, *optical switches* or *smart probes*.

[64] *Quenching* refers to a decrease in the intensity of the fluorescent signal under constant excitation energy and rate.

R.N.	decay mode	$T_{1/2}$	E_{max} (MeV)	alternative usage	reference
^{18}F	β^+	1.83 h	0.634	PET	[Delacroix et al., 2002]
^{11}C	β^+	20.4 min	0.96	PET	[Delacroix et al., 2002]
^{15}O	β^+	2.04 min	1.732	PET	[Delacroix et al., 2002]
^{13}N	β^+	9.97 min	1.199	PET	[Delacroix et al., 2002]
^{64}Cu	β^+	12.7 h	0.653	PET	[Delacroix et al., 2002]
^{67}Cu	β^-	2.58 days	0.575	SPECT	[Delacroix et al., 2002]
^{124}I	β^+	4.18 days	2.135	PET	[Delacroix et al., 2002]
^{68}Ga	β^+	1.13 h	1.899	PET	[Delacroix et al., 2002]
^{82}Rb	β^+	75 s	1.523	PET	[Jadvar and Parker, 2005]
^{89}Zr	β^+	3.3 days	0.897	PET	[Zhang et al., 2011b]
^{90}Y	β^-	2.7 days	2.284	therapy	[Delacroix et al., 2002]
^{131}I	β^-	8 days	0.606	SPECT	[Delacroix et al., 2002]
^{32}P	β^-	14.3 days	1.710	therapy	[Delacroix et al., 2002]
^{225}Ac	α	10 days	5.417	therapy	[Delacroix et al., 2002]

Table 2.3: Non-exhaustive list of charged particle emmiters used *in vivo* and eligible for Cerenkov imaging. $T_{1/2}$ is the radioactive helf-life of the radionuclide, E_{max} is the maximum energy of the emitted charged particle reported in this table.
- R.N. = radionuclide
- PET = positron emission tomography
- SPECT = single photon emission tomography
- max = maximum
- dec. mode = decay mode

with [^{18}F]-FDG, [Robertson et al., 2009] using an optical imaging system dedicated to fluorescence and bioluminescence imaging. In 2010, the previous proof of concept is extended to ^{18}F and ^{68}Ga, and the perspective of using CLI instead of PET/SPECT in studies is formulated [Spinelli et al., 2010]. CLI gives the possibility to use several radionuclides, including i) β^+ emitters used in Positron Emission Tomography, ii) β^- emitters and iii) α emitters. Some of the radionuclides eligible for Cerenkov imaging are listed in Table 2.3. It is noteworthy that the pure β^- and α emitters such as ^{90}Y and ^{225}Ac are used for therapy but cannot be observed using other imaging modality in a whole-body context *in vivo* because of their short path length. Cerenkov imaging therefore provides an unique opportunity to measure their activity non invasively. Some β^-/γ emitters used for SPECT imaging, such as ^{131}I can also be used for CLI. Various isotope producing Cerenkov radiation in biological tissues – assuming that the soft tissues are made mostly of water – are listed in Table 2.3.

A biomedical luminescence imaging system is mostly made of a detection device, typically enclosed in a black-box – or *tight-light box* – that isolates it from visible light coming from the exterior. In fluorescence imaging devices, fluorophores are typically excited by an external light source, such as a laser, a Light-Emitting Diode (LED), a tunable laser, filament or gas lamp, depending on the hardware design [Leblond et al., 2010]. A source of white light can also be used to illuminate the subject under observation, for photographic acquisitions. Other purpose-specific components can be part of the system, involved either in the data acquisition, control-command, animal handling, or a combination of these functions.

2.3 Device under study

The PhotonIMAGER$^{\mathrm{TM}}$ Optima is a biomedical luminescence imaging device developed and commercialized by the French company Biospace Lab[65] [BiospaceLab, 2014]. It has been designed to acquire of fluorescence and bioluminescence signals. In 2012, it was shown in our institute that Cerenkov luminescence signals could as well be acquired with the system [Brasse et al.,]. Figure 2.7 shows the planar Cerenkov luminescence imaging of $^{3}2$P injected in a mouse in the form of phosphoric acid, using bandpass filters centered at various wavelengths. The main components of the device are:

- a detection system placed on top of the object under study made of a filtering system with 10 filters allowing to detect photons between 370 and 900 nm, a photographic objective of focal length 50 mm and aperture $f/1.2-16$, a photon-electron converter, a phosphor plate for electron-photon conversion and a square CCD[66] camera of edge size 25 mm and a pixel size of 2.5 μm associated to a cooled Micro-Channel Plate (MCP)[67]. This setup distinguishes the PhotonIMAGER$^{\mathrm{TM}}$ Optima from most similar systems which use no light intensifier but a cooled CCD camera to reduce the electronic noise caused by thermoionic emission – or *dark current noise* [Leblond et al., 2010]. The device can be operated in photon *counting mode* – as opposed to *integration mode* – thanks to the enormous gain of MCP – of the order of 10^4 to 10^6 for single stage MCP and three-stages MCP, respectively [Hamamatsu, 2013]. Light intensifications is of the order of 10^6 thus the readout noise is generally negligible compared to the optical signal. The dark current noise of the CCD is 25 e$^-$ $s^{-1}cm^{-2}$. The dynamic range of the device is greater than 10^5.
- a cryostat used to cool the MCP at $-25°$ during operation;
- an *epi-illumination system*[68] made of a Xenon 100 W halogen lamp, a linear wavelength filter ranging from 400 to 760 nm, and a set of light guides made of optical fibers is used to illuminate the object for fluorescence studies. For these imaging studies, the illumination system is operated in *continuous wave* mode[69].
- a *pico-projector*[70] used for the projection of *structured light* patterns for surface estimation[71];
- a platform used to elevate some of the components;

---

[65] The company was created in 1989 – as *Biospace Mesures* – by the Polish-born French physicist Georges Charpak (1924–2010) – who was awarded the Nobel prize in 1992 "for his invention and development of particle detectors, in particular the multiwire proportional chamber" [www.nobelprize.org, 2015]. The company's activity was originally dedicated to the development of molecular imaging tools using Charpak's discoveries from high energy physics and particle detection, and specialized in the development of small-animal imaging devices.

[66] *Charged Coupled Devices* (CCD) are commonly used in luminescence imaging devices. They are one of the two main types of image sensors, CCDs and CMOS, which were both invented in the 1970s[Taylor, 1998]. Alternatives for luminescence imaging include the use of intensified CCD, electron multiplication CCDs (EMCCD), avalanche photodiodes (APD) and photomultiplier tubes (PMT) [Leblond et al., 2010].

[67] Micro-Channel Plate (MCP) derive from the continuous-dynode electron multiplier proposed by Farnsworth in 1930 [Huber et al., 2013]. In a typical MCP, electrons get accelerated through the channels and create secondary electrons when hitting the walls.

[68] *Epi-illumination* and *trans-illumination* are the two typical setups for illumination of the subject in fluorescence imaging devices [Leblond et al., 2010]. Epi-illumination – or reflectance mode – consists in an illumination with the light source or light guide on the same side of the tissues as the detector. In transillumination, the subject is placed between the light source or light guide.

[69] *Continuous wave* mode (CW) – or *steady-state*, as opposed to *pulsed mode*, consists in a constant amplitude and frequency wave operation of the illumination. In fact, CCDs are typically limited to CW measurements [Leblond et al., 2010]; this is, however, sufficient for fluorescence *intensity* measurement when no high-frequency sampling in time is needed.

[70] The term *pico-projector* refers to a compact device allowing for image projection.

[71] *Structured light surface estimation* refers to the projection of a geometrical pattern on an object, its measurement, and depth map estimation using dedicated algorithms [Fechteler et al., 2007].

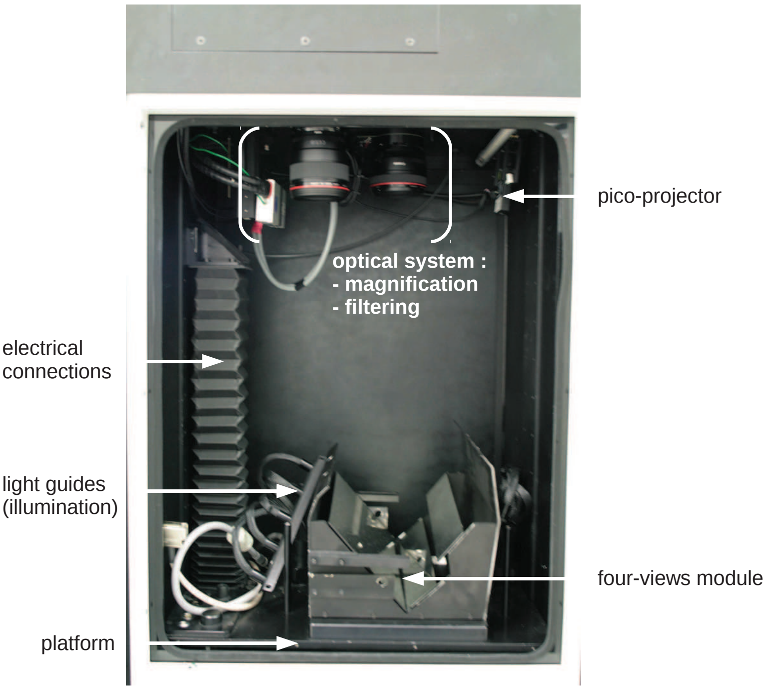

Figure 2.5: Interior of the black box of the PhotonIMAGER$^{\mathrm{TM}}$ Optima.

- numerical links, electrical connections, etc.;
- a black box of absolute dimensions $50\ \mathrm{cm} \times 40\ \mathrm{cm} \times 70\ \mathrm{cm}$ (W x D x H), enclosing optics of the detection system, the platform, the pico-projector and the front-end of the illumination system;
- a *macrolens module* can be placed in the field of view and used to magnify the detected image.
- optionally, a module refered to as *the four-views module* can be placed in the black box. It allows to acquire luminescent signal with four view angle – on top, bottom and both sides of the animal by reflexions on mirrors.

The system has a temporal resolution of $23\ \mathrm{ms}$. Most of these components - except the cryostat - are enclosed in the imager structure. The features of the PhotonIMAGER$^{\mathrm{TM}}$Optima make it suitable to realize planar luminescence acquisitions; luminescence tomography is worth being considered as well.

2.4 Luminescence Tomography

Initially developed for *in vitro* microscopy studies, luminescence imaging studies typically consisted in the acquisition and use of two-dimensional images. This approach, called *planar imaging*, has then been extended to whole-body *in vivo* studies. The luminescence image is typically fused, in these cases, with an optical photograph of the subject under study, to facilitate interpretation – as shown in Figures 2.6 and 2.7. Two-dimensional luminescence images make possible to achieve qualitative analysis of the photon current going through the animal surface – by, identifying roughly the location of the emission spots, as well as relative quantification – e.g. emission intensity in a given region over time. Typically, the analysis of planar images can consist in localizing the source of light in

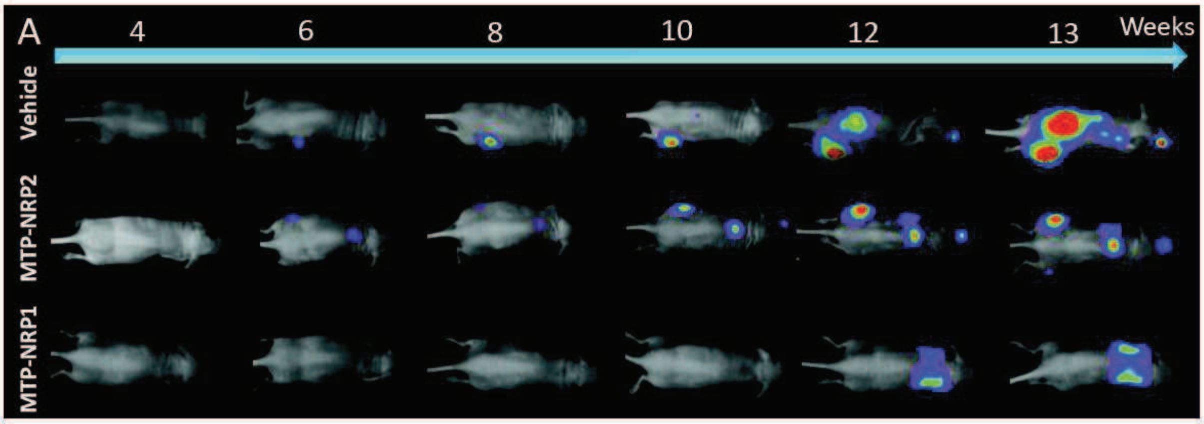

Figure 2.6: An example of longitudinal study using bioluminescence. Three experimental samples of mice are considered, which develop tumors over time, under the action of peptides. The aim of the study is to characterize the action of these peptides in the development of breast cancer. Images were realized at IPHC with PhotonIMAGER^{TM}RT Images kindly provided by Dr. Alexia Arpel - INSERM, IPHC/CNRS, Université de Strasbourg.

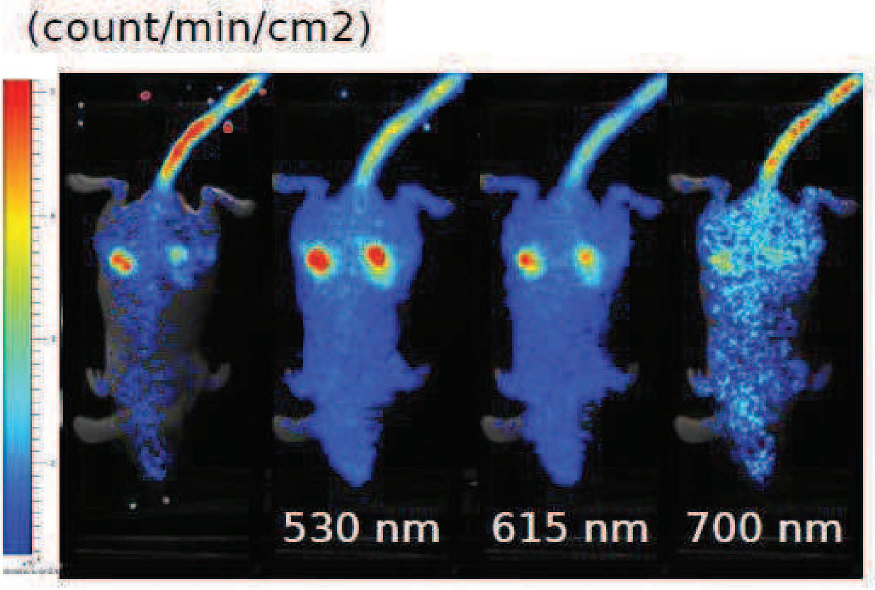

Figure 2.7: Planar acquisitions of Cerenkov luminescence from the beta minus emitter ^{32}P-ATP in biological mouse tissues, realized at IPHC with PhotonIMAGER^{TM}RT. Images were acquired using narrow bandpass filters, centered on the indicated wavelengths – no wavelength indicated means no filter. Image kindly provided by Dr. David Brasse - IPHC/CNRS, Université de Strasbourg.

tissues and achieving a relative quantification, using the linear dependance of the measured signal and the fluorophore concentration. Typically, a specific probe yielding a measurable luminescent signal and targetting a feature of tumor cells would allow to i) localize a tumor and ii) estimate the tumor growth or reduction rate, by counting the photons in surface at various time steps - for example, every week. Such a protocol can be used, for example, to assess the impact of a drug on the tumor development process - by estimating the change in growth rate induced by the administration of the drug [Paroo et al., 2004]. This is the case of the longitudinal study which visual results are displayed in Figure 2.6. One major drawback is that as such, planar imaging does not provide any depth resolution. Besides, the relation between the intensity recorded, the depth of emission and the optical properties in tissues is highly non linear [Ntziachristos, 2006]. Luminescence tomography has been introduced for its potential to overcome these limitations and provide an three-dimensional localization and absolute quantification of the luminescent distribution.

2.4.1 Image acquisition

Image acquisition for tomography is generally performed using more than one view, to maximize the number of measurements and the coverage of visible animal surface. Various experimental setups have been investigated, including three-views based on two mirrors [Li et al., 2010, Guggenheim et al., 2013], a rotating mouse holder as in [Wang et al., 2006, Hu et al., 2010, Zhong et al., 2011] or a fixed animal holder coupled to a rotating detection system [Liu et al., 2010], six light detection modules such as OPET [Alexandrakis et al., 2005] as well as a conical mirror design [Li et al., 2009]. In the case of PhotonIMAGER$^{\mathrm{TM}}$ Optima, a specific animal support – the four-view module described in Section 2.3 – can be used to acquire images at four angle of views, namely 0°, 90°, 180° and 360°.The module is visible in Figure 2.5. A similar module was proposed in [Chaudhari et al., 2005] to provide several views of the animal and thus to maximize the visible domain of the animal surface. The aim in [Chaudhari et al., 2005] is to use this information to perform multispectral and hyperspectral[72] image reconstruction - and thus to overcome the limitations of two-dimensional planar acquisitions.

2.4.2 Modeling of the light transport in tissues

The propagation of light in a diffusive and absorptive medium can be modelled analytically or statistically. Formally and from the analytical point of view, the general form of the Radiative Transport Equation (RTE) or Boltzmann equation[73] is the starting point of most methods. The propagation of optical photons through matter can be modelized by the RTE as follows:

$$\left(\frac{1}{c}\frac{\delta}{\delta t} + \hat{s}\nabla + (\mu_a(r)+\mu_s(r))\right) L(r,\hat{s},t) = \mu_s(r)\int_{4\pi} f(\hat{s},\hat{s'})L(r,\hat{s'},t)d\hat{s'} + q(r,\hat{s},t) \tag{2.10}$$

μ_a and μ_s being the medium absorption and diffusion coefficient. $L(r,\hat{s},t)$ is the energy radiance at point r within the medium, at time t and unit of solid angle $\hat{s}$. $f(\hat{s}.\hat{s'})$ is the normalized differential scattering function, which represents the probability of scattering from angle $\hat{s'}$ to $\hat{s}$. The various terms of this equation represent, respectively:

- first term: the change in energy radiance with time
- second term: the net change due to energy flow through the medium

---

[72] As opposed to multispectral which typically consist in the acquisition of light over different wavelength bands, hyperspectral imaging aims at measuring a much more important number of wavelengths to constitute a spectrum.

[73] This equation was introduced by the Austrian physicist Ludwig Eduard Boltzmann (1844–1906) in 1872. It allows the derivation of various equations such as in fluid mechanics or neutron transport.

- third term: the decrease in radiance due to absorption and scatter
- fourth term: the gain in radiance due to in-scatter from all directions
- fifth term: the contributions in radiance from the sources located in the medium

In a steady-state context, the equation becomes:

$$\left(\hat{s}\nabla + (\mu_a(r) + \mu_s(r))\right) L(r, \hat{s}) = \mu_s(r) \int_{4\pi} f(\hat{s}, \hat{s'}) L(r, \hat{s'}) d\hat{s}' + q(r, \hat{s}). \tag{2.11}$$

The diffusion and absorption coefficients are unknown in practice. This model is not commonly used in biomedical applications, due to the computational complexity if the radiance is highly anisotropic [Pekar and Patterson, 2010]. Various approximations of the RTE have been derived, including spherical harmonic expansion [Zhong et al., 2011], discrete ordinates method, finite element methods [Li et al., 2010] as well as the widely used Diffusion Approximation[74]. Monte Carlo methods offer a statistical alternative to the analytical formulation by the simulation of the path of each photon using probabilities of diffusion and absorption, namely the diffusion and absorption coefficient. Such light transport simulators have been developed to this end [Li et al., 2004, Shen and Wang, 2010], and constitute the gold standard for simulation of the transport of optical photons in biological tissues.

It is mandatory, to perform luminescence tomography, to map the measured signal onto the surface of the object. Indeed, interaction probabilities of photons in the air are negligible compared to interaction probabilities in tissues. Traditionally, the prior on the animal surface is obtained with a structured light measurement and estimation of the surface. One of the functionalities of PhotonIMAGER$^{\mathrm{TM}}$ Optima is to estimate the animal surface through such a process. The structured light projection and acquisition are performed, respectively, by means of a pico-projector and the optical detection system. A dedicated algorithm then performs the estimation of the surface. Such an approach is described for example in [Basevi et al., 2013] using a three-views acquisition. Alternative approaches include an algorithm based on Fourier transform and a phase-unwrapping used by Kuo *et al.* in [Kuo et al., 2007] to estimate the object surface from the structured light measurement, as well as a space carving approach proposed in [Lasser et al., 2008]. In [Li et al., 2009], a conical mirror design is alternatively proposed to realize both the luminescent signal measurement and the structured light measurement for surface estimation. In [Cong et al., 2010] Cong *et al.* propose to extract the surface from a micro-Computerized Tomography reconstruction. This approach is also used in [Li et al., 2010], while Optical / MRI combination is proposed in [Allard et al., 2007] for small animal luminescence imaging.

In luminescence tomography, the object domain is typically represented by cubic voxels, surface meshes or tetrahedron meshes. The cubic voxel representation is flexible because any cubic volume element can be assigned specific optical properties. Nevertheless, it loses its flexibility when a fine representation of the boundary is sought. Indeed in this case a piecewise planar representation is often sought, for example in Monte Carlo models [Shen and Wang, 2010]. It has, however, been used for tomographic imaging in [Kuo et al., 2007] associated to a tangent plane approximation of the boundary surface. Surfaces meshes approximate boundaries in a piecewise linear manner. Typically, this representation uses triangular surface elements. Such representations are commonly used in the computer graphics field. The flexibility of such a representation is debatable because a surface mesh encloses a domain which properties are generally assumed to be homogeneous. Tetrahedral meshes constitute an interesting compromise which combines a discretization of the domain to a piecewise linear representation of the boundary. These meshes can be generated with an adaptive sampling, which increases computational efficiency. Moreover, a surface mesh can generally be easily derived from a tetrahedron

---

[74] The Diffusion Approximation is considered valid only in the optical window [Arridge et al., 2000]

mesh. Tetrahedral meshes are commonly used as Finite Element Models (FEM) for modelling light propagation in tissues [Shen and Wang, 2010]. This discretization is used in most direct and inverse methods in optical tomography.

2.4.3 Image reconstruction

Luminescence tomography algorithms are typically iterative. It is indeed generally possible to model the light emission and measurement as a linear system, since the domains of interest are usually represented in a discrete form. Thus the algorithms consist in a *forward model* and an *inverse model*. The forward model aims at simulating the detectable light intensity, corresponding to the estimated source distribution. The inverse model aims at correcting the estimation using the measured light intensity. In [Ntziachristos, 2006], Ntziachristos reports the use of a linear model based on Born or Rytov approximations [Ntziachristos, 2006, Cairns and Wolf, 1990] for fluorescence tomography, which can be solved iteratively via regularized inversion methods such as Tikhonov regularization[75]. One of the advantages of such an approach is that prior anatomical information can be explicitly included in the minimization [Zhou et al., 2008].

The inverse problem is generally severely ill-posed in luminescence tomography, because in practice i) the optical coefficients within the tissues are unknown, ii) boundaries between tissues are unknown iii) few measurements are available and iv) the relation between source depth, intensity, and the optical properties is non-linear. To deal with the two first obstacles, the optical coefficients are typically assumed to be homogeneous and set to arbitrary values, for example the coefficients of water. Iterative inverse models generally use a Tikhonov regularization associated to a minimization algorithm [Li et al., 2010, Li et al., 2009, Lu et al., 2009]. A Non-Negative Least Square method (NNLS) is used in [Kuo et al., 2007] associated to a forward model based on Green's function as the solution to the Diffusion Approximation, valid in the *optical window*.

2.4.4 Multispectral tomography

Multispectral tomography is generally performed using acquisitions of light at various bandwidths. Reconstruction algorithms use the information of these measurements to estimate the luminescent source distribution. The comparison of the reported works on this topic is delicate due to the variety of protocols involved.

In [Chaudhari et al., 2005], a multispectral and hyperspectral acquisition system and associated algorithms are proposed. The authors make use of several views to estimate the light distribution on the surface of the animal. A set of mirror providing four views of the subject under study is specifically designed. The use of this system is also reported in [Ahn et al., 2008] with an extensive study of iterative reconstruction strategies. In 2007, multispectral reconstruction is applied to bioluminescence imaging [Kuo et al., 2007] in a simulation study and preclinical experiment, using a single view measurement. The authors claim to reach an error less than 6% in intensity and 0.5 mm in depth. In [Lu et al., 2009], a simulation study of bioluminescence tomography using a sparsity prior is carried out. In [Li et al., 2009], a conical mirror design is proposed to realize the surface light acquisition. This setup is used i) to estimate the animal surface and ii) to acquire the multispectral data. More recently,

---

[75] In image reconstruction, regularization refers to the application of constraints to enforce some features of the image, e.g. qualitative properties such as smoothness or sparsity. *Tikhonov regularization* is named after its inventor, the Russian mathematician Andrei Nikolaievitch Tikhonov (1906-1993). Considering an ill-posed linear system $Ax = b$, this method solves the regularized least square minimization:

$$\min_{x}\{\|Ax-b\|_2^2+\lambda^2\|x\|_2^2\} \tag{2.12}$$

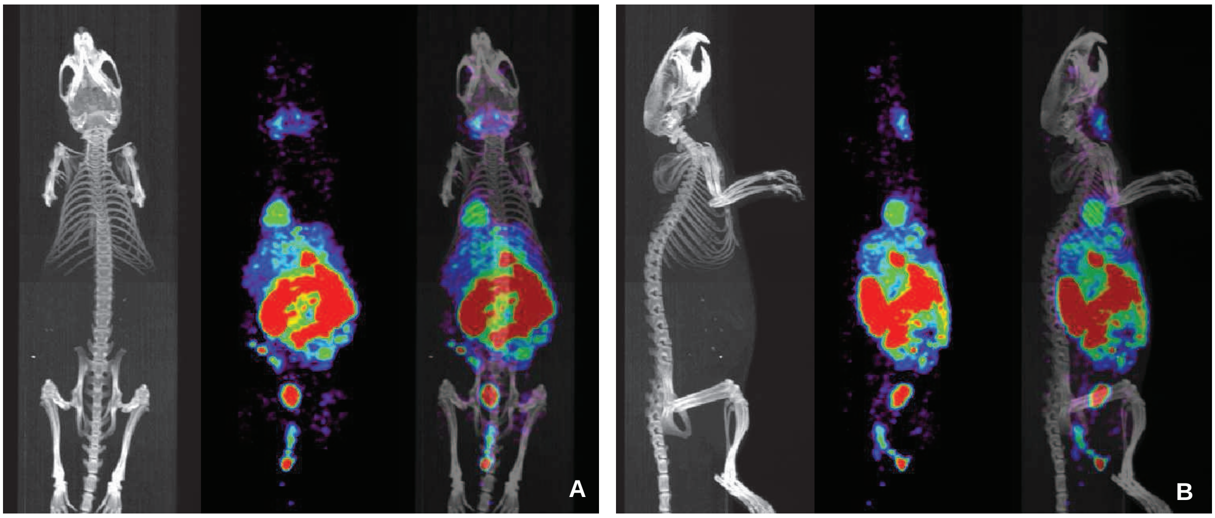

Figure 2.8: Example of micro-SPECT+micro-CT with cardiac imaging medium Technetium 99mTc sestamibi: From left to right in A and B: CT only, maximum intensity projections (MIP) of micro-CT image only, micro-SPECT image only, superimposition of micro-SPECT and micro-CT images. Heart, kidneys, bladder, thyroid, as well as a part of the digestive system can be identified with help of the micro-CT image. Images kindly provided by Dr. Virgile Bekaert (IPHC).

this acquisition and reconstruction technique has been applied to Cerenkov imaging [Spinelli et al., 2011], where the multispectral sgnal is used to estimate the depth of a point source without seeking to reconstruct a three-dimensional distribution.

In [Alexandrakis et al., 2005], several tissues[76] are used for simulation with the MOBY atlas [Segars et al., 2004]. In this simulation study, an Expectation Maximization algorithm is used to estimate the source distributions from measurements performed with the OPET system - which provides six views of the animal surface. Results suggest that source localization is likely to be poor when the biological tissues optical properties are assumed to be homogeneous, while using more than one wavelength in the reconstruction tends to improve the localization of bioluminescent sources. Reconstructions using the exact optical properties used for the simulation show improved accuracy. As for Guggenheim *et al.*, they achieve a source depth estimation within about $1\ \mathrm{mm}$ and a quantification of the source within 11% of relative error, in an experimental study using a homogeneous phantom and multispectral measurements [Guggenheim et al., 2013]. A complementary approach to multispectral acquisitions and reconstructions consists in using explicitly anatomical priors in the image reconstruction problem.

2.5 Anatomical Priors for Optical Luminescence Tomography

The use of luminescence imaging in a multimodal fashion has been reported in [Leblond et al., 2010] as a support for interpretation of the spatial location of fluorescent sources. The use of a white-light imaging system, a profilometry system, or a planar X-ray system are mentioned. This can, obviously, be extended to bioluminescence and Cerenkov luminescence.

Using a secondary image as a complement for optical images belongs to the variety of *multimodal imaging techniques*. Such techniques include, for example, the use of a micro-CT image as a

---

[76] The tissues modeled in their study are adipose, bone, bowel, heart wall, kidneys, liver and spleen, lung, muscle, skin, stomach wall and blood.

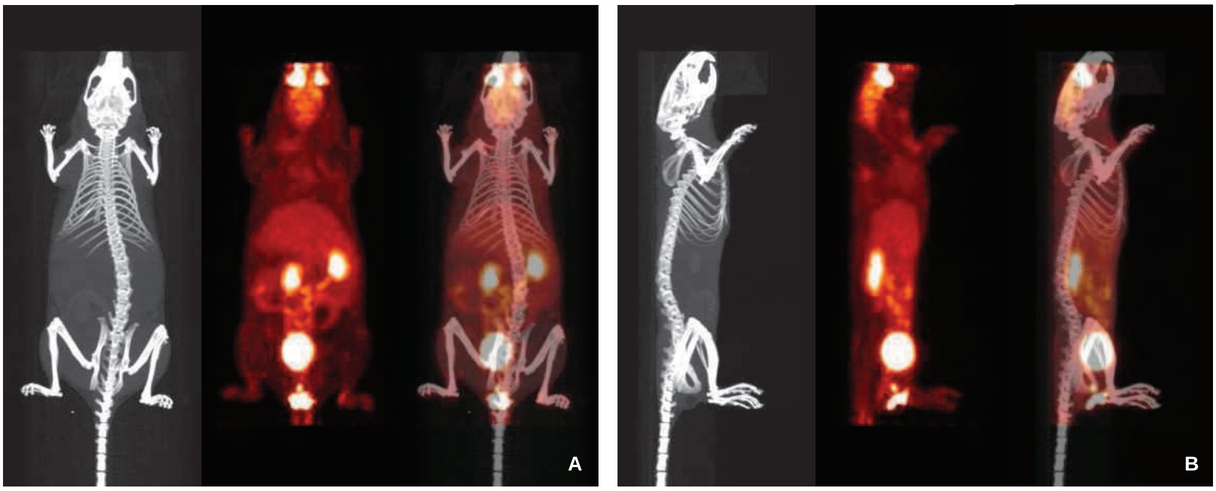

Figure 2.9: Example of PET+CT with ^{18}FDG: From left to right in A and B: CT only, maximum intensity projections (MIP) of micro-CT image only, micro-PET image only, and superimposition of micro-PET and micro-CT images. Various emission spots such as the kidneys, bladder, eyes, brain and liver can be identified with help of the micro-CT image. Images kindly provided by Dr. Virgile Bekaert (IPHC).

morphological support for the analysis of emission tomography images, such as Single Photon Emission Computed Tomography (SPECT), as shown in Figure 2.8. Micro-SPECT allows to reconstruct a tri-dimensional image of the gamma-emmiting radionuclide distribution with a submillimetric spatial resolution [van der Have et al., 2009]. Similarly, micro-Positron-Emission Tomography (micro-PET) – example shown in Figure 2.9 – allows to estimate positron-emitting radiotracers with a resolution of about 1 mm [Missimer et al., 2004]. In both cases, this is typically done without any anatomical prior. The fundamental difference between these emission tomographies and optical tomography is the physical processes involved. In the case of PET and SPECT, indeed, the assumption of a photon transport in biological tissues in straight line is usually sufficient - with respect to the considered photon energy range. This assumption thus underlies most reconstruction algorithms for these modalities. By contrast, in the case of optical tomography, the photon flux measured at the animal surface is the result of multiple scatterings of photons, while a relatively large number get absorbed in the tissues before getting out.

Extracting an anatomical information from a morphological imaging modality thus makes it possible to attribute scattering and absorption coefficients to regions identified as being part of a particular tissue. It is consequently possible to include a prior knowledge of the optical properties of these tissues in the direct model of the luminescence tomography iterative reconstruction, to account for their inhomogeneity within the animal body - while homogeneity is assumed within a single tissue. The use of priors for tomographic reconstruction is generally performed through the following steps:

Anatomical priors are generally derived from another imaging modality, which fullfils specific characteristics of resolution and contrast between tissues of interest - so that these tissues can be readily distinguished through an image processing workflow. As such, the estimated surface of the animal constitutes valuable information for coarse tomographic reconstructions, because it provides the support of the animal image. Nevertheless, it does not provide, as such, any information about the inner structure of the biological tissues. Such an information has been subsequently used as the target of a registration process, as reported in [Joshi et al., 2010]. The performances of such an approach remain limited by the fact that the whole model is transformed non-rigidly using a transformation derived only from the surface correspondence between the source and target: the correlation of the surface and internal tissue shapes is debatable. In other words, all the tissues of the animal are deformed in a non-rigid fashion, including rigid components such as bones. Moreover, the non-rigid registration utilizes the skin surface as a template and a target, though correlation between skin and internal tissues is generally poor except in a few regions of the body.

Magnetic Resonance Imaging, X-ray tomography or tomosynthesis, Ultrasound Imaging have been cited as possible providers of morphological information [Li et al., 2003]. It has been shown that this can improve the quantification and localization of the luminescent sources. This has been first proposed in 2003 by Brooksby *et al.* [Brooksby et al., 2003] then in 2005 by Guven *et al.* [Guven et al., 2005] for a combined MRI/optical reconstruction in the context of breast imaging and Diffuse Optical Tomography (DOT)[77]. In 2007, Optical / MRI combination has been proposed in [Allard et al., 2007]. In [Wang et al., 2006], a numerical model of the abdominal and thoracic region of the mouse is matched to a micro-CT image of the subject under study. The micro-CT and optical image are then coregistered to perform bioluminescence tomography using morphological priors. The tissues represented in their model are: kidneys, stomach, liver, muscle, lungs, heart. Moreover, the authors study the influence of precision of the optical coefficients within the tissues. They claim to reach an error less than $1\ \mathrm{mm}$ in location, to be compared with $3,5\ \mathrm{mm}$ in a model considered homogeneous. Also, they report an error inferior to 20% in intensity to be compared with 200% in the case of a homogeneous model. In [Liu et al., 2010], Liu *et al.* use an optical/X-ray micro-Computerized Tomography multimodal system and derive a tetrahedral mesh representations of heart, lungs, liver, muscle and bone in the thoracic region, associated to a reconstruction algorithm based on spherical harmonics approximations of the problem, and reach an average error of $1.14\ \mathrm{mm}$ for the source location. In 2010, the application of the heterogeneous model to Cerenkov imaging is compared to SPECT by Hu *et al.* [Hu et al., 2010]. The authors claim to reach an error around $1\ \mathrm{mm}$ in location to be compared with $4.4\ \mathrm{mm}$ in the homogeneous model. In this work, a X-ray imaging modality has been chosen to provide the morphological prior, through an image processing workflow including the registration of an anatomically realistic numerical model on the reconstructed images.

Various methods to realize the registration of whole-body atlases on the segmented high-contrast tissues from micro-CT images have been reported. Automatic methods to derive the anatomical information from micro-CT images include, mainly:

- locally rigid registration of an articulated model of the skeleton, which estimation is used to drive a non-rigid registration of the soft tissues – such as the method proposed in [Baiker et al., 2011];
- nonrigid registration of a model, in a 3D/3D fasion or in a 2D/3D fashion [Wang et al., 2012a, Wang et al., 2012b, Wang et al., 2012c];
- fully non-rigid registration such as the method introduced in [Li et al., 2008] – in this work, the authors register the image of the same individual acquired at various time steps;
- the use of a Statistical Atlas of the whole body [Wang et al., 2012b, Wang et al., 2012c] to estimate the high contrast tissues, and then use this estimation to estimate the shape of the low contrast tissues.

In 2011, Baiker *et al.* have reported the use of an articulated skeleton model to drive the registration of a generic numerical model of the other tissues [Baiker et al., 2011]. The use of two main generic models has been reported in the literature for similar purpose:

---

[77] On the contrary to luminescence tomography, diffuse optical tomography aims at estimating the distribution of the optical coefficients within tissues.

- MOBY, a licensed atlas generated from a Magnetic Resonance Microscopy (MRM) scan, was developed in 2004 by Segars *et al.* [Segars et al., 2004]. The morphological model is part of a simulation framework in which various functions such as the simulation of the respiratory motion are implemented, in line with the human torso NCAT phantom [Segars and Tsui, 2009].

- Digimouse, a free numerical model built using micro-CT images and cryosection data, developed in 2007 by Dogdas *et al.* [Dogdas et al., 2007].

Such generic models are criticized because they are built using images of a single individual, and it is probable that in many cases the target individual does not resemble much the model, at least locally. In 2012, Wang *et al.* authors develop a statistical atlas made of two statistical shape models – one for the high-contrast tissues, and the other for the low-contrast tissues [Wang et al., 2012b]. The outline of the high-contrast tissues is first estimated and is used as an input for estimating the outline of the low-contrast tissues, through a Conditional Gaussian Model. Except from the application to micro-CT, attempts have been made with original devices such as Wang *et al.* in 2012, which do not use a tomographic reconstruction, but directly registrate a statistical atlas on two-dimensional measurements from a X-ray planar imaging modality and a webcam [Wang et al., 2012c]. In this work, this approach was chosen to realize automatically the anatomical interpretation of the images reconstructed from X-ray tomography.

It was decided, indeed, to incorporate a X-ray tomographic modality in the PhotonIMAGER$^{\text{TM}}$ Optima. To prevent the X-ray imaging modality from interfering with other components the device, it was decided to keep the same configuration and to reduce the angular range of the X-ray modality. The first challenge has been to reconstruct a tomographic image from data acquired over a limited angular range.

2.6 Chapter Summary

- This work addresses the development of a luminescence tomography modality using a commercial luminescence optical imaging device developed by the company Biospace Lab, the PhotonIMAGER$^{\mathrm{TM}}$ Optima.
- Luminescence tomography constitutes a severely ill-posed problem.
- Two complementary approaches have been proposed to address this problem, namely i) multispectral measurements and reconstruction, and ii) the use of anatomical priors in the reconstruction. Both approaches contribute to improve the quantification and localization of the luminescent sources. In this work, the second is explored.
- The primary aim of this work is, therefore, to extract an anatomical information from tomographic images reconstructed with the X-ray tomographic system under study.

Chapter 3

Limited Angle Micro-CT

Contents

Micro-CT was introduced in the early 1980's by Elliot and Dover [Elliott and Dover, 1982]. A wide range of applications of micro-CT using mice have emerged since this time, including :

- the determination of the body composition [Habold et al., 2010] such as, more specifically, adipose tissues [Judex et al., 2010, Marchadier et al., 2011];
- oncology studies including the study of metastatic development such as in bone, lungs or liver [Johnson et al., 2011, Kim et al., 2008]; *angiogenesis* [Savai et al., 2009, Ehling et al., 2014] ; models of tumors such as *xenotransplanted* breast tumors [Jensen et al., 2008];
- specific organ characeristics such as bone density[78] [Habold et al., 2011, Saeed et al., 2008] or bone healing [Di et al., 2014], the liver [Boll et al., 2011], or the lungs with the study of various pulmonary diseases such as fibrosis [Schofer and others., 2007, Johnson, 2007];
- cardiovascular diseases [Sheikh et al., 2010] and the vascular system [Zagorchev et al., 2010].

Today, this modality is involved in various multimodality combinations, including PET/CT, SPECT/CT, Optical/CT and PET/SPECT/CT[79] In this work, an existing micro-CT device developed at our institute was used to acquire radiological projections, therefore the use of a part of this data in a limited-angle context was straightforward.

Limited angle tomography, *digital tomosynthesis* and *computerized laminography* all refer to computerized image reconstruction from non-circular tomographic acquisition geometries. In limited angle tomography, the geometry is the same as in cone beam CT[80], except that the source and detector system describe only a part of the full circular range around the object under study – this circular motion is a characteristic of cone beam CT [Feldkamp et al., 1989]. In digital tomosynthesis, the source typically describes an arc in the vertical plane above a detector which remains immobile in the horizontal plane – both move reciprocally and proportionally with respect to the object under study [Dobbins and Godfrey, 2003]. In some cases, the X-ray tube has a linear motion parallel to the detector plane – this is called *linear tomosynthesis*. In laminography, the motion of the source and the detector are enclosed in two parallel planes, from either side of the object under study [Gondrom and Schröpfer, 1999]. Trajectories of the X-ray tube and the detector are typically linear, circular, or spiral. It is interesting to consider the evolution of these acquisition geometries from the historical standpoint[81]. The basic design of *conventional tomography* was introduced by Bocage[82] in 1917. He patented his invention in 1921. His work was followed by Vallebona[83] with two designs, i) an auto-tomography where the patient rotated while the X-ray tube and film remained fixed, and ii) a pivot of the X-ray tube and film around an axis, around the patient. He obtained his first radiotomographic images in 1930. The second pioneer of conventional tomography is Ziedses des Plantes[84]. For him, a linear movement was not sufficient, and a spiral movement was needed for a satisfactory tomography. The french company Massiot et Cie sold the first commercial *planigraphy* devices[85] after his design in 1936. In 1934, Grossman[86] patented a device for performing tomography. He had previously determined

---

[78] The loss in bone density can result for example from the carence in D-vitamin resulting from *Cystic Fibrosis* – or *mucovicidosis*.

[79] These combinations have been reported, respectively, by 28%, 12%, 7% and 3% of the respondents of the HTStec survey [Comley, 2011]. In terms of functional/morphological coupling, the combination of optical imaging and CT was reported by only 7% of the respondents, to be compared to 13% for Optical/MRI and 3% for the Ultrasound. Optical and planar X-ray was also reported by 4% of the respondents. Functional multimodality has also been reported such as Optical/SPECT – 4% – and Optical/PET – 12%.

[80] In the remainder, CT refers to cone beam CT if not specified differently.

[81] More details related to this historical introduction can be found in the booklet of the European Society of Radiology [European Society of Radiology, 2013].

[82] The French physician André Bocage (1892-1953) was a french physician and is considered as the father of tomography.

[83] The Italian Allessandro Vallebona (1899-1987) developed the concept of *stratigraphy* – from the Latin *stratum*, layer.

[84] Bernard Ziedses des Plantes (1902-1993) was a dutch physician .

[85] The term *planigraphy* – from the Latin *planus*, flat, was introduced by Ziedses des Plantes.

[86] Gustav Grossman (1878-1957) was a German manufacturer. He introduced the term *tomography*.

that the spiral motion preconised by Ziedses de Plantes was too complicated to put in practice in a clinical context. He also pointed out the increase in exposure time to X-rays – ten to fifteen times – caused by the spiral acquisition geometry compared to linear acquisitions. He introduced an appartus characterized by a linear movement of the film in the horizontal plane and an arc of the X-ray tube in the vertical plane. The same year, Jean Kieffer[87] patented a device called a "X-ray focusing machine" after the work he conducted on planigraphy since 1928. In 1936, Edward W. Twinning built a homemade device as a simplification of the original device from Grossman, and that could be adapted to standard radiographic tables. In 1938, the *laminagraph*[88] was commercialized by the Keleket X-ray company after Kieffer's design and developments made after he met Moore[89] in 1936. Kieffer and Moore disagreed about the benefits of the pluridirectional acquisition – Kieffer thought that no particular motion was better in all cases. Conversely, Moore supported the idea that the pluridirectional acquisition setup gave better results. The linear acquisition setup had become the rule, although pluridirectional acquisition turned out to give effectively better results. It is important to keep in mind that at that time, all the experiments had been performed to acquire images of a coronal slice. In 1936, Vieten[90] invented a device capable of axial transverse tomography. At about the same time, Watson[91] independently invented a similar device, under the name of *sectograph*. Axial transverse tomography had, in fact, been invented previously – but not put into practice – by Kieffer. The first modern *polytome*[92] – a pluridirectional axial transverse tomographic device – was commercialized by Massiot et Cie in 1951 and the first clinical results were published in 1953 [Thoyer-Rozat and Moussard, 1953]. Since that time, various improvement have been made to the polytome until conventional tomography was progressively replaced by CT, until the early 1990s [Dobbins and Godfrey, 2003]. The non-circular acquisition geometries remained used for various applications, and took benefits from the advent of the digital revolution. From the clinical standpoint, the need for non-circular tomography remains likely to arise when dose considerations and geometrical constraints come into play, as it is the case in breast tomosynthesis, dental imaging, and various other applications. This lead to the introduction and progressive development of *tomosynthesis* followed, in the late 1960s, by the invention of *digital tomosynthesis* [Dobbins and Godfrey, 2003]. Meanwhile, laminography was applied to Non-Destructive Assay of materials and objects which shape or extent prevents a CT system to rotate around – typically, Printed Circuit Board (PCB), helicopter rotor blades, welding of flat plates, or satellite solar panels [Gondrom and Schröpfer, 1999, Maisl et al., 2010]. Finally, several clinical applications of CT require to limit the angular range of a circular CT acquisition, as it is the case in short scan interventional C-arm CT [Zhang et al., 2011b].

Digital tomosynthesis has developed upon two complementary axes, namely i) the evolution of the image acquisition technologies and ii) the introduction of image reconstruction techniques and their evolution, greatly stimulated by the advent of digital acquisition and processing[93]. This evolution is somehow similar to the evolution of CT but with fundamental differences in the setups causing fundamental differences in the image reconstruction problems. From the standpoint of the image acquisition technology, the first image obtained by the *backprojection* of radiological data subsequent to the acquisition dates back to 1969 and constitutes the first step of a three-step evolution of these techniques. This approach differentiated from the conventional tomography in that in conventional tomography, the image of a single plane is created throughout the continuous acquisition, whereas

---

[87] Jean Kieffer (1897-1972) was a Franco-American technologist.

[88] *Laminagraph* comes from the Latin *lamina*, "a thin plate".

[89] Sherwood Moore (1880-1963) was a radiologist of the Washington University and director of the Malinckrodt Institute of Radiology.

[90] Heintz Vieten (1915-1985) was a German radiologist.

[91] William Watson (1895-1966) was a British radiographer.

[92] *Polytome* refers to the first commercialized devices that enabled pluridirectional acquisitions. The prototype was developed by the French engineers Raymond Sans and Jean Porcher in 1949 at the Salpêtrière Hospital.

[93] More details about the history of tomosynthesis can be found e.g. in [Dobbins and Godfrey, 2003].

in tomosynthesis a discrete series of radiological projections was measured by individual films and backprojected altogether in a physical display volume, and could be used to generate an arbitrary number of planes. One of the main drawbacks was the need to change the film at each projection. The second step has been the introduction of coded-aperture techniques since 1974, which allowed to measure a set of radiological projections on a single film and to decode them at the subsequent backprojection step. In this case, again, the visualization was made possible by backprojection in a physical support. The last step of this evolution is the advent of digital measuring and storing devices, namely the coupling of an image intensifier screen coupled to a video camera in the late 1960s – which enabled the storage of a discrete set of radiological projections, and the introduction of Charged Coupled Device (CCD) cameras in the late 1970s. The last step towards modern digital tomosynthesis systems has been the introduction of compact flat panel detectors in the 1990s, enabling the measurement of high-resolution images at rapid readout rate.

The second axis is the development of image reconstruction approaches. As mentioned, the original works involved backprojection of the radiological projections in a physical medium, by illumination of the measured projection data. The first computerized approaches for obtaining the image – *shift and add* methods – imitate this process. The main drawback is that the image of the plane of interest are corrupted by a residual blur of out-of-plane objects. A series of work has focused on the removal of this blur through the direct application of various filters to the measured data, since the late 1960s. Other approaches, introduced in 1980 jointly to the introduction of ectomography, aim at recovering the image by inversion of the system impulse response – these methods are convolution-backprojection methods similar to the CT filtered backprojection algorithm. The main drawback is that regions of the frequency space are not sampled at the acquisition step, which makes the inversion of the system impulse response problematic. This constitutes a *limited data problem* of the framework of tomographic reconstruction, and more precisely a *limited angle problem* [Natterer and Wübbeling, 2001]. Finally, iterative reconstruction techniques have been applied to tomosynthesis image reconstruction since 1975 [Dobbins and Godfrey, 2003].

3.1 Device under study

This work aims at integrating a X-ray tomographic imaging modality in an existing luminescence imaging system, the PhotonIMAGER$^{\mathrm{TM}}$ Optima. The black box shown in Figure 2.5 contains some of the components described in Sectoin 2.3, namely the detection system, the platform, the animal support and the illuminating end part of the light guides. Overall dimensions of the system are: $60 \times 85 \times 140$ cm (W x D x H). Accounting for the instruments present in the black box – including the four-views module, remaining space is enclosed in a parallelepiped of dimensions 50 cm $\times$ 40 cm $\times$ 33 cm (W x D x H). Facing the challenge of incorporating a micro-CT system in such a reduced space, it was decided, upstream in the conception choices, to reduce the angular range of the micro-CT. This results in a challenge in terms of image reconstruction. A micro-CT system developed at IPHC was used to model the limited angle micro-CT system.

The device under study is a Cone Beam[94] micro-CT system developed at our institute and represented in Figure 3.1. The system consists in i) a flat panel sensor Hamamatsu C7942-CA22 [Hamamatsu, b] and ii) a X-ray source Hamamatsu L9181-02 [Hamamatsu, a]. Both components are fixed to a rotating

---

[94] Typical Micro-CT system setups include *parallel beam*, *helical fan-beam* and *cone beam*. Helical fan beam micro-CT is characterized by a helical motion of the source/detector system along the transverse axis. The sensor is typically a one-dimensional array of detectors and the source flux is generally collimated to direct the X-rays on the detector active region. Cone beam micro-CT is characterized by a circular motion of the source and detector around the transverse axis. The sensor is typically a two-dimensional "flat panel" array of detectors, and the source flux has a conical shape covering the detector active region.

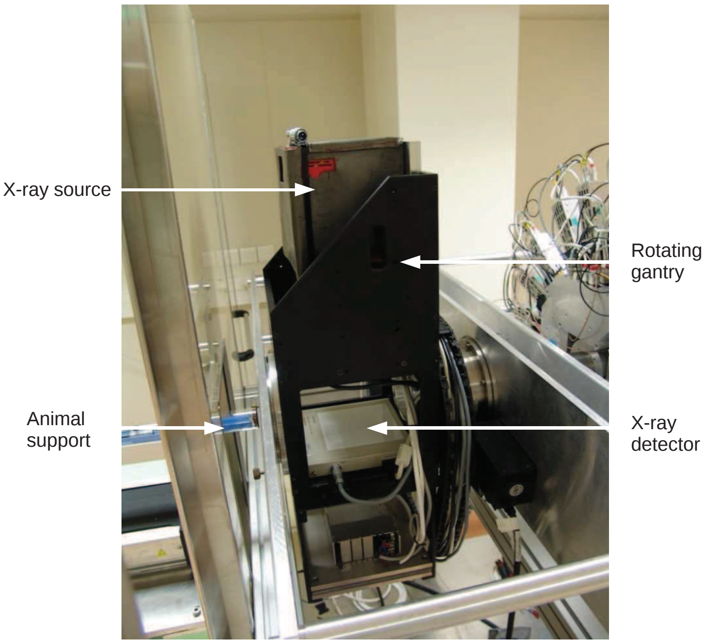

Figure 3.1: The micro-CT device used in this work [IPHC, 2014].

gantry, and an animal holder can be placed in the field of view during the acquisition. The source-to-detector distance is thus fixed and equal to 228 mm, while the radius of the circular rotation of the source is 172 mm. Radiological data is readout from the flat panel sensor and sent to an image reconstruction server.

The flat panel sensor is made of a 200 μm thick CsI (Tl) – Thallium doped Cesium Iodure – scintillator plate coupled to a CMOS photodiode array[95]. A 1 mm thick Aluminium filter covers the scintillator layer. It contains 2400×2400 square pixels of edge size 0.05 mm. Three pixel binnings are possible with the flat panel sensor, namely 1×1, 2×2 and 4×4 pixel arrangement. The output is encoded on 12 bits. The resolution of the sensor is 8 line pairs per mm. The dynamic range is 2×10^3 and the root mean square of the noise is of 1100 electrons.

The X-ray source is a tungsten anode tube. Two filters – Beryllium, 200 μm thick and Aluminium, 0.5 mm thick – are placed in the X-ray flux. It can be operated with a voltage between 30 kV and 130 kV therefore it can emit photons in the range $[30; 130]$ keV, with intensities up to 300 μs. The focal size is related to the power settings and ranges from 5 μm to 40 μm at 4 W and 39 W, respectively. The maximum emission angle is 45°. A typical spectrum, produced by the X-ray source and attenuated by the filters of the source and detector of the described setup is shown in Figure 3.2.

In this work, all the acquisitions were performed in continuous mode, in binning 1×1. The number of projections over 360° is set to 768 and the integration time is fixed to 470 ms. The acquisition is supervised using a dedicated user interface running on a front end command computer. Acquisitions can be carried out in continuous mode or step and shoot mode. The raw data can optionally be stored on a storage device for further processing.

X-ray measurements exploit the attenuation of X-rays through matter. Therefore, any X-ray tomographic reconstruction algorithm relies on more or less complex models of this attenuation, which

---

[95] X-rays induce fluorescence in the scintillator layer. The generated optical photons are detected by the photodiodes. This constitutes a typical indirect conversion sensor – as opposed to direct conversion sensors in which typically the X-ray directly produces electrons while going through a semi-conductor material.

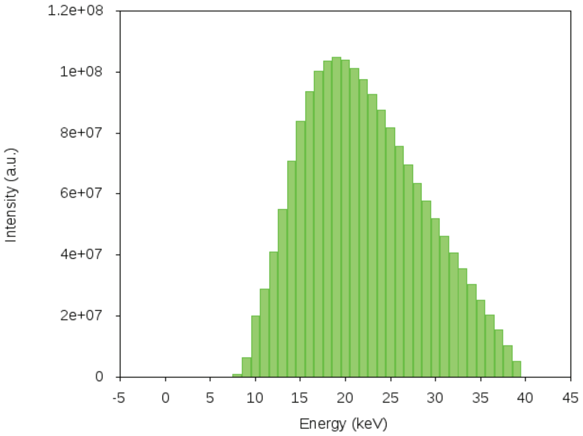

Figure 3.2: Typical X-ray spectrum corresponding to the device under study, after attenuation by the filtering materials of the X-ray source and detector, with a difference of potential of 40 kV applied on the X-ray source – analytical simulation after [Koubar et al., 2011].

results from the interactions of X-rays with matter. X-ray imaging relies on three main processes involving X-rays, namely i) their generation, ii) their interaction with biological tissues, and iii) their detection.

3.2 X-ray interactions with matter

In biomedical imaging, X-rays are typically produced by *bremsstrahlung* effect, which refers to the emission of a photon caused by the deflection of an electron by the electromagnetic field of the electrons and nucleus of an atom altogether[96]. This results in the production of X-rays over a continuous bremsstrahlung spectrum, which maximal energy is directly related to the applied voltage, as shown in Figure 3.2. Interactions with matter of X-ray having an energy inferior to the MeV are mainly i) photo-electric effect, ii) Compton scattering[97], iii) Rayleigh scattering[98]. Other interactions such as pair production occuring at energies greater than 1.022 MeV are not discussed in this section. The probability of interaction for each of these processes depends on the energy of the X-ray and is represented for a given material by the physical quantity called *cross section* expressed in barn[99]. X-rays travel in straight line until they undergo interactions such as scattering or absorption.

The *photo-electric* effect is the interaction of a photon with an entire atom. It results in the ejection of an electron from the electronic layers of the atom, with an energy

$$E_e = E_\gamma - E_b \tag{3.1}$$

where E_γ is the photon energy E_b is the electron bounding energy. Usually, electrons of the K-shell are responsible for photo-electric effect. As a consequence, fluorescence - characteristic - X-rays or Auger electrons are emitted by electronic recombination.

Compton – incoherent – scattering refers to the case where a photon gets scattered by a free electron - that is to say, an electron from the outer orbitals of the atom. Rayleigh – coherent – scattering is

---

[96] More detailed description of X-ray interactions with matter can be found e.g. in [Shultis and Faw, 2010].

[97] The American physicist Arthur Compton (1892–1962) earned half of the Nobel prize in Physics of 1927 "for his discovery of the effect named after him" [www.nobelprize.org, 2015].

[98] Rayleigh scattering was named after its discovery by the British physicist John William Strutt Rayleigh (1842–1919).

[99] $1 \text{ barn} = 10^-24cm^2$.

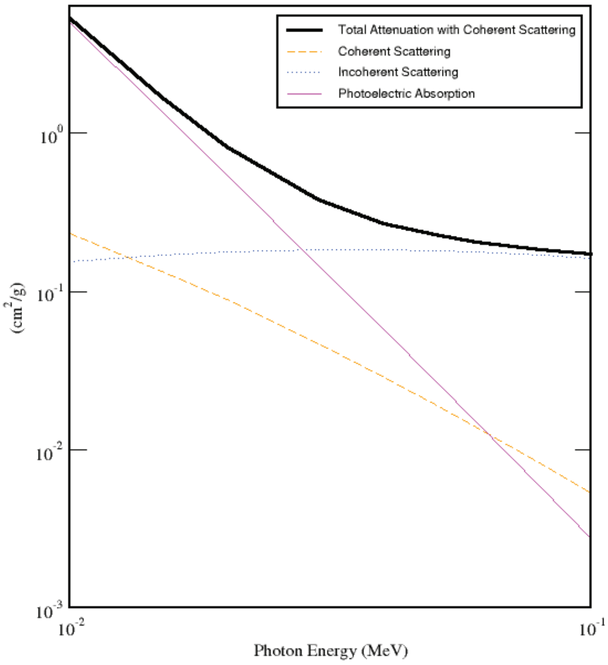

Figure 3.3: X-ray mass interaction coefficients over the energy range 10 keV - 100 keV - data from [National Institute of Standards and Technology, 2015]

an elastic scattering characterized by a slight energy loss and a slight deviation angle. This scattering is coherent in the sense that it results from the combined effect of multiple electrons over the photon. Although it is the source of artifacts in the reconstructed images, the modeling of scattering is commonly ignored from calculations and basic simulation kernels [Zhu et al., 2006].

Radiation interaction with matter is a statistic process. For small path length, the energy-dependant probability that a photon undergoes any interaction per unit distance in a given material is denoted μ. In fact for a fixed energy, given the probability $P_i(\Delta x)$ that the particle causes a reaction of type i while travelling a distance Δx along a straight line in the material, μ_i can be expressed as:

$$\mu_i(E) = \lim_{\Delta x \to 0} \frac{P_i(\Delta x, E)}{\Delta x} \tag{3.2}$$

The total attenuation coefficient μ is called the effective total linear attenuation coefficient and can be approximated as the sum of linear attenuation coefficients for photo-electric effect, Compton scattering and Rayleigh scattering, denoted respectively μ_{ph}, μ_c and μ_r:

$$\mu(E) \sim \mu_{ph}(E) + \mu_c(E) + \mu_r(E) \tag{3.3}$$

From the macroscopic point of view, the total linear attenuation coefficient can be related to the attenuation of a flux in straight line by Beer-Lambert's law. Considering an intensity $I_0(E)$ of X-rays of energy E incident to a slab of homogeneous material of total linear attenuation coefficient $\mu(E)$, the intensity of uncollided X-rays after a distance l can be expressed as:

$$I(l, E) = I_0(E)e^{-\mu(E)l} \tag{3.4}$$

This relation is fundamental in X-ray Computerized Tomography and underlies most reconstruction algorithms. The mass attenuation coefficient μ/ρ - in units of square distance over mass - where ρ is

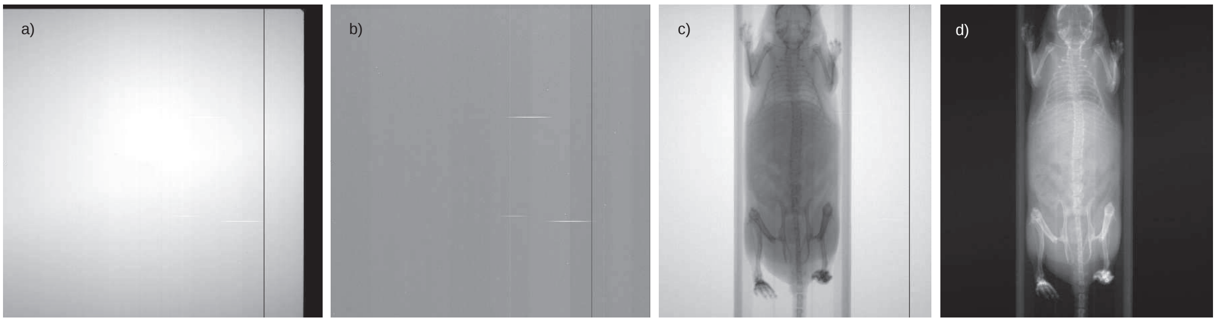

Figure 3.4: a) blank scan image, b) dark current image, c) intensity projection of a mouse, d) corresponding log image. Inactive pixels appear black on the blank scan and dark current images. Data generated with the micro-Computerized Tomography system developed at IPHC [IPHC, 2014].

the volumetric mass of the material, is also commonly used. Figure 3.3 dhows the X-ray mass attenuation coefficient for Compton and Rayleigh scattering as well as the photoelectric effect.

An example of radiological image is shown in Figure 3.4. A radiological image or intensity projection is measured by integrating charges in the detector array, over a time window $t_{integration}$. Once the time is elapsed, the charges are read out and sent to a processing unit. The set of read pixel values referenced by the pixel index constitute the image. The following operations have to be realized prior to the acquisition:

- measure the dark current[100] image, which is the image measured by the detector when no X-ray flux is sent to it. An example of dark current image is shown in Figure 3.4
- measure the blank scan image, which is an image of the X-ray flux integrated with the same characteristics as the radiological projections throughout the acquisition, with a clear field of view. An example of blank scan image is shown in Figure 3.4

Pre-processing of the radiological projections is usually performed assuming a mono-energetic beam. Indeed, in the – real – case of a polychromatic beam, the intensity emitted by the source is:

$$I_0 = \int_0^{E_{max}} I(E)dE \tag{3.5}$$

Considering a discrete representation, with N energy bins ΔE:

$$I_0 = \sum_{i=0}^{N} I(E_i) \tag{3.6}$$

with $E_i = i \times \Delta E$. Therefore the attenuated intensity of uncollided X-rays transmitted through the slab of thickness $l = x_1 - x_0$ is:

$$I(l, E) = \int_0^{E_{max}} I(E)e^{-\int_{x_0}^{x_1} \mu(E,t)dt} dE \tag{3.7}$$

and for the discrete form:

$$\hat{I}(l, E) = \sum_{i=0}^{N} I(E_i)e^{-\mu_i l} \tag{3.8}$$

---

[100] The dark current noise is mainly due to *thermoionic emission* in the electronic system – that is to say the emission of electrons and holes in the depletion region of the semi-conductor cristals.

where μ_i represents the mean attenuation coefficient on the energy range $[E_i; E_{i+1}]$. In the mono-energetic case, we have:

$$\int_{x_0}^{x_1} \mu(E,t)dt = -ln\left[\frac{I(l,E)}{I_0}\right] \tag{3.9}$$

Since this expression can not be easily generalized to the polychromatic case. the monochromatic assumption underlies most tomographic reconstruction algorithms. Therefore, the projection images are processed prior to reconstruction, as follows:

$$g(u,v) = -ln\left[\frac{I(u,v) - I_{dc}(u,v)}{I_{bs} - I_{dc}(u,v)}\right] \tag{3.10}$$

where $g(u,v)$ is the *log value* of pixel (u,v), $I_{dc}(u,v)$ is the dark-current value of pixel (u,v), I_{bs} is the mean blank-scan value. This simplistic model produces characteristic artifacts in tomographic reconstructions, mainly due to:

- beam-hardening, caused by the predominant attenuation of low energy X-rays and the assumption of a monochromatic spectrum, all along the path of X-rays [Herman, 1979]
- scattering, which is assumed to be negligible in most models [Zhu et al., 2006]

3.3 Tomographic Image

Images are typically reconstructed from cone beam micro-CT acquisitions using the Feldkamp, Davis and Kress algorithm (FDK) [Feldkamp et al., 1984]. In this document, the term tomographic image designates a finite discretization of the euclidean space in three dimensions on a cubic voxel lattice[101]. A tomographic reconstruction algorithm attributes a value to each voxel by processing the radiological data acquired with any tomographic system using a reconstruction algorithm. In fact, it estimates a discrete representation of the three-dimensional distribution $f(x,y,z)$, from a set of discrete two-dimensional measurements $g(\theta)$, with

$$\gamma(\theta) = a(f,\theta) \tag{3.11}$$

where a is a continuous function called the *projection operator*. Each $g(\theta)$ is a two-dimensional vector of dimensions $N_u \times N_v$. Noting $\tilde{g} = \{\gamma(h\mathrm{d}\theta), \forall h \in \{0,1,...,N-1\}\}$ where $d\theta$ is an elementary angle and N is a finite number of measurements such as $N\mathrm{d}\theta = 2\pi$, we can note

$$\tilde{g} = \{a(f, h\mathrm{d}\theta), \forall h \in \{0,1,...,N-1\}\}. \tag{3.12}$$

The function f is represented, in discrete form, by the $M_x \times M_y \times M_z$ three-dimensional vector $f_{i,j,k} \forall (i,j,k) \in \{0,...,M_x\} \times \{0,...,M_y\} \times \{0,...,M_z\}$ such that $f_{i,j,k} = f(i\mathrm{d}x, j\mathrm{d}y, k\mathrm{d}z)$ for discrete steps dx, dy and dz. The operation in discrete form can be represented using the algebraic formulation, with f noted as a one-dimensional vector of $M_x \times M_y \times M_z$ elements, as:

$$\tilde{g} = Af \tag{3.13}$$

where $\tilde{g}$ is a one-dimensional vector of $N_u \times N_v$ elements and A represents the *projection matrix* of size $[N_u \times N_v] \times [M_x \times M_y \times M_z]$. In X-ray tomography, the projection operator or matrix models the attenuation of X-rays through matter, by the physical processes explained in Section 3.2. In a continuous representation, the values of f at a points $(x,y,z) \in \mathbf{R}^3$ is the lineic attenuation coefficient μ, expressed in inverse length unit. In the discrete representation, the value of a voxel is the average of the lineic attenuation coefficient in this cubic element.

---

[101] Alternative representations of tomographic images have been proposed, including non-cubic voxels and spherically symmetric volume elements [Momey et al., 2011].

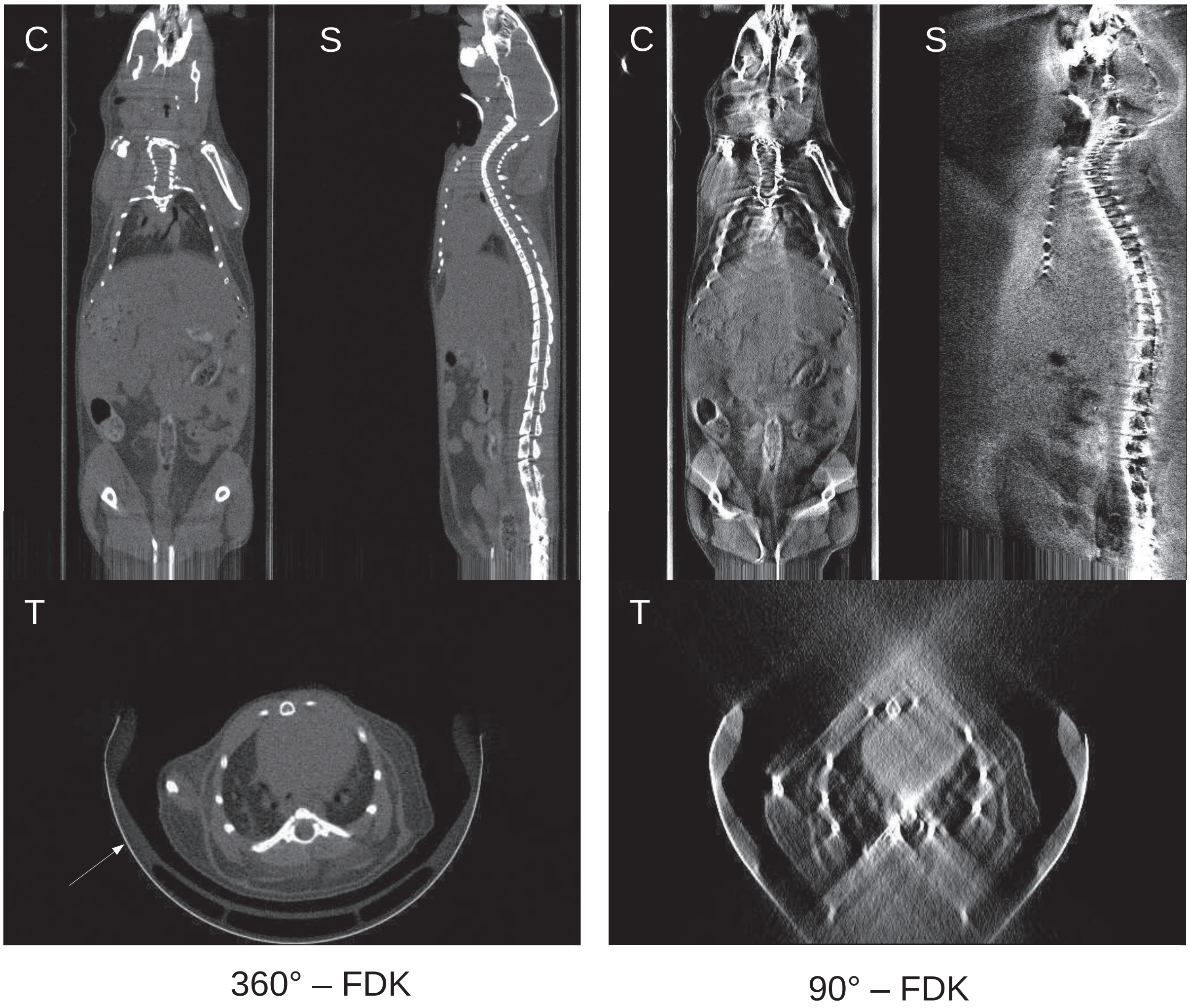

Figure 3.5: Transverse (T), coronal (C) and sagittal (S) cross sections through images reconstructed with FDK, respectively from 768 projections acquired over 360° and from 192 projections acquired over 90°. Images are made of cubic voxels of edge size 0.1 mm. Windows are, respectively: $[0.0; 0.1]$ mm^{-1}, $[0.0; 0.02]$ mm^{-1}. The white arrow indicates the animal holder.

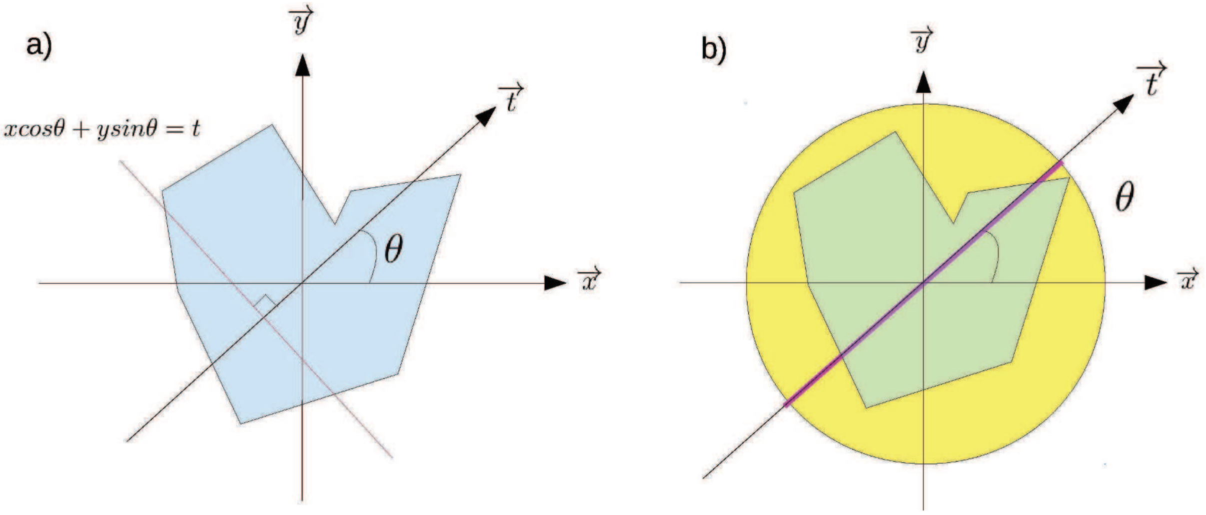

Figure 3.6: Radon transform in two dimensions. The purple segment represents the support of the Radon transform at angle θ in parallel beam geometry for a detector of finite size.

3.4 A formal description of the limited angle problem

One of the main challenges with the limited angle problem is that in most cases, it prevents from achieving exact reconstruction of the object under observation. The artifacts visible in Figure 3.5 in the reconstruction from the limited angle dataset constitutes a good illustration of the direct application of a cone beam CT algorithm to limited angle preclinical data. To formalize this, it is interesting to have a look at the analytical formulation of the tomographic reconstruction problem, and to the conditions that have been formulated for exact reconstruction.

3.4.1 The Fourier Slice Theorem in two dimensions

Tomographic reconstruction algorithms generally use the integrated value of the attenuation coefficient along a ray – provided X-rays travel in straight line when not interacting in matter. Indeed, Equation 3.8 corresponds to the Radon transform of the distribution of X-ray attenuation coefficients, a relation between the distribution of the attenuation coefficients and their integral along straight parallel rays[102]. The *Radon transform* of the function $f(x, y)$ - called the *object*, in this section - models the projection of the object on the line directed by the vector $(\cos\,\theta, \sin\,\theta)$:

$$P_\theta(t) = \int_{-\infty}^{+\infty}\int_{-\infty}^{+\infty} f(x,y)\delta(x\cos\theta + y\sin\theta - t)dxdy \tag{3.14}$$

which integrates the object values along the line of equation

$$x\,\cos\,\theta + y\,\sin\,\theta \;=\; t \tag{3.15}$$

as represented in Figure 3.6.

Let the Fourier transform of a two-dimensional function be:

$$F(u,v) = \int_{-\infty}^{+\infty}\int_{-\infty}^{+\infty} f(x,y)e^{-j2\pi(ux+vy)}dxdy \tag{3.16}$$

---

[102] Extensions to fan beam and cone beam geometries have also been introduced [Kak and Slaney, 1988, Feldkamp et al., 1984].

Let the coordinate system (O, t, s) be (O, x, y) rotated from θ:

$$\begin{cases} t = x\cos\theta + y\sin\theta \\ s = -x\sin\theta + y\cos\theta \end{cases} \tag{3.17}$$

A projection at angle θ is defined in cylindrical coordinates as:

$$P_\theta(t) = \int_{-\infty}^{+\infty} f(t, s)ds \tag{3.18}$$

and its Fourier transform is defined as:

$$S_\theta(w) = \int_{-\infty}^{+\infty} P_\theta(t)e^{-j2\pi(wt)}dt. \tag{3.19}$$

Then for a frequency line crossing the origin:

$$S_\theta(w) = \int_{-\infty}^{+\infty} \left[\int_{-\infty}^{+\infty} f(t, s)ds\right] e^{-j2\pi(wt)}dt \tag{3.20}$$

$$S_\theta(w) = \int_{-\infty}^{+\infty}\int_{-\infty}^{+\infty} f(x, y)e^{-j2\pi w(x\cos\theta+y\sin\theta)}dxdy \tag{3.21}$$

The Fourier Slice theorem states that, as:

$$S_\theta(w) = F(w, \theta) = F(w\cos\theta, w\sin\theta), \tag{3.22}$$

the values of $F(u, v)$ on radial lines can be determined, and the object can be estimated from an infinite number of projections, taking the inverse Fourier Transform of F:

$$f(x, y) = \int_{-\infty}^{+\infty}\int_{-\infty}^{+\infty} F(u, v)e^{j2\pi(ux+vy)}dudv. \tag{3.23}$$

In this formalism, one line in the Fourier domain is associated to each projection angle θ. Considering a finite detector centered on the origin and rotating in the plane, about the origin, large enough to contain the projection of the object at any projection angle, the measured Radon domain is a disc, as represented in Figure 3.6. In this case, the collection of an infinite number of continuous projections over the whole angular domain $\theta \in [0\ ;\ \pi]$ makes possible to recover the object exactly using equation 3.23. If an infinite number of projections is collected over an angular domain $\theta \in [\theta_{min}\ ;\ \theta_{max}]$ - as represented in Figure 3.7, with $\theta_{max} - \theta_{min} < \pi$, the conditions of the Fourier Slice theorem are not verified. The measured domain in Radon space for a finite detector identical to this represented in Figure 3.6 is the intersection of the circle represented in Figure 3.6 and the measured part of the domain - represented in white in Figure 3.7. The description of the image is therefore incomplete and inversion using inverse Fourier transform - for example, assuming that the unknown coefficients are null - is likely to yield a poor estimate of the image. In the fan beam case, one projection corresponds to an arc in the Radon domain, as represented in Figure 3.8. The measured domain is the continuous union of the arcs rotated over the considered angular range. For a rotation over the range $\theta \in [0\ ;\ 2\pi]$, the measured domain is the disc C represented in Figure 3.8. In this case, the Fourier domain is, once again, completely measured. It would have been measured even for an angular range of $\beta = 180° + \alpha$, where α is half the angle of the fan. For an angular range $\theta \in [\theta_{min}\ ;\ \theta_{max}]$, the measured part of Radon space is the domain represented in green in Figure 3.8. It is intuitive, from this visual representation of the Radon domain, that the Fourier domain is not likely to be properly estimated in most cases and thus,

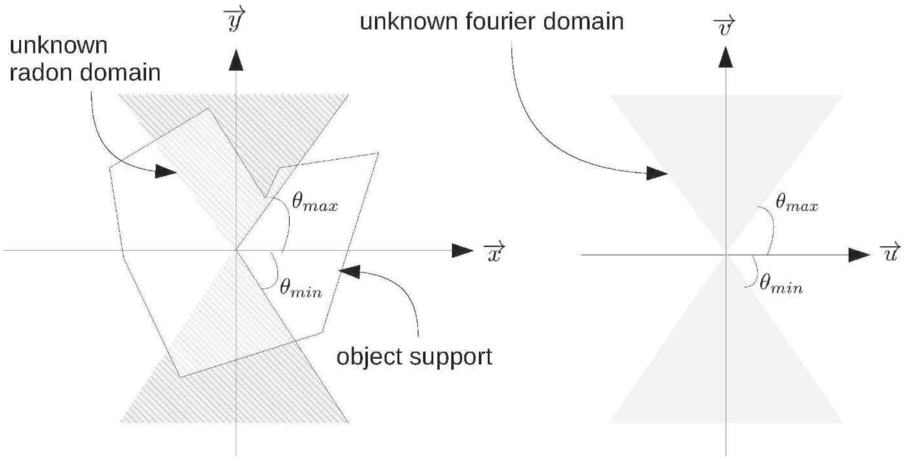

Figure 3.7: Image domain and Fourier domain in the case for an infinite number of projections over the domain $\theta \in [\theta_{min} ; \theta_{max}]$. This representation corresponds to an infinite detector. The shaded areas represent the unknown regions of each space.

similarly to the parallel beam case, that the object is not likely to be recovered by the application of image reconstruction algorithms based on the Fourier Slice theorem. These considerations made in a continuous formalism can be viewed as a best case of the discrete formalism, for which signal sampling considerations come into play[103].

3.4.2 Extension to three dimensions

Both the cases presented in the previous section - parallel beam and fan beam - can be extended to three dimensions - yielding three-dimensional parallel beam and cone beam geometries, respectively. In the parallel beam case, a plane is measured in the Radon space - and, consequently, in the Fourier domain. In the cone beam case, the portion of a sphere is measured in the Radon space for each projection. Once again, the continuous union of these projections over a sufficiently broad angular range makes possible to obtain a complete description of the image in the Fourier domain in three dimensions, and consequently to recover the object. Similarly, limiting the angular range prevents from obtaining a complete representation of the Fourier domain, thus the object is unlikely to be recovered.

3.4.3 Data Sufficiency Conditions

The previously described acquisition geometries can be observed with respect to Orlov's and Tuy's conditions [Natterer, 2008, Metzler et al., 2003]. The representation of an imaging system in Orlov's sphere is done as follows, in the two-dimensional parallel beam geometry: to each measurement direction in spherical coordinates (θ, ϕ) is associated a point on the unit sphere, $(1, \theta, \phi)$. Let Ω denote the union of the points associated to the set of measurements. Therefore, for a rotation of an ideal system over $\theta \in [0 ; 2\pi]$, and a continuous measurement on this domain, Ω is the circle of unit radius contained in the plane $(O, \vec{x}, \vec{y})$. Three parallel beam imaging system are represented on Orlov's sphere in Figure 3.9. Orlov's condition states that a correct reconstruction is likely to be obtained if the

---

[103] This is out of the scope of this thesis. The fundamental signal sampling considerations of CT are explained in [Kak and Slaney, 1988].

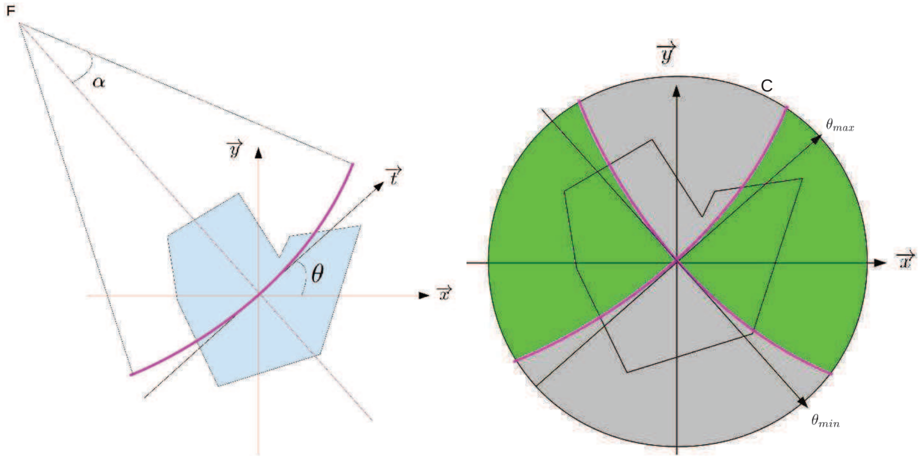

Figure 3.8: Left : Fan beam acquisition geometry. The purple arc represents the support of the Radon transform in the fan beam case at angle θ. Right : Radon space in fan beam acquisition geometry over a limited angular range. The green region represents the domain of Radon space which is measured.

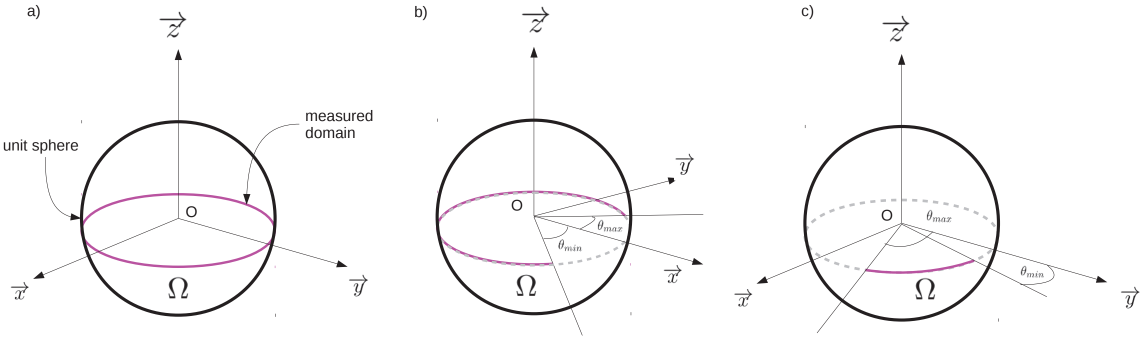

Figure 3.9: Representation of a parallel beam imaging system on Orlov's sphere. The complete acquisition is represented in grey, whereas the effective acquisition is represented in purple. Three cases are represented: a) the acquisition is complete over the range $\theta \in [0 ; 2\pi]$; b) the acquisition is incomplete but the angular coverage is greater than 180° ; c) the angular coverage is less than 180°.

domain Ω has an intersection with any great circle of the sphere. This is obviously the case for the rotation over $\theta \in [0 ; 2\pi]$. This is still the case for $\theta \in [0 ; \pi]$, but not $\theta \in [0 ; \pi[$. More generally, if $\theta \in [\theta_{min} ; \theta_{max}]$ with $\theta_{max} - \theta_{min} < \pi$, there exist great circles of the spheres which do not intersect the domain Ω. In this cases, the acquisition system does not respect Orlov's condition and exact reconstruction of the object is unlikely to be achieved.

In cone beam, Tuy's condition states that an exact reconstruction is likely to be achieved if any plane that intersects the object contains at least one intersection with the source trajectory. In cone beam with a circular motion of the source and detector *around* the object, this is true for $\theta \in [0 ; \pi + \alpha]$ and only in the central slice - in other words, the intersection of the object and the plane containing the source and detector throughout the acquisition. Out of the central slice, exact reconstruction is not guaranted. This consideration can be related to the fact that transform-based algorithms for cone-beam geometry - for example, the Feldkamp, Davis and Kress (FDK) algorithm [Feldkamp et al., 1984] - are always approximate out of the central slice. It must be moderated by the fact that even though approximate and even though no formal proof has been derived, to our knowledge, FDK gives very satisfactorily results for narrow cone angles and in the sphere of radius $R \times \cos(\alpha)$ - which corresponds to the domain illuminated by the X-ray flux throughout the acquisition in a conventional circular cone-beam acquisition. In fact, the quality of the reconstruction degrades as the distance from the central slice increases. Reducing the angular range below $\pi + \alpha$ will therefore invalidate Tuy's condition and an exact reconstruction is unlikely to happen even in the central slice.

These conditions are valid in parallel beam in two and three dimensions. Fan beam geometry can be related to parallel beam geometry by rearrangement of the measurements, so the derivation of a similar conditions corroborates the fact that an exact reconstruction of the object is unlikely to be achieved if $\theta \in [0 ; \pi + \alpha[$. These conditions are, however, not rigorously respected in cone beam. Nevertheless, practical cone beam algorithms such as FDK show enable quasi-exact reconstructions for narrow cone angles [Feldkamp et al., 1984, Feldkamp et al., 1989]

3.5 Dealing with the limited angle problem : state of the art

Limited angle CT, digital tomosynthesis and laminography, although they have been developed for various applications and despite the difference of their designs, have a very common point when it comes to image reconstruction. Indeed, from this standpoint, they all suffer of the limited angle problem. The state of the art of algorithmic approaches dedicated to dealing with these acquisition geometries can be constituted from the approaches developed for each of them. Table 3.1 summarizes various publications reporting the use of one of the three geometries. From this state of the art, the algorithms addressing the limited angle problem in tomographic reconstruction can be classified in i) *transform-based* methods, ii) *sinogram*[104] *domain* methods and iii) *image domain* methods. Table 3.2, Table 3.3 and Table 3.4 summarize the algorithmic strategies developed in the various cases listed in Table 3.1. These tables gather information about, respectively, i) ectomography and circular laminography, ii) tomosynthesis and linear laminography, iii) limited angle CT.

Transform-based methods – or convolution-backprojection methods – are analytical formulations of the reconstruction problem. It is generally not possible, with these methods, to include a prior knowledge to the reconstruction process. Such methods include the conventional Filtered Backprojection algorithm, which has been reported for Digital Breast Tomosynthesis in [Zhang et al., 2006, Dobbins and Godfrey, 2003, Reiser et al., 2009]. These methods are appreciated for their speed and provide valuable visual results. FBP is sometimes coupled to other approaches such as wavelet transform-

---

[104] The *sinogram* refers to the expression of the measurements as a function of the acquisition angle. The *sinogram domain* covers the angular range $[0; 360°]$.

ref.	modality	geometry	application
[Dale et al., 1985]	gamma camera	ectomography	C: head/abdomen
[J. L. Prince, 1990]	CT	circular	n.s.
[Kudo and Saito, 1991]	CT	circular	n.s.
[Sahiner and Yagle, 1993]	CT	circular	n.s.
[Yau and Wong, 1996]	CT	circular	n.s.
[Fahrig et al., 1997]	CT	C-arm	C: angiography
[Kalukin and Sankaran, 1997]	laminography	rotation in plane	NDA
[Badea et al., 1998]	tomosynthesis	arc	C: n.s.
[Gondrom and Schröpfer, 1999]	laminography	trans. / rotation in plane	NDA
[Persson et al., 2001]	gamma camera	ectomography	C: abdomen/head
[Chen and Earner, 2004]	tomosynthesis	rotation in plane	n.s.
[Rantala et al., 2006]	tomosynthesis	arc	C: dental/breast
[Zhang et al., 2006]	tomosynthesis	arc	C: breast
[Sidky et al., 2009a]	CT	circular	n.s.
[Lu et al., 2010]	CT	circular	n.s.
[Reiser et al., 2009]	tomosynthesis	arc	C: breast
[Sidky et al., 2009b]	tomosynthesis	arc	C: breast
[Fu et al., 2010]	laminography	rotation in plane	n.s.
[Lu et al., 2011]	CT	circular	n.s
[Gomi et al., 2011]	tomosynthesis	linear	C: chest; hip & TM joints
[Heusser et al., 2012]	CT	circular	C: whole-body
[Schäfer et al., 2012]	CT	C-arm	C: cardiac
[Zhang et al., 2011b]	CT	C-arm	C:n.s.
[Levakhina et al., 2013]	tomosynthesis	arc	C: hand
[Ritschl et al., 2015]	CT	C-arm + linear shift	C:n.s.

Table 3.1: Non-exhaustive state of the art of tomosynthesis / laminography / ectomography devices.
- TM = temporomandibular
- CT = computed tomography
- C = clinical
- n.s. = not specified
- NDA = non destructive assay

ref.	ϕ (°)	N	algorithm	data
[Dale et al., 1985]	30	128/64	FBP	clinical
[Kalukin and Sankaran, 1997]	32	n.s.	s&a	exp.
[Persson et al., 2001]	*40	128	MAP-EM OSL(TV)	sim. (discrete)
[Chen and Earner, 2004]	n.s.	8	MRF-MAP	sim. (discrete)
[Fu et al., 2010]	45	256	FBP	sim. (analytical)

Table 3.2: Non-exhaustive state of the art of ectomography and circular laminography. ϕ is the projection angle. The $\star$ denotes the angle of the slant-hole collimator.
- FBP = filtered backprojection
- MAP = maximum *a posteriori*
- EM = Expectation Maximization
- OSL = one step late
- TV = total variation minimization
- MRF = Markov random fields
- sim. = simulated

ref.	α (°)	N	algorithm	data
[Badea et al., 1998]	40	20	s&a + wavelets	exp.
[Rantala et al., 2006]	187	23	FBP+wavelets	exp.
[Zhang et al., 2006]	60	21	BP/SART/ML-convex	exp.
[Reiser et al., 2009]	90	11	FBP/EM/ART+TV	sim. (analytical)
[Sidky et al., 2009b]	50	11	ART+TV	clinical
[Gomi et al., 2011]	40	67(hip,TM joints)/74(chest)	mod. FBP	clinical
[Levakhina et al., 2013]	50	25	SART	exp.
[Ritschl et al., 2015]	165	431/431+91(shift)	SART	sim. (n.s.)/ pC

Table 3.3: Non-exhaustive state of the art of tomosynthesis and linear laminography. - FBP = Filtered BackProjection
- mod. = modified
- ART = algebraic reconstruction techniques
- SART = simultaneous algebraic reconstruction techniques
- EM = expectation maximization
- MAP = maximum *a posteriori*
- TV = total variation minimization
- sim. = simulated
- exp. = experimental
- n.s. = not specified
- pC = preclinical

ref.	α (°)	N	algorithm	data
[J. L. Prince, 1990]	120	60	S.R.	sim. (analytical)
[Kudo and Saito, 1991]	112	765	S.R.	sim. (analytical)
[Sahiner and Yagle, 1993]	157/135	112/96	FBP+wavelets	sim. (n.s.)
[Yau and Wong, 1996]	157.5	28	S.R.	sim. (n.s.)
[Fahrig et al., 1997]	200	130	FBP	clinical
[Sidky et al., 2009a]	90	64	ART/ART+TV/EM	sim. (discrete)
[Lu et al., 2010]	20/40/60/80	20/40/60/80	wavelet galerkin	sim. + exp.
[Lu et al., 2011]	25	25	ART+TV (conj. grad.)	sim. (discrete) + exp.
[Heusser et al., 2012]	120+fan(n.s.)	n.s.	FBP+priors	clinical
[Schäfer et al., 2012]	200	116	FBP	clinical
[Zhang et al., 2011b]	193.8	587	FDK/ART+TV	clinical

Table 3.4: Non-exhaustive state of the art of limited angle CT.
- S.R. = sinogram recovery
- sim. = simulated
- ART = algebraic reconstruction techniques
- TV = total variation minimization
- EM = expectation maximization
- FBP = filtered backprojection
- FDK = Feldkamp, Davis and Kress algorithm
- exp. = experimental

based restoration such as in [Sahiner and Yagle, 1993].

Sinogram-domain methods have been developed to deal with the problem by considering the measured domain of the Radon space - which constitutes a discrete set of the sinogram domain. In a full-scan geometry - and assuming the object is completely contained in the imager Field of View, the sinogram is known within the region corresponding to the object support through Radon transform. In [Yau and Wong, 1996], a non-iterative linear extrapolator is developed and applied prior to a Convolution-Backprojection method. The method is evaluated on a $157,5^\circ$ angular range. In [Kudo and Saito, 1991], the sinogram is reconstructed using specific consistency conditions and a priori knowledge on its support, for a 112° angular range. The approach developed in [Prince and Willsky, 1993] includes prior probabilistic knowledge of the shape of the object to estimate the sinogram support. Sinogram interpolation - or inpainting - has been proposed in [Li et al., 2012], based on sinusoid-like curves. Though limited to sparsely sampled datasets - with 14° angular steps - and bad detector region, it is conceivable that this approach could be extended to the limited angle problem. In [J. L. Prince, 1990], the Ludwig-Helgason consistency condition[105] and a smoothness constraint are used to reconstruct the sinogram prior to a Filtered Backprojection Algorithm. The approach makes possible to include a prior knowledge about the sinogram support and its features. These methods have been proposed in two dimensions and, to our knowledge, no extension to three-dimension has been reported.

Image domain methods, applied to limited angle tomography, include algebraic and statistical methods. These methods are iterative, by nature, and use directly the pre-processed projections. Such methods can be regularized either by the addition of a secondary iterative loop - this is generally

---

[105] The Ludwig-Helgason consistency conditions describes the consistency of the Radon transform in two dimensions [J. L. Prince, 1990].

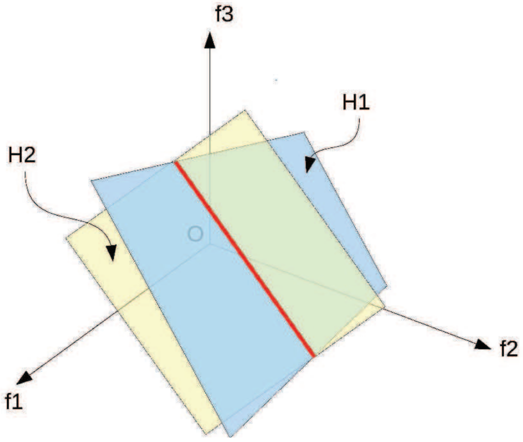

Figure 3.10: Hyperplanes in a three-dimensional image space for two measurements which corresponding lines in the projection matrix are equations of planes of $\mathbb{R}^3$. the red segment belongs to the line of solutions. Therefore if only H1 and H2 are available to estimate the solution in the form of a point, the problem is ill-posed since no unique solution can be found.

the case for algebraic techniques - or in the update formula - this is generally the case for statistical methods, including Maximum A Posteriori algorithms. Statistical methods consider the attenuation coefficient of the object as a probability distribution to be estimated from a set of observation collected by detector - the projection dataset. Reconstruction is typically derived from the Expectation Maximization algorithm, through an iterative maximization of log-likelihood of the projection data and projection of the estimated image. The use of priors in the reconstruction is generally made possible by statistical methods such as in [Nguyen and Lee, 2010] and [Persson et al., 2001]. Statistical methods constitute a completely different approach and was also applied to tomosynthesis [Williams et al., 2008, Reiser et al., 2009, Rantala et al., 2006] as well as in a conventional acquisition setup [Nguyen and Lee, 2010]. In algebraic methods, a linear system relates the measured projections and the object. The aim of these methods is to inverse a projection matrix, and this inversion is practically carried out using numerical methods. They have been reported as an alternative to convolution-backprojection methods in the case of penalized acquisitions - in other words, limited data problems [Verhoeven, 1993, Kak and Slaney, 1988]. Applications of these algebraic methods to tomosynthesis reconstruction have been reported in [Dobbins and Godfrey, 2003, Zhang et al., 2006, Reiser et al., 2009] for breast and [Levakhina et al., 2011] for hands.

3.5.1 Algebraic Reconstruction Technique

Algebraic reconstruction technique (ART)[106] has been proposed as an alternative for analytical reconstruction techniques - especially in cases where there is a sampling non-uniformity, or that the sampling rate of the angular range is not high enough [Verhoeven, 1993, Kak and Slaney, 1988]. They rely on an algebraic formulation of the reconstruction problem and a numerical solving of the linear system. In

---

[106] Considering an ill-posed linear system $Ax = b$, Algebraic Reconstruction Technique (ART) – or Kaczmarz method, named after its invention by the polish mathematician Stefan Kaczmarz (1895–1939) in 1937 [Kaczmarz, 1937] – solves numerically the least square minimization problem:

$$\min_x ||Ax - b||_2^2 \tag{3.24}$$

by iteratively updating the image estimate.

other words, the acquisition is modeled by

$$\tilde{g} = P\ f + \epsilon \tag{3.25}$$

where $\tilde{g}$ is the dataset of measured projections, P is called the *projection matrix*, f is the unknown image to be estimated, and ϵ is an error term which includes mainly the detection noise and the noise in the X-ray flux. The system is solved numerically through an iterative process using the following formula:

$$f^{k+1} = f^k + r\frac{P^b(\tilde{g} - Pf)}{\|P\|^2} \tag{3.26}$$

where P^b is the *backprojection matrix* which assigns a value from the sinogram domain all along the ray in the image domain.

Let f, the image, be considered as a variable with n degrees of freedom. In other words, f is a point in a n-dimensional space. Formally, ART consists in finding the intersection of all hyperplanes defined by the equations of the linear system. In a determined or overdetermined system, the intersection of the hyperplanes is a point, and constitutes the unique solution of the system. In the case of limited angle tomography, the intersection of the known hyperplanes is not a point. In other words, there is an infinity of solutions yielding the same projections as the measured data. Therefore, ART will generally fail at finding the solution which corresponds to the object under observation. The normal vector of each hyperplane, $\overrightarrow{w_i}$, which corresponds to a line in the projection matrix. As lines of P correspond to consecutive projections, the scalar product of two consecutive lines is maximal. The convergence speed can be related to the orthogonality of the hyperplanes used in the reconstruction. Therefore, one would choose orthogonal hyperplanes to achieve faster convergence. Various extensions to ART have been proposed in the litterature, including Simultaneous Algebraic Reconstruction Techniques (SART), Simultaneous Iterative Reconstruction Technique (SIRT) [Kak and Slaney, 1988].

In this work, the linear system is underdetermined and poorly orthogonal - this means that no matter how numerous the projections would be in the measured angular range, the corresponding equations are not orthogonal enough and thus there is an infinity of solutions to the system. In other words, convergence of the algorithm is not guaranted. Therefore, the direct application of ART to the problem under consideration is not likely to yield an acceptable estimation of the object. To our knowledge, satisfactorily results have indeed not been reported in a system as underdetermined and poorly orthogonal as the system under study. Examples of the results of ART in such penalized cases can be found in [Sidky et al., 2009a, Reiser et al., 2009]. ART has the advantage of making possible the addition of a prior information in the reconstruction, as a supplementary hyperplane - for example, a positivity constraint. The prior information can also be introduced using a secondary iterative loop to minimize an energy function.

3.5.2 Minimization of the Total Variation Norm

The Total Variation norm[107] is defined as the continuous convex functional defined on the class of derivable functions on $\Omega \subset \mathbb{R}^3$ [Arbeláez and Cohen, 2003]:

$$F(f) = \int_\Omega |\nabla f(x,y,z)| dxdydz \tag{3.27}$$

or in discrete form

$$\|f\|_{TV} = \sum_{i,j,k} |\nabla f_{i,j,k}| \tag{3.28}$$

---

[107] The notion of *total variation* was introduced in 1881 by the French mathematician Camille Jordan (1838-1922) [Arbeláez and Cohen, 2003].

ref.	modality	ill-posed problem	strategy
[Persson et al., 2001]	ectomography	**limited angle**	(TV)MAP-EM OSL
[Candès et al., 2006b]	CT	sparse sampling	FBP, TV regularization
[Sidky et al., 2009a]	CT	sparse view /**limited angle** / BDB	ART, TV reg.
[Sidky and Pan, 2008]	CT	sparse sampling	ART, TV reg.
[Herman and Davidi, 2008]	CT	sparse sampling	ART, TV reg.
[Reiser et al., 2009]	tomosynthesis	**limited angle**	ART, TV reg.
[Sidky et al., 2009b]	tomosynthesis	**limited angle**	ART, TV reg.
[Bian et al., 2010]	CT	sparse sampling	ART, TV reg.
[Sidky et al., 2011]	CT	low intensity	ART, TV reg.
[Han et al., 2011]	CT	low intensity	ART, TV reg.
[Ritschl et al., 2011]	CT	sparse view /**limited angle** / TP	SART, TV reg.
[Defrise et al., 2011]	PBCT	sparse sampling	TV-RSART
[Lee et al., 2012]	CT	sparse sampling	ART,TV reg.+prior

Table 3.5: Non exhaustive state of the art of the applications of algorithms minimizing the total variation norm in image reconstruction.
- TP = truncated projections
- PBCT = parallel beam CT
- reg. = regularization
- BDB = bad detector bins
- TP = truncated projections

This function is derivable on Ω and convex. The operator ∇ associates to f its Gradient Magnitude Image (GMI), as follows:

$$\nabla f_{i,j,k} = \sqrt{\triangle^2_{i+1,j,k} + \triangle^2_{i,j+1,k} + \triangle^2_{i,j,k+1}} \tag{3.29}$$

with, in the discrete case, the differential operator $\triangle$ defined as:

$$\triangle_{l,m,n} = f_{l,m,n} - f_{i,j,k}. \tag{3.30}$$

The Total Variation norm of f is therefore the $\mathbf{L}_1$ norm of the Gradient Magnitude Image of f. Let f, the image, remain considered as a variable with n degrees of freedom. As explained in the previous section, ART aims at finding the point in this n-dimensional space, which constitutes the solution of the system. The problem in limited angle tomography is that an infinity of points in a domain of this n-dimensional space could yield a set of observation identical to the measured data, as shown in Figure 3.10. It is intuitive that with no complementary information, ART is likely to fail in the limited angle case, because i) convergence is not guaranted and ii) if it converges to a point in the domain of possible solutions, this point is not likely to be the closest to the observed object. A well-chosen regularization strategy is likely to constrain the algorithm to iterate in a region where the solution closest to the object is likely to be found or even to converge to this solution. Regularizations are generally put into practive through the minimization of an energy functional such as a quadratic sum or the total variation norm.

The use of the total variation as a regularizer in tomographic reconstruction has been reported since 2001 [Persson et al., 2001]. Since then, it has been in the scope of an active investigation area, especially with the advent of the Compressed Sensing theory (CS). Indeed, from the signal processing point of view, an exact reconstruction from such an undersampled measurement as in limited angle tomography is unlikely to be achieved – since a large region of the frequency domain, with respect to the angular sampling between projections on the sampled range, is not measured. The *Sampling Theorem*[108] states that the minimum sampling rate required to determine completely a signal from measurements is twice the maximum frequency present in the signal [Jerri, 1977]. The Compressed Sensing theory[109] has brought a framework to deal with undersampled measurements, provided the signal is sparse – that is to say, that they have concise representation when expressed in a proper basis – and that, conversely, the sampling waveforms have "an extremely dense representation" in the considered basis [Candès and Wakin, 2008]. This is typically the case in the context of filtered backprojection, where the Fourier transform expresses the signal in the frequency domain. In 2005 [Candès et al., 2006b], Candès *et al.* have presented an example of signal recovery from highly incomplete measurements - namely, the measure of as few as 22 parallel projections regularly spaced on the 180° angular range. In this case, an algorithm seeking the optimal image g^* verifying:

$$FT(g^*) = FT(f) \tag{3.31}$$

with a minimal Total Variation of g has been used. Results are shown for a severely underconstrained acquisition setup, provided 22 radial lines. In this ideal case study, exact recovery of the discrete signal is realized, at a sampling rate 50 times lower than the Nyquist rate. The underlying idea has inspired the development of iterative reconstruction algorithms regularized by a minimization of the Total Variation, making the assumption that the gradient magnitude image of the image is sparse. Various publications report the minimization of the total variation norm as a regularizing strategy, including sparse – thus, few – view CT, low intensity CT, reconstructions where the data is corrupted by noise or bad detector bins, and limited angle CT. A number of these works is summarized in Table 3.5. These algorithms are mainly based on an ART – or a variant of ART, such as SART – regularized by the minimization of the total variation. It is, in particular, the case of the Adaptive Steepest Descent – Projection Onto Convex Sets algorithm (ASD-POCS) [Sidky et al., 2009a].

3.5.3 Description of the ASD-POCS algorithm

As suggested by its name, the Adaptive Steepest Descent – Projection Onto Convex Sets algorithm (ASD-POCS) algorithm acts in two steps, namely a projection onto convex sets[110] and a steepest descent[111]. Practically, the algorithm is made of a primary iterative loop of ART, which includes a secondary iterative loop, aiming at minimizing the Total Variation norm (TV) of the estimated image. ASD-POCS therefore belong to the class of $\mathbf{L}_1$ norm algorithms. Minimizing the $\mathbf{L}_1$ norm of the Gradient Magnitude image or a given estimate is equivalent to restorating a *degraded* image assuming this Gradient Magnitude Image is sparse. In other words, it is equivalent to restrain the domain of possible solutions to these solutions which Gradient Magnitude Image is sparser than the estimate. Incorporation of this minimization depends on the algorithm design. In the case of ART, it is easy to incorporate it at each iteration, once the image has been estimated from the available projections. ASD-POCS uses a Gradient Descent to realize the minimization of the *convex problem*:

$$f^* = \text{argmin}\|f\|_{TV} \text{ subject to } |Pf - \tilde{g}| \leq \kappa, f \geq 0 \tag{3.32}$$

---

[108] The Sampling theorem was formally formulated by Claude Shannon (1916–2001) in 1948 [Luke, 1999], although it was commonly known and had been used precedently by other researchers since the advent of communication technology in the early twentieth century.

[109] The foundation of the Compressed Sensing theory are set up in [Candès et al., 2006b], [Candès et al., 2006a] and [Donoho, 2006].

[110] In ASD-POCS, the *projection onto convex sets* includes the update of the estimate by ART and the application of a positivity constraint.

[111] *Steepest descent* – also called Gradient Descent – is an optimization algorithm and consists in pulling the estimate towards the minimum of a function, in the opposite direction of its gradient.

where κ is a small positive real parameter. This first-order optimization algorithm pulls the solution towards a local minimum as

$$f^{l+1} = f^l - \alpha \frac{\partial \|f^l\|_{TV}}{\partial f^l} \tag{3.33}$$

with a step size regulated by α. Therefore it consists in calculating the vector in the n-dimensional image space which points from the current estimate towards the local minimum. An iterative shift of the solution following these iteratively calculated directions pulls the solution towards the images which optimize the compromise between data-consistency and the sparseness of the Gradient Magnitude Image. Under certain conditions, this minimization alternating with an iterative algebraic reconstruction algorithm can lead to a correct estimate of the object.

The derivation of this optimization statement proposed by Sidky *et al.* is made of a main iterative loop, in which each of the K iterations can be summed up as follows:

$$f^{n+1} = f^n + r \frac{P^b(\tilde{g} - Pf^n)}{\|P\|} \tag{3.34}$$

$$f^{l+1,n+1} = f^{l,n+1} - w * |\bar{f}^{l,n+1} - f^{l,n+1}| \times \frac{\partial \|f\|_{TV}}{\partial f^{l,n+1}} \tag{3.35}$$

for $0 \leq l < L$ and $0 \leq n < N$, with:

$$\bar{f}_{i,j,k} = \begin{cases} f_{i,j,k} & \text{if } f_{i,j,k} \geq 0 \\ 0 & \text{otherwise.} \end{cases} \tag{3.36}$$

The derivative of $\|f\|_{TV}$ with respect to f can be caclulated as:

$$\begin{aligned} \left[\frac{\partial \|f\|_{TV}}{\partial f}\right]_{i,j,k} &= \frac{f_{i-1,j,k} - f_{i,j,k}}{\sqrt{(f_{i,j,k} - f_{i-1,j,k})^2 + (f_{i-1,j+1,k} - f_{i-1,j,k})^2 + (f_{i-1,j,k} - f_{i-1,j,k})^2 + \epsilon}} \\ &+ \frac{f_{i,j-1,k} - f_{i,j,k}}{\sqrt{(f_{i+1,j-1,k} - f_{i,j-1,k})^2 + (f_{i,j,k} - f_{i,j-1,k})^2 + (f_{i,j-1,k+1} - f_{i,j-1,k})^2 + \epsilon}} \\ &+ \frac{f_{i-1,j,k-1} - f_{i,j,k}}{\sqrt{(f_{i+1,j,k-1} - f_{i,j,k-1})^2 + (f_{i,j+1,k-1} - f_{i,j,k-1})^2 + (f_{i,j,k} - f_{i,j,k-1})^2 + \epsilon}} \\ &+ \frac{f_{i+1,j,k} + f_{i,j+1,k} + f_{i,j,k+1} - 3f_{i,j,k}}{\sqrt{(f_{i+1,j,k} - f_{i,j,k})^2 + (f_{i,j+1,k} - f_{i,j,k})^2 + (f_{i,j,k+1} - f_{i,j,k})^2 + \epsilon}} \end{aligned} \tag{3.37}$$

3.5.4 Implementation of the ASD-POCS algorithm

Current trends in biomedical image reconstruction and processing make use of General Purpose Graphical Processing Units (GPU) to fasten reconstructions [Eklund et al., 2013]. Indeed, parallelized implementation make possible to reduce drastically the processing time compared to a single Central Processing Unit (CPU). The use of a GPU makes possible to perform reconstruction and processing tasks in the same time as a cluster of multi-CPU computing units, and thus drastically reduces the cost of the reconstruction and processing facility. Such applications have been developed in the recent years, as for example in our group for statistical image reconstruction in transmission tomography [Vintache et al., 2010]. In this work, the ASD-POCS algorithm has been implemented in C++ as a monothreaded version on CPU.

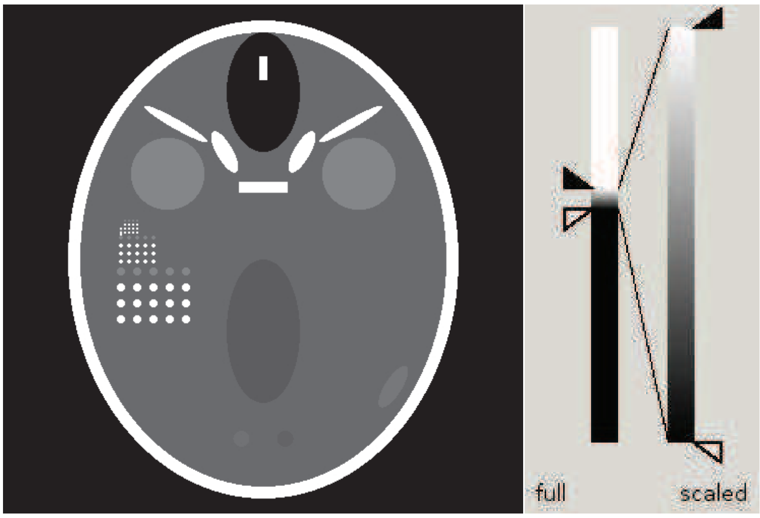

Figure 3.11: Representation of the custom FORBILD phantom. The greyscale is $[0.1025; 0.1152]$ mm^{-1}, for a total range $[0; 0.18]$ mm^{-1}.

A parallelized version was implemented by the author with CUDA[112] on GPU. Indeed, several of the operations could be parallelized, namely:

- the projection operator, where each pixel can be processed by a different thread;
- the backprojection operator, where each voxel can be processed by a different thread;
- operations such as the positivity constraint, the computation of the Total Variation gradient or the gradient descent, for the same reason.

On the contrary, operations such as the calculation of the sum of all voxels can not be performed in parallel. In practice, the main practical difference in the use of either one or the other implementation is the reconstruction time. Also, memory transfers between the host (CPU) and the device (GPU) must be considered. The workflow and dataflow of each implementation are represented in Appendix A. The implementation makes use of a ray-driven projection operator and a voxel-driven backprojection operator described in [Vintache et al., 2010]. Since ASD-POCS has not been previously applied to limited angle micro-CT, an evaluation of the algorithm performance in this case was realized with various datasets, based on measures of the reconstruction accuracy.

3.6 Evaluation of the implemented algorithm for limited angle tomography in the central slice

3.6.1 Data description

This study uses three datasets - namely i) projections simulated analytically from a discrete model using the same projection operator as the reconstruction algorithm, ii) projections simulated analytically from an analytical model, as well as iii) preclinical data acquired with a micro-CT system developed at IPHC.

---

[112] Compute Unified Device Architecture (CUDA) is a parallel computing platform developed by Nvidia Corporation. The first version was released in 2007. Alternatives to CUDA include Open Computed Language (Open CL) framework, first released in 2009.

The phantom used in this study is a customized FORBILD head phantom [Lauritsch and Bruder,] represented in Figure 3.11 and fully described in Appendix C. It is made of several mathematical primitives including cylinders, elliptical cylinders, spheres and ellipsoids. Each object is attributed a value of attenuation coefficient. The phantom includes inserts to evaluate the resolution and contrast. This evaluation, however, is not in the scope of this thesis. The discrete phantom is a discretized version of the analytical phantom. The discretization was achieved by testing if each pixel is enclosed in the mathematical primitives, with a binary assignment – that is to say, no interpolation.

To acquire the preclinical data, a wild type mouse was anesthetized with 2 percent of isoflurane and positioned on the animal support in the center of the field of view. The X-ray tube was operated at 40 kV and 200 μA with a 470 ms exposure time per projection. The raw data set were made, in the three cases, of 768 projections of 2048×2350 pixels with 0.05 mm pitch encoded on 12 bits, covering the whole 360° angular range. The acquisition was realized in continuous mode and without respiratory nor cardiac gating. The projection data was rebinned into 512×578 square pixels projections with 0.2 mm edge size, after pre-processing. For the study in two dimensions, we extracted in each case the pixels corresponding to the object central slice, and cast these pixels into a 512 pixel projection with 0.2 mm square pixel size.

Projections over various angular ranges were used to reconstruct images and evaluate the performances of the algorithm. The angular range between two consecutive projections was kept equal to $0.47°$ in all the configurations – which corresponds to 768 projections over $360°$. The sizes of the reconstructed two-dimensional image are 128×128 and 120×90 cubic voxels with 0.4 mm edge size for the phantom and in the preclinical case, respectively.

3.6.2 Evaluation of the reconstructed images

Image quality was evaluated quantitatively, using a measure of the distance from a *reference image* as well as the Total Variation of the estimated image. The distance measure, or relative reconstruction error, is defined as:

$$\mathrm{M}_{\mathrm{re}}(f, f_{\mathrm{ref}}) = \frac{||f - f_{\mathrm{ref}}||}{||f_{\mathrm{ref}}||} \tag{3.38}$$

with f the estimate and f_{ref} the reference image. The image obtained by FDK reconstruction using the same data is used to compute the M_{re} for the analytical phantom data and preclinical data as the reference image. The phantom itself is used to compute the M_{re} in the case of the discrete phantom data.

As explained in Section 3.5.3, the algorithm includes several parameters which tuning can affect features of the reconstructed image. One of the aims of this preliminary study is to deal with these parameters, study their respective influence on image quality, and, if possible, find the set of parameter which yields the *closest* – or optimal – estimate - in the sense of a minimal M_{re}. To this end, a domain of the three-dimensional parameter space was discretized and reconstructions were carried out over the chosen domain, to determine the solution which minimizes the M_{re}. Each parameter set was used to estimate an image with 1000 iterations of ASD-POCS, for each angular range. The M_{re} was used to quantify the relative error between the image to the reference image. Qualitative evaluation was then performed using the closest estimate of the object under study. The closest estimate is defined as the image which minimizes the value of M_{re}, over the sampled parameter space - assuming that M_{re} is convex in the considered domain.

The total variation of the reconstructed images was also calculated with Equation 3.28 and the ratio of the TV of the estimated image over the TV of the FDK reconstruction, denoted N_{TV}, has been calculated for comparison:

$$\mathrm{N_{TV}}(f, f_{\mathrm{ref}}) = \frac{||f||_{\mathrm{TV}}}{||f_{\mathrm{ref}}||_{\mathrm{TV}}} \tag{3.39}$$

The $\mathrm{M_{re}}$ measure was assumed to be convex over the parameter space – and thus to reach a global minimum. An optimal parameter set yielding this minimal value of $\mathrm{M_{re}}$ was determined by scanning the discretized interval of possible values of $\{r, K, w\}$. In this study, a coarse discretization was used, with steps of 0.2 for r between 0.2 and 1.0, steps of 0.1 for w between 0.1 and 0.5, and steps of 10 iterations for K between 10 and 30.

3.6.3 Results

Figure 3.12 displays the value of $\mathrm{M_{re}}$ for the closest estimate, for the various datasets, with respect to the angular range. It can be observed that the $\mathrm{M_{re}}$ increases as the angular range is reduced – in other words, the estimate gets farther from the ground truth. Tables 3.6, Table 3.7 and Table 3.8 summarize, respectively, the quantitative results obtained with the discrete, analytical and preclinical data.

Figure 3.13 shows the trajectory of the estimated image for the various datasets and the various angular ranges. The point of coordinates $(0, 1)$ in this plane will be reffered to as the *target point* and corresponds to the exact recovery of the reference image. The trajectory of the estimate from the discrete phantom data with 360° is not visible in the plot because it is hidden by the 180 and 150° trajectories.

As for the representation of the reconstructed images corresponding to the minimal $\mathrm{M_{re}}$, they are displayed in Figure 3.14 along with the corresponding parameters.

α (°)	$360/\alpha$	N	coverage (%)	r	l	w	$\mathrm{M_{re}}$	TV	N_{TV}
360	1	768	100.0	1	10	0.1	0.0	129.58	1.0
180	2	384	50.0	1	10	0.1	0.0	129.58	1.0
150	2.4	320	41.7	1	30	0.1	0.0	129.57	1.0
120	3	256	33.3	1	20	0.1	0.01	129.23	1.0
90	4	192	25.0	1	20	0.2	0.07	129.93	1.0

Table 3.6: Quantitative results obtained using the preclinical phantom: angular range, number of projections and coverage of the complete angular range, as well as the optimal parameter set, the $\mathrm{M_{re}}$ value, the TV and the N_{TV} values in the various configurations.

α (°)	$360/\alpha$	N	coverage (%)	r	l	w	$\mathrm{M_{re}}$	TV	N_{TV}
360	1	768	100.0	0.2	20	0.1	0.08	130.17	1.04
180	2	384	50.0	0.2	20	0.1	0.08	128.11	1.03
150	2.4	320	41.7	0.2	10	0.1	0.09	131.2	1.05
120	3	256	33.3	0.2	10	0.1	0.14	125.93	1.01
90	4	192	25.0	0.2	20	0.1	0.18	106.82	0.86

Table 3.7: Quantitative results obtained using the analytical phantom: angular range, number of projections and coverage of the complete angular range, as well as the optimal parameter set, the $\mathrm{M_{re}}$ value, the TV and the N_{TV} values in the various configurations.

The trajectory of the estimate depends obviously i) on the angular range and ii) on the data. The trajectories are somehow similar in the case of the reconstructions from simulated data. On the contrary,

α (°)	$360/\alpha$	N	coverage (%)	r	l	w	M_{re}	TV	N_{TV}
360	1	768	100.0	0.2	30	0.5	0.17	45.08	0.77
180	2	384	50.0	0.2	30	0.4	0.17	42.26	0.72
150	2.4	320	41.7	0.2	30	0.2	0.24	40.34	0.69
120	3	256	33.3	0.2	20	0.4	0.31	32.60	0.56
90	4	192	25.0	0.2	20	0.4	0.35	26.49	0.45

Table 3.8: Quantitative results obtained using the preclinical data: angular range, number of projections and coverage of the complete angular range, as well as the optimal parameter set, the M_{re} value, the TV and the N_{TV} values in the various configurations.

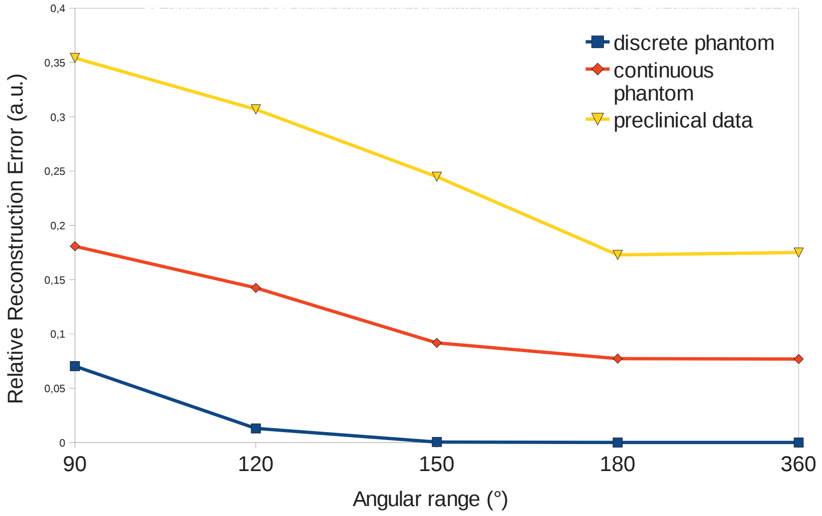

Figure 3.12: M_{re} of the closest estimate for 1000 iterations of ASD-POCS with the various data sets, as a function of the angular range.

inflexions of the curves are different, between these cases and the preclinical data. In the case of the projections generated from the discrete phantom, the trajectory reaches the target point in less than 1000 iterations for the 360, 180 and 150° angular ranges. Regarding the analytical phantom data, the optimal reconstruction error is just less than 8% even with data collected over 360°. It is about 17% with the preclinical data.

It is possible to determine the starting point of the degradation of the estimate with respect to the angular range, considering the visual representations of the reconstructed images and the quantitative evaluation. Artifacts are noticeable in the visual display, from the 150° angular range acquisition. Regarding the value of the M_{re} measure, compared to the value obtained with the 360° acquisition – refered to as the *original value* – it can be observed that:

- In the case of the discrete phantom, it deviates slightly from its original value, from the 120° setup. As for the observation of the images, no artifacts are noticeable, up to 90°.
- In the case of the analytical phantom and preclinical setup, it deviates slightly from its original

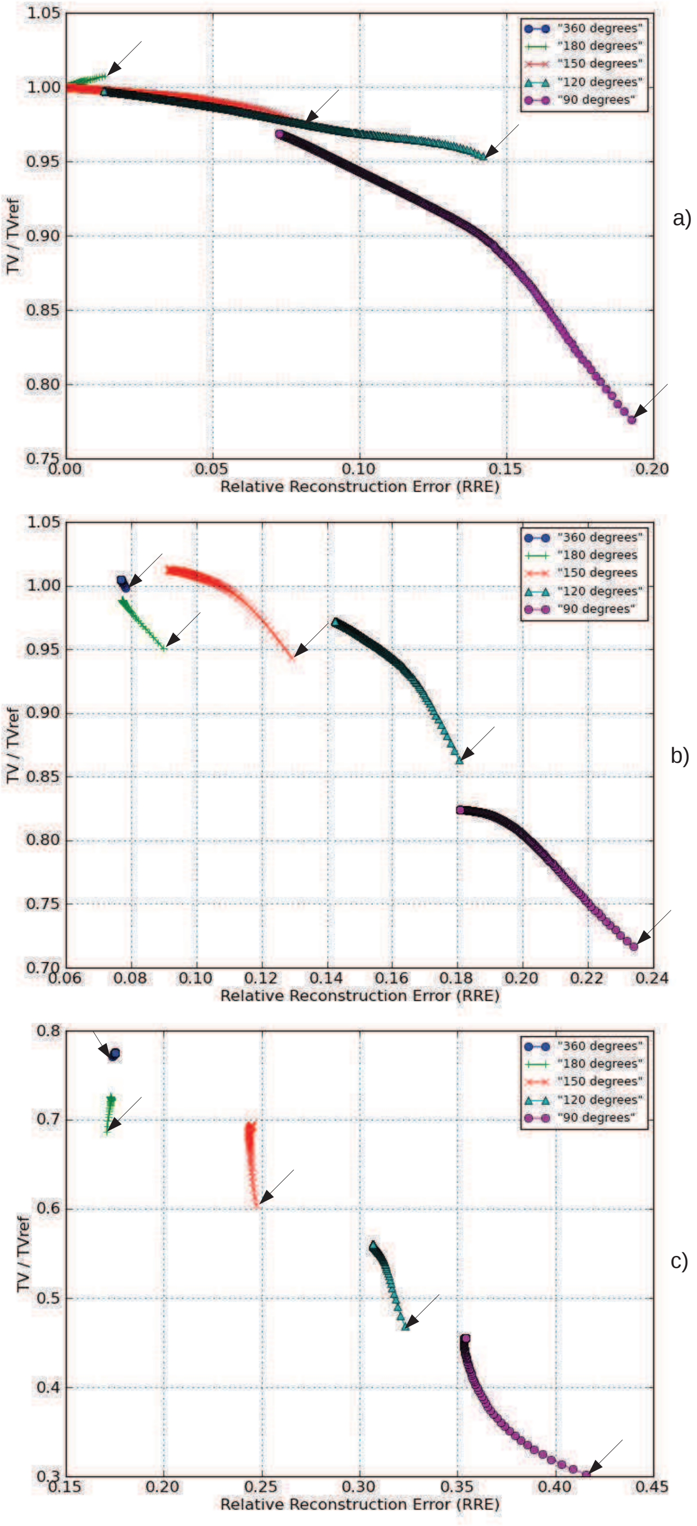

Figure 3.13: Trajectories of the algorithm for the various data sets: a) with the discrete phantom, b) with the analytical phantom, c) with the preclinical data. The black arrows indicate the starting point of each trajectory.
NB: on this figure, the Relative Reconstruction Error (RRE) refers to the M_{re}.

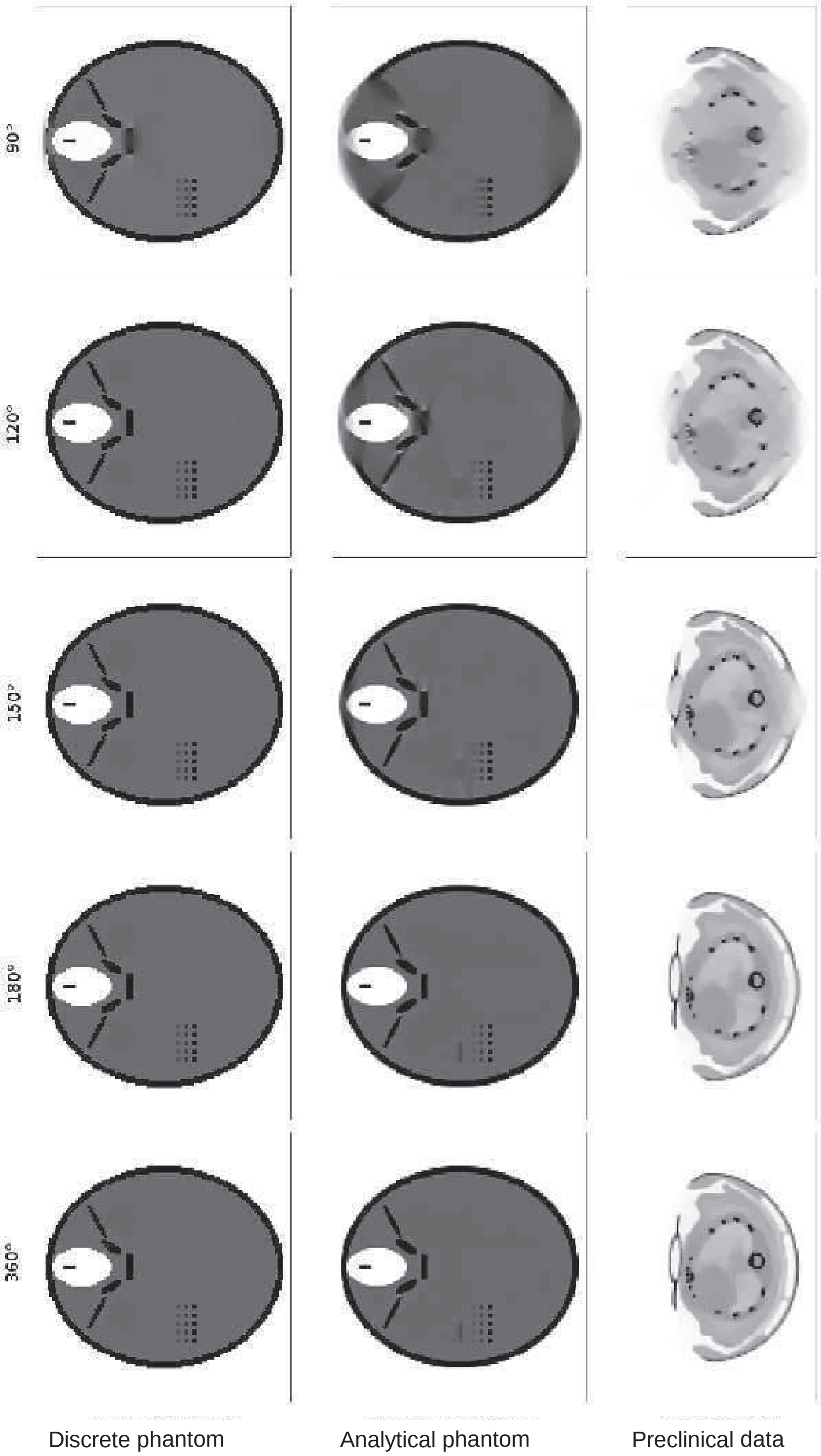

Figure 3.14: Representation of the images reconstructed from the discrete phantom, analytical phantom and preclinical datasets, for various angular ranges, and corresponding to the minimal distance to their respective reference image.

value, from the 150° setup. Visual artifacts appear from the 150° angular range reconstructions. In this case, there are noticeable differences in the reconstructed image, where directional artifacts are visible. Regions of the image are consequently under or over estimated.

3.7 Extension to three dimensions

The extension of the implementation to three dimensions was straightforward. The study in the central slice presented in Section 3.6 can be considered as an optimal case because in the full scan configuration, the setup satisfies the data sufficiency conditions explained in Section 3.4.3. Therefore, realizing exactly the same study in three dimensions was considered superfluous and was avoided. Instead, a study of the performance in three dimensions was carried out directly using preclinical data to address practical problematics with respect to the aim of this work, namely the contrast between tissues. The space available in PhotonIMAGER$^{\mathrm{TM}}$ Optima lead to the design of a X-ray tomographic system of 90° angular range. Therefore, the remainder of this work focuses on a system characterized by this angular range.

3.7.1 Description of the data

The protocol to acquire the preclinical data was the same as described in Section 3.6.1. Images were reconstructed using the FDK algorithm with the whole dataset with a voxel edge size of 0.1 mm. Images were reconstructed using the data acquired over 90° by 100 iterations of the ASD-POCS algorithm, with a voxel edge size of 0.2 mm and a set of parameters chosen by exploring the parameter space and iteratively refining the interval of possible values until an optimum was found. As explained in Section 3.6.2, the value of the M_{re} over the parameter space was assumed to be convex on the considered interval and thus to have a global minimum on this interval. Subsequently, the parameter set minimizing the M_{re} was kept as the optimal parameter set. Two iterations of refinement were done using an arbitrary image acquired with the same conditions and compared to its FDK reconstruction. The optimal parameter set was found to be $\{r = 0.6; L = 30; w = 0.003\}$

3.7.2 Attenuation coefficient estimation and contrast

A quantitative study of the attenuation coefficient in regions of interest was realized. The aim was to determine the mean value of the attenuation coefficient and its standard deviation in various tissues, and to compare these values between the FDK reconstruction and the ASD-POCS reconstruction. The comparision of these values informs about the accuracy of the reconstruction of each region. Regions of interest were defined i) for the high contrast tissues, as the results of the segmentation by the automatic segmentation workflow described in Chapter 4 and applied to the micro-CT images, and ii) for the low contrast tissues, from the manual segmentations realized following the same protocol as described in Chapter 5 from contrast enhanced micro-CT images. To make it clearer, the region of each tissue was constituted by all the voxels identified as this tissue in the FDK reconstruction from a full set of projections acquired on the 360° angular range.

The mean attenuation coefficient of a tissue A was defined as:

$$\bar{\mu_A} = \frac{\sum \mu_{Ai}/\sigma_{Ai}^2}{\sum 1/\sigma_{Ai}^2} \tag{3.40}$$

and its standard deviation is:

$$\sigma_{\bar{A}} = \frac{1}{\sum 1/\sigma_{Ai}^2}. \tag{3.41}$$

The contrast between two tissues A and B was defined as:

$$C_{AB} = \frac{|\bar{\mu_A} - \bar{\mu_B}|}{\bar{\mu_A} + \bar{\mu_B}}. \tag{3.42}$$

3.7.3 Reconstruction time

Reconstruction time was evaluated for various configurations of the acquired data and the reconstructed image. More precisely, it was evaluated for various combinations of the number of pixels and the number of voxels for a fixed image size. This time study was realized on one CPU thread, on Intel Core i7 980 – 3.33GHz, and one GPU Nvidia GTX 580. The comparison of the reconstruction times is reported in Figure 3.15. Practically, the 100 iterations mentioned in Section 3.7.1 were realized in less than 10 minutes, to be compared to 6 minutes with FDK for an image of the same size but with voxels of 0.1 mm edge size..

3.7.4 Results

Figure 3.17 represents cross sections of the three-dimensional reconstruction. Blurring artifacts caused by the limited angle acquisition can be observed, in the directions to which no beam is tangent during the acquisition. A characteristic cone beam artifact can be observed at the ends of the image along the transverse axis, due to the fact that the object under study is longer than the field of view. It can also be observed that the image reconstructed with ASD-POCS exhibits considerably less noise than this reconstructed with FDK.

lungs	liver	heart	spleen	l. kid.	r. kid.	
57⋆	36⋆	36⋆	35⋆	39⋆	38⋆	skeleton
	26⋆	26⋆	27⋆	23⋆	24⋆	lungs
		1	2	3	2	liver
			1	4	3	heart
				5	4	spleen
					1	l. kid.

Table 3.9: Contrast between tissues in the FDK reconstructions. The ⋆ denotes contrasts greater or equal to 20%.

lungs	liver	heart	spleen	l. kid.	r. kid.	
43⋆	16⋆	16⋆	15⋆	16⋆	17⋆	skeleton
	28⋆	28⋆	30⋆	28⋆	27⋆	lungs
		0	2	0	1	liver
			2	0	1	heart
				2	3	spleen
					1	l. kid.

Table 3.10: Contrast between tissues in the ASD-POCS reconstructions. The ⋆ denotes contrasts greater or equal to 15%.

Figure 3.15 displays the reconstruction time for various configurations of the imaging system, with the CPU and GPU implementation. Figure 3.16 displays the mean value of the attenuation coefficient

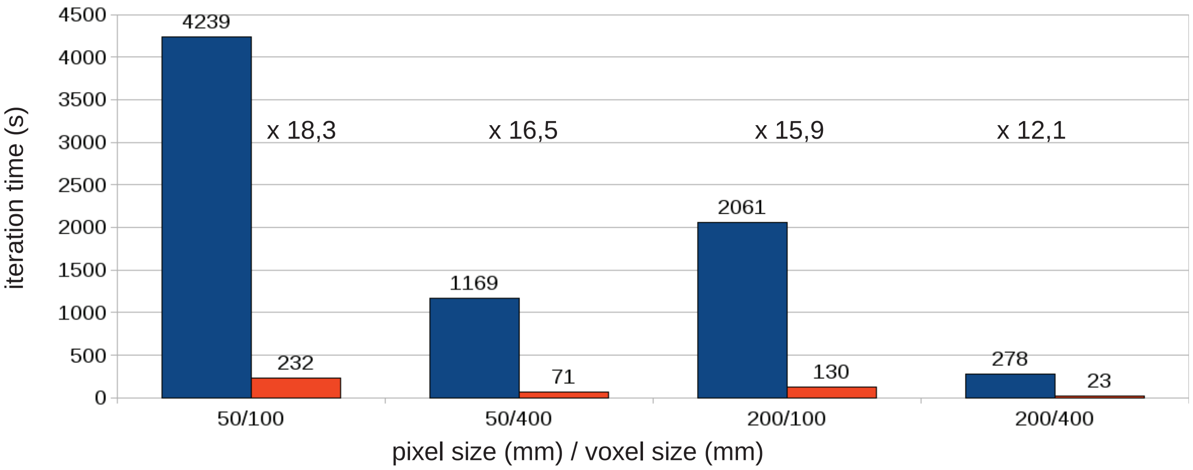

Figure 3.15: Time spent for one iteration in the CPU implementation (blue) and GPU implementation (red). Reconstructions were performed using 192 projections and 20 iterations of the steepest descent. Above each bar, the $\times\beta$ means that the CPU implementation is β times longer than the GPU implementation.

determined in each region of interest defined in Section 3.7.2. Table 3.9 and Table 3.10 display, respectively, the contrasts calculated between the different regions of interest, in the micro-CT and limited angle micro-CT reconstructions.

3.8 Discussion

3.8.1 Results from the central slice study

Observation of the results makes it clear that the performance of the algorithm depends on the data, and on the angular range. The outstanding results obtained in the case of the data simulated from the discrete phantom can be explained by the occurence of an *inverse crime*; These results are coherent with the results presented in [Sidky et al., 2009a] for limited angle tomography. Such exact reconstruction is, however, not likely to be achieved with more realistic data – e.g. simulated from an analytical phantom – or preclinical data. In 2008, G.T. Hermann and Davidi sound the alarm of using TV-minimization based algorithms [Herman and Davidi, 2008]. The authors explain, aside their numerical demonstration, that such algorithms may yield *good results, if images to be reconstructed at the data collection process meet usually unrealistic mathematical criteria.* It is noted that the fact of extending the voxelized phantom recovery to the case of an analytical phantom would constitute an inverse crime, defined as *the procedure of first simplifing the model, developing an estimator based on this model and then testing it against data produced with the same simplified model.* Similar warnings have been made in the context of optical tomography, such as in [Lu et al., 2009] where the authors highlight the fact that "much attention should always be given to the *inverse crime* when new algorithms are verified using synthetic data" and that "the same discretized modes used in the forward simulation and inverse reconstruction will significantly affect the evaluation".

The differences between the algorithm trajectories can therefore be explained by i) an occurence of inverse crime with the data simulated from the discrete phantom. and ii) the presence of noise and various degrading factors in the case of the preclinical data. The case of the discrete phantom is not considered further in the remainder of this discussion. Although the estimates appear to have

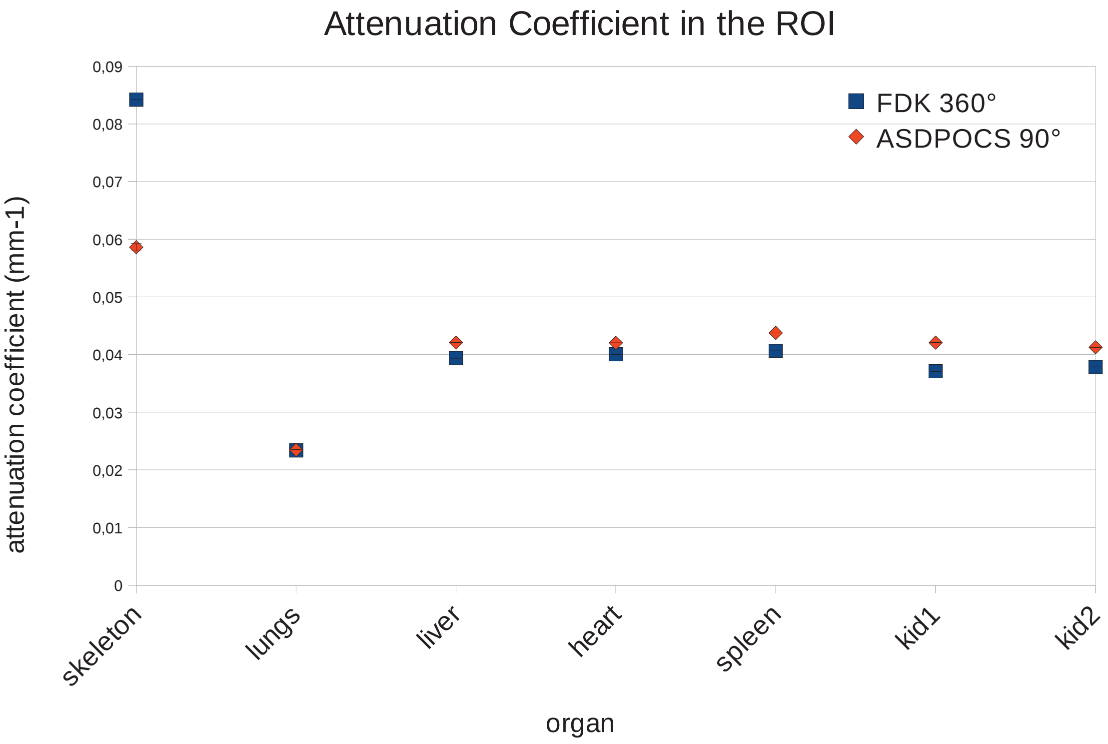

Figure 3.16: Mean value of the attenuation coefficient in the regions of interest.

reached stationary points, as can be observed in the trajectories drawn in Figure 3.13 – more iterations would possibly reduce the directional artifacts. Although no convergence has been proofed for ASD-POCS [Defrise et al., 2011], a study of the convergence would allow to characterize the convergence in the studied case. Regarding the reconstructions of the analytical phantom and the preclinical image, the progress of the estimate along the trajectory is rather slow compared to the previous case. In addition, it becomes stationary beyond a certain number of iterations. In other words, it reaches a region of images in the image space i) which projections are too close to the measured or simulated data to pull the estimate towards a *better* estimate - in terms of M_{re} and ii) in which the total variation cannot be further reduced while respecting the data consistency. In other words, the estimate reaches an equilibrium between the action of the total variation minimization and the data consistency: the estimate gets "trapped in a local minimum" of the total variation functional. Alternative formulations of the descent algorithm, such as Conjugate Gradient Descent, deals with this problem – at the expense of a greater computational cost. An optimization of ASD-POCS using Conjugate Gradient Descent has been proposed by Lu *et al.* in [Lu et al., 2011]. From the point of view of the reconstruction accuracy from the limited angular range acquisitions, investigation in this direction sounds promising.

The *closest estimate* to the reference image in each configuration is shown in Figure 3.14. Regarding the choice of the measures, it is to be kept in mind that the M_{re} indicates the *global* distance of the image to the reference and does not account for the local accuracy of the algorithm. In the case of the preclinical data, noise is present in the image reconstructed with FDK. On the contrary, images reconstructed using ASD-POCS are smooth, because the minimization of the TV pulls the estimate to an image made of distinct homogeneous regions [Pan et al., 2009, Sidky et al., 2009a]. For this reason, the M_{re} is not always zero even with a $360°$ angular range, when the reference image is the FDK reconstruction. With respect to the ratio of the total variations, it is to be kept in mind that the noise of the FDK reconstruction has the effect of increasing the total variation of these images.

Some elements can be distinguished with high contrast in the reconstructed images. In the case of the preclinical data, the bones of the mouse remain mostly visible, though corrupted by artifacts. It is obvious, from the observation of the images reconstructed of the analytical phantom, that the recovery of these elements depends mostly of their i) size, ii) location in the field of view and iii) contrast with respect to neighbor structures. There are two reasons to this effect, namely i) the directional blur caused by the *missing* measurements and ii) the smoothing caused by the minimization of the Total Variation norm. The first effect is determined by the chosen angular range and the position of the object in the field of view. The second effect depends on the algorithm parameters chosen to achieve the reconstruction. A study of the resolution and contrast throughout the field of view would be an interesting development. It is, however, out of the scope of this thesis.

3.8.2 Results from the extension to three-dimensions

From these results, it can be observed that the coronal cross section through the ASD-POCS reconstruction presents interesting characteristics compared to its counterpart in the FDK reconstruction. Some out-of-plane structures corrupt it, but at least in-plane structures appear relatively well reconstructed in the plane shown, and even small elements such as the ribs are visible as well as in the FDK reconstruction. As for the transverse and sagittal plane, the artifacts are more problematic since the directional blur considerably affects the morphology of the animal. For example, the animal holder and the animal back cannot be visually distinguished. As for the skeleton, regions appear well reconstructed though distorted – e.g. the lumbar vertebrae in the sagittal cross section – whereas others appear clearly badly estimated – such as the top of the skull in the sagittal cross section. The fact that the ASD-POCS images are considerably smoother than the FDK reconstructions can be recognized as one of the features of TV minimization – it has been used for deblurring [Oliveira et al., 2009].

From Table 3.10, Table 3.9 and Figure 3.16, it can be observed that:

- In the micro-CT images, the constrast between the skeleton and lungs on the one hand, and each other tissues on the other hand, is relatively high – more than 20% contrast between the skeleton or lungs and other tissues, to be compared to less or equal to a 5% contrast between the other tissues.

- The attenuation coefficient estimated in the various regions of interest is considerably lower for the skeleton, equivalent for the lungs and slightly higher for other tissues, in the limited angle micro-CT images compared to the micro-CT images. The relative difference between the values of the attenuation coefficient, represented in Figure 3.16, between the ASD-POCS reconstruction for the $90°$ angular range and the FDK reconstruction from the $360°$ angular range represent -30% for the skeleton, 0.4% for the lungs, and from 5 to 13.4% for the other tissues.

- In terms of contrast, the skeleton and lungs keep a contrast greater than 15% in the ASD-POCS reconstruction while the contrast between the other tissues remains inferior or equal to 3%.

3.8.3 Reconstruction time

Reconstruction time is greatly reduced by the GPU implementation. In all the configurations represented in Figure 3.15, the reconstruction time with the GPU implementation is less than 10% this of the CPU implementation. The plot emphasizes the notorious differences achieved for the various configurations. Even in the GPU implementation, the reconstruction time is ten times less with the configuration 200 mm$/400$ mm than with the configuration 50 mm$/100$ mm.

3.8.4 Room for improvement

Several axes of improvement can be considered. With respect to the information used for the image reconstruction, the use of a hard prior such as the surface of the animal, estimated from another imaging modality, could contribute to constrain the reconstruction algorithm and reduce the extent of the space of possible solutions. The problem is the poor resolution – more than 1 mm – of such estimations due to the irregular animal surface due to its hair and possible occlusions. Also, explicitly removing the animal holder from the image at each iteration would reduce the region of allowed solutions.

As for the algorithmic strategy, gradient descent is known to be likely to fall in local minima. Conjugate gradient descent constitutes an interesting alternative. It was investigated by [Lu et al., 2011]. It is, however, more computationally expensive.

As for the choice of the parameters, it is highly problematic, since the performance of the algorithm depends on the object for a given parameter set. Therefore, no parameter set can handle all cases with success. The most straightforward approach for choosing the parameters is to realize an exhaustive search over the domain of authorized values. Such a "calibration" can be realized e.g. through a study using an object which known attenuation coefficients are comparable to this of the object under study – as it was done in this work. Other approaches such as evolutionary algorithms are successful at optimizing the choice of multiple parameters. The implementation and use of such and algorithm would surely constitute an elegant improvement of the presented approach.

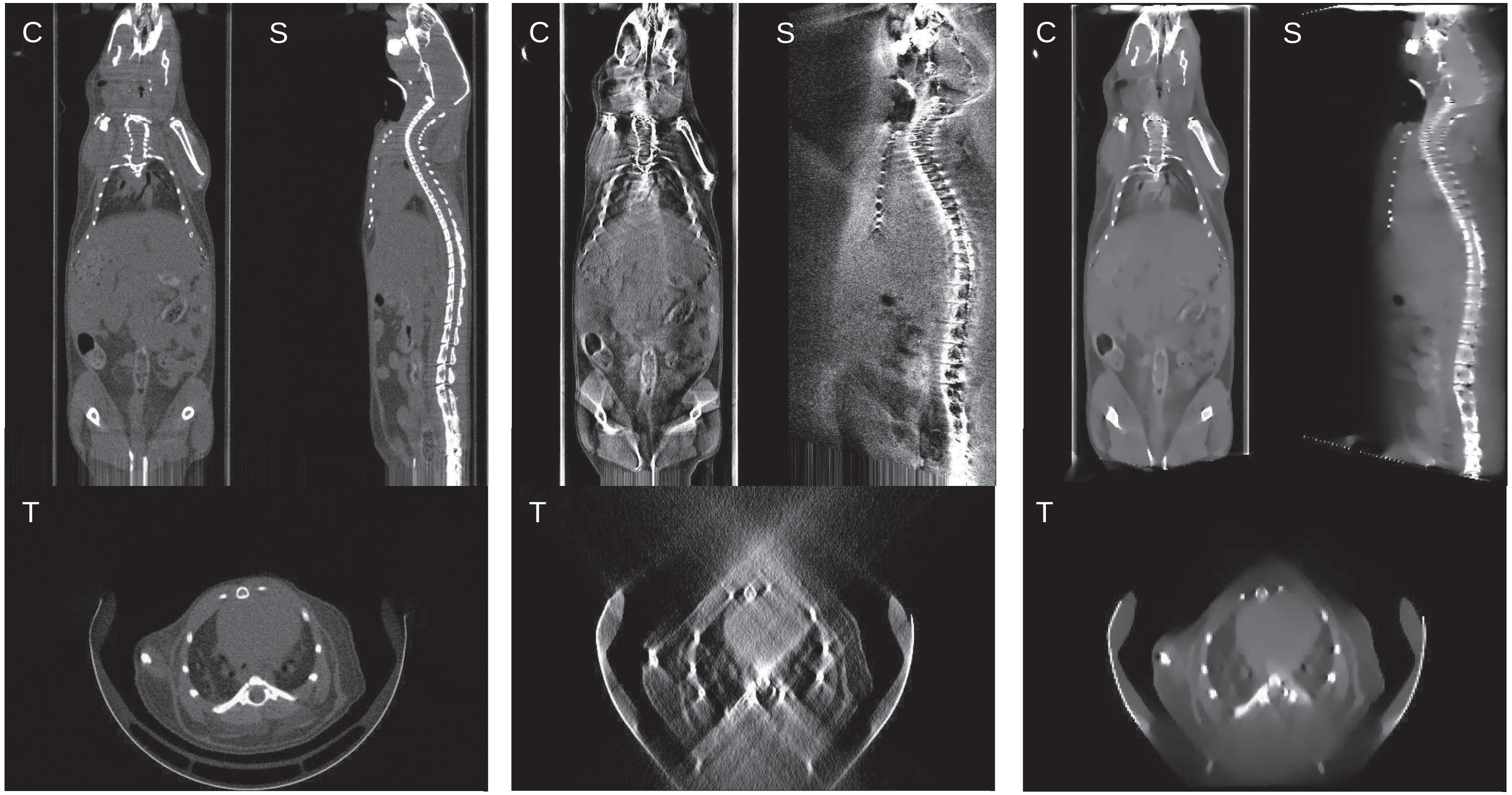

360° – FDK

90° – FDK

90° – ASD-POCS

Figure 3.17: Transverse (T), coronal (C) and sagittal (S) cross sections through images reconstructed, respectively, with FDK from 768 projections acquired over $360°$, with FDK from 192 projections acquired over $90°$ and with ASD-POCS from 192 projections acquired over $90°$. Windows are, respectively: $[0.0; 0.1]\ \mathrm{mm}^{-1}$, $[0.0; 0.02]\ \mathrm{mm}^{-1}$ and $[0.0; 0.1]\ \mathrm{mm}^{-1}$. FDK and ASD-POCS images are made of cubic voxels of edge size respectively $0.1\ \mathrm{mm}$ and $0.2\ \mathrm{mm}$.

3.9 Chapter Summary

The work presented in this chapter leads us to draw the following conclusions:

- In this work, a X-ray tomographic modality imaging modality characterized by a reduced angular range has been studied, to fulfil the constraints following on the configuration of the PhotonIMAGER$^{\text{TM}}$ Optima. The X-ray tomographic modality under study was design based on an existing micro-CT device, therefore comparison with micro-CT was possible.
- The limited angle problem has to be dealt with when the angular range of the CT acquisition is reduced.
- This problem is common to limited angle CT, tomosynthesis and laminography.
- The development of these imaging modalities has lead to the formulation of dedicated image reconstruction algorithms including convolution-backprojection, sinogram recovery, and iterative techniques of the image domain.
- In this work, an algebraic reconstruction technique regularized by minimization of the total variation norm of the image has been implemented and applied to limited angle micro-CT.
- Two implementations were realized, one on CPU and one on GPU.
- The algorithm performances was studied in two dimensions and three dimensions using data from numerical simulation and preclinical acquisitions.
- The study of the contrast between tissues in images reconstructed from preclinical data in the three-dimensional setup indicate a high contrast between the skeleton or lungs and the neighbor tissues, in the micro-CT images as well as in the limited angle micro-CT images.

Chapter 4

Automatic Segmentation of High Contrast Tissues in Tomographic Images

Contents

The process of segmentation aims at identifying regions of interest in an image. In this work, we distinguish fully manual, interactive – or semi-automatic, and fully automatic methods. Interactive and fully automatic segmentation method differ in their degree of automation and can be further distinguished in low-level and high-level methods. Low-level methods differentiate regions of the image considering the values of each voxel and its neighbors, or based on features derived from them, such as the gradient. High-level methods use a prior information to label a region. In the context of medical image interpretation, high-level segmentation attributes a meaning to a given region based on an anatomical representation of the observed subject. In other words, it realizes an *anatomical interpretation* of the image. For example, one could focus on the head region to identify the voxels representing the brain, with the prior knowledge that the brain is contained in the skull. To this end, a robust identification of the head region would be needed. This is just an illustrative example and the brain will not be considered in the remainder of this work. In general, the higher the level of the method, the higher the degree of automation.

Fully manual segmentation methods include all the methods which consist in manually attributing a label to a region, voxel by voxel. Fully manual approach is time consuming, tedious, and results are generally not reproducible, even from the same operator. Interactive – or semi-automatic – segmentation methods include all the methods characterized by a certain degree of automation, such as user input, control or corrections. It is notable that micro-CT images are characterized by a relatively high contrast of tissues such as the skeleton, the skin and the lungs over surrounding tissues. Therefore micro-CT constitutes a good candidate for obtaining the prior information for luminescence tomography, mainly because of the high contrast it provides between bone, lungs, and surrouding soft tissues, as well as the skin. The robust segmentation of these tissues is generally possible with *low-level* segmentation techniques [Baiker et al., 2011, Wang et al., 2012c]. As such, this information can already constitute an anatomical prior for luminescence tomography constrained reconstruction – for example, bone accounts for a stronger scattering of optical photons than other tissues over an important part of the visible spectrum, as suggested by the values of the reduced scattering coefficient reported in Figure 2.2 of Chapter 2. One of the drawbacks of Micro-CT is the generally poor contrast between soft tissues because of the trade-off between dose and the integration time - when the contrast is not enhanced using injectable contrast media. Indeed, various *contrast media* can be adminstrated in the mouse organism to enhance specific structures such as the liver, the heart, the lungs or the gastro-intestinal system[113]. Nevertheless, the use of contrast media does not mean the segmentation of the structure can be done fully automatically: the contrast with the surrounding structures is *enhanced*, but the differenciation of the enhanced structures is generally human assisted. Moreover, the use of contrast media increases the complexity of the acquisition protocol, makes it more invasive and can disturb the physiological conditions.

Fully automatic segmentation methods include all the methods for which no user input is needed to perform the segmentation. Some of these methods make it possible to avoid the use of contrast media. Fully automatic methods have been proposed to realize organ-specific segmentation such as for the liver in clinical CT [Heimann et al., 2009, Mharib et al., 2011]. Automatic whole-body segmentation methods for small animal micro-CT images have been more seldom proposed. Interactive methods can be used to supervise segmentation tasks, for example when the image characteristics make fully automatic methods fail and when it is chosen to avoid manual segmentation. These methods can be implemented with various degrees of automation.

In Chapter 3, the implementation of a reconstruction algorithm and its application to various limited angle datasets, including a preclinical dataset acquired with an existing micro-CT system, has been described. The images obtained were compared to images reconstructed with the FDK algorithm – a reference for cone beam CT reconstructions. As explained in the introduction of this thesis and in Chapter 2, segmentation of biomedical images plays a key role in their interpretation, since it makes possible to identify regions of the image and to label them with an anatomical information. Logically the next step is the assessment of the possibility for robust identification of the tissues in the reconstructed images. As mentioned in Chapter 3, some elements characterized by a high contrast in micro-CT images appear to be reconstructed with high contrast in the case of limited angle tomography as well. An automatic segmentation workflow has been developed for the segmentation of the high contrast tissues

---

[113] Typical contrast media, characterized by a strong attenuation because of a high atomic number, include gold for the vasculature, iodine for the vascular system, iodine or alkaline earth-based compounds for the liver, and baryum [Wathen et al., 2013, Fiebig et al., 2012]. This topic is developed in Chapter 5.

in micro-CT image – in the remainder of this thesis, high contrast tissues (HCT) refer to bone, lungs and skin. The underlying idea is to subsequently apply this workflow to limited angle tomographic images.

Various methods have been reported in the litterature for performing the segmentation of High Contrast Tissues. A state of the art of these methods is presented in Table 4.1. Most of these methods are fully automatic and low-level methods. They are, moreover, mostly based on thresholding – either the simplistic binary thresholding or more elaborated techniques, e.g. accounting for the overlap of the histograms of values of various tissues. Departing from a *seed* – that is to say, a point specified by a human to belong to a certain tissue, or automatically found by thresholding – a number of methods use, additionally, a region growing algorithm to identify all the voxels of a region. A few fully automatic methods have been reported in the litterature for performing the automatic segmentation of these three tissues in the same workflow. These works include mainly [Baiker et al., 2010] and [Wang et al., 2012b].

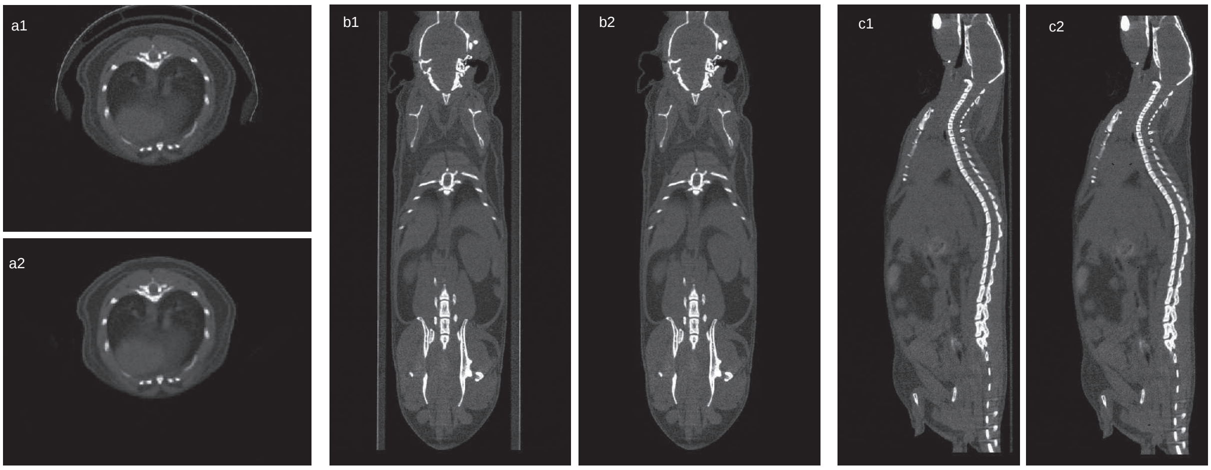

Figure 4.1: The transverse, coronal and sagittal slices are indexed respectively with the letter a, b and c. The image with the mouse support and the image without the mouse support are indexed with number 1 and 2, respectively.

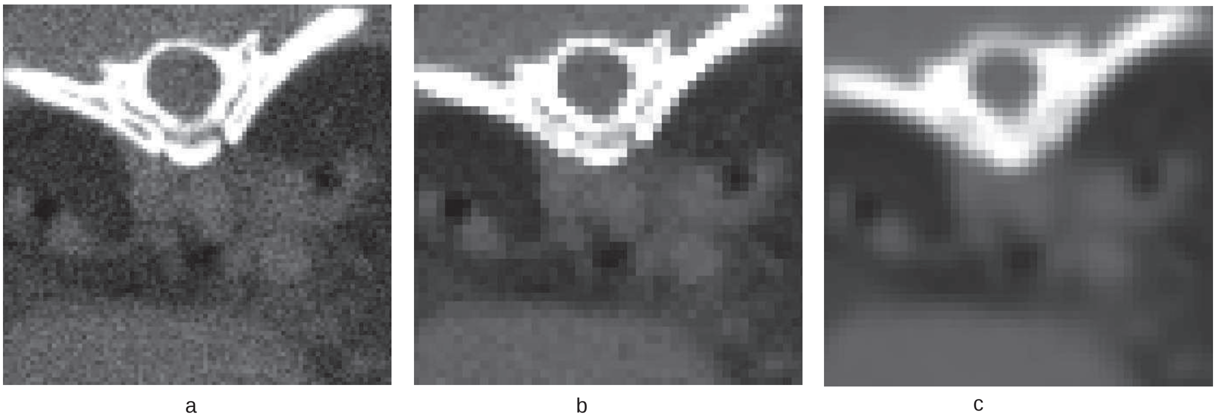

Figure 4.2: Transverse cross-section in the thoracic region. a: the original image. b: $2 \times 2 \times 2$ rearrangement of the voxels. c: the image after Gaussian filtering.

reference	tissue	method	DOA	level	context
[Kang et al., 2003]	skeleton	adaptive RG + boundary adjust.	2	L	C
[Zhou et al., 2004]	skeleton	bin. thres.+RG	2	L	C (torso)
[Zhou et al., 2004]	skin	bin. thres.+distance+connectivity	2	L	C (torso)
[Zhou et al., 2004]	adipose	bin. thres.	2	L	C (torso)
[Li et al., 2008]	skeleton	bin. thres.	2	L	pC (WB)
[Liu et al., 2008]	skeleton	edge-detection	2	L	C
[Artaechevarria et al., 2009]	airway	seed+marching wavefront	2	L	pC (WB)
[Hu et al., 2001]	lungs	bin. thres.+connectivity+morph.	2	L	C
[Baiker et al., 2010]	skeleton*	GF+R&C thres.	2	L	pC (WB)
[Baiker et al., 2010]	skin*	ISODATA thres.	2	L	pC (WB)
[Baiker et al., 2010]	lungs*	"triangle" thres.	2	L	pC (WB)
[Wang et al., 2012b]	skeleton*	ISODATA thres.	2	L	pC (WB)
[Wang et al., 2012b]	skin*	ISODATA thres.	2	L	pC (WB)
[Wang et al., 2012b]	lungs*	ISODATA thres.	2	L	pC (WB)
[Judex et al., 2010]	adipose	GF+bin. thres.	2	L	pC
[Xiao et al., 2010]	skeleton	bin. thres.	2	L	pC
[Marchadier et al., 2011]	VAT/SAT	GMM of the histogram	2	L	pC (WB)
[Shi et al., 2013]	VAT/SAT	bin. thres.+anatomical prior	2	H	pC (WB)
[Wathen et al., 2013]	lungs	bin. thres.	1	L	pC (WB)
[Wathen et al., 2013]	adipose	bin. thres.	2	L	pC (WB)

Table 4.1: Non-exhaustive list of methods for HCT segmentation. The * indicates that the segmentation of the specific tissue has been reported as a part of a multi-tissue automatic segmentation workflow.
- thres. = thresholding
- bin. = binary
- RG = region growing
- C = clinical
- pC = preclinical
- WB = whole body
- morph. = morphological operations
- GF = Gaussian filtering
- VAT = visceral adipose tissue
- SAT = subcutaneous adipose tissue
- GMM = Gaussian mixture model
- MSF = Mean Shift Filtering
- R&C = Ridler and Calvard's
- DOA = degree of automation (0=fully manual, 1=interactive, 2=fully-automatic)

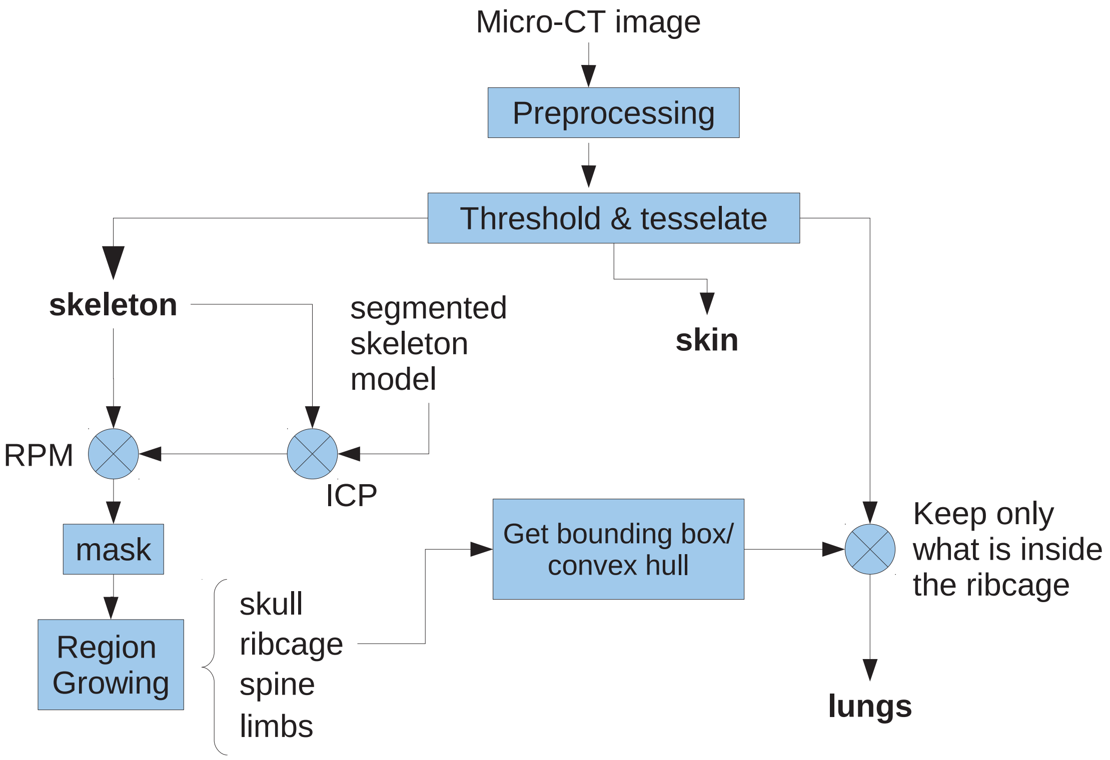

Figure 4.3: Workflow for the segmentation of HCT. RPM refers to nonrigid registration using the "Robust Point Matching" algorithm ([Chui and Rangarajan, 2003], implemented by the author with the C++ linear algebra library Eigen).

In this work, an automatic segmentation workflow was designed to identify robustly the high contrast tissues. It includes three main steps, namely a low level segmentation yielding the skeleton and skin, then the non-rigid registration of a skeleton model and middle-level segmentation of the skeleton into subparts and finally the segmentation of the lungs – more precisely, the lungs and a part of the trachea – using a high level information derived from the skeleton segmentation in subparts. These three steps are preceeded by a preprocessing of the images, aiming at removing ambiguities that would degrade the segmentation.

The workflow has been implemented as a bash script using various C++ compiled executables and python scripts. The mesh processing functions are either existing functions of the trimesh2 [Rusinkiewicz, 2013] and CGAL [CGAL, 2013] libraries. Some custom functions have also been implemented for the purpose of the study. Various functions were parallelized on multi-CPU, using OpenMP [OpenMP Architecture Review Board, 2008 There is an important room for optimization of the various programs, including the optimization of the datastructures, as well as the parallelization of various operations.

4.1 Image preprocessing

Some image preprocessing operations are required to initiate the automatic segmentation. First of all, the voxels corresponding to the animal holder are set to zero in the reconstructed images. The result of this operation is shown in Figure 4.1. To this end, a binary mask has been created – it is assumed to contain all the voxels corresponding to the holder – and substracted from the reconstructed image. Then, the

tissue	**min.** μ (mm^{-1})	**max.** μ (mm^{-1})	**seed** (mm^{-1})	**other criteria**
skeleton	0.05 / 0.06	0.3	0.07	threshold on the number of vertices
skin	0.01	0.3	∅	skin is the biggest connected element
lungs	0.01	0.028 / 0.038	0.025 / 0.02	lungs are enclosed in the ribcage b.b./c.h.

Table 4.2: Summary of the threshold values and other criteria used for the segmentation of the High Contrast Tissues. Two values separated by a "/" mean that the left value has been used for micro-CT images while the right value has been used for limited angle micro-CT images.
- b.b. = bounding box
- c.h. = convex hull

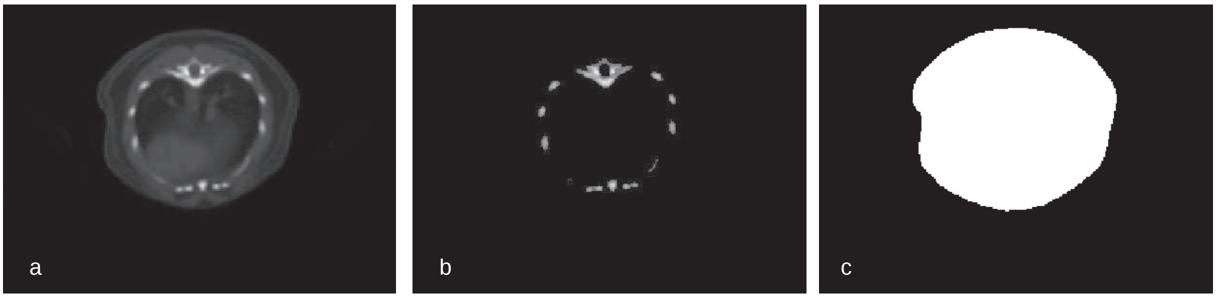

Figure 4.4: Result of the low-level segmentation displayed in one transverse cross section. The indexes a, b and c correspond, respectively, to the preprocessed image, the segmented skeleton region and the segmented skin region.

images were downsampled, using a $2 \times 2 \times 2$ re-arrangement of the reconstructed image, in order to reduce further processing time. The result is a cubic voxel lattice, with cubic voxels of 0.2 mm edge size. Finally, the images were filtered by applying a uniform and isotropic Gaussian filter in the image domain, with a standard deviation of 2 voxels, in a cube of $11 \times 11 \times 11$ voxels around the voxel of interest. The results of the downsampling and filtering operations are shown in Figure 4.2.

4.2 Segmentation of tissues from the micro-CT image

The segmentation of high contrast tissues rely on thresholds defining an interval of values for the attenuation coefficient, and a seed value, chosen through a ROI study. All points of the image which value is equal to the seed value are used as seeds to initiate a region-growing algorithm. In this workflow, the boundaries of the resulting regions are *tesselated*[114]. Various other criteria based on the triangle meshes have been used to robustly identify these regions. Information regarding the thresholds and criteria for the various tissues is summarized in Table 4.2.

4.2.1 Skeleton and skin

The segmentation of the skeleton by the threshodling and region growing approach is likely to yield a mesh composed of disconnected components. Three disconnected component are kept, in the case

---

[114] *Tesselation* of a surface refers to the generation of a piecewise planar approximation of the surface using a mesh – typically made of triangle surface elements, in the case of the triangle mesh.

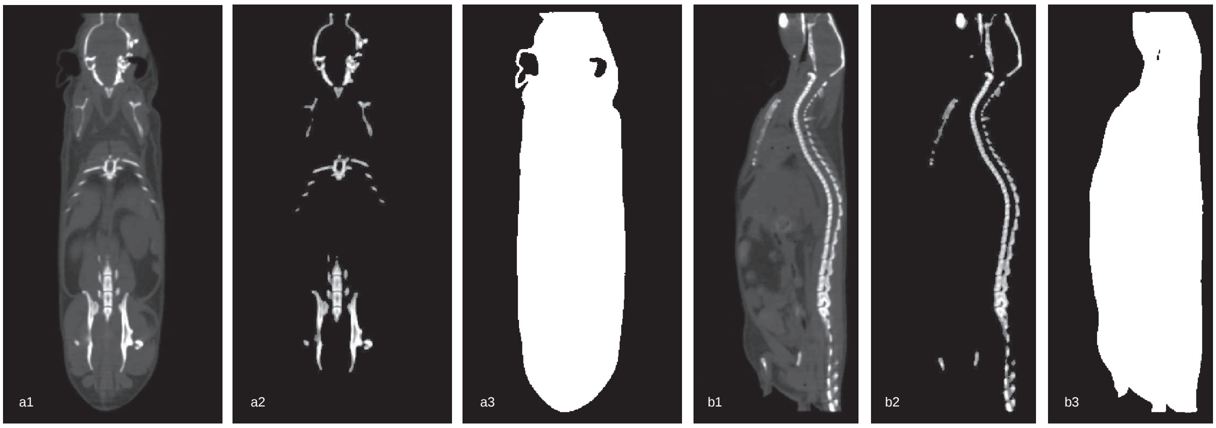

Figure 4.5: Result of the low-level segmentation displayed in coronal (a) and sagittal (b) cross sections. The indexes 1, 2 and 3 correspond, respectively, to the preprocessed image, the segmented skeleton region and the segmented skin region.

where both forelimbs were disconnected from the remainder of the skeleton, at the point where the clavicle is close to the sternum. In some cases, the whole skeleton is fully connected, and in other cases, only one limb is disconnected from it. Then, an appropriate filtering on the number of vertices makes it possible to get rid of the disconnected elements which are probably not part of the skeleton. These small elements can be, for example, high contrast objects present in the food and circulating through the gastro-intestinal track. In the case of micro-CT images, keeping these three components have proved robustness over 12 individual. In the case of limited angle micro-CT images, it is more delicate since several disconnected components can belong to the skeleton. It was decided, however, to apply the same rejection criterion in this case.

Figure 4.6: Representation of one skeletons segmented using the automatic segmentation workflow, from a micro-CT image. A catheter which was inserted in the jugular vein of the animal is visible and is connected to the skeleton near the junction between the claviculae and sternum.

Figure 4.6 and Figure 4.7 represent, respectively, the surface mesh of a skeleton and a skin segmented with the automatic workflow.

Peforming the segmentation of the skin by thresholding and region growing is likely to yield a mesh composed of many disconnected components, for example when air bubbles are present in the stomach. The skin is considered to be the biggest component.

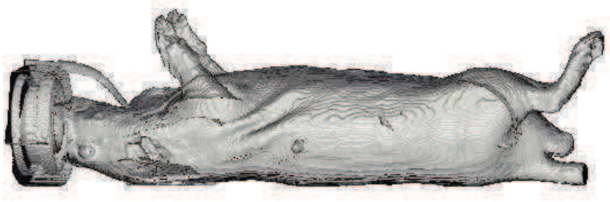

Figure 4.7: Representation of the skin segmented with the automatic segmentation workflow, from one individual. The animal's muzzle is placed in the nose piece of the gaseous anesthesia system. The catheter is visible as in Figure 4.5.

4.2.2 Segmentation of the skeleton in subparts

Some of the various methods that have been reported for automatic segmentation of skeletons are listed in Table 4.3. There is no real tendency since these proposals are seldom. The reported approaches use either graphs or segmented models. Various approaches from the computer vision enable the segmentation of meshes, but they focus on the mesh features, and a robust anatomical meaning of the segments is generally not sought [Kalogerakis et al., 2010]. Combination of these approaches would surely provide interesting possibilities. In this work, the middle-level segmentation of the skeleton uses a segmented model to segment the skeleton in subparts. A methodology to achieve this task has been proposed in [Baiker et al., 2011], and represent the skeleton as an articulated system of rigid segments and joints. The model segments are hierarchically segmented on the target with constraints on the rigid transformations allowed at each joint. A more straightforward approach is to directly register the whole skeleton in a nonrigid fashion and to subsequently apply the transformation to an underlying segmentation of the model. Advantages and drawbacks of such an approach are discussed in the discussion section of this chapter. Our segmented model was built using the skeleton of one of the instances which was tesselated and then manually segmented with basic mesh cutting tools present in the Meshlab package [meshlab, 2005]. In our work, it is segmented into the following subparts: spine, ribs, pelvis and tail, skull, and each of the limbs, as represented in Figure 4.8. Our motivation to build a custom model is that the acquisition settings are identical as these of the targets and the mouse is of the same strain. Therefore, there is no issue of different CT resolution involved in the subsequent registration tasks. Moreover, the model is more likely to resemble the targets than if it was from another strain.

The registration of this model on the image of the skeleton of an arbitrary instance is carried out as follows: first, the simplified model and the instance meshes are downsampled to 3500 faces, to reduce computation time. Second, they are roughly aligned by matching their barycenters. Then, an affine Iterative Closest Point algorithm (ICP, [Besl and McKay, 1992], implemented in the trimesh2 library [Rusinkiewicz, 2013]) – described in Appendix G – is used to align more precisely the model mesh and the instance mesh. Finally, a non-rigid Robust Point Matching (RPM, [Chui and Rangarajan, 2003], implemented by the author with the C++ linear algebra library Eigen) – also described in Appendix G – algorithm is run to match the points of both sets. The TPS deformation field determined by the RPM registration is used to transform the high resolution meshes of the skeleton segments. The resulting meshes are used to create a binary mask gathering each part of the skeleton, which is multiplied by the binary mask of the whole skeleton of the instance. A region growing is then performed to fill the unidentified regions, using as seeds for each regions all the voxels identified as part of it. The regions of each part are grown simultaneously with a constant rate at each iteration and the regions are not allowed to overlap. The growth stops when all the voxels identified as the skeleton have been attributed to a skeleton segment. The result of the region growing step is shown in Figure 4.9. A subsequent segmentation and tesselation makes it possible to get a mesh of each the skeleton segment. Figure 4.10 represents the surface meshes of a skeleton segmented in subparts.

reference	**method**	**DOA**	**elements**	**context**
[Liu et al., 2008]	graph cuts	1 (seed)	various	C
[Baiker et al., 2010]	ARSM	2	spine, skull, ribcage, limbs	pC
[Wang et al., 2012b]	NRR of a model	2	trunk region	C
[Wiens, 2013]	reeb graphs	2	various	pC

Table 4.3: Non-exhaustive list of methods for segmentation of the skeleton in subparts.
- C = clinical
- pC = preclinical
- ARSM = Automatic registration of a skeleton model
- NRR = Non rigid registration - DOA = degree of automation (0=fully manual, 1=interactive, 2=fully-automatic)

4.2.3 Lungs

Regarding the lungs, thresholding generally yields a combination of voxels which belong to the lungs, adipose and air bubbles of the gastro-intestinal track. It is typically difficult to differentiate them from adipose in some regions since their attenuation coefficient are very close, they are locally not always distinguishable – this is partly due to the preprocessing operations such as enlargement of the voxel size and filtering of the voxels. In this work, the criterion used for the lungs is that they are enclosed in the ribcage.

Computational geometry operations make it possible to determine the convex hull of the ribcage. Considering, a set S in a n-dimensional space, any collection of $m > 1$ vectors of n dimensions $\{e_1, ..., e_m\}$ in S and any collection of scalars $\lambda_k / k \in \{1, ..., m\}$ such that $\lambda_k \in \mathbb{R}^+$ and verifying $\sum_{k=0}^{m} \lambda_k = 1$, S is a *convex set* if and only if:

$$\sum_{k=1}^{m} \lambda_k e_k \in S. \tag{4.1}$$

Given a point set X of the Euclidean space, the *convex hull* of X is defined as the smallest that contains X. The convex hull was determined and tesselated, and then the mesh was filtered with 5 iterations of Laplacian smoothing which had the effect of shrinking the hull while preserving its outline. This hull is taken as the domain where the lungs must be found, and the voxels obtained from the region growing segmentation and contained in this domain are kept as representing the lungs. Figure 4.11 shows the ribcage and lungs of an individual, as well as the bounding box of the ribcage and the surface mesh enclosing its convex set. Therefore, an intermediate step of indentification of the ribcage is obviously needed.

A different high level criterion has been previously used to process some of the images presented in this work, namely the segmentation of images from FDK reconstructions. This criterion was that the lungs are the biggest connected component enclosed in the ribcage bounding box. It has proved robustness over 12 datasets. The main difference with the convex hull criterion, in the case of the micro-CT images, is that sometimes a greater part of the trachea is kept as part of the lungs region. However, this criterion was not sufficient in the case of limited angle tomography, for which using the

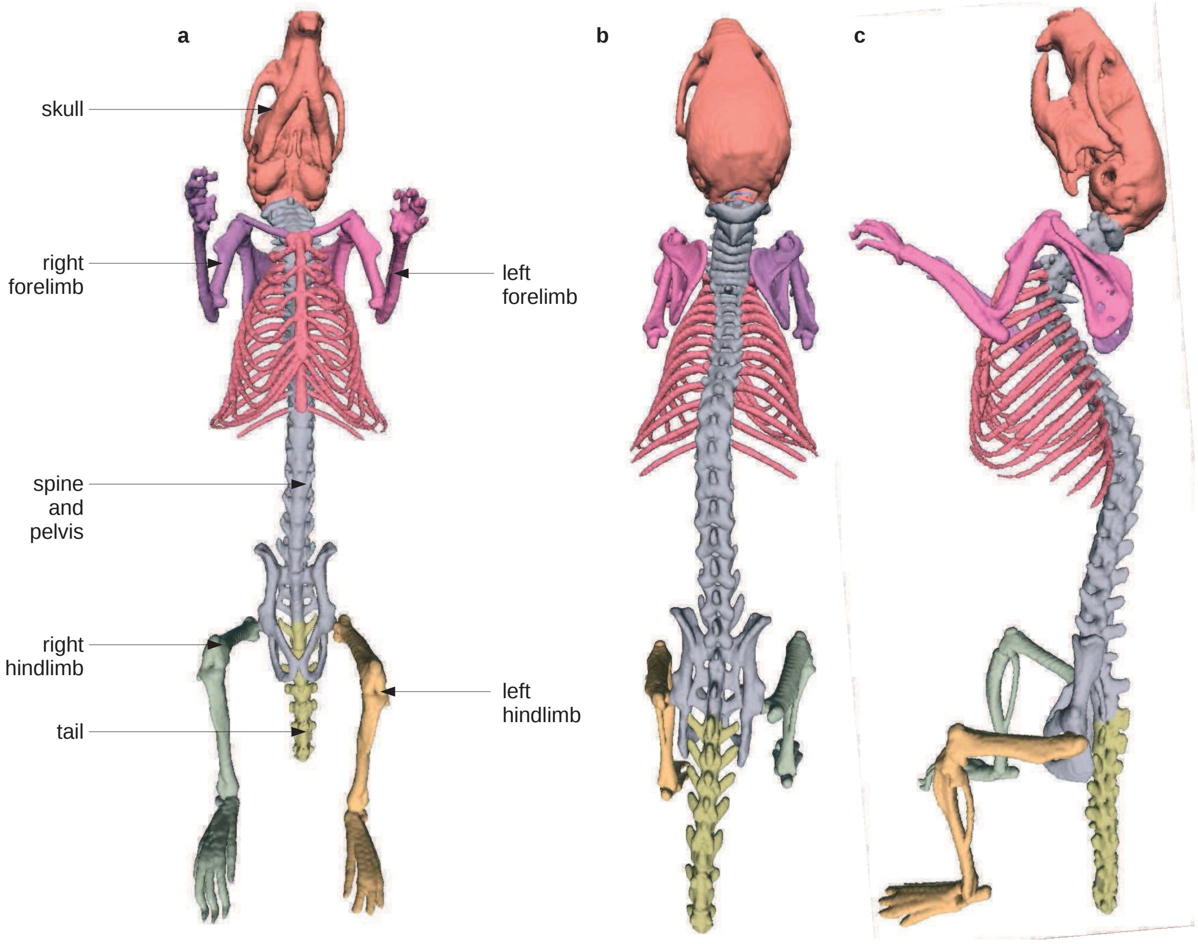

Figure 4.8: Annotated skeleton model. Indexes a, b and c correspond to the bottom-to-top view, top-to-bottom view and side view. In the legend, "left" and "right" are defined with respect to the sagittal plane.

convex hull was necessary. Figure 4.12 represents the surface meshes of the lungs segmented from the micro-CT images.

4.3 Application of the workflow to micro-CT images

Keeping in mind the aim of segmenting limited angle tomography images, the application of the workflow to micro-CT images constitutes a best case because images do not suffer from the characteristic artifacts of the limited angle reconstructions. It was therefore straightforward to evaluate the performance of the approach on micro-CT images, then to limited angle micro-CT images, and to compare both.

4.3.1 Description of the data

Several datasets were collected with the protocol described in Chapter 3.

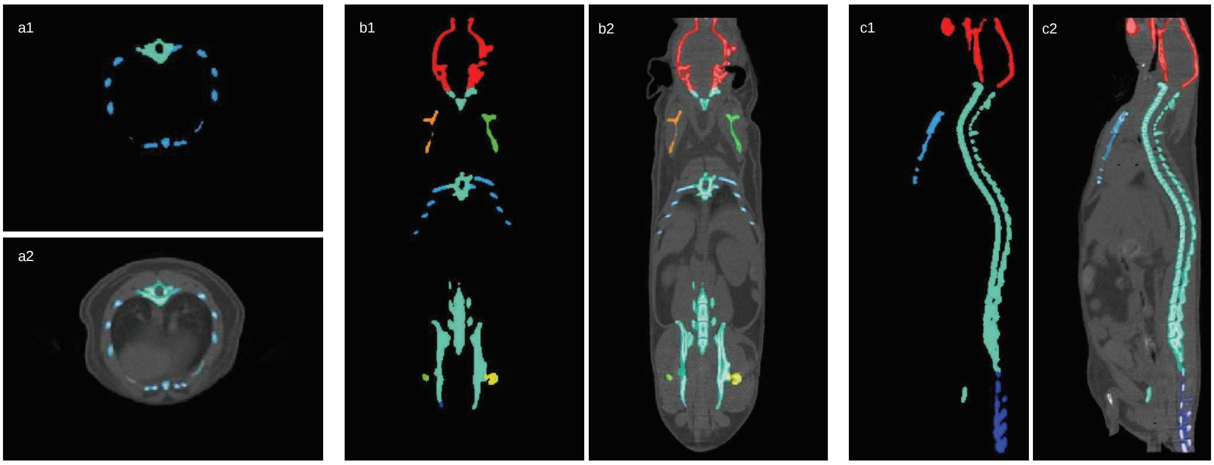

Figure 4.9: The transverse, coronal and sagittal slices are indexed respectively with the letter a, b and c. The indexes 1 and 2 represent, respectively, the mask and the mask overlaid on the preprocessed micro-CT image.

Figure 4.10: Representation of the subparts segmented with the automatic segmentation workflow. Each color represents a skeleton segment.

4.3.2 Evaluation of the skeleton segmentation method

The performance of the skeleton segmentation algorithm was evaluated qualitatively, following the idea of [Heckel et al., 2014]. The protocol for the evaluation was defined as follows:

- A set of ten micro-CT images was segmented automatically by the algorithm.
- A qualitative grading scale was defined, characterizing the qualitative observations. The grading scale is reported in Table 4.4.
- Eight human observers evaluated independently the segmentation result. A booklet displaying a representation of each skeleton segments was provided to the evaluator as a reference for the morphology of the segments.
- The evaluators were asked to evaluate the segmentation of nine subparts of the skeleton, namely i) the skull, ii,iii) each forelimb as a whole, iv,v) each hindlimb as a whole, vi) the tail, vii) the ribcage, viii) the spine and pelvis as a whole, as well as ix) the spine, ribcage and pelvis as a whole.
- The results of the evaluations of the other evaluators were not communicated to the evaluator doing the evaluation.

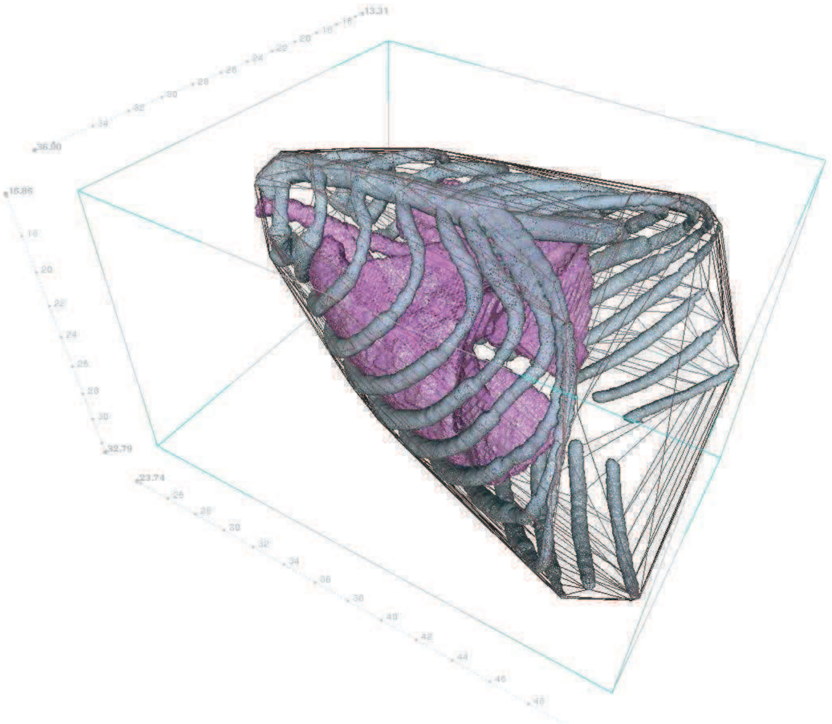

Figure 4.11: Representation of the surface meshes of a mouse ribcage, its bounding box and its convex hull. The scale is in mm.

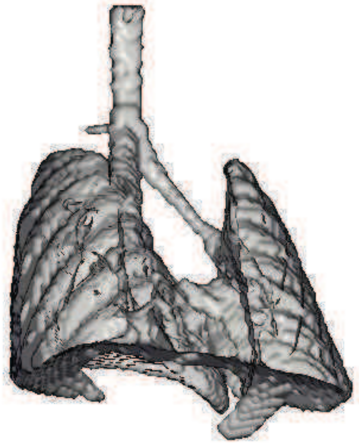

Figure 4.12: Representation of the lungs segmented with the automatic segmentation workflow from one individual.

- The evaluator were not allowed to modify their rating of a previously segmented skeleton.

- Only the assignment of the labels was evaluated, not the morphology of the segments – for example, missing regions of a scapula are not supposed to decrease the score, except if a wrong label was attributed to it.
- No time constraints were set up for the evaluation.

Figure 4.13 displays the summary of the scores of the qualitative evaluation of the skeletons in subparts.

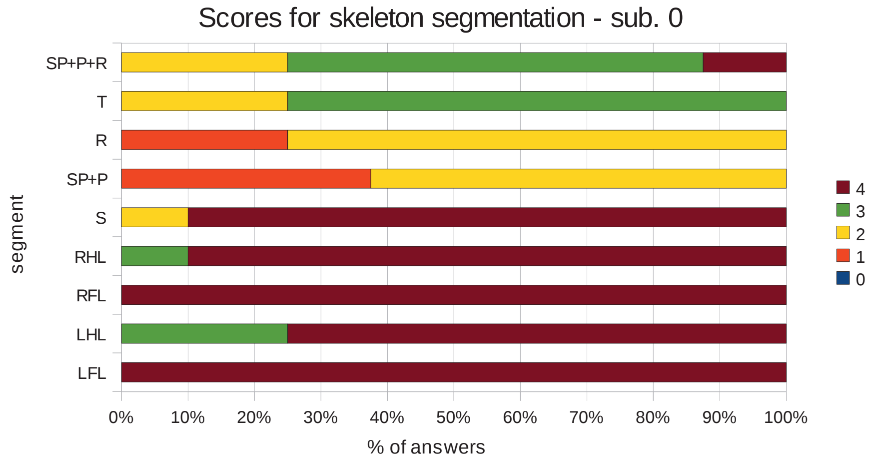

Figure 4.13: Summary of the scores of the skeleton segmentation in subparts with the automatic segmentation workflow, for one subject, as described in Section 4.3.2. **Abscissa:**
The percentage of answers.
Ordinates:
- LFL = left forelimb
- lhl = left hindlimb
- RFL = right forelimb
- RHL = right hindlimb
- SK = skull
- SP+P = spine+pelvis
- RC = ribcage
- T = tail
- SP+P+RC = spine+pelvis+ribcage.

		rating	meaning
S	4	perfect	perfectly identified, no overlap with neighbouring regions
S	3	good	well identified, small overlap with neighbouring regions
S	2	acceptable	mainly identified, but not completely, overlap with neighbouring regions
I	1	bad	partially and poorly identified, important overlap with neighbouring regions
I	0	unacceptable	not identified at all.

Table 4.4: Rating scale given to the 8 persons who evaluated the results. In the first column, S stands for *Sufficient*, I for *Insufficient*

4.3.3 Results

The results of the segmentation of twelve individuals are represented in Appendix C.

4.4 Application of the workflow to limited angle micro-CT images

The application of the workflow to limited angle micro-CT images was straightforward and made possible to evaluate its performance at extracting information about the high contrast tissues from limited angle micro-CT images reconstructed with ASD-POCS from data acquired over $90°$.

4.4.1 Description of the data

Four preclinical datasets were acquired with the same protocol as presented in Section 3.7.1. Images were reconstructed, as well, with FDK from the complete datasets and with ASD-POCS from the projections acquired over $90°$, with the same parameters as described in 3.7.1.

4.4.2 Quantitative evaluation

The segmentation of the tissues from the micro-CT images is considered to be the ground truth. The evaluation of the accuracy of this segmentation – for example, by comparison with manual segmentation results – is out of the scope of this thesis. Surfaces were compared using i) the averaged distance between estimated mesh vertices and the reference mesh A_{sd}, ii) the ratio of the estimated volume over the reference volume, R_{v} and iii) the Dice coefficient D [Dice, 1945] which allows to quantify the overlap of the two meshes. The measures are defined as follows:

$$\mathrm{D} = 2 \times \frac{|Sr \cap Sm|}{|Sr| + |Sm|} \tag{4.2}$$

$$\mathrm{R}_{\mathrm{v}} = \frac{V_r}{V_m} \tag{4.3}$$

$$\mathrm{A}_{\mathrm{SD}} = \frac{1}{2}\left[\frac{1}{n_r}\sum_{i=1}^{n_r} d_i + \frac{1}{n_m}\sum_{j=1}^{n_m} d_j\right] \tag{4.4}$$

where S represents a domain - that is to say, a portion of space - V denotes the volume of a domain, n denotes the number of vertices of a mesh and d denotes the distance from one mesh to another. The indices r and m denote the reconstructed image and the model, respectively. The distances d_i and d_j in the formula of A_{SD} denote, respectively, the distance from the points of the reconstructed mesh to the model surface and inversely. Surface-to-surface distance maps were generated to provide visual support and to emphasize the locality of the estimation accuracy. The point-to-point distances were calculated using a *K-d tree*[115]. The colorization of meshes brings interesting possibilities for their comparison. Typically, a color is encoded by a vector of octets (r, g, b)[116] – where r, g and b represent, respectively, the value of red, green and blue. The color map between two meshes M_1 and M_2 was defined as:

$$\begin{cases} r(v_{1i}, M_2) = 128 + 127 \times \frac{d(v_{1i}, M_2) - d_{min}(M_1, M_2)}{d_{max}(M_1, M_2) - d_{min}(M_1, M_2)} \\ g(v_{1i}, M_2) = 255 - r \\ b(v_{1i}, M_2) = 0 \end{cases} \tag{4.5}$$

---

[115] The *K-dimensional tree* data structure, introduced in 1975 by Bentley [Bentley, 1975], enables fast closest point search.

[116] An octet can have $2^8 = 256$ values therefore this system encodes $256 \times 256 \times 256$ colors.

if $d(v_{1i}, M_2) > \bar{d}(M_1, M_2)$, and

$$\begin{cases} r(v_{1i}, M_2) = 0 \\ g(v_{1i}, M_2) = 255 \\ b(v_{1i}, M_2) = 0 \end{cases} \tag{4.6}$$

otherwise, where:

- v_{1i} represents the vertex of index i of M_1;
- $d(v_{1i}, M_2)$ is the distance between v_{1i} and its closest point in M_2 – or, equivalently, the distance between v_{1i} and M_2;
- $d_{max}(M1, M2)$ and $d_{min}(M1, M2)$ are, respectively, the measure of the smallest and the greatest point-to-point distances between $M1$ and $M2$.

4.4.3 Results

Figure 4.14 and Figure 4.15 show, respectively, representations of the lungs and skeleton of a subject under various view angles, with the color map defined in Equation 4.5 and 4.6. The outlines of these tissues estimated from the limited angle micro-CT images exhibit defects compared to their counterpart segmented from the micro-CT image. Some outliers are visible in the images of the skeleton segmented from the limited angle micro-CT images due to the fact that in this case, many disconnected components belong to the skeleton. In this study, they were kept, though in practice they were removed prior to the registration of the skeleton model.

Table 4.5, Table 4.6 and Table 4.7 summarize the values of the measures for mesh comparison for the skin, skeleton and lungs, respectively. The mean dice values are superior to 0.75 for the skin, skeleton and lungs. The mean distance values are always inferior to 0.6 mm and their standard deviation is inferior to 0.8 mm in all cases. It is inferior to 0.3 mm in the case of the skeleton, with a standard deviation of 0.69 mm. The ratio of the volume calculated from the objects segmented from the limited angle micro-CT image and the micro-CT images indicate a greater volume in the case of the skin and skeleton, and conversely a smaller volume for the skeleton.

sub. ID	D	$\mathrm{A_{SD}}$	$\sigma_{\mathrm{A_{SD}}}$	$\mathrm{R_v}$
11	0.93	0.56	0.66	1.09
12	0.95	0.47	0.57	1.06
13	0.94	0.62	0.57	1.10
14	0.94	0.54	0.67	1.02
median	**0.94**	**0.55**	**0.62**	**1.07**

Table 4.5: Calculated values of the measures of mesh similarity for the skin.

4.4.4 Processing time

In the current implementation, some operations have not been optimized and are time consuming. An average processing time of 40 minutes was recorded. Performing the segmentation with the current implementation would therefore be prohibitive for a routine usage. The preprocessing represents 10 minutes mainly due to the Gaussian filtering. As for the non-rigid registration, it represents 25 minutes – mainly due to memory transfers and matrix inversions.

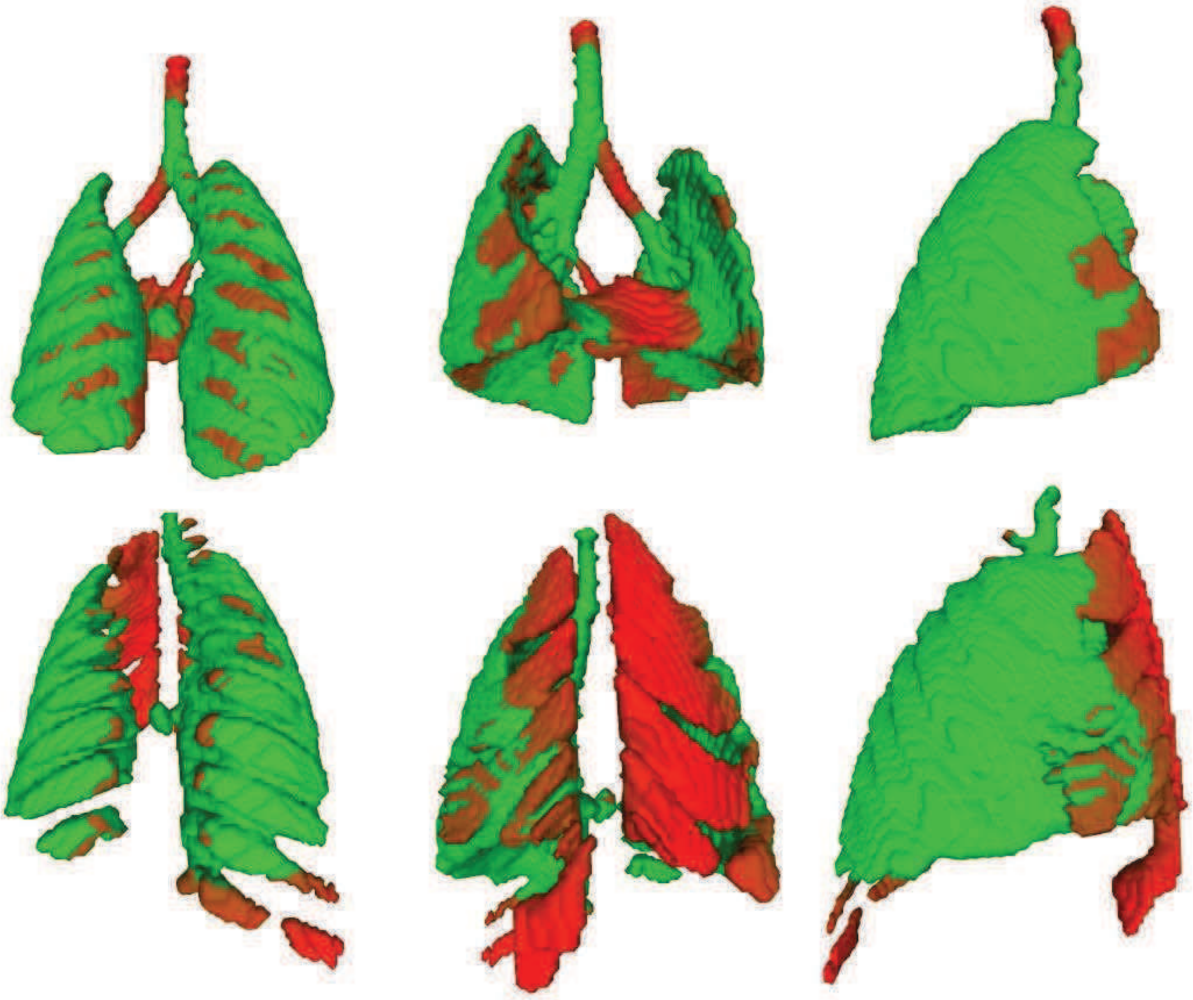

Figure 4.14: Representation of the surface meshes of the lungs of one subject, extracted from the FDK reconstruction from the 360° dataset (top) and the ASD-POCS reconstruction from the 90° dataset (bottom). The three columns show, respectively, a back, face and side view. The colormap indicates the distance to the corresponding mesh as defined by Equations 4.5 and 4.6 – the more red the mesh appears, the farther from its counterpart it is, and conversely the more green it is, the closer it is to its counterpart. The green color is homogeneous below the A_{SD} value. The parts that are completely missing in their counterpart are enhanced by the color map and appear in red.

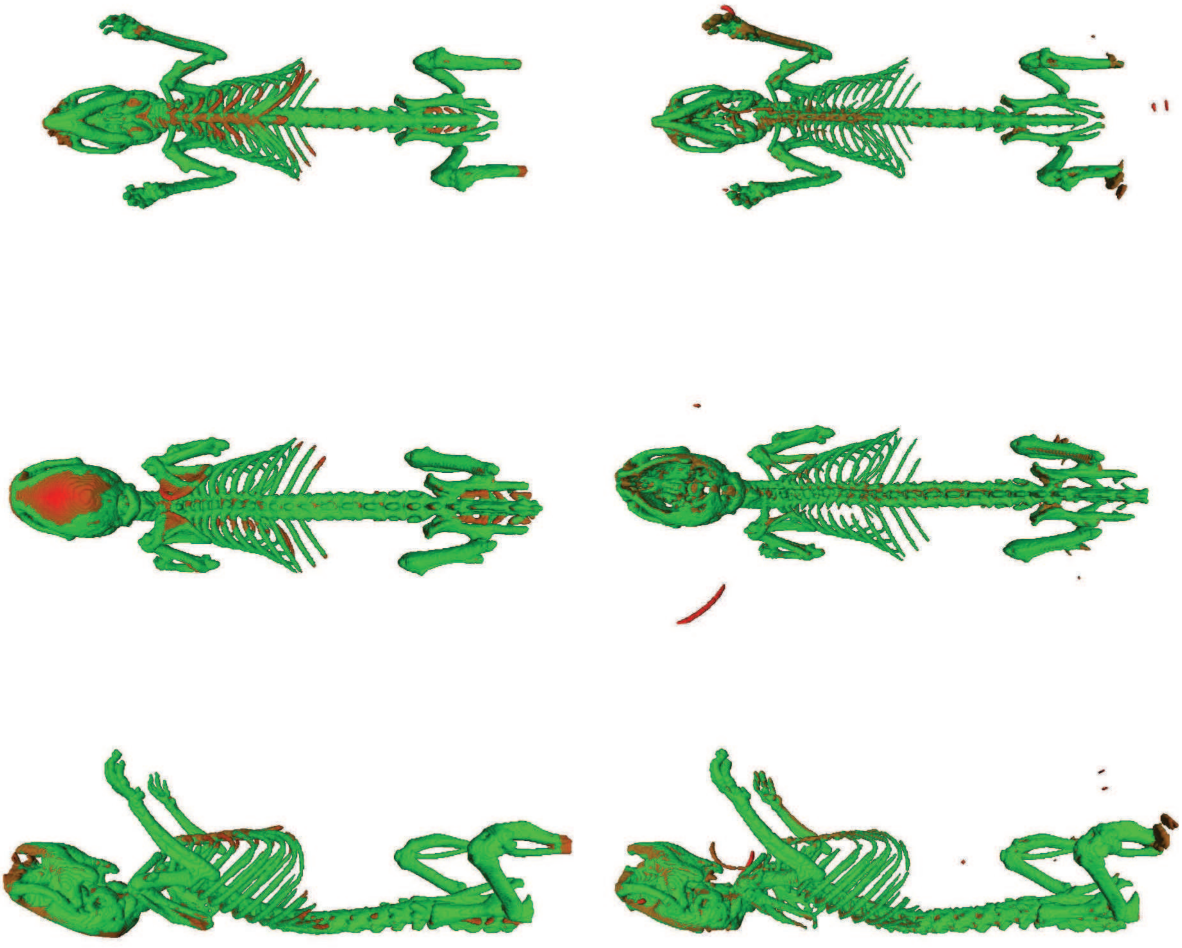

Figure 4.15: Representation of the surface meshes of the skeleton of one subject, extracted from the FDK reconstruction from the 360° dataset (left column) and the ASD-POCS reconstruction from the 90° dataset (right column). The three rows show, respectively, a face, back and side view. The colormap indicates the distance to the corresponding mesh as defined by Equations 4.5 and 4.6 – the more red the mesh appears, the farther from its counterpart it is, and conversely the more green it is, the closer it is to its counterpart. The green color is homogeneous below the A_{SD} value. The parts that are completely missing in their counterpart are enhanced by the color map and appear in red.

sub. ID	D	A_{SD}	$\sigma_{A_{SD}}$	R_v
11	0,80	0,29	0,75	0,76
12	0,80	0,23	0,32	0,74
13	0,77	0,39	1,05	0,70
16	0,77	0,37	0,65	0,71
median	**0,79**	**0,32**	**0,69**	**0,73**

Table 4.6: Calculated values of the measures of mesh similarity for the skeleton.

sub. ID	D	A_{SD}	$\sigma_{A_{SD}}$	R_v
11	0,78	0,55	0,75	1,26
12	0,75	0,67	0,83	1,46
13	0,77	0,51	0,74	1,32
14	0,78	0,59	0,82	1,22
median	**0.77**	**0.58**	**0.79**	**1.32**

Table 4.7: Calculated values of the measures of mesh similarity for the lungs.

4.5 Discussion

4.5.1 Processing time

The application of the Gaussian filter on GPU will allow to reduce this time. The time required to achieve matrix inversions could be greatly reduced by realizing the inversion on GPU as proposed in [Sharma et al., 2013]. The implementation of RPM on GPU as proposed in [Mourning et al., 2010] would also contribute to reduce the computation time. Other tasks including mesh processing routines were implemented on CPU for development but could be accelerated on GPU as well. Another way to reduce the computation time would be to register the skeleton centerlines instad of the whole meshes – this would allow to reduce the number of points to be registered.

4.5.2 Segmentation of micro-CT images

The evaluation of the results is mainly qualitative. To evaluate them quantitatively, a ground truth would be needed and could be obtained either using a reference workflow – such as these reported in [Baiker et al., 2010] or in [Wang et al., 2012b] – or segmentations realized by human observers. The enormous time that would be needed to process several datasets made this last solution prohibitive so it remained out of the scope of this study. As for the approaches of Baiker *et al.* and *Wang et al.*, their implementation would surely allow to give an interesting comparison, though their result can neither be viewed rigorously as a ground truth.

The presence of outliers shown in Figure 4.6 may be partly due to effect of the preprocessing step. Indeed, downsampling and applying a Gaussian filter has the effect of smoothing the image and therefore to degrade the edges. Working at the original sampling would reduce this effect – at the expense of an increase of processing time. Using an adaptive Gaussian filter could jointly address this issue.

With respect to the evaluation of the skeleton segmentation in subparts, the algorithm generally yields an acceptable segmentation. The errors are localized in regions where the segments overlap or are close to each other, as it is the case for the spine and ribcage, for the junction between the pelvis and femurs, the junction between the first cervical vertebra and the skull, as well as between the lumbar vertebrae and the tail vertebrae. Tuning the parameters of the RPM algorithm or the use of another registration algorithm such as Coherent Point Drift (CPD) [Myronenko and Song, 2009], registration using shape contexts [Xiao et al., 2010] or the non rigid registration algorithm based on Gaussian mixture models (GMMREG) [Bing and Vemuri, 2011] would make possible to match more robustly these parts of the skeleton.

Regarding the segmentation of the lungs, it is obvious that the threshold window used is correct in most case, yet in some cases it seems incorrect since artifacts are present in the mesh and do not correspond to a morphological abnormality, from the observation of the micro-CT images (not shown). Using an adaptive threshold would be an option to address this issue. In a complementary manner, more elaborated region growing approach could make possible to enforce a smoothness prior, for example, to get rid of the observed outliers.

4.5.3 Segmentation of limited angle micro-CT images

The values reported in Table 4.5, Table 4.6 and Table 4.7 indicate clearly that the outline of the high contrast tissues is degraded in the case of limited angle micro-CT compared to micro-CT. Nevertheless, the Dice value is always more than 0.75, which indicate a fair overlap of the structures, the $\mathrm{A_{SD}}$ value is inferior to $0.6\ \mathrm{mm}$ which denotes the fact that the outlines are different but remain close. The value of $\mathrm{A_{SD}}$ is increased by the presence of outliers and structures that are completely absent in the counterpart. The value of the standard deviations can be explained by the fact that some parts are well recovered, whereas others are completely absent in the case of the limited angle micro-CT, due to the thresholding. The ratio of the volumes clearly denotes the same effects. From Figure 4.14 and Figure 4.15, it is obvious that the artifacts noted in the limited angle micro-CT images, which are due to local under and over-estimations, result in degraded estimates of the tissues outline. It can be observed, morerover, that the regions of the outline which are, at some point of the acquisition, tangent to X-rays, are better estimated than those which are never tangent to X-rays. It is the case, for example, of the top of the skull, as well as various parts of the skeleton such as the sternum, various ribs, parts of the pelvis as well as parts of the tail vertebrae. The same effect can be observed for the lungs which extent appear to correspond between micro-CT and limited angle micro-CT, in the coronal planes, whereas it appears to be more important in the sagittal planes in the limited angle reconstructions.

As visible in Figure 4.15 some bone regions, badly reconstructed in the limited angle micro-CT images, for example parts of the ribs, constitute connected components disconnected from the main skeleton structure. Therefore the filtering aiming at removing the small skeletal elements explained in Section 4.2.1 is likely to fail to represent correctly the whole skeleton. As for the segmentation of the lungs, the use of the convex hull filtered by Laplacian filter is not completely satisfactory and lacks robustness. Indeed the choice of the number of iterations is arbitrary and the results is not guaranteed to be effectively included in the ribcage. A more robust approach such as growing a region inside the ribcage with elastic constraints would constitute an interesting development.

Despite a lot of work remains to be done to characterize robustly the method, such as the evaluation of the overlap between the model registered on the tissues extracted from the limited angle micro-CT images and the tissues extracted from the micro-CT images, the results presented in this Chapter encouraged the consideration of the use of the segmented high contrast tissues as registration features for a high level model-based segmentation.

4.6 Chapter Summary

The work presented in this chapter can be summarized as follows:

- An automatic workflow for segmenting high contrast tissues from micro-CT images has been implemented.
- The workflow includes low level segmentation of the skin and skeleton, middle level segmentation of the skeleton in subparts through the nonrigid registration of a segmented model, and high level segmentation of the lungs based on an anatomical prior.
- The results yielded by the workflow for the micro-CT images and the limited angle micro-CT images were compared. The results indicate a fair agreement, that encourages to explore the registration of a more complete anatomical model of the mouse on the segmented tissues.

Chapter 5

Automatic Segmentation of Low Contrast Tissues using a Statistical Atlas

Contents

This work aims at estimating the outline of various organs from a X-ray tomographic modality in order to provide *a priori* information for optical luminescence tomography. As developed in Chapter 4, the segmentation of various tissues exhibiting generally a high contrast with the surrounding structures is feasible in micro-CT images as well as in limited angle micro-CT images reconstructed with the ASD-POCS algorithm. In the case of limited angle micro-CT, however, the outline of the segmented tissues is degraded compared to the outline obtained from micro-CT images. Conversely, the segmentation of tissues that do not exhibit a high contrast with the surrounding tissues is much more challenging. Indeed, the tissues which cannot typically be distinguished from surrounding tissues in micro-CT images due to a poor contrast exhibit *a fortiori* the same characteristics in limited-angle micro-CT.

This chapter describes the development of an automatic segmentation workflow for micro-CT images. The aim is to reach a method which could be applied to limited-angle micro-CT images as well, to estimate explicitly the shapes of high contrast organs as well as some low contrast organs. This work focuses on the development of a fully-automatic method for the segmentation of thoracic and abdominal organs of the mouse in tomographic images. The idea is to develop a program which takes as input a micro-CT image and yields an estimation of the various organ outlines. While some tissues can be identified relatively robustly using low-level fully automatic methods [Wang et al., 2012b, Baiker et al., 2011], other are generally difficult to distinguish one from another due to a poor contrast. This consideration prevents from realizing the segmentation manually without any contrast medium to enhance the structures. In other words, fully-automatic whole-body segmentation workflows need, if no contrast media are used, a high-level processing of the image. This high-level requires the robust identification of specific structures either manually or using low-level methods with a certain degree of automation.

As mentioned in Chapter 2 and Chapter 4, a few works have been reported to realize automatically the segmentation of micro-CT images – and more generally CT images – including low contrast tissues. A number of works aiming at performing this segmentation is summarized in Table 5.1. These works rely on various models and registration methods, which are summarized in Table 5.2. They can be broadly classified in two categories, namely i) those based on the registration of a generic model on the point sets representing high contrast tissues[117] and the propagation of a deformation to the model of the low contrast tissues, and ii) those based on the registration of a statistical atlas, that is to say a combination of statistical shape models. Statistical shape models, as any *statistical model*[118], are typically

---

[117] When not specified differently, it is implicit that a point set is registrated on another point set.

[118] "A statistical model is a probability distribution constructed to enable inferences to be drawn or decisions made from the data." [Davison, 2003]

computed from a set of observations – which are, in this case, observations of the outline of an object across a sample. In other words, building a statistical shape model aims at mathematically describing the shape of an object using the observation of the outline of various instances of this object. It is claimed that this way, the model encapsulates a statistical description of the morphological variations across the sample. In this work, two statistical shape models have been built – one for the high contrast tissues, and one for the low contrast tissues. They have been related by a conditional Gaussian model to constitute a statistical atlas.

5.1 Automatic Segmentation of Low Contrast Tissues using a Statistical Atlas

Statistical Shape Models have been introduced as a part of the geometric morphometrics framework [Mitteroecker and Gunz, 2009] to describe the morphological variations of biological objects among populations, and have rapidly be used in the field of biomedical imaging [Bookstein, 1997a, Bookstein, 1997b]. They have become popular because they provide a way to represent statistical variations of the shape of organs within a population [Heimann and Meinzer, 2009, Park et al., 2003, Heimann et al., 2009, Wang et al., 2012b, Wang et al., 2012c]. The development and use of such models in the field of biomedical image interpretation has been reported for various applications, including mainly diagnostic support and segmentation. An extensive review of the use of Statistical Shape Models in biomedical imaging has been proposed by Heimann and Meinzer in [Heimann and Meinzer, 2009].

The litterature exhibits several examples of the use of such models for diagostics, focused on the local morphological properties of tisses or group of tissues, including knee [Van Haver et al., 2014], femur [Wu et al., 2009], prostate [Rusu et al., 2013], brain [Shen et al., 2006], etc. This is made possible because any outline can be represented by a – low dimensional – set of *shape parameters*, which allows to generate any outline by adding a linear combination of variation modes to a mean outline. Consequently, the parameters that describe the outline of any instance of the object can be infered through a registration procedure. For example, a statistical shape model can describe the shape of an object across a population made of healthy and diseased subjects with certain probability. Given an arbitrary instance of the object of interest, the set of parameters that corresponds to its outline can be infered. If a *healthy region* and a *diseased region* of the parameter space can be determined at the construction step, then estimating the parameters corresponding to an arbitrary instance allows to decide if the object is characteristic from a healthy subject or a diseased subject. Various examples have also been reported for segmentation, including an abdominal model for clinical CT [Park et al., 2003], a heart model [Ordas et al., 2007], or vertebrae in planar radiographs [Iglesias and de Bruijne, 2007]. Multiorgan models such as [Park et al., 2003] have been, however, seldom proposed. The methods reported in [Wang et al., 2012b] and [Wang et al., 2012c], use statistical shape models of the mouse tissues embedded in a statistical atlas, to perform the segmentation. In a statistical atlas, various statistical shape models are related by a conditional model. This enables the inference of the outline of one of these models given the parameters describing the others.

5.2 Formalism

Practically, Statistical Shape Models are generated using a training set with robustly identified landmarks distributed on the outline. A multivariate statistical analysis – refered to as *statistical shape analysis* – is carried out on the landmarks locations to build the model. Typically, such statistical analysis provides a way to reduce the dimensionality of a problem, by expressing any outline as a linear combination of a certain number of variation modes.

	HCT			**LCT**						
reference	**skel.**	**skin**	**lungs**	**heart**	**liver**	**kid.**	**spl.**	**others**	**atlas**	**app.**
[Park et al., 2003]	∅	∅	∅	∅	✓	✓	∅	spinal cord	custom, SSM	C
[Li et al., 2008]	✓	✓	✓	∅	∅	∅	∅	∅	custom	pC
[Baiker et al., 2010]	✓	✓	✓	✓	✓	✓	✓	intestine	MOBY	pC
[Joshi et al., 2010]	✓	✓	✓	✓	✓	✓	✓	various	digimouse	pC
[Wang et al., 2012a]	✓	✓	✓	✓	✓	✓	✓	bladder	custom	pC
[Wang et al., 2012c]	✓	✓	✓	✓	✓	✓	✓	∅	custom, SSM	pC
[Wang et al., 2012b]	✓	✓	✓	✓	✓	✓	✓	∅	custom, SSM	pC

Table 5.1: List of the tissues represented in the various multi-organ registration methods of Table 5.6.
- skel. = skeleton
- kid. = kidneys
- spl. = spleen
- app. = application
- SSM = statistical shape model
- pC = preclinical
- C = clinical

reference	**type**	**registration method**	**NOI**
[Park et al., 2003]	SSM	Bayesian framework	31
[Li et al., 2008]	AI	skeleton : RPM – other: NR Adaptive Basis Algorithm (MI)	1
[Baiker et al., 2010]	GM	skeleton : articulated – skin: geodesics – other: TPS interpolation	1
[Joshi et al., 2010]	GM	skin: NR + asymmetric L^2 pseudo-distance minimization	1
[Wang et al., 2012a]	GM	BSMI 2D/3D NR : top X-ray (WB) + OV (skin) + SW (skin surface)	1 (×5)
[Wang et al., 2012c]	SSM	BSMI 2D/3D NR : top X-ray (WB) + OV (skin) / ASM search – LCT: CGM	83
[Wang et al., 2012b]	SSM	HCT: 3D/3D ASM search – LCT: CGM	45

Table 5.2: Description of the models used in the multi-organ registration methods of Table 5.6.
- AI = arbitrary instance.
- PB = point based.
- IB = intensity based.
- GM = generic model.
- SSM = statistical shape model.
- CGM = conditional Gaussian model.
- ASM = active shape model.
- NOI = number of individuals involved in the model construction.
- n.c. = not concerned.
- HCT = high contrast tissues
- LCT = low contrast tissues
- BSMI = B-splines using Mutual Information
- OV = optical view
- TPS = Thin Plate Splines
- RPM = Robust Point Matching

Let the training set be represented as a set of landmarks $\mathbf{L} = \{L_1, L_2, ..., L_N\}$ such as $\forall i$, the cardinality of L_i is M. Let us express the landmarks as points in the Cartesian reference frame $(O, \overrightarrow{x}, \overrightarrow{y}, \overrightarrow{z})$. In this representation, for a given index $i \in 1, .., N$, $L_i = \{x_1, y_1, z_1, x_2, y_2, z_2, ..., x_M, y_M, z_M\}$ where x_j, y_j and z_j represent the cartesian coordinates of the $j-\mathrm{th}$ landmark. Let the $j-\mathrm{th}$ landmark of the $i-\mathrm{th}$ instance be noted L_{ij}, and let a bijective mapping associate each landmark to a corresponding landmark in any other set, such as $\forall (i, k) \in \{1, .., N\}^2 / i \neq k$, $\exists$ a transformation T_j^{ik} verifying $L_{kj} = T_j^{ik}(L_{ij})$. The set of transformations T_j^{ik} is typically determined by establishing explicit point correspondence between the model and each instance of the training set.

5.2.1 Point correspondence

The construction of a Statistical Shape Model therefore relies on the analysis of the statistical variations in the location of specific points in space – the *landmarks*. The identification of the landmarks over a sample is necessary to achieve this task. In [Heimann and Meinzer, 2009], the authors point out that the manual placement of landmarks in three dimensions and the inter and intra-observer variance make it a prohibitive method. Finding dense point correspondence is "generally the most challenging part of 3D model construction, and at the same time one of the major factors influencing model quality". Point correspondence can be established by means of "mesh-to-mesh", "mesh-to-volume", "volume-to-volume", "parametrization-to-parametrization", or "population-based optimization" registration [Heimann and Meinzer, 2009].

Formally, let L_0 be a set of landmark called the *model point set*, distributed on the *model surface* S_0, and let S_i be an instance of the observed object. The assumption is made that each landmark is present in any instance of the object part of the sample, so that a set of landmarks L_i can be associated to S_i. L_i is called an observation of the landmark set. Formally,

$$\exists\ L_i, \forall\ i \in \{1, .., N\} / L_i \in S_i. \tag{5.1}$$

Each of the L_{ij} is the same anatomical point as the point L_{0j}, $\forall (i, j) \in \{1, .., N\}^2 / i \neq j$ and the sets of landmarks are not known a priori. In this process, which aims at determining *point correspondences*, each of the L_i, $\forall i \in \{1, .., N\}$ is called a *target point set*. The construction of a Statistical Shape Model requires the determination of a set of transformations associating L_0 to any other set of landmark $L_i\ /\ i\ \in 1, .., N$ of the sample. In other words, a set of transformations $\mathbf{T}\ =\ \{T_1, .., T_N\}$ verifying

$$S_i\ =\ T_i(S_0), \forall i \in \{1, .., N\} \tag{5.2}$$

has to be determined. Landmark correspondence is then determined by

$$L_i\ =\ T_i(L_0), \forall i \in \{1, .., N\}. \tag{5.3}$$

Establishing point correspondences is a key step in the construction of the model as well as in the process of registrating this model on an arbitrary instance. In this work, a "mesh-to-mesh" registration - stated in [Heimann and Meinzer, 2009] as "the straightforward solution to landmark creation in 3D" has been used to establish the correspondence. As for the methods, several possibilities, including rigid registration methods such as the Iterative Closest Point (ICP, [Besl and McKay, 1992]), as well as non-rigid registration methods, in which a set of landmarks is used to guide a Thin-Plate-Spline deformation. The point correspondence was established as follows – the registration algorithms are described in Appendix 5.10:

- For the low contrast tissues, an arbitrary instance was chosen and registered on the others by matching their barycenter and applying the standard Iterative Closest Point algorithm (ICP). Then, the non-rigid registration algorithm based on Gaussian Mixture Models (GMMREG) was applied to establish the point correspondence.

- For the high-contrast tissues, an arbitrary instance was chosen and registered on the others using Iterative Closest Point (ICP). This step was followed by a non rigid registration using the Robust Point Matching algorithm (RPM). This was embedded in the workflow presented in Chapter 4, as shown in Figure 5.1.

5.2.2 Statistical Shape Analysis

Once the point correspondences have been established, that is to say once the position of each landmark has been determined in each instance of the training set, the application of statistical data analysis methods to this set of *observations* is possible. It is referred to as Statistical Shape Analysis. The underlying idea is to associate a Statistical Model to the training set. The result of such an analysis is a reduction of the dimensionality of the problem. One popular method to achieve this goal is the popular Principal Component Analysis (PCA) method, introduced in 1933 by Hotelling [Jackson, 1991]. This method of multivariate statistical analysis makes possible to reduce the dimensionality of a p-variable problem, by expressing the variables as a linear combination of k Principal Components, with $k \leq p$. Considering a p-variable problem and a set of n vectors of p dimensions, which components are the observations of each variable, denoted L_i, with $i \in \{1, .., n\}$ – the sample or *observation matrix* is

$$\begin{pmatrix} L_1^1 & L_1^2 & \cdots & L_1^p \\ L_2^1 & L_2^1 & \cdots & L_2^p \\ \vdots & \vdots & \ddots & \vdots \\ L_n^p & L_n^p & \cdots & L_n^p \end{pmatrix}. \tag{5.4}$$

– standard statistical methods make possible to calculate the mean observation vector $\bar{L}$ as well as i) the variance σ_i associated to the observation L_i and ii) the covariance σ_{ij} of variables L_i and L_j. At this point, the direct observation of the data can lead to the observation that each of the p variable varies across the set of observations. Principal Components Analysis consists typically in quantifying the main variation directions of the observation vectors – defined by p-dimensional vectors, the principal components. The covariance matrix Σ of the p variables is:

$$\Sigma = \begin{pmatrix} \sigma_1^2 & \sigma_{12} & \cdots & \sigma_{1p} \\ \sigma_{12} & \sigma_2^2 & \cdots & \sigma_{2p} \\ \vdots & \vdots & \ddots & \vdots \\ \sigma_{1p} & \sigma_{2p} & \cdots & \sigma_p^2 \end{pmatrix}. \tag{5.5}$$

with each covariance being defined as:

$$\sigma_{ij} = E[(L_i - \bar{L})(L_j - \bar{L})]. \tag{5.6}$$

and the mean of the p variables being defined as:

$$\bar{L} = \frac{1}{p} \sum_{i=0}^{p} L_i. \tag{5.7}$$

As long as two variables L_i and L_j are linearly dependent, then $\sigma_{ij} \neq 0$. Σ is a square, symmetrical p x p matrix. Linear algebra makes it possible to express Σ as:

$$P^{-1} \Sigma P = \Lambda \tag{5.8}$$

where P is an orthogonal matrix and Λ is a p x p diagonal matrix of elements $\{\lambda_1, \lambda_2, ..., \lambda_p\}$, and P^{-1} denotes the inverse of P - or equivalently, its transpose. The values λ are the solutions of the equation:

$$|\Sigma - \lambda I| = 0 \tag{5.9}$$

and are called the *characteristic roots* or *eigenvalues* of Σ. The columns p_j of P are called the eigenvectors of Σ and the *principal components* of the observation matrix L. The eigenvalues characterize the variance of the observation matrix along each of the corresponding principal component. A linear combination of these components makes possible to represent any instance of the training set such as:

$$L_i = \bar{L} + Pb \tag{5.10}$$

where b is a p-dimensional vector which coordinates are the coefficients of the linear combination.

Applied to the outlines of biological tissues, this method allows to represent the shape by a mean outline and a few principal components. In this context, the basic idea is to constitute a set of observation vectors with the outlines L_i of the training set – as defined in Section 5.2.1, and to analyze it with PCA. As a result, a mean outline $\bar{L}$ and a matrix P of principal components are calculated. A vector of *shape parameters* b_i uniquely represents any outline of the training set. Considering any instance of the outline, the corresponding vector of shape parameters can be calculated as:

$$b = P^t(L - \bar{L}). \tag{5.11}$$

The indices of the training set are not present anymore in the notation since this can be applied to any instance of the considered object. In practice, a limited number of variation modes is used, which leads to:

$$L \approx \bar{L} + Pb \tag{5.12}$$

such that the number of variation modes is small compared to the number of points representing the shape. Usually, the principal components accounting for $m\%$ of variation - that is to say, the first k components verifying:

$$100 \times \sum_{i=1}^{k} \frac{\lambda_i}{\sum_{i=1}^{p} \lambda_i} \geq m \tag{5.13}$$

are linearly combined to represent the sample. The use of PCA for Statistical Shape Analysis is discussed in [Heimann and Meinzer, 2009]; in the same article, the authors state that "in <their> experience, a good model should be able to capture 90% of the total variance in the training set with less than a dozen modes. In this work, we set $m = 95$. In this work, randomized PCA [Rokhlin et al., 2009] was prefered to PCA for its ability to handle a big amount of data.

5.3 Gathering Statistical Shape Models into a Statistical Atlas

In [Iglesias and de Bruijne, 2007], the author use an original idea of relating a dense point distribution – 67 points – to six characteristic manually specified landmarks around a vertebra in 2d radiographs. The goal is achieved by building a Conditional Gaussian Model based on a manually annotated training set. In [Wang et al., 2012b], the idea is extended to a whole-body Statistical Atlas of the mouse, and a Conditional Gaussian Model is built to link the shape parameters of the high contrast tissues and the shape parameters of the low contrast tissues. In this work, the same idea is put into practice.

The probability density function of a random vector X in $\mathbb{R}^n$ following a multivariate Gaussian distribution, that is to say $X \sim N(\mu, \Sigma)$, where μ is the mean vector and Σ is the covariance matrix, is given by:

$$f(x) = f(x|\mu, \Sigma) = \frac{1}{(2\pi)^{n/2}|\Sigma|^{1/2}} e^{-\frac{1}{2}(x-\mu)^T \Sigma^{-1}(x-\mu)}. \tag{5.14}$$

In this work, we make the assumption that the shape parameter vectors for the low contrast tissues and for the high contrast tissues follow multivariate Gaussian distributions. The conditional probability distribution of the shape parameter vector for the low contrast tissues is defined as:

$$f(x^{l|h}) = f(x^{l|h}|\bar{x^{l|h}}, \Sigma^{l|h}) \tag{5.15}$$

where the conditional mean is defined as:

$$\bar{x^{l|h}} = \bar{x^l} + \Sigma^{l,h}(\Sigma^h)^{-1}(x^h - \bar{x^h}) \tag{5.16}$$

and the conditional covariance matrix is defined as:

$$\Sigma^{l|h} = \Sigma^{l,h}(\Sigma^h)^{-1}\Sigma^{h,l}. \tag{5.17}$$

with the covariance matrix defined as in Equation 5.6 and Equation 5.5.

5.4 Fully-automatic segmentation workflow

The developed approach follows closely the approach described in [Wang et al., 2012b]. The corresponding workflow is represented in Figure 5.2. The input of the segmentation workflow is a micro-CT reconstruction, represented by an image on a cubic voxel lattice. The segmentation is carried out in three steps, namely i) image preprocessing, ii) automatic segmentation of the high-contrast tissues and tesselation of their surfaces, and iii) estimation of the outlines of the low-contrast tissues. Image preprocessing and the segmentation of the high contrast tissues are realized as described in Chapter 4. The registration of an arbitrary instance is included in the process as represented in Figure 5.1. Supplementary steps are included, namely the generation of a skin model covering the thoracic and abdominal region only, and its registration on the segmented skin. The propagation of the deformation to a high resolution skin model to which the limbs have been manually removed – to get rid of unuseful shape variability.

The statistical shape model of the high contrast tissues is registered on the high contrast tissues by an iterative process, alternating i) the affine registration of the target on its counterpart – the model – with a Generalized Procrustes Analysis (GPA) – described in Appendix G – registration and an affine ICP registration, ii) the estimation of the corresponding shape parameters using Equation 5.11. The outlines of the low-contrast tissues are estimated by inference of the shape parameter describing the outline of the high contrast tissues, using Equation 5.15.

In this work, an appropriate model must represent the shapes of various organs, including low contrast tissues. Yet, as mentioned in Chapter 3, the segmentation of low contrast tissues is generally not feasible when the contrast is not enhanced by a contrast medium. It is important to keep in mind that the atlas developed in this work has been realized "from scratch" – that is to say that no automatic segmentation workflow for the low contrast tissues was available at our institute prior to this study. Therefore, it has been mandatory to collect observation of the outline of the tissues.

5.5 Manual and interactive segmentation of the low contrast tissues

The idea here is to describe the outline of biological objects without removing them from the organism. Table 5.3 summarizes techniques of segmentation dedicated to low-contrast abdominal and thoracic

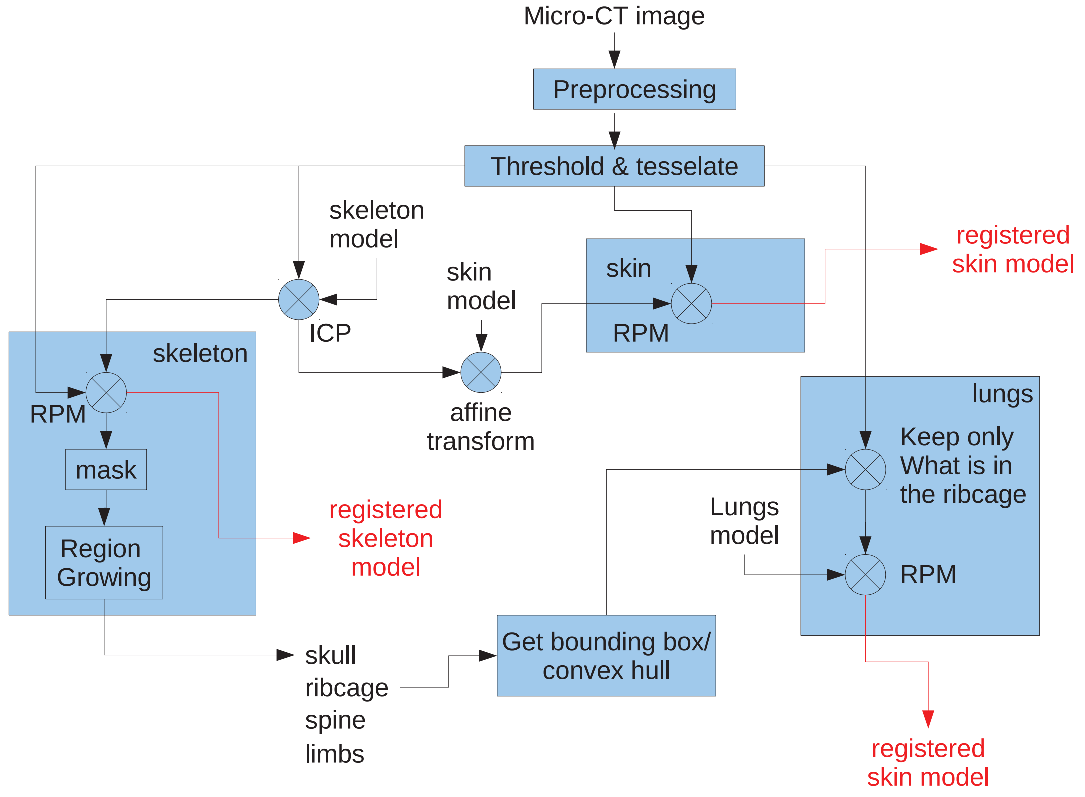

Figure 5.1: Workflow for the segmentation of HCT. RPM refers to nonrigid registration using the "Robust Point Matching" algorithm.

tissues. All the reported techniques make use of contrast media, associated to various approaches. Table 5.4 summarizes contrast media typically used for enhancement of low-contrast organs. These contrast media target different tissues. Those presented as targeting the blood pool generally provide a relative enhancement of tissues such as the liver and spleen as well. They are eliminated mostly through the urinary system, therefore kidneys and bladder are also enhanced in the images.

5.5.1 Liver

Several works report the development of interactive and automatic methods for liver segmentation, especially for clinical CT. A selection of these methods are reviewed in [Mharib et al., 2011] and [Heimann et al., 2009]. Some of these works include the use of Statistical Shape Models – this is the aim of this work to build one, and we did not have such a method implemented at our institute. As no such interactive or automatic method had been previously implemented at our institute, and the manual segmentation, despite its drawbacks, was the most straightforward approach, it was chosen for delineating the livers. The liver region outline was therefore defined manually with the help of interactive methods of thresholding and supervised region growing available in the software ITKsnap. Segmenting the liver is a difficult task because of the numerous adjacent structures sharing a common range of intensities: spleen, stomach, intestine, kidney, heart and surrounding muscles. As displayed in Table 5.3, reports of the segmentation of livers in preclinical images tend to use the alkaline earth contrast medium Exitron. One of the main

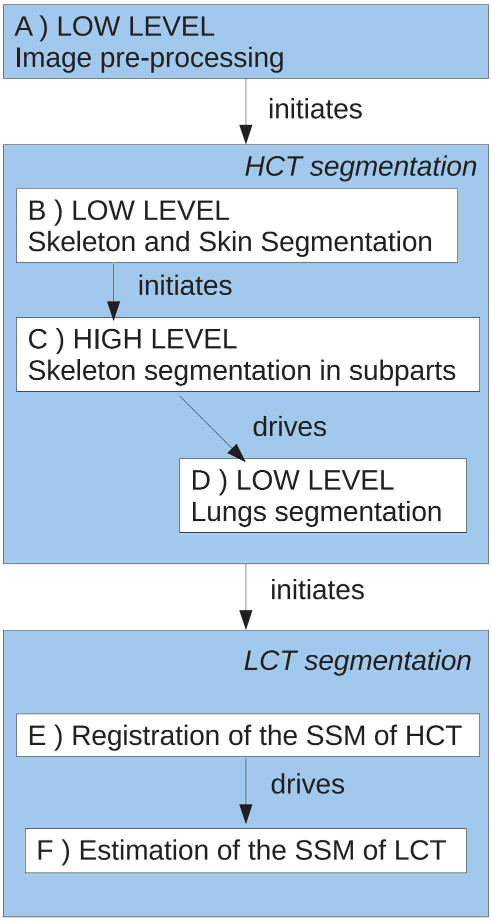

Figure 5.2: Workflow for whole-body segmentation.

advantage of Exitron Nano is its long lifetime in the liver [Wathen et al., 2013]. As displayed in Table 5.4, several alternatives exist to the use of Exitron Nano, and these are mainly iodine-based compounds.

5.5.2 Spleen

Some works have focused on the segmentation of the spleen from micro-CT images. Among the works summarized in Table 5.3, level set deformable models have been used to carry out the spleen segmentation. No such method had been previously implemented at our institute, and the manual segmentation was chosen as the most straightforward option, as well as for the liver. As for the contrast media used for spleen segmentation, they are mostly similar to these used for the liver, as displayed in Table 5.4. In this work, as no such method had been previously implemented at our institute, the segmentation was performed manually and with the same interactive tools as for the liver.

5.5.3 Kidneys

Kidney segmentation from micro-CT images have been addressed automatically, such as cited in Table 5.3. In this work, kidneys were segmented using the same region growing algorithm as presented in Section 4.2. The fact that the contrast media are mostly eliminated through the urinary system results

reference	C.M.	tissue	segmentation technique	auto.	context
[Cuingnet et al., 2012]	yes (n.s.)	kidney	random forests	2	C
[Rothe et al., 2015]	Exitron, eXIA	BP/liver/spleen	manual (liver) / SA (lesions)	1	pC
[Zheng et al., 2007]	yes (n.s.)	heart chamber	MSL+SF	2	C
[Heckel et al., 2011]	yes(n.s.)	liver	EMIF	1	C
[Zhong et al., 2013]	yes(n.s.)/no	heart PC	MSL	2	C
[Heimann et al., 2007]	yes(n.s.)	liver	SSM	2	C
[Fiebig et al., 2012]	Exitron	liver subparts	manual	0	C
[Aykac et al., 2005]	Fenestra LC	spleen	AC-LS	1 (seed)	pC
[Price et al., 2006]	yes(n.s.)	spleen	3D LS	1 (seed)	pC
[Clark et al., 2012]	liposomal I	heart chambers	manual	0	pC
[Soler et al., 2001]	yes(n.s.)	liver	TS + atlas registration	2	C
[Wathen et al., 2013]	AuroVist	heart	manual	0	pC
[Wathen et al., 2013]	Exitron	liver+spleen	manual	0	pC
[Wathen et al., 2013]	Visipaque	kidneys	manual	0	pC
[Wathen et al., 2013]	$BaSO_4$	GI track	manual	0	pC

Table 5.3: Non-exhaustive list of segmentation techniques for various low-contrast tissues.
- C.M. = contrast medium
- MSL = marginal space learning
- SF = steerable features
- EMIF = energy minimizing implicit functions
- PC = pericardium
- AC-LS = active contours - level sets
- SA = semi automatic
- auto. = level of automation; 0 means no automation – thus, manual segmentation – while 1 and 2 mean, respectively, interactive – or semi-automatic – and fully-automatic segmentation.

in the enhancement of the kidneys on their route to the bladder. Mainly, the contrast media targeting the blood pool, such as these summarized in Table 5.4 have a shorter lifetime than those targeting a specific tissue, and therefore are eliminated faster through the kidneys.

5.5.4 Heart

The segmentation of the heart from micro-CT images has been addressed in various ways. Automatic methods have been proposed, including marginal space learning – methods reported in Table 5.3. As for the liver and the spleen, the segmentation was performed manually with the help of interactive methods.

5.6 Segmentation of a set of micro-CT images

As explained, the construction of a statistical shape model relies on the collection of several observation of the outline of the object of interest. To obtain the outline, a specific protocol was set up, including the use of a contrast medium to enhance low contrast tissues.

agent	**generic / commercial name**	**manufacturer**	**target**
I + A.E. NP	Exitron Nano	Miltenyi Biotech	liver / BP / spleen
I	- / eXIA	Binitio Biotech	liver / BP / spleen
I	Iohexol / Omnipaque^{TM}	GE Healthcare	liver / BP
Au NP	- / AuroVist^{TM}	Nanoprobes	BP
I	- / Fenestra^{TM} LC	ART Inc.	liver / spleen
I	- / Fenestra^{TM} VC	ART Inc.	BP
I	Iodixanol / Visipaque^{TM}	GE Healthcare	kidney
I	Iomeprol / Iomeron®	Bracco Imaging	BP
I	- / Telebrix®	Guerbet	GI track
Si	- / Microfil®	FlowTech Inc.	BP
$BaSO_4$	baryum sulfate / ∅	∅	GI track

Table 5.4: Non-exhaustive list of commercial and non commercial contrast media for low-contrast organs enhancement in microCT images. Microfil® cannot be used for *in vivo* imaging.
- I=iodine
- AE = alkaline earth
- BP = blood pool
- GI = gastro-intestinal
- NP = nanoparticle

tissue	min. μ (mm^{-1})	max. μ (mm^{-1})	seed (mm^{-1})	other criteria
kidneys	0.045	0.3	variable	manually specified bounding box

Table 5.5: Threshold values and citeria used for the interactive segmentation of the kidneys.

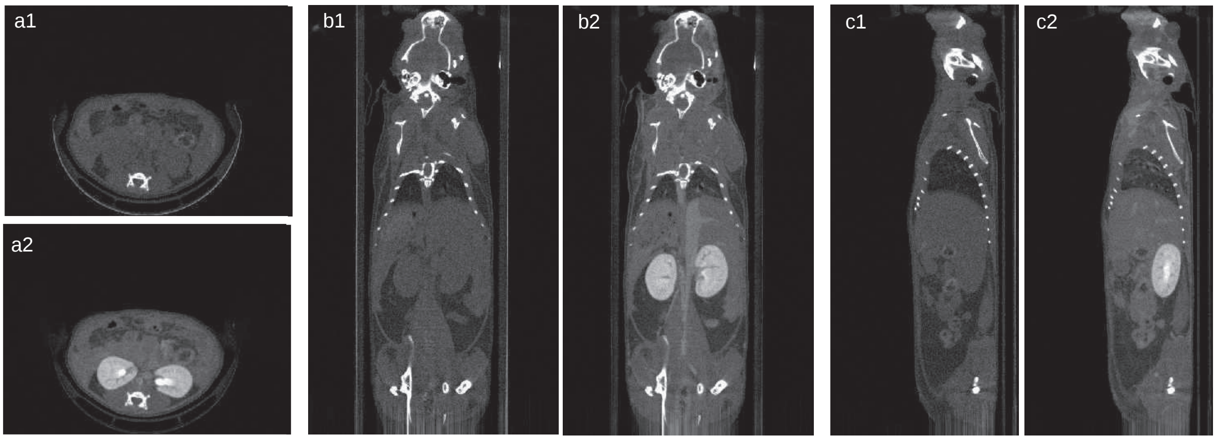

Figure 5.3: Transverse (a), coronal (b) and sagittal (c) cross sections through micro-CT images reconstructed from a standard acquisition (1) and a subsequent contrast enhanced acquisition (2) using Iomeron®. The power settings are not the same for both; this is explained in Section 5.6.4.

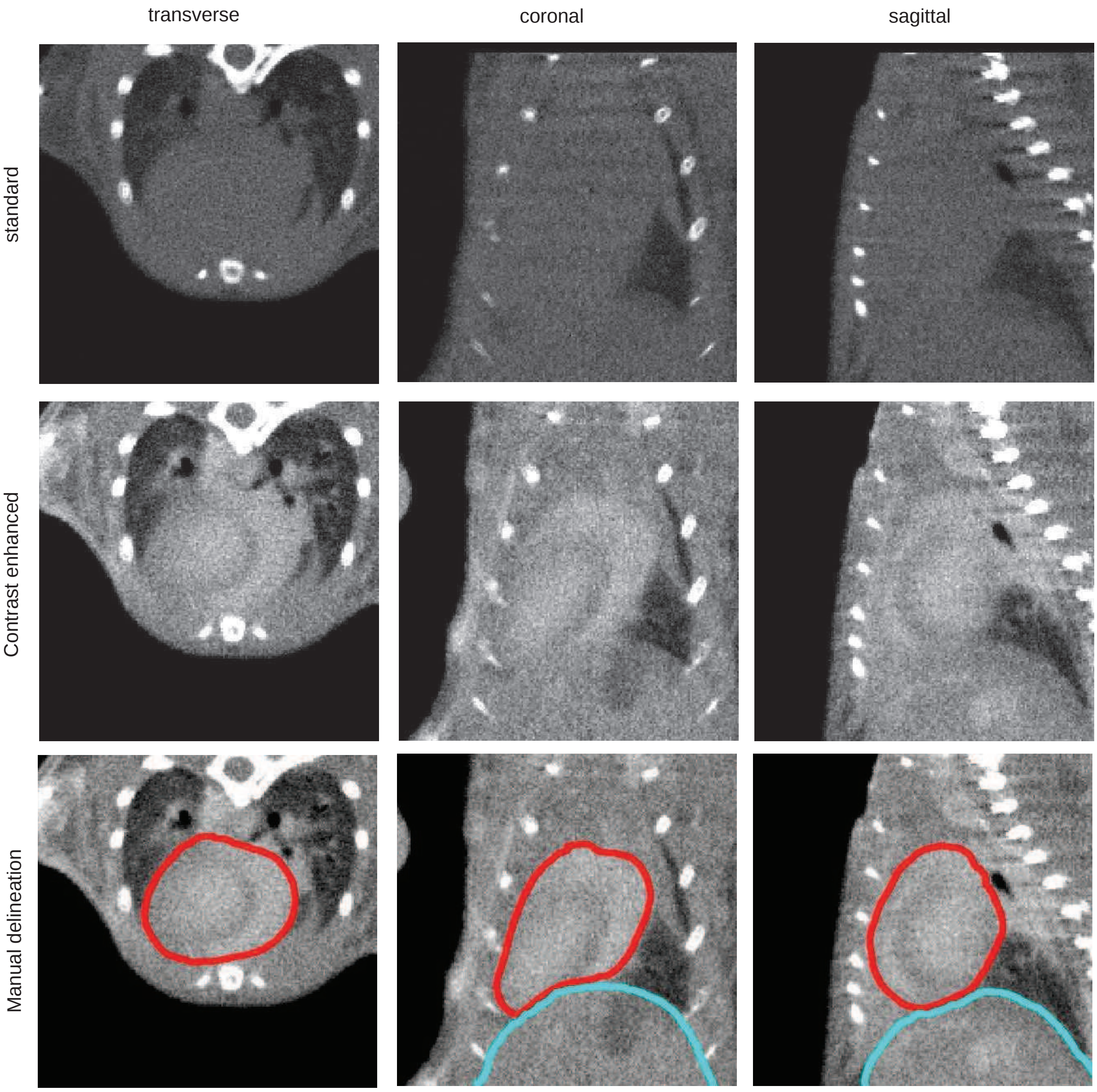

Figure 5.4: Representation of transverse, coronal and sagittal cross sections through micro-CT reconstructions, focusing on the heart. In the third row, the heart and liver have been manually outlined, respectively in red and blue. *Standard* means with no contrast medium, whereas *contrast enhanced* means using Iomeron®. The power settings are not the same for both; this is explained in Section 5.6.4.

5.6.1 Micro-CT system settings

A systematic study was realized in our group prior to this thesis, to find a tradeoff between the power settings of the X-ray source and the contrast obtained between various concentrations of Iodine and water. The results showed that the power settings $60kV/134\mu A$ were to be considered for an optimal contrast. Conversely, the $40kV/200\mu A$ settings are used to optimize the contrast between the bone and the surrounding tissues. The integration time for the projections was set to $470\mathrm{ms}$, and the pixel edge

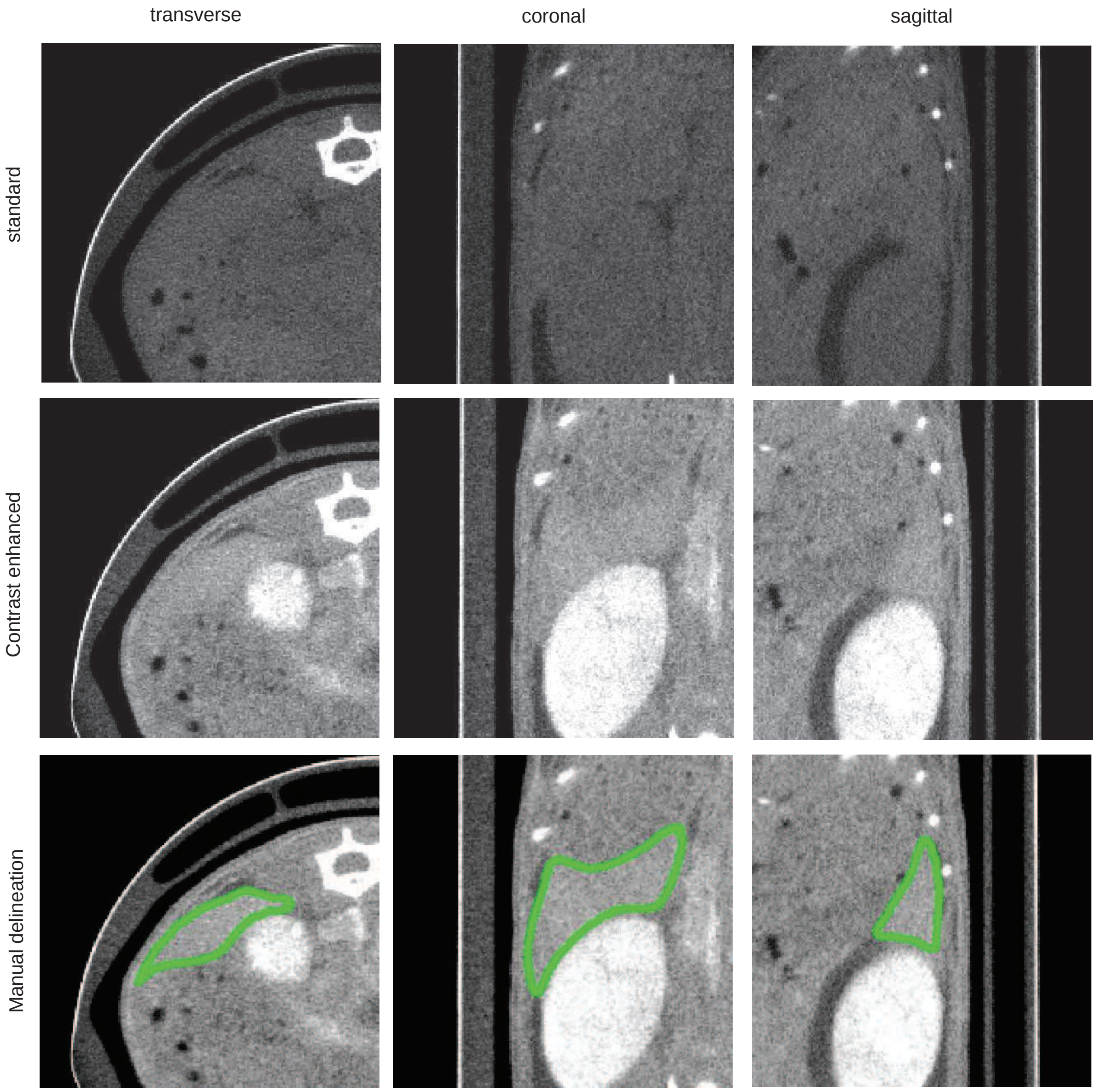

Figure 5.5: Representation of transverse, coronal and sagittal cross sections through micro-CT reconstructions, focusing on the spleen. In the third row, the spleen has been manually outlined in green. *Standard* means with no contrast medium, whereas *contrast enhanced* means using Iomeron®. The power settings are not the same for both; this is explained in Section 5.6.4.

size to 0.05 mm. The acquisitions were performed in continuous motion mode and no specific gating – neither respiratory nor cardiac – was used.

5.6.2 Acquisition protocol

The mice underwent small surgery, to put a catheter in their jugular vein, for contrast medium intravenous injection. Five acquisitions were performed for each animal, namely two acquisitions without contrast medium – for the anterior and posterior parts, respectively – and then three acquisitions with $300\ \mu\mathrm{L}$ of Iomeron® diluted in phosphate buffered saline solution (PBS) for a total volume of $1\ \mathrm{mL}$ injected throughout the first acquisition. All the protocol went through with the mice under general anesthesia. The mice were anesthetized and sedated before surgery. To this end, the mice underwent an intra-peritoneal injection of $200\ \mu\mathrm{L}$ of a mix of ketamine/xylazine diluted in PBS, for a total volume of $1\ \mathrm{mL}$. Sedation was ensured during the acquisition by a continuous gaseous input of air to the mouse nose with 2% isoflurane. As the acquisition time is of 6 minutes, the injection speed of the contrast medium was set to $10\ \mathrm{mL}/\mathrm{h}$.

All operations were realized with respect to the agreements of the experimentation facility. Furthermore, seen through the scope of the preconisations in [Kostomitsopoulos and Djurasevic, 2010]:

- For the specific task under consideration - the construction of a Statistical Shape Model of a mouse, it is mandatory to use mice. The public availability of such an atlas would make possible to capitalize the work done by several teams in the world and would make possible to standardize the evaluations.

- The number of animals has been chosen as a reasonable compromise for performing the chosen task. Ten animals out of the sample were used to establish the protocol. Each of the remaining animals underwent the protocol and the resulting images were carefully studied. Twelve out of them were usable and made possible to build the model. It is important to consider that the Statistical Shape Model could be enriched by complementary acquisitions and segmentations: there would be no need to start again the experiment from scratch.

- The animals were treated by trained personnel, from their housing to the realization of surgery, anesthesia, sedation, image acquisition, and until their euthanasia.

5.6.3 Sample

A bunch of 30 mice of the strain CD-1 was constituted to carry out the protocol. Only 12 were used to build the model – 10 others were used to establish the protocol and the images of the 8 were not exploitable for the manual segmentation. These 12 individuals are designated as the *sample* in the remainder of this document. The sample contains 5 males and 7 females. The ages are distributed between 8 and 38 weeks, with a mean age of 15 weeks and standard deviation of 11 weeks. The mass is distributed between $28\ \mathrm{g}$ and $48\ \mathrm{g}$, with a mean of $37\ \mathrm{g}$ and standard deviation of $6.8\ \mathrm{g}$. Details on the sample are reported in Appendix 5.10.

5.6.4 Contrast medium

Various contrast media have been proposed to enhance the contrast between adjacent tissues in micro-CT images, as presented in Table 5.4. In this work, Iomeron®, an iodine based contrast medium, has been used to enhance the structures of interest. This compound targets the blood pool, that is to say that the whole vascular system is enhanced, and specific enhancement is observed in the liver, and the urinary pool – mainly the kidneys, as well as the bladder.

5.6.5 Automatic segmentation of the high contrast tissues

The high contrast tissues are realized as described in Chapter 4, from the standard acquisitions – that is to say, without contrast medium. The registration of a model is included in the process as represented in Figure 5.1, to establish the point correspondences as explained in Section 5.2.1.

reference	modality	application	context
[Park et al., 2003]	abdominal CT	automatic segmentation	C
[Li et al., 2008]	μCT	longitudinal studies	pC
[Baiker et al., 2010]	μCT	automatic segmentation	pC
[Joshi et al., 2010]	structured light	optical luminescence tomography	pC
[Wang et al., 2012a]	2D X-ray + 2D optical + structured light	n.s.	pC
[Wang et al., 2012c]	2D X-ray + 2D optical	PETbox [Zhang et al., 2011a]	pC
[Wang et al., 2012b]	μCT	automatic segmentation	pC

Table 5.6: List of multi-organ registration methods for small animal, the modality of concern and the application.
- n.s. = not specified
- C = clinical
- pC = preclinical

5.6.6 Semi-automatic segmentation of the kidneys

The kidneys were segmented from the contrast enhanced micro-CT images, as explained in Section 5.5.3. The meshes were subsequently filtered by Laplacian smoothing. Meshes were post-processed using 10 iterations of Laplacian smoothing [Nealen et al., 2006] to obtain a smooth representation of the considered tissue.

5.6.7 Manual delineation of the heart, liver and spleen

Heart, liver and spleen were manually delineated from the contrast enhanced images with the help of interactive methods – thresholding and supervised region growing, using the free software itk-SNAP [itk SNAP, 2005] and a combination of manual and semi-automatic tools. The segmentation was realized with the help of the book [Cook, 1965]. Again, the meshes were post-processed using 10 iterations of Laplacian smoothing [Nealen et al., 2006] to obtain a smooth representation of the considered tissue.

5.7 Construction of the Statistical Atlas

The development of Statistical Shape Models includes standard steps, namely i) identification of the landmarks, ii) point matching and iii) statistical shape analysis. In this work, the aim is to build a Statistical Atlas made of two Statistical Shape Models, which lead to the following steps for the development of the Statistical Shape Models:

1. Acquisition of a set of images of the sample;
2. Segmentation of the organs of interest in the images;
3. Establishment of the point correspondences between the organ model and each of the organ instances;
4. Concatenation of the high contrast tissues on the one hand, of the low contrast tissues on the other hand;
5. Statistical shape analysis of the high contrast tissues on the one hand, and of the low contrast tissues on the other hand;

tissue	vertices	facets
lungs	1491	3000
ribs	1498	3000
spine + pelvis	1368	3000
skin (thorax + abdomen)	6153	12000
total	**10510**	**21000**

Table 5.7: Number of vertices and facets of the surface meshes constituting the statistical shape model of the high contrast tissues.

6. Estimation of the shape parameter vectors of the high contrast tissues on the one hand, and of the low contrast tissues on the other hand;
7. Construction of the Conditional Gaussian Model.

5.7.1 Statistical Shape Model of the High Contrast Tissues

Firstly, the high contrast tissues were automatically segmented using the workflow shown in Chapter 4, including the registration of the skeleton, skin and lungs model as shown in Figure 5.1. Prior to the application of the automatic segmentation workflow, the reconstructions from the two first acquisitions were concatenated to maximize the field of view of the images, to make sure that a major part of the skull and the pelvis were present in the images. Once the model had been registered on the HCT instance, the region comprised between i) the junction of the skull and the first cervical vertebra and ii) the first sacred vertebra was isolated in the skin model. The forelimbs of the skin model which was registered on the skin instance were manually removed from the mesh, in order to remove this variability from the statistical model. The ribcage and the spine were isolated in the skeleton model, with the pelvis kept entirely. The limbs were removed in order to get rid of the variability of their configuration in the statistical model. At that point, point correspondence between the model and each instance had been established.

Once the HCT had been automatically segmented the set of meshes representing the HCT of each instance were concatenated as a single object. Then, Generalized Procrustes Analysis (GPA, [Bookstein, 1989], implemented by the author with the linear algebra C++ programming library Eigen) was applied to the set of instances to remove variability in translation, rotation, size and orientation – when this had been done, the only remaining variability is assumed to be the shape. Finally, the statistical shape analysis was performed on the set of HCT instances. To this end, vectors of observations of the 10510 landmarks describing each instance were re-written under the form of $n = 3 \times 10510$ dimensional vectors L_i, whose each component is one of the cartesian coordinates of a landmark:

$$L_i = (x_1^i, y_1^i, z_1^i, x_2^i, y_2^i, z_2^i, ..., x_n^i, y_n^i, z_n^i) \tag{5.18}$$

As a result, the first eight principal components account for more than 95% of the variance. The cumulated variance ratio is shown in Figure 5.6. The changes in outline of the various high contrast tissues induced by the first three variation modes are illustrated in Figure E.1 of Appendix E.

5.7.2 Statistical Shape Model of the Low Contrast Tissues

Once all the instances had been segmented in the contrast enhanced images, point matching was realized separately for each instance, using the nonrigid registration algorithm based on Gaussian

Figure 5.6: Cumulated variance ratio as a function of the number of considered components for the High Contrast Tissues Statistical Shape Model. The plot shows only the first principal components accounting for more than 95% of the variance.

Mixture Models (GMMREG). Then, the transform determined by GPA for each instance of the HCT, as described in 5.7.1 was applied to the corresponding set of meshes representing the LCT of that individual. This step is mandatory since the aim is to achieve the construction of a conditional model of the LCT, knowing the HCT: the LCT position must be determined by the HCT position in the training set. Finally, the statistical shape analysis was performed on the set of LCT instances. In a similar fashion as for the HCT instances, $m = 3 \times 3060$-dimensional vectors composed by the coordinates of each of the 3061 landmarks:

$$L_i = (x_1^i, y_1^i, z_1^i, x_2^i, y_2^i, z_2^i, ..., x_m^i, y_m^i, z_m^i) \tag{5.19}$$

As a result the first eight principal components account for more than 95% of the variance. The cumulated variance ratio is shown in Figure 5.7. The changes in outlines in the various low contrast tissues induced by the first three variation modes are illustrated in Figure E.2 of Appendix E.

tissue	vertices	facets
heart	583	1162
left kidney	663	1274
right kidney	622	1208
liver	591	976
spleen	602	1200
total	**3061**	**5820**

Table 5.8: Number of vertices and facets of the surface meshes constituting the statistical shape model of the high contrast tissues.

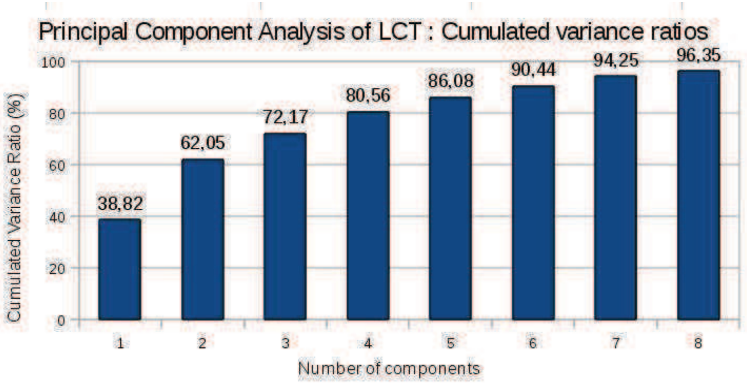

Figure 5.7: Cumulated variance ratio as a function of the number of considered components for the Low Contrast Tissues Statistical Shape Model. The plot shows only the first principal components accounting for more than 95% of the variance.

5.7.3 Conditional Gaussian Model

A Conditional Gaussian Model was used to generate a conditional probability distribution of the LCT, knowing the HCT for an arbitrary instance. To this end, the shape parameters of each instance involved in the construction of each Statistical Shape Model was calculated, according to Equation 5.11 as:

$$b_i = P^T(L_i - \bar{L}) \tag{5.20}$$

Once the shape parameters of each Statistical Shape Model had been calculated, the shape vectors were used to compute the Conditional Gaussian Model according to Equations 5.15, 5.16 and 5.17. For each SSM, the mean shape parameter vectors of the training set made of N individuals was calculated with Equation 5.7. and the covariance matrix of the shape parameters on the training set was calculated with Equation 5.6 and Equation 5.5. Figure E.3 of Appendix E represents the changes in the outline of the low contrast tissues induced by the first three variation modes of the HCT SSM.

5.8 Estimation of the shape of the Low-Contrast Tissues using the Statistical Atlas

The automatic segmentation was carried out using the Statistical Atlas, following the workflow displayed in Figure 5.2. The trunk region is isolated automatically from the skeleton segmentation, by cutting the meshes between the extremal points of the spine along the longitudinal axis. In fact, the registered model is used as the estimate of the high-contrast tissues of the instance. The registered skin, spine, ribs and lungs are concatenated to form a HCT instance.

Two processes have been used to estimate the location and shape of the low-contrast tissues. In the first process, which we designate as *Statistical Shape Model registration*, the registration was initiated by registration of the mean of the HCT SSM to the HCT instance, using GPA and affine ICP. Once this has been done, the parameters were tuned iteratively by:

1. application of GPA and affine ICP to the estimate;
2. application of RPM to match the estimated HCT model and the target.

The number of iterations was fixed.

In the second process, which we designate as *Thin Plate Spline registration*, the Thin Plate Spline transformation (TPS,[Bookstein, 1989], implemented by the author with the C++ linear algebra library Eigen) estimated at the last iteration of the HCT matching is applied to the mean LCT.

5.8.1 Description of the data

The acquisitions of four animals were performed following the same protocol as described in Section 5.6.2, except that the two first acquisitions were replaced by a single acquisition with the animal centered in the field of view. Details on the animals are in Appendix 5.10. The images reconstructed from the whole datasets were segmented manually as described in the Section 5.5.

5.8.2 Quantitative evaluation

The quantitative evaluation was performed using the same metrics as in Section 4.4.2.

5.8.3 Results from micro-CT images

Figure 5.8 represents the median Dice coefficient values, median ratio of the volumes and median distances between organ outlines, for various organs, calculated between the result of the automatic segmentation results and the manual segmentation results from the micro-CT images.

5.8.4 Results from limited angle micro-CT images

Figure 5.9 represents the median Dice coefficient values, median ratio of the volumes and median distances between organ outlines, for various organs, calculated between the result of the automatic segmentation of limited angle micro-CT images and the manual segmentation results of the micro-CT images.

5.8.5 Probability maps of organs

One interesting feature of the statistical atlas is that it allows to generate probability maps of organs location based on a set of randomly generated outlines. A probability map for each organ was generated using the Conditional Model, as proposed in [Wang et al., 2012b]. To this end, a number of 100 shape parameter vectors were randomly generated following the multivariate Gaussian distribution. All the binary images were summed and normalized to generate the map. Formally, considering a set of

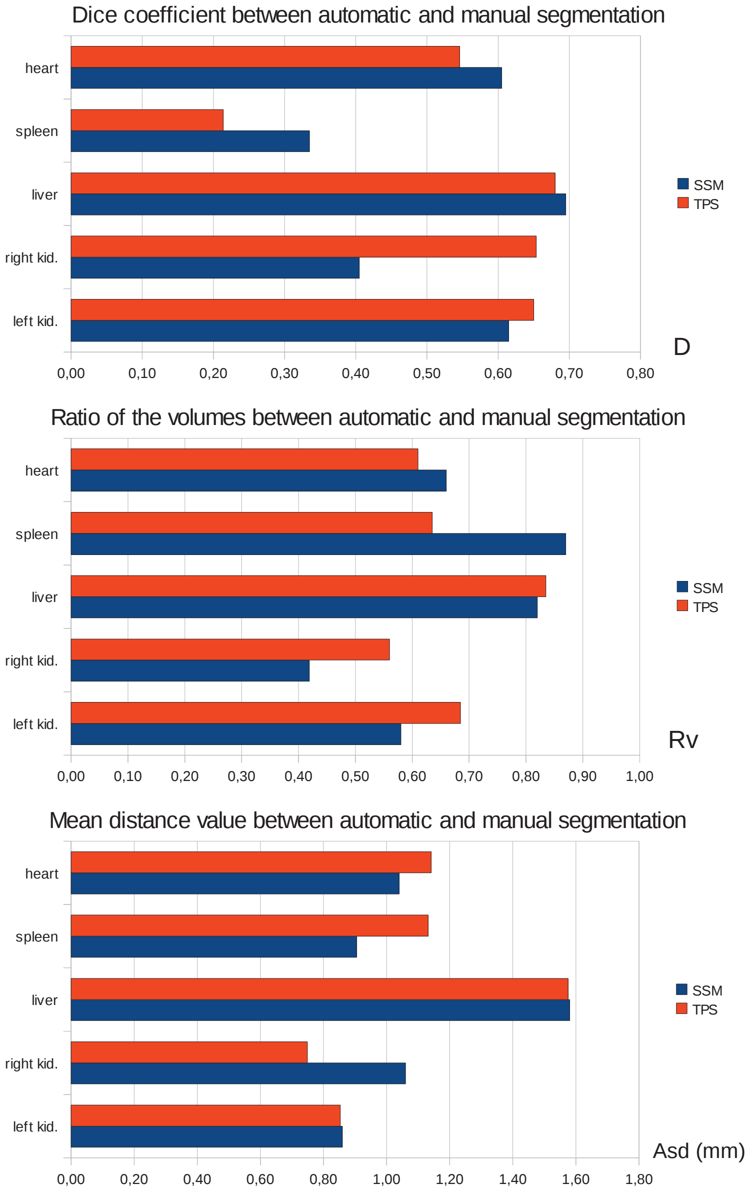

Figure 5.8: Median values of the D, A_{SD} and R_v calculated from the results of the segmentation of the micro-CT image (360° angular range) reconstructed with FDK.

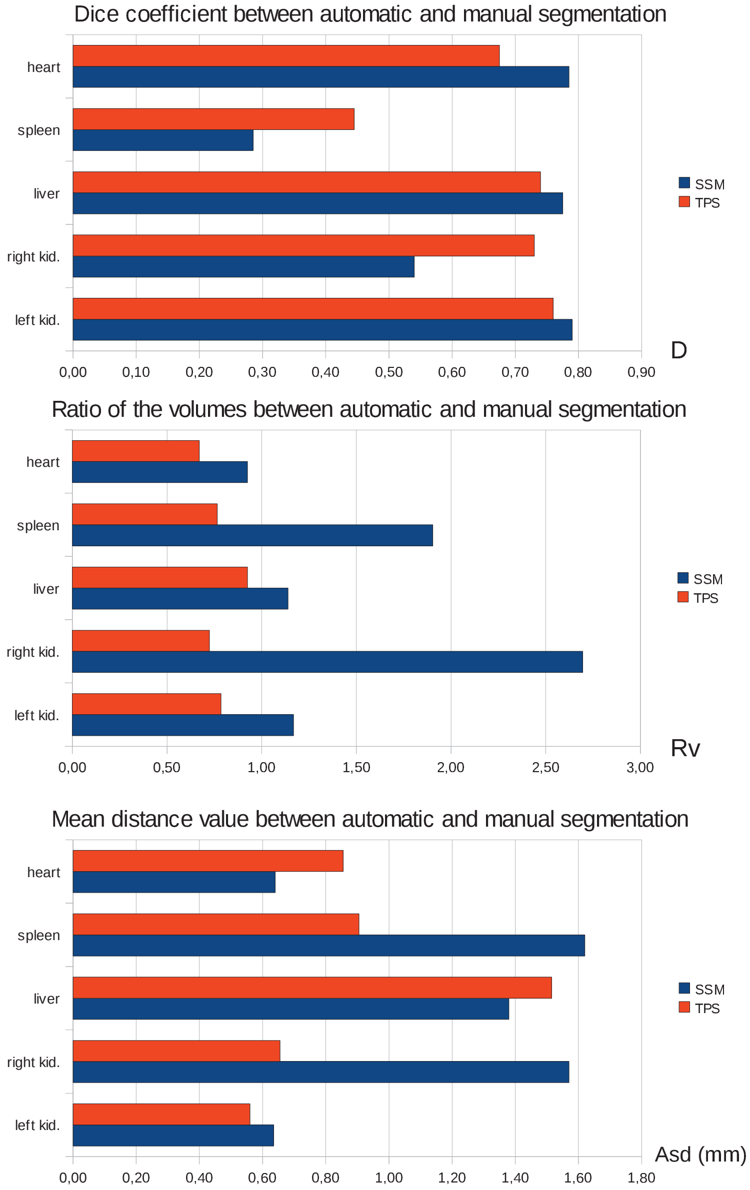

Figure 5.9: Median values of the D, A_{SD} and R_v calculated from the results of the segmentation of the limited angle micro-CT image (90° angular range) reconstructed with ASD-POCS.

N randomly generated shape parameter vectors $B = \{b_1, b_2, ..., b_{100}\}$ and the associated outlines $L = \{L_1, L_2, ..., L_{100}\}$, the probability map is generated on a three-dimensional voxel grid as:

$$p^{\text{map}}_{x,y,z} = \sum_{h=1}^{N} \frac{\Xi(L_h, x, y, z)}{N} \tag{5.21}$$

where (x, y, z) are the coordinates of the voxel in the cartesian reference frame, and Ξ is the function defined as:

$$\Xi(L, x, y, z) = \begin{cases} 1 & \text{if } (x, y, z) \in L \\ 0 & \text{otherwise.} \end{cases} \tag{5.22}$$

In the case of the Thin Plate Spline Registration, the TPS transform was applied to each instance before the generation of the map.

5.8.6 Processing time

The time required to achieve the registration – including the generation of the probability map – has been measured to 20 minutes for the SSM registration and 40 minutes for the TPS registration. In the TPS registration workflow, 20 minutes were necessary to apply the TPS mapping to each of the random instances generated by the CGM. Conversely, in both workflows, the RPM registration is the most time-consuming task, and represents 85% of the initial 20 minutes common to both workflows.

5.9 Discussion

5.9.1 Processing time

The time required to achieve the registration – including the generation of the probability map – has been measured to 20 minutes for the SSM registration and 40 minutes for the TPS registration. In the TPS registration workflow, 20 minutes were necessary to apply the TPS mapping to each of the random instances generated by the CGM. Conversely, in both workflows, the RPM registration is the most time-consuming task, and represents 85% of the initial 20 minutes common to both workflows. This is due to the inversion of large matrices. The required computation time could be greatly reduced by realizing the inversion on GPU as proposed in [Sharma et al., 2013]. Several other operations on the meshes – decimation, cleaning, etc. – were implemented on CPU for development purpose; their transfer on GPU should contribute to reduce the reconstruction time.

5.9.2 Discussion of the results

From the visual observation of the results, it can be observed that overall, the location of the various organs is correct. As for the mean shapes of the low contrast tissues, estimated using the CGM, they present important variations depending on the acquisition setup and the chosen registration approach. Especially, the spleen and right kidney appear to yield poor results. This observation corroborates the conclusions of Wang *et al.* in [Wang et al., 2012b] where they suggested that the poor registration of the spleen was due to its high variability in size, shape, and configuration due to the fact that it is near the stomach, which is flexible and which size varies depending on the quantity of food in it. In [Wang et al., 2012b] the poor results of the left kidney are also explained by the flexibility of the stomach and the variation of its size. It is, however, difficult to conjecture the superiority of one approach on the other for each organ, and if the registration is more accurate in the case of the full scan compared to the limited angle setup solely from the visual evaluation. Observing the results of the quantitative evaluation provides trails for further analyzing the results of the statistical atlas registration.

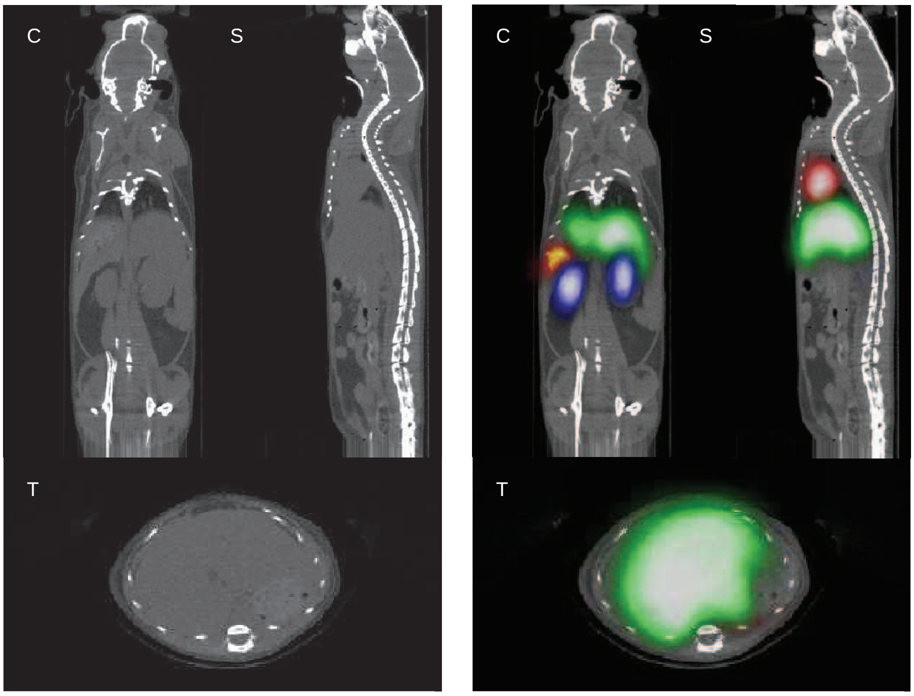

Standard Standard and probability maps

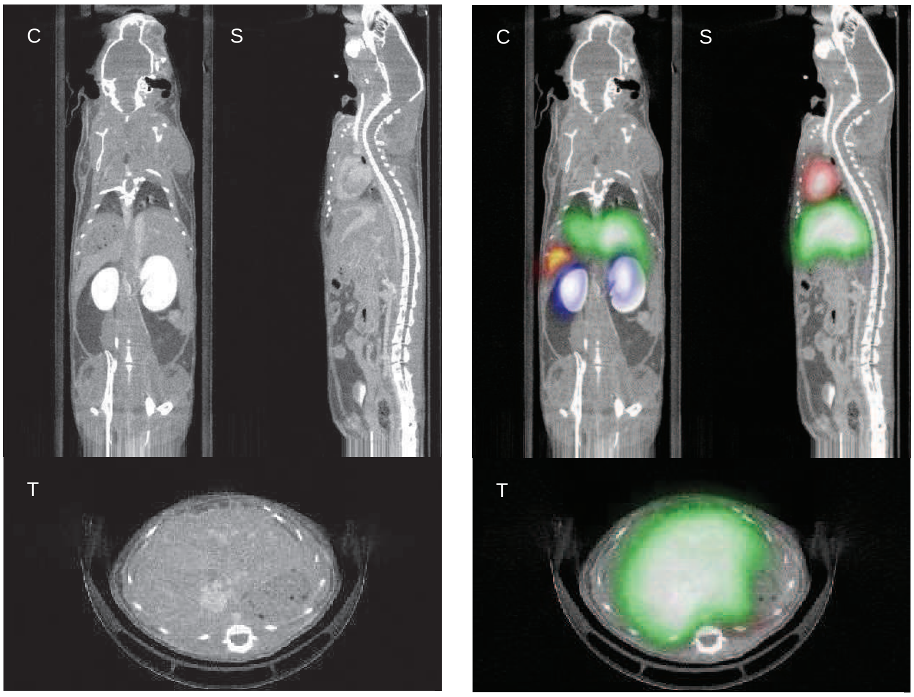

Contrast enhanced Contrast enhanced and probability maps

Figure 5.10: Transverse (T), coronal (C) and sagittal (S) slices through micro-CT images reconstructed from a standard acquisition (top row) and a contrast enhanced acquisition (bottom row). The intensity windows are $[0; 0.1]\ \mathrm{mm}^{-1}$ and $[0; 0.05]\ \mathrm{mm}^{-1}$, respectively. *Standard* means with no contrast medium, whereas *contrast enhanced* means using Iomeron®. The power settings are not the same for both; this is explained in Section 5.6.4. Probability maps of the heart (red), liver (green), kidneys (blue) and spleen (orange) are overlaid on the images of the right column.

From the quantitative evaluation of the whole-body registration, it can be observed that the absolute evaluation of the results would require either the comparison to another registration method, such as these proposed in [Baiker et al., 2010] or [Wang et al., 2012b]. The application to a large number of datasets – more than 50 – and the comparison with their manual segmentation would also contribute to evaluate the robustness of the approach. Nevertheless, in this study such a large number of segmented datasets was not available.

It was decided to split the results for each reconstruction and registration algorithm, with respect to the median value of D, $\mathrm{A_{SD}}$. The organs falling on each side of the median are considered jointly. A D equal or greater to the median means, in this discussion, that the registration is *relatively good* with respect to the overlap, whereas below the median it is *relatively bad*. Similarly, a $\mathrm{A_{SD}}$ equal or smaller to the median means, in this discussion, that the registration is *relatively good* with respect to the distance between meshes, whereas beyond the median it is *relatively bad*. As for $\mathrm{R_v}$, the limit is at 1 which means that the volumes are equal. Thus $\mathrm{R_v} < 1$ means that the volume was underestimated, and $\mathrm{R_v} > 1$ means it was overestimated.

Dice coefficient

Considering the value of the Dice coefficient, it can be observed that in the case of the FDK reconstructions from the full scan, the SSM registration of the heart, liver and left kidney are relatively good, with a median of 0.6. Conversely the SSM registration of the spleen and right kidney are relatively bad. The TPS registration of the liver and kidneys is relatively good with a median of 0.65, whereas the TPS registration of the heart and spleen is relatively bad. The SSM registration outperforms the TPS registration for the heart, spleen and liver, with respect to D. Conversely, the TPS registration outperforms the SSM registration for the kidneys.

In the case of the ASD-POCS reconstructions from the limited angle scan, the SSM registration of the heart, liver and left kidneys are, as well, relatively good, with a median of 0.78. Conversely, the SSM registration of the spleen and right kidney are relatively bad. The TPS registration of the liver and kidneys is relatively good, with a median of 0.73, while for the heart and spleen it is relatively bad. Therefore, the SSM registration outperforms the TPS registration for the heart, spleen and liver with respect to D. Conversely, the TPS registration outperforms the SSM registration for the kidneys.

The fact that the values of D indicate, overall, a better overlap in the case of the limited angle scan was not expected. The remainder of this discussion sketches possible explanations. It should be kept in mind that a poor value of D does not mean in all cases that the organ location is badly estimated – local differences and scaling can contribute to degrade the D value.

Ratio of the volumes

The ratio of the volumes differ substantially from these reported in [Wang et al., 2012b], which were much closer to 1. With respect to the ratio of the volumes, the organs are always underestimated in the registration of the atlas on the micro-CT images, with SSM registration as well as with TPS registration. The median values of the ratio are, respectively 0.66 and 0.64.

In the case of the limited angle setup, the SSM registration overestimates the volumes of the spleen, liver and kidneys. A considerable overestimation of the right kidney and spleen can be observed in this case with respectively 170% and 90% relative differences, to be compared to 16.8%, which is the median of the relative difference in volumes in this cases. Conversely, the TPS registration underestimates the organ volumes similarly as in the case of the full scan, with a median ratio of 0.77.

Averaged distance between the meshes

The values of $\mathrm{A_{SD}}$ are greater than those reported in [Wang et al., 2012b]. It can be observed from the quantitative results that the SSM registration of the heart, spleen and left kidney are relatively good with respect to the $\mathrm{A_{SD}}$ value, with a median of $1.04\ \mathrm{mm}$. Conversely it is relatively bad for the liver and right kidney. In the case of the TPS registration, it is relatively good for the spleen and kidneys, while it is relatively bad for the heart and liver, with a median of $1.13\ \mathrm{mm}$

With the limited angle setup, the SSM registration is relatively good for the heart, liver and left kidney, with a median of $1.38\ \mathrm{mm}$. Conversely it is relatively bad for the spleen and right kidney. In the case of the TPS registration, it is relatively good for the heart, spleen and right kidneys, with a median of $0.86\ \mathrm{mm}$.

Comparison to other works

Table 5.9, Table 5.10 and Table 5.11 summarize the values of D, $\mathrm{A_{SD}}$ and $\mathrm{R_v}$ for various works aiming at segmenting micro-CT images automatically. Despite the comparison with the other approaches is also interesting, the following remarks focus on the comparison to [Wang et al., 2012b], which is the closest to this work. The values reported in [Wang et al., 2012b] are used to define margins to evaluate the performance of the work presented in this thesis. It is to be kept in mind that the comparison is made difficult due to the different applications reported, the variety of segmentation and registration methods involved and the different evaluation protocols. Moreover in the litterature, the results are often displayed in a form which does not allow a precise quantification. Finally, we suggest that the use of the same data for evaluation, and the publication of one reference implementation for the elementary registration algorithm would greatly help comparing a homemade implementation to the available litterature. From the comparison of these values, it can be observed that:

- With respect to the Dice coefficient, the results obtained in this work from the segmentation of limited angle micro-CT images fall in the margins of a relatively good estimation – that is to say, a greater Dice value – compared to the results reported in [Wang et al., 2012b], for the liver – $D = 0.78$ with SSM registration and $D = 0.74$ with TPS registration. It is also the case for the right kidney with, respectively, 0.79 and 0.76 median Dice value for the SSM and TPS registration, as well as for the left kidney with $D = 0.73$ for the TPS registration. Conversely, results appear to be relatively bad for the spleen with both SSM and TPS registration and the left kidney with the TPS registration. The results obtained for the kidneys do not really match those of Wang *et al.*, who found a greater Dice coefficient for the right kidney compared to the left kidney. In their discussion, they explain that by the fact that the right kidney is closer to the liver and more stable than the left kidney, which is subject to the deformations of the stomach. In our work a similar tendency is not observable, and can be explained by the large error in volume of the estimated kidney outlines. The results obtained for the spleen are coherent with these obtained in [Wang et al., 2012b] and can be explained by the high variability of the spleen shape and configuration with respect to the other organs. With respect to the results reported in [Joshi et al., 2010], where the authors have registered an atlas nonrigidly on the topographic range of the mouse surface, our results indicate similar results for the overlap of the heart with a dice of 0.79 to be compared to 0.8, and significantly better results for the kidneys with both SSM and TPS registration.

- With respect to the averaged surface distance, the only result falling in the margins of a relatively good estimation – that is to say, a smaller $\mathrm{A_{sd}}$ value – is $\mathrm{A_{SD}} = 0.56\ \mathrm{mm} \pm 0.37$ for the left kidney with the TPS registration. Other values obtained in this work are overall greater than the mean values reported in [Wang et al., 2012b] associated to large variations especially for the spleen and left kidney.

- With respect to the ratio of the volumes, most of the results reported in the litterature fall in the range $0.8 < \mathrm{R_v} < 1.2$ – except for the spleen, which is subject to considerable errors. In this work, the results of the liver estimation for both SSM and TPS registration fall in this range with values of respectively 1.14 and 0.93, as well as the heart and left kidney with the SSM registration, with values of 0.93 and 1.17, respectively. Conversely, the right kidney and spleen are subject to large differences in volume with respect to their manually segmented counterpart. In the case of the spleen, the observations of [Wang et al., 2012b] are similar.

	Dice coefficient D (without unit)					
method	liver	heart	spleen	left kidney	right kidney	remarks
[Li et al., 2008]	$\varnothing$	> 0.8	$\varnothing$	0.8		mean value
[Joshi et al., 2010]	$\varnothing$	0.64	$\varnothing$	0.11		rigid
[Joshi et al., 2010]	$\varnothing$	0.80	$\varnothing$	0.32		non rigid
[Wang et al., 2012a]	$0.4 \leq D \leq 0.6$	≤ 0.35	≤ 0.35	$0.3 \leq D \leq 0.5$	$0.3 \leq D \leq 0.6$	mean value
[Wang et al., 2012c]	0.56 ± 0.06	0.57 ± 0.18	0.23 ± 0.1	0.53 ± 0.07	0.65 ± 0.11	mean±sd
[Wang et al., 2012b]	$\underline{\geq 0.7}$	$\underline{\geq 0.7}$	$\underline{\leq 0.5}$	$\underline{\geq 0.7}$	$\underline{\geq 0.7}$	mean value
[Baiker et al., 2010]	> 0.6	0.5	$\varnothing$	> 0.8		mean value
360°, SSM	0.7	0.61	0.34	0.41	0.62	median
360°, TPS	0.68	0.55	0.21	0.65	0.65	median
90°, SSM	$0.78^{\star}$	$0.79^{\star}$	0.29	0.54	$0.79^{\star}$	median
90°, TPS	0.74	0.68	$0.45^{\star}$	$0.73^{\star}$	0.76	median

Table 5.9: Dice coefficient: comparison of this work to other whole-body registration methods. The number of individuals used to compute these values is 4 in [Li et al., 2008], one in [Joshi et al., 2010], 23 in [Wang et al., 2012a], 5 in [Wang et al., 2012c] and in [Wang et al., 2012b] it is 44. In this work, four images have been used to compute the values. The results of [Wang et al., 2012b] are underlined. The * indicates the best value obtained for the automatic segmentation of limited angle micro-CT images.

method	Averaged Surface Distance A_{sd} (mm)					remarks
	liver	heart	spleen	left kidney	right kidney	
[Li et al., 2008]	∅	∅	∅	∅	∅	intra., mean
[Li et al., 2008]	∅	∅	∅	∅	∅	inter., mean
[Wang et al., 2012c]	1.1 ± 0.28	1.35 ± 0.2	1.09 ± 0.58	1.12 ± 0.39	1.01 ± 0.29	mean±sd
[Wang et al., 2012b]	$\underline{> 0.4}$	$\underline{> 0.2}$	$\underline{> 0.7}$	$\underline{> 0.6}$	$\underline{> 0.4}$	mean
[Baiker et al., 2010]	∅	∅	∅	∅	∅	mean±sd
360°, SSM	1.58 ± 1.36	1.04 ± 0.54	0.91 ± 0.74	0.86 ± 0.59	1.06 ± 0.65	median±sd
360°, TPS	1.58 ± 1.32	1.13 ± 0.62	1.13 ± 0.8	0.85 ± 0.48	0.75 ± 0.45	median±sd
90°, SSM	$1.38 \pm 1.34^{\star}$	1.38 ± 0.37	1.62 ± 1.52	0.64 ± 0.44	1.57 ± 0.75	median±sd
90°, TPS	1.52 ± 1.33	$0.86 \pm 0.52^{\star}$	$0.91 \pm 0.59^{\star}$	$0.56 \pm 0.37^{\star}$	$0.66 \pm 0.4^{\star}$	median±sd

Table 5.10: Averaged Surface Distance (A_{sd}) : comparison of this work to other whole-body registration methods. The number of individuals used to compute these values is 4 in [Li et al., 2008], one in [Joshi et al., 2010], 23 in [Wang et al., 2012a], 5 in [Wang et al., 2012c] and in [Wang et al., 2012b] it is 44. In this work, four images have been used to compute the values. The results of [Wang et al., 2012b] are underlined. The * indicates the best value obtained for the automatic segmentation of limited angle micro-CT images.

	Volume ratio R_v (without unit)					
method	liver	heart	spleen	left kidney	right kidney	remarks
[Wang et al., 2012c]	1.12 ± 0.16	1.09 ± 0.15	1.05 ± 0.35	1.21 ± 0.15	1.11 ± 0.12	mean±sd
[Wang et al., 2012b]	$\underline{0.8 \leq R_v \leq 1}$	$\underline{1 \leq R_v \leq 1.2}$	$\underline{1.2 \leq R_v \leq 1.4}$	$\underline{1 \leq R_v \leq 1.2}$	$\underline{1 \leq R_v \leq 1.2}$	mean
360°, SSM	0.82	0.66	0.87	0.58	0.42	median
360°, TPS	0.84	0.61	0.64	0.69	0.56	median
90°, SSM	1.14	$0.93^{\star}$	1.90	$1.17^{\star}$	2.7	median
90°, TPS	$0.93^{\star}$	0.67	$0.77^{\star}$	0.78	$0.72^{\star}$	median

Table 5.11: Ratio of the volumes between the automatic segmentation method and a manual segmentation: comparison of this to other whole-body registration methods. The number of individuals used to compute these values is 4 in [Li et al., 2008], one in [Joshi et al., 2010], 23 in [Wang et al., 2012a], 5 in [Wang et al., 2012c] and in [Wang et al., 2012b] it is 44. In this work, four images have been used to compute the values. The results of [Wang et al., 2012b] are underlined. The $\star$ indicates the best value obtained for the automatic segmentation of limited angle micro-CT images.

What to conclude?

Guided by the observation of the estimated outlines overlaid on the micro-CT images, the analysis of the quantitative evaluation allows to draw the following conclusions:

1. the registration of a SSM on limited angle micro-CT images allows to estimate the location of thoracic and abdominal organs;
2. the visual comparison of the outlines and the quantitative evaluation suggest that the high variability of the results is mainly due to the small number of instances that was used to construct the statistical atlas;
3. the availability of the probability maps overlaid on the micro-CT reconstructions provides an interesting complement to the mean outline. Indeed it accounts for the uncertainty on the exact path of the outline, which could not have been determined even manually.
4. supplementary information could be retrieved from the probability map, such as for example the outline of the region where the probability to be in the organ is greater than 90 %.
5. the use of an Active Shape Model search to refine the registration, including constraints related to the intensity in the image [Cootes et al., 1995, Heimann et al., 2007] is a possible extension of this work in the case of the micro-CT reconstructions. This possibility, however, would be more difficult to put in practice in the case of the limited angle micro-CT because of the blur and loss of contrast.

5.9.3 Registration of the Statistical Atlas

The registration of the SSM of HCT was realized using an iterative registration of the model with GPA, affine ICP and RPM, and the estimation of the shape parameters using Formula 5.11. In this work, the HCT meshes were registered altogether on the target. On the contrary, in [Wang et al., 2012b], each tissue was registered separately to the others before the estimation of the shape parameters. This surely affects the result, since registering the tissues altogether adds constraints to the point correspondences.

Moreover, this approach differs from ASM, which has been preconised in several works. It was adopted by simplicity, because the ray tracing step of ASM resulted in aberrations in the estimated shape, due to the low number of vertices and facets of the SSM. A robust implementation of ASM remains obviously to be investigated.

5.9.4 Conditional Gaussian Model

Building and using a conditional Gaussian model in the context of this work relies on the assumption that the shape parameter vectors follow Gaussian probability distributions. This point is debatable. In [Wang et al., 2012b], the authors checked the distributions and determined that it could be reasonably considered as Gaussian. This point remains to be investigated to evaluate the relevance of the model in this work. Yet, it is also to be kept in mind that the number of individuals used in this study is dramatically low. The construction of statistical shape models from such low number of individuals can results in a loss of robustness of the model.

5.9.5 Quantitative Evaluation

Regarding the quantitative evaluation it is notable that it has been carried out on a small number of instances. Moreover, it has not been carried out as a cross-validation study. For example, in [Wang et al., 2012b], a leave-one-out test has been used to evaluate the atlas performance. This can be seen as a weakness of this study. Conversely, the leave-one-out test would have further reduced the number of individuals involved in the construction of the statistical atlas. Validating the approach using a cross-validation study with an atlas constructed from a large number of individuals, remains to be done. The question of the minimum number of individuals needed to represent accurately a population has not been addressed directly in the litterature. Observing that Meinzer et al. suggest that a satisfactory model should represent more than 90° of the variance with 12 principal components or less, and considering that the number of shape vectors should be small compared to the cardinality of the sample, a minimum number of 120 individuals would be needed to represent the shape with a satisfactory statistical model – the number of individuals of the training set would be one order of magnitude greater than the number of shape vectors. This indication can be adjusted by dichotomy if it turns out that the number of components needed is smaller than 12.

As for the measures, the Dice, averaged point to mesh distance and volume ratio provide interesting information. These measures are complementary; each of them considered individually does not provide all the information needed to carry out an adequate quantitative evaluation of the counterpart surfaces – for example, considering the Dice's coefficient only does not allow to quantify the difference in volume between the compared surfaces. Other measures such as the Hausdorff distance could be used as well [Heimann et al., 2006].

5.9.6 Dense landmark generation and point correspondences

A statistical shape model relies on the statistical analysis of a distribution of landmarks accross a sample. In this work, the landmarks are the vertices of the surface meshes generated by tesselation of the delineated regions in a reference subject. Their location in each instance of the training set is estimated by registration of the reference – or model – mesh on it. The Marching Cubes algorithm [Lorensen and Cline, 1987] yields uniform density of landmarks, but this uniformity is lost at the simplification step. The distribution of the landmarks could be optimized subsequently to the simplification, for example as proposed [Heimann et al., 2006].

In this work, two different algorithms were used to registrate non rigidly the reference meshes on the meshes generated from the instances of the training set. The choice to use two different algorithms is debatable, and can be explained by the progressive development of the workflow. For the non rigid registration algorithm using Gaussian mixture models, the publicly available implementation of Jian and Vemuri [Bing and Vemuri, 2011] was used. The processing time of this python implementation for point sets exceeding 500 points is prohibitive. Therefore, it was practically possible to use it for the low contrast tissues, whereas for the high-contrast tissues, a homemade implementation of the RPM algorithm was preferred.

It is to be noted that in both cases, and as it is the case of most registration algorithms, the registration is tuned by various parameters, that can significantly affect the results. In this work, the parameters were chosen arbitrarily. A methodical determination of the optimal parameters would be a key development to ensure the robustness of the approach.

5.9.7 Image segmentation

In this work, the image segmentation of the low contrast tissues has been carried out manually and interactively i) prior to the construction of the statistical atlas and ii) for defining "ground truth" outlines. In terms of manual segmentation, it is notable that the downsampling and filtering of the images degrade the achievable accuracy of the segmentation, though it enables to realize it faster and is likely to yield a smoother description of the objects of interest. As mentioned previously, manual segmentation has several drawbacks including the subjectivity and poor reproducibility.

The adaptation for small animal and implementation of some of the interactive methods, such as these reported in Table 5.3 would surely make possible to standardize the segmentation results and to reduce their subjectivity. In fact it has to be noted that now that a statistical atlas is available, it can be used to initiate the segmentation of tissues, for example using the probability maps of each organ. Its integration in a Statistical Appearance Model workflow would also contribute to provide an accurate initialization to the manual or interactive segmentation of the low contrast tissues.

The development of a specific method for the liver was not sought in this work, but this perspective is a possible improvement of the developed approach. Using the iodine based contrast medium makes it possible to enhance the kidney with respect to the liver, and, to some extent, the liver with respect to the stomach. Moreover, the heart chambers are enhanced, which makes it possible to get a better mental representation of the heart shape than without the contrast medium. Nevertheless, robustly identifying the junction – diaphragm – remains problematic. The junction between liver and intestine also remains problematic. It should be kept in mind that no respiratory or cardiac gating was used to carry out the acquisitions, and that such a gating could improve the image quality, especially in the regions that are subject to the alternate motion caused by the animal breathing motion. In our approach, the raw contrast enhanced image was directly used to perform the segmentation. More elaborate approaches using a weighted difference of the contrast enhanced and non-contrast enhanced images could reveal some useful information. The surface mesh representing the liver in the SSM has a low number of vertices compared to the kidneys, spleen and heart – with respect to their respective sizes. As the liver has a complex shape, it would be preferable to use a greater number of vertices, wich would allow to represent more faithfully the liver outline.

As for the spleen, similar difficulties were encountered. It was mainly difficult to distinguish it from the liver, and to distinguish its other end. However, the enhancement of the left kidney provided a fair contrast in that region so it helped indirectly to carry out the spleen segmentation.

As mentioned, kidneys are rather easy to distinguish from the surrounding tissues in contrast-enhanced images, because they are part of the urinary system, which constitutes the main elimination path of the contrast medium. Therefore, the segmentation by thresholding and region growing yielded overall acceptable results. Nevertheless, in some cases, the segmentation had to be corrected manually, especially when the ureter filled with some of the contrast medium was identified as the kidneys. Also, in some cases, ischemia of the kidney locally prevented the blood circulation and caused variable enhancement of the contrast in a single kidney. Finally, depending on the time course of the contrast medium in the blood, the renal pelvis appeared much brighter in the images than the medulla and cortex. In these cases, it has been necessary to adjust the predefined thresholds.

The delineation of the heart from the surrounding lungs was rather easy. It was more difficult to delineate the bottom of the heart wall from the top of the liver, due to the motions in this area and the relatively low contrast between them.

As mentioned in Section 5.6.6 and Section 5.6.6, the meshes were post-processed by Laplacian filtering. The aim was to obtain a smooth representation of the surface. The drawback of Laplacian smoothing is that, despite it preserves the outline appearance, it shrinks the meshes – that is to say that the volume is decreased and therefore the outline is affected. This surely affects the results of the registration workflow, introducing a systematic error in the evaluation of the organ outlines.

The segmentation of the adipose tissues and its inclusion in the statistical model would constitute an promising extension to this work, since adipose can be distinguished in micro-CT images with low-level methods [Habold et al., 2010] and its distribution can be related to the organs considered in this work. To our knowledge, such an approach has not yet been reported.

5.9.8 Acquisition protocol

The acquisitions were realized using a contrast medium, Iomeron®. It is legitimate to wonder i) if Iomeron® is the best choice for enhancing the contrast of the targeted tissues and ii) if the acquisition parameters – power settings and integration time – were optimal for enhancing the contrast between the tissus. With respect to the choice of the contrast medium, the answer is not trivial, since contrast media are characterized by the tissue they target, the speed of transfer to this tissue, the speed of elimination by the organism, and the attenuation coefficient. Thus for example to enhance the heart chambers, it is better to perform the acquisition while the contrast medium is injected in the blood pool, that is to say before it has been transfered to the tissues. As it takes time for Iomeron® to enhance the liver and spleen sufficiently for segmentation, it is also good to perform an acquisition after the injection is complete. By that time, an important fraction of the injected medium has already arrived to the urinary system, and has possibly already passed the kidneys to accumulate in the bladder. The fact that the animal has to remain anesthetized and stay in place throughout the protocol, since the aim is to delineate the tissues and to statistically describe their configuration in place, brings more complexity to the protocol.

From the state of the art presented in Table 5.4, it is notable that some contrast media have long lifetime in the tissues, at the expense of an increased toxicity. The combination of a contrast medium such as Exitron, to another such as Iomeron®, would possibly enable improved contrast of individual tissues. Conversely, this would also make it more difficult to distinguish tissues that were easily distinguishable with Iomeron®, such as the kidneys.

It is also noticeable that the contrast enhancement allowed by Iomeron® appeared to be variable as the protocol was carried out. This encourages to pay attention to the degradation of the compound with time and storage conditions. Regarding the fact that the acquisitions were not gated, of course from the point of the distinguishability of the structures in the micro-CT images and thus the accuracy of the delineations, it would be preferable to apply a gating on the respiratory motion as well as on the heart beat. Indeed, the reconstructed images are characterized by a blur at the frontier between the lungs and the liver, thus their delineation is more difficult and potentially not realistic from the anatomical point of view. Conversely, i) performing gated acquisition would increase drastically the acquisition time – multiplied by 4 with respiratory gating – and ii) it has to be seen through the scope of the precedent remarks. Indeed, for a long-lived contrast medium in the organism – of the order of the day, there is no obstacle to performing a gated acqusition since it remains in the organism with a lifetime considerably greater than the acquisition duration. In some – rare – cases, artifacts caused by other movements have been observed, such as the limbs – probably due to the end of anesthesia – or even the entire abdomen, which can be caused by the change in volume of the bladder due to the accumulation of urin in it, as well as the gastro-intestinal track while it degrades the food. Another reason for the deformation of the abdomen during the protocol is the quantity of liquid injected intravenously – $1\ \mathrm{mL}$, to be compared to the blood volume of mice, which is about $2\ \mathrm{mL}$. The effect of the injection of this volume is the increase in size of the blood vessels – in the abdominal region, the aorta, which runs along the spine, is dilated and can push surrounding tissues – as well as the kidneys and mostly the bladder, which fill throughout the protocol, and mostly during and after the injection. Finally, as the mouse holder is not heated, the mouse is likely to chill during the injection, which could make the whole body and holder shake.

With respect to the sample, it can be observed from Appendix H, that the individuals included in the training set include male and female, with various ages and mass. On the contrary, the bunch used for validation is composed only of female individuals with similar wheight and age – but with differences between eleven weeks more and twenty weeks less than the individuals of the training set. This variability surely affects the result, due to the morphological and physiological differences between animals of different sex, age and wheight. The development of a specific atlas from groups of individuals with shared characteristics such as a common certain age, sex and weight is likely to yield a better performance.

5.9.9 Estimation of the local optical coefficient

The results provide two ways of estimating the local optical coefficients. First, they can be attributed inside the deterministic outline constituted by the mean shape of the organ, using the same model as in Chapter 2. Second, the effective coefficient μ^λ of any interaction at wavelength λ can be estimated at each point (x, y, z) of space using the probability maps $P_j(x, y, z)$ generated with the statistical atlas and the attenuation coefficient μ_j^λ at wavelength λ of each of the M tissue of index j. Formally:

$$\mu_{x,y,z}^\lambda = \begin{cases} \alpha \sum_{j=0}^{M} P_j(x,y,z) \times \mu_j^\lambda + (1-\beta)\mu_{H_2O}^\lambda & \text{if } (x,y,z) \text{ belongs to the body,} \\ 0 & \text{otherwise.} \end{cases} \tag{5.23}$$

with:

$$\alpha = \begin{cases} \frac{1}{\sum_{j=0}^{M} P_j(x,y,z)} & \text{if } \sum_{j=0}^{M} P_j(x,y,z) > 1 \\ 1 & \text{otherwise.} \end{cases} \tag{5.24}$$

and:

$$\beta = \begin{cases} \sum_{j=0}^{M} P_j(x,y,z) & \text{if } 0 \leq \sum_{j=0}^{M} P_j(x,y,z) < 1 \\ 1 & \text{otherwise.} \end{cases} \tag{5.25}$$

The interaction coefficient of the water at wavelength λ is denoted $\mu_{H_2O}^\lambda$. Every optical coefficients can be estimated as well using the same semi-empirical model as cited in Chapter 2. This second approach has the advantage of relaxing the constraint of fully homogeneous regions and accounts for the uncertainty on the organ boundaries. The obvious drawback of the proposed model approach is that it does not allow to model the effects of the boundaries on photon transport. An alternative is to estimate the organ region within a certain probability interval; the overlap of various tissues could be treated by a heuristic method, which would attribute a region to one or another tissue depending on the probability compared to the other tissues, and its configuration with respect to the tissue identified within a certain probability interval. The impact of the choice of one of these models should be assessed quantitatively with a known test object.

5.10 Chapter Summary

The content of this chapter can be summarized as follows:

- The Statistical Shape Model (SSM) has been introduced in biomedical imaging for various applications including automatic segmentation of images. Several SSMs can be associated to constitute a statistical atlas of more than one organ and encapsulate the conditional variation of a group of organs with respect to another.
- In this work, a statistical atlas of the mouse tissues has been constructed, made of one SSM for the high contrast tissues (HCT) – skeleton, skin and lungs – and one SSM for the low contrast tissues (LCT) – heart, liver, spleen, kidneys.
- An acquisition protocol was designed to realize standard and contrast enhanced acquisitions of the same animal; twelve of the resulting micro-CT reconstructions were segmented i) automatically for the high contrast tissues – skeleton, skin and lungs, ii) semi-automatically for the kidneys and iii) manually for the heart, liver and spleen.
- The statistical models were constructed by statistical shape analysis of the outlines of each organ – concatenated together to form two sets of meshes, the high contrast tissues – skeleton, skin and lungs, and the low contrast tissues – heart, liver, spleen and kidneys. Point correspondence was established using non rigid registration algorithms.
- The statistical atlas was registered on the outlines of high contrast tissues segmented from micro-CT images as well as from limited angle micro-CT images by iterative estimation of the shape parameters. It allowed to estimate the locations and outlines of the heart, the liver, the spleen and the kidneys, from the configuration of the outlines of skeleton, skin and lungs.
- The results were evaluated qualitatively and quantitatively and compared to existing works. It appears clearly that the number of individuals used to build the atlas is small and that increasing this number would certainly improve the results. Other improvements in the protocol defined to build the atlas would surely increase the robustness of the approach. The results allow to locate this work in a good position with respect to other whole-body segmentation approaches, even in presence of morphological differences between the HCT resulting from the limited angle acquisition.
- It cannot be decided whether the mean outlines determined by the whole-body segmentation workflow are better or worse when the atlas is registered on the micro-CT images or on the limited angle micro-CT images.
- Probability maps of the organ locations can be generated using the statistical atlas. A method has been proposed to estimate the local optical coefficients of the mouse tissues based on them and a semi-empirical model of the optical coefficients in biological tissues.

Conclusion

Realized at IPHC jointly with the company Biospace Lab, in the framework of the CIFRE 2011/1616, this work addresses the derivation of an anatomical prior for luminescence tomography. This approach, indeed, has been reported in the litterature to reduce drastically the errors in localization and quantification of the luminescent sources. More specifically, the aim was to integrate a X-ray tomographic modality in the PhotonIMAGER$^{\mathrm{TM}}$ Optima, an *in vivo* luminescence imaging device commercialized by Biospace Lab, and to extract an anatomical information from the tomographic reconstructions. Upstream conception choices consisted in the incorporation of the X-ray tomographic modality without modification of the existing device. This lead to the reduction of the angular range of the X-ray imaging system to 90°, to prevent this new modality from interfering with existing components of the device.

Several obstacles had to be overcome in order to make the idea concrete. Firstly, it was mandatory to answer the question: "can a faithful estimation of the X-ray attenuation coefficient be estimated from measurements acquired over such a limited angular range?". The use of a regularized algebraic reconstruction algorithm made it possible to bring a positive answer to this question. The answer to the corollary question: "how faithful is the estimation?" was not as unequivocal, since the images are characterized by directional blurring artifacts and local errors are made in the estimation – causing local loss of the contrast and resolution. But still, overall the image carries morphological information about the mouse tissues. This was certainly encouraging, but an open question remained: how to exploit this information?

The aim being to provide a prior for luminescence tomography, the whole development presented in this thesis has to be seen through the scope of a practical use in routine. Exploiting this information in a fully supervised manner – manually or semi-automatically – is mostly impractical due to the size of the datasets and the degraded nature of the images. Moreover, images obtained from a standard acquisition would, at best provide information about the skeleton, skin and lungs, which are typically characterized by a high contrast in the micro-CT images with respect to the tissues surrounding them. These considerations have lead to focus on realizing the segmentation fully automatically. Recent works have proposed to derive information about other tissues, characterized by a low contrast, using the outline of these high-contrast tissues. More precisely, these approaches use a model which is registered on the outline of the high contrast tissues. Aiming at estimating the low contrast tissues in a similar fashion, the second question, arising from the observation of the results, was therefore: "can an anatomical information be extracted from such an image using mostly low level methods"? The answer is yes; in images reconstructed from the limited angle acquisition, the contrast is locally lower, but overall, it remains sufficient to extract a valuable anatomical information. It was straightforward to segment the skin and skeleton with low level methods, despite distorsions and missing regions due to the missing information and blurring effect of the TV minimization. The segmentation of the lungs was a bit more tricky – again due to the missing information and to the blurring effect of TV minimization which cause the lung region to be linked to the background as their attenuation coefficients are of the same order of magnitude – but using the anatomical information provided by the skeleton, it turned out that the lung region can be estimated as well. When it comes to estimating the accuracy of the outline estimation, measures of mesh similarity indicate a fair estimation of the outline despite locally missing regions and outliers unveiled by visual inspection.

The problem gets a supplementary dimension and another question arises at this step: "can the outlines of tissues that cannot be typically distinguished even in micro-CT images be estimated, using the outlines of the high contrast tissues?". Interestingly, the segmented high contrast tissues turn out to constitute registration features robust enough to consider registering an anatomical model on them. The registration of a statistical atlas is able to provide an estimation of the outlines of low contrast tissues based on the outlines of the high contrast tissues. To the question "how accurately?", the answer is again, not unequivocal. Indeed, in terms of estimation of the mean outline of the tissue, the results suggest that a wide room for improvement remains. Conversely the probability maps of the location of each tissues, generated with the statistical atlas, provide a fuzzy representation of the tissues. These probability maps open the path to a straightforward estimation of the optical coefficients which distribution is heterogeneous in the mouse tissues. It is noteworthy that improving the estimation of the mean outline would consequently improve the accuracy of the probability maps.

At the endpoint of this thesis, the aim of deriving an anatomical prior from limited angle micro-CT images has been reached, and the lessons learnt have allowed to determine key improvements that would contribute to achieve a more accurate estimation of the organ outlines. The effective use of the extracted information to constrain luminescence tomographic reconstruction remains to be done; embedding the proposed approach in a multispectral reconstruction framework also constitutes a promising extension to this work.

Appendix A : ASD-POCS algorithm workflow on CPU and GPU

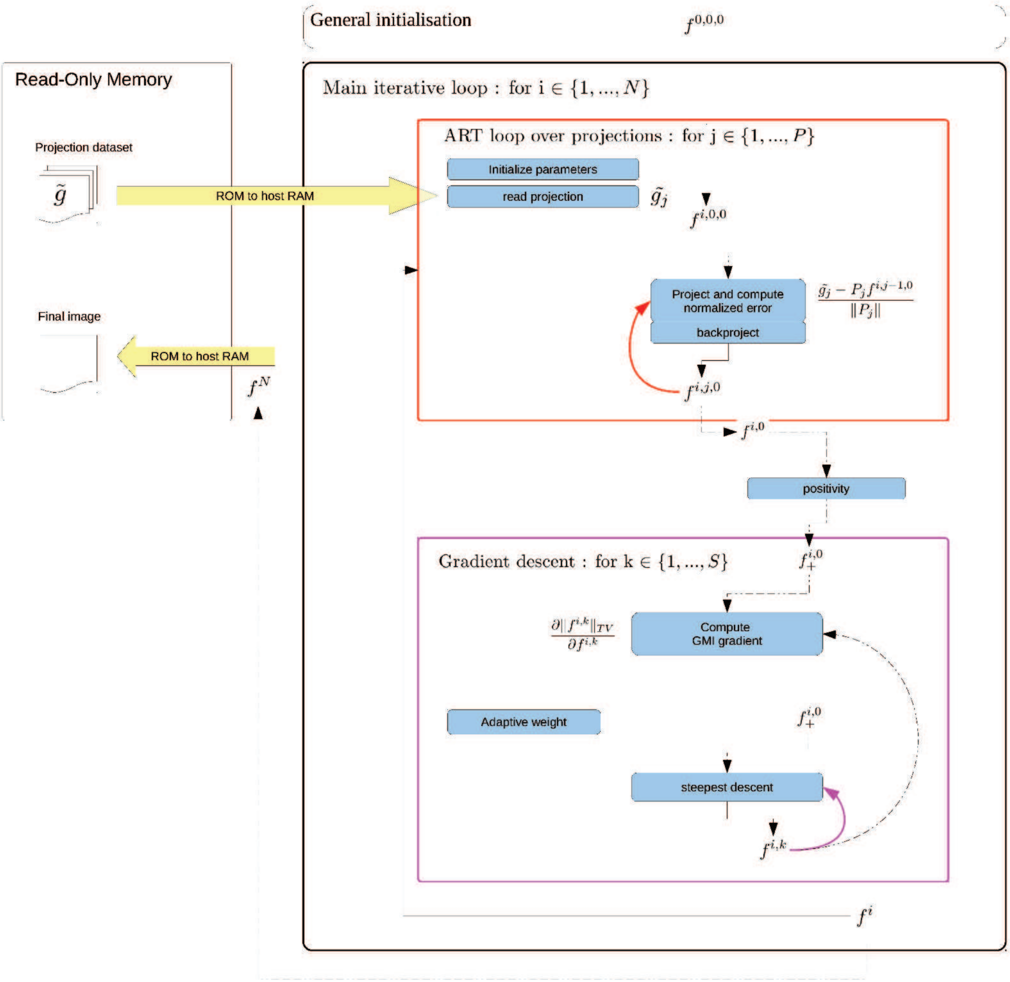

Figure A.1: Representation of the workflow of the ASD-POCS algorithm on CPU.

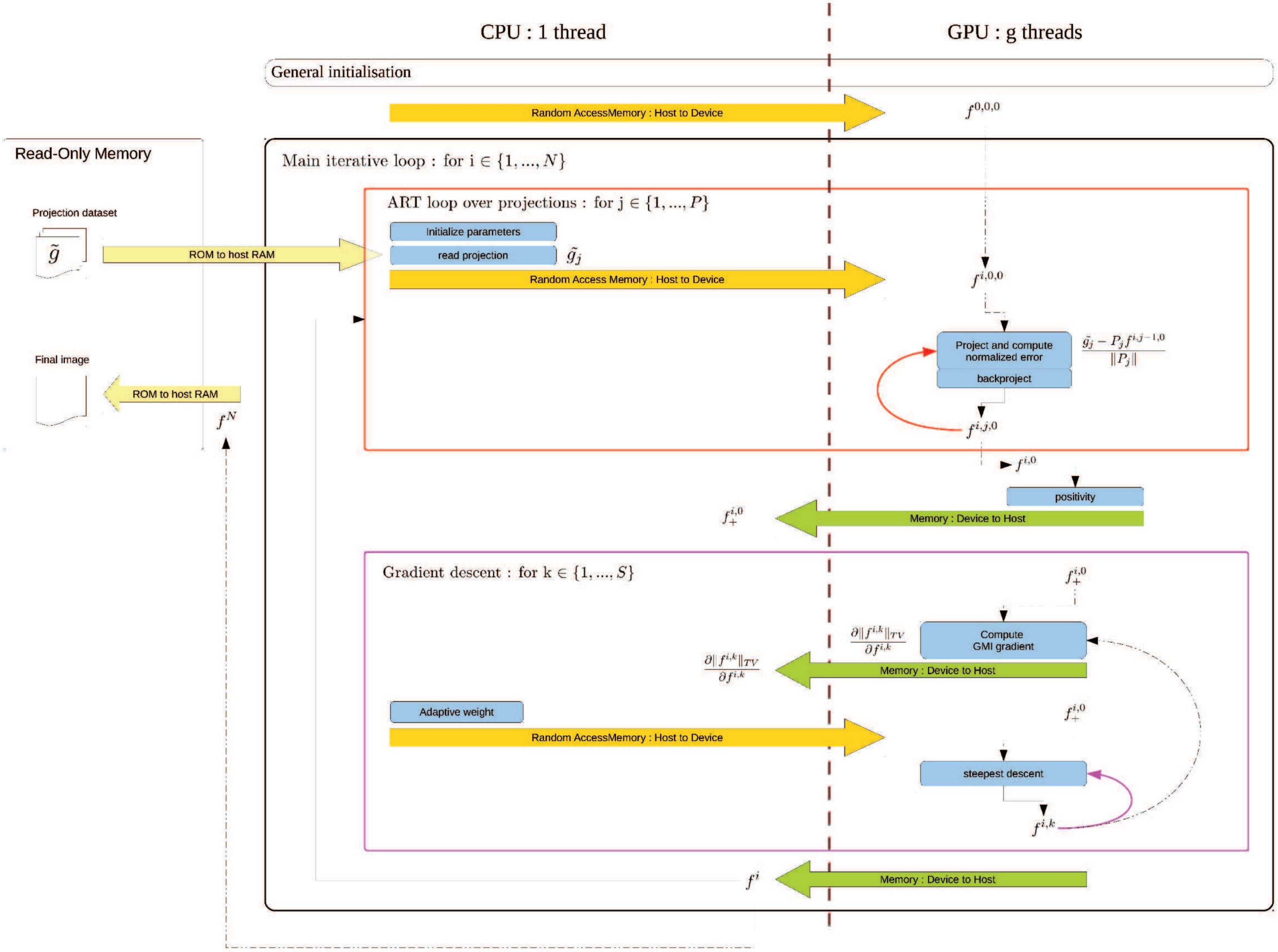

Figure A.2: Representation of the workflow of the ASD-POCS algorithm on GPU including memory transfers.

Appendix B : Description of the custom head phantom

Ellipsoids of the main structures

	center			axes					
id	x	y	z	x	y	z	ϕ	θ	value
1	0	0	0	19.2	24	25	0	0	0.18
2	0	0	0	18	22.8	23.8	0	0	-0.075
3	0	-7.2	0	3.6	7.2	7.2	0	0	-0.0005
4	0	16.8	0	3.6	7.2	7.2	0	0	-0.105
5	-9.4	8.6	1.744	4	4	4	0	0	0.001
6	9.4	8.6	1.744	4	4	4	0	0	0.001
7	-2.16	-18	0	0.8	0.8	0.8	0	0	0.00025
8	2.16	-18	0	0.8	0.8	0.8	0	0	-0.00025
9	-3.8	10.8	0	6	0.8	2.32	-82.6	-60.85	0.075
10	3.8	10.8	0	6	0.8	2.32	-82.6	60.85	0.075
11	12.78	-12.78	0	2.4	0.84	2.4	0	58.12	0.0005

Table B.1: Description of the ellipsoids involved in the main structure of the phantom.

Elliptical cylinders of the main structures

	half-axis			center						
id	x	y	length	x	y	z	ϕ	θ	b.o.	value
1	2.4	8	0.9658	0	7.2	0	-60	90	90	0.075
2	1.051	4	0.8	0	19.2	0	90	0	-60	0.18
3	3.6	0.48	8	-8.6	13.6	-2	0	0	150	0.075
4	3.6	0.48	8	8.6	13.6	-2	0	0	30	0.075

Table B.2: Description of the elliptical cylinders involved in the main structure of the phantom.

Inserts (ellipsoids) of 800 μm

	center			axes					
id	x	y	z	x	y	z	ϕ	θ	value
800 μm / contrast 1.8									
1	-14	-6	0	0.4	0.4	0.4	0	0	0.075
2	-12.4	-6	0	0.4	0.4	0.4	0	0	0.075
3	-10.8	-6	0	0.4	0.4	0.4	0	0	0.075
4	-9.2	-6	0	0.4	0.4	0.4	0	0	0.075
5	-7.6	-6	0	0.4	0.4	0.4	0	0	0.075
800 μm / contrast 1.4									
6	-14	-4.4	0	0.4	0.4	0.4	0	0	0.035
7	-12.4	-4.4	0	0.4	0.4	0.4	0	0	0.035
8	-10.8	-4.4	0	0.4	0.4	0.4	0	0	0.035
9	-9.2	-4.4	0	0.4	0.4	0.4	0	0	0.035
10	-7.6	-4.4	0	0.4	0.4	0.4	0	0	0.035
800 μm / contrast 1.2									
11	-14	-2.8	0	0.4	0.4	0.4	0	0	0.015
12	-12.4	-2.8	0	0.4	0.4	0.4	0	0	0.015
13	-10.8	-2.8	0	0.4	0.4	0.4	0	0	0.015
14	-9.2	-2.8	0	0.4	0.4	0.4	0	0	0.015
15	-7.6	-2.8	0	0.4	0.4	0.4	0	0	0.015
800 μm / contrast 1.06									
16	-14	-1.2	0	0.4	0.4	0.4	0	0	0.001
17	-12.4	-1.2	0	0.4	0.4	0.4	0	0	0.001
18	-10.8	-1.2	0	0.4	0.4	0.4	0	0	0.001
19	-9.2	-1.2	0	0.4	0.4	0.4	0	0	0.001
20	-7.6	-1.2	0	0.4	0.4	0.4	0	0	0.001

Table B.3: Description of the spherical (ellipsoids) inserts of diameter $800\mu m$.

Inserts (ellipsoids) of 400 μm

	center			axes					
id	x	y	z	x	y	z	ϕ	θ	value
400 μm / contrast 1.8									
1	-14	-0.2	0	0.2	0.2	0.2	0	0	0.075
2	-13.2	-0.2	0	0.2	0.2	0.2	0	0	0.075
3	-12.4	-0.2	0	0.2	0.2	0.2	0	0	0.075
4	-11.6	-0.2	0	0.2	0.2	0.2	0	0	0.075
5	-10.8	-0.2	0	0.2	0.2	0.2	0	0	0.075
400 μm / contrast 1.4									
6	-14	0.6	0	0.2	0.2	0.2	0	0	0.035
7	-13.2	0.6	0	0.2	0.2	0.2	0	0	0.035
8	-12.4	0.6	0	0.2	0.2	0.2	0	0	0.035
9	-11.6	0.6	0	0.2	0.2	0.2	0	0	0.035
10	-10.8	0.6	0	0.2	0.2	0.2	0	0	0.035
400 μm / contrast 1.2									
11	-14	1.4	0	0.2	0.2	0.2	0	0	0.015
12	-13.2	1.4	0	0.2	0.2	0.2	0	0	0.015
13	-12.4	1.4	0	0.2	0.2	0.2	0	0	0.015
14	-11.6	1.4	0	0.2	0.2	0.2	0	0	0.015
15	-10.8	1.4	0	0.2	0.2	0.2	0	0	0.015
400 μm / contrast 1.06									
16	-14	2.2	0	0.2	0.2	0.2	0	0	0.001
17	-13.2	2.2	0	0.2	0.2	0.2	0	0	0.001
18	-12.4	2.2	0	0.2	0.2	0.2	0	0	0.001
19	-11.6	2.2	0	0.2	0.2	0.2	0	0	0.001
20	-10.8	2.2	0	0.2	0.2	0.2	0	0	0.001

Table B.4: Description of the spherical (ellipsoids) inserts of diameter $400\mu m$.

Inserts (ellipsoids) of 200 μm

	center			axes					
id	x	y	z	x	y	z	ϕ	θ	value
200 μm / contrast 1.8									
1	-14	2.7	0	0.1	0.1	0.1	0	0	0.075
2	-13.6	2.7	0	0.1	0.1	0.1	0	0	0.075
3	-13.2	2.7	0	0.1	0.1	0.1	0	0	0.075
4	-12.8	2.7	0	0.1	0.1	0.1	0	0	0.075
5	-12.4	2.7	0	0.1	0.1	0.1	0	0	0.075
200 μm / contrast 1.4									
6	-14	3.1	0	0.1	0.1	0.1	0	0	0.035
7	-13.6	3.1	0	0.1	0.1	0.1	0	0	0.035
8	-13.2	3.1	0	0.1	0.1	0.1	0	0	0.035
9	-12.8	3.1	0	0.1	0.1	0.1	0	0	0.035
10	-12.4	3.1	0	0.1	0.1	0.1	0	0	0.035
200 μm / contrast 1.2									
11	-14	**3.5***	0	0.1	0.1	0.1	0	0	0.015
12	-13.6	3.5	0	0.1	0.1	0.1	0	0	0.015
13	-13.2	3.5	0	0.1	0.1	0.1	0	0	0.015
14	-12.8	3.5	0	0.1	0.1	0.1	0	0	0.015
15	-12.4	3.5	0	0.1	0.1	0.1	0	0	0.015
200 μm / contrast 1.06									
16	-14	**3.9***	0	0.1	0.1	0.1	0	0	0.001
17	-13.6	3.9	0	0.1	0.1	0.1	0	0	0.001
18	-13.2	3.9	0	0.1	0.1	0.1	0	0	0.001
19	-12.8	3.9	0	0.1	0.1	0.1	0	0	0.001
20	-12.4	3.9	0	0.1	0.1	0.1	0	0	0.001

Table B.5: Description of the spherical (ellipsoids) inserts of diameter $200\mu m$. The values denoted with a * exposant are the correct values, while the values used in the study are 2.5 and 2.9, respectively, for the contrasts 1.2 and 1.06.

Inserts (ellipsoids) of 100 μm

	center			axes					
id	x	y	z	x	y	z	ϕ	θ	value
100 μm / contrast 1.8									
1	-14	4.15	0	0.05	0.05	0.05	0	0	0.075
2	-13.8	4.15	0	0.05	0.05	0.05	0	0	0.075
3	-13.6	4.15	0	0.05	0.05	0.05	0	0	0.075
4	-13.4	4.15	0	0.05	0.05	0.05	0	0	0.075
5	-13.2	4.15	0	0.05	0.05	0.05	0	0	0.075
100 μm / contrast 1.4									
1	-14	4.35	0	0.05	0.05	0.05	0	0	0.035
2	-13.8	4.35	0	0.05	0.05	0.05	0	0	0.035
3	-13.6	4.35	0	0.05	0.05	0.05	0	0	0.035
4	-13.4	4.35	0	0.05	0.05	0.05	0	0	0.035
5	-13.2	4.35	0	0.05	0.05	0.05	0	0	0.035
100 μm / contrast 1.2									
1	-14	4.55	0	0.05	0.05	0.05	0	0	0.015
2	-13.8	4.55	0	0.05	0.05	0.05	0	0	0.015
3	-13.6	4.55	0	0.05	0.05	0.05	0	0	0.015
4	-13.4	4.55	0	0.05	0.05	0.05	0	0	0.015
5	-13.2	4.55	0	0.05	0.05	0.05	0	0	0.015
100 μm / contrast 1.06									
1	-14	4.75	0	0.05	0.05	0.05	0	0	0.001
2	-13.8	4.75	0	0.05	0.05	0.05	0	0	0.001
3	-13.6	4.75	0	0.05	0.05	0.05	0	0	0.001
4	-13.4	4.75	0	0.05	0.05	0.05	0	0	0.001
5	-13.2	4.75	0	0.05	0.05	0.05	0	0	0.001

Table B.6: Description of the spherical (ellipsoids) inserts of diameter $100\mu m$.

Appendix C: Segmentation of the high contrast tissues from micro-CT images

Figure C.1 represents the surface meshes of the skeletons, segmented from 12 micro-CT images. Some of the skeletons are truncated, but this is not due to the algorithm, but to the fact that their size exceeded the field of view. Over the set of segmented skeletons, it can be observed that all the skeletons are complete and that they do not contain outliers, except in two cases near the claviculae. The outlier in these cases is the end of a catheter inserted in the jugular vein, which was filled with a small quantity of contrast medium. It has been assimilated to bone because of the value of its lineic attenuation coefficient, and it has been considered as a part of the skeleton because it was connected to it because no region under the threshold completely separated it from the skeleton.

Figure C.2 represents the surface meshes of each skeleton segmented in subparts. Each color is associated to a given subpart. At this scale, no major error in the assignment of the labels can be detected.

Figure C.3 displays the summary of the scores of the qualitative evaluation of the skeletons in subparts. The observation of these histograms allows to consider that the method generally succeeds at identifying the limbs, and especially the forelimbs. It also identifies rather successfully the skull on the one hand, and the spine, pelvis and ribs as a whole on the other hand. Conversely, according to the evaluation, the assignment of the labels to i) the ribcage and to ii) the spine and pelvis as a whole is subject to errors.

Figure D.3 represents the surface meshes of the skin segmented from the micro-CT images. It can be observed that the outline is mostly well defined. The air bubbles lying in the gastro-intestinal track are visible because the meshes displayed have not been filtered. Some outliers can be observed, either due to the catheters inserted in the jugular veins or to the holder. In nine of the twelve images, the gaseous anesthesia hose is visible and encloses the mouse muzzle.

Figure D.4 represents the surface meshes of the lungs segmented from the micro-CT images. It can be observed that the lungs outline is mostly well defined. All the instances exhibit local outliers.

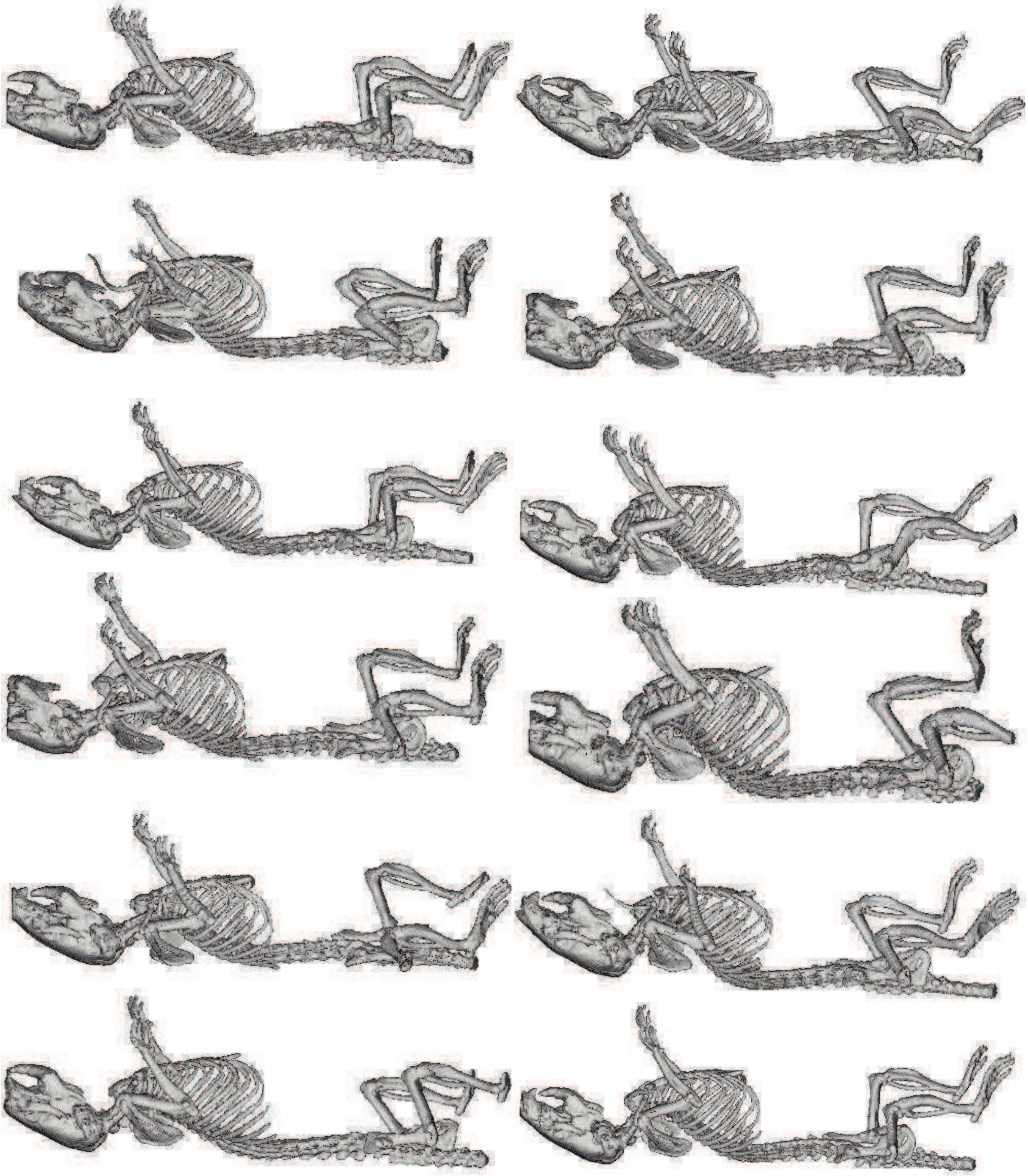

Figure C.1: Representation of the skeletons segmented with the automatic segmentation workflow, from the micro-CT images of 12 individuals.

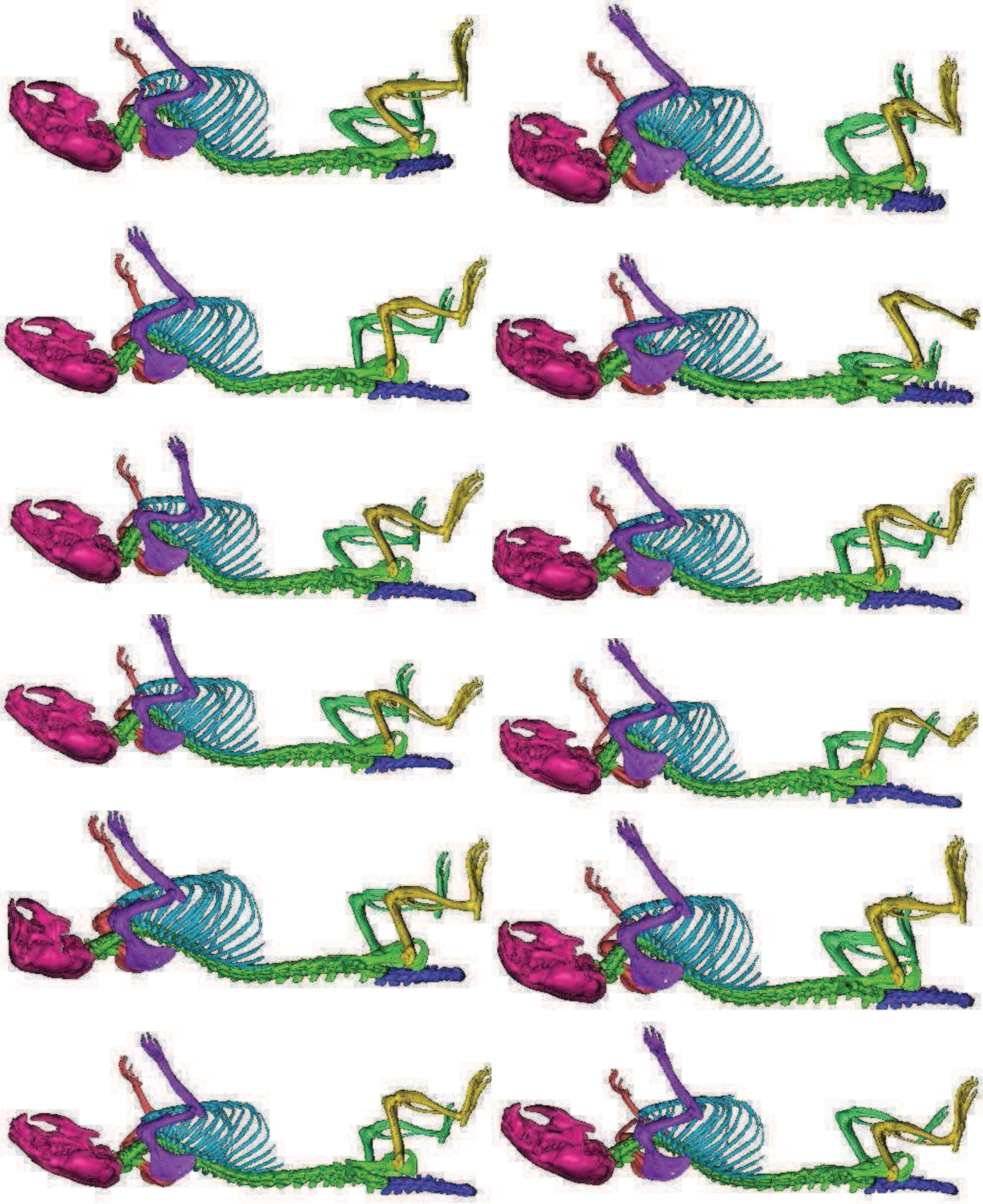

Figure C.2: Representation of the subparts segmented with the automatic segmentation workflow, from the skeletons represented in Figure C.1. Each color represents a skeleton segment. NB : the colors do not match the colors in Figure 4.9.

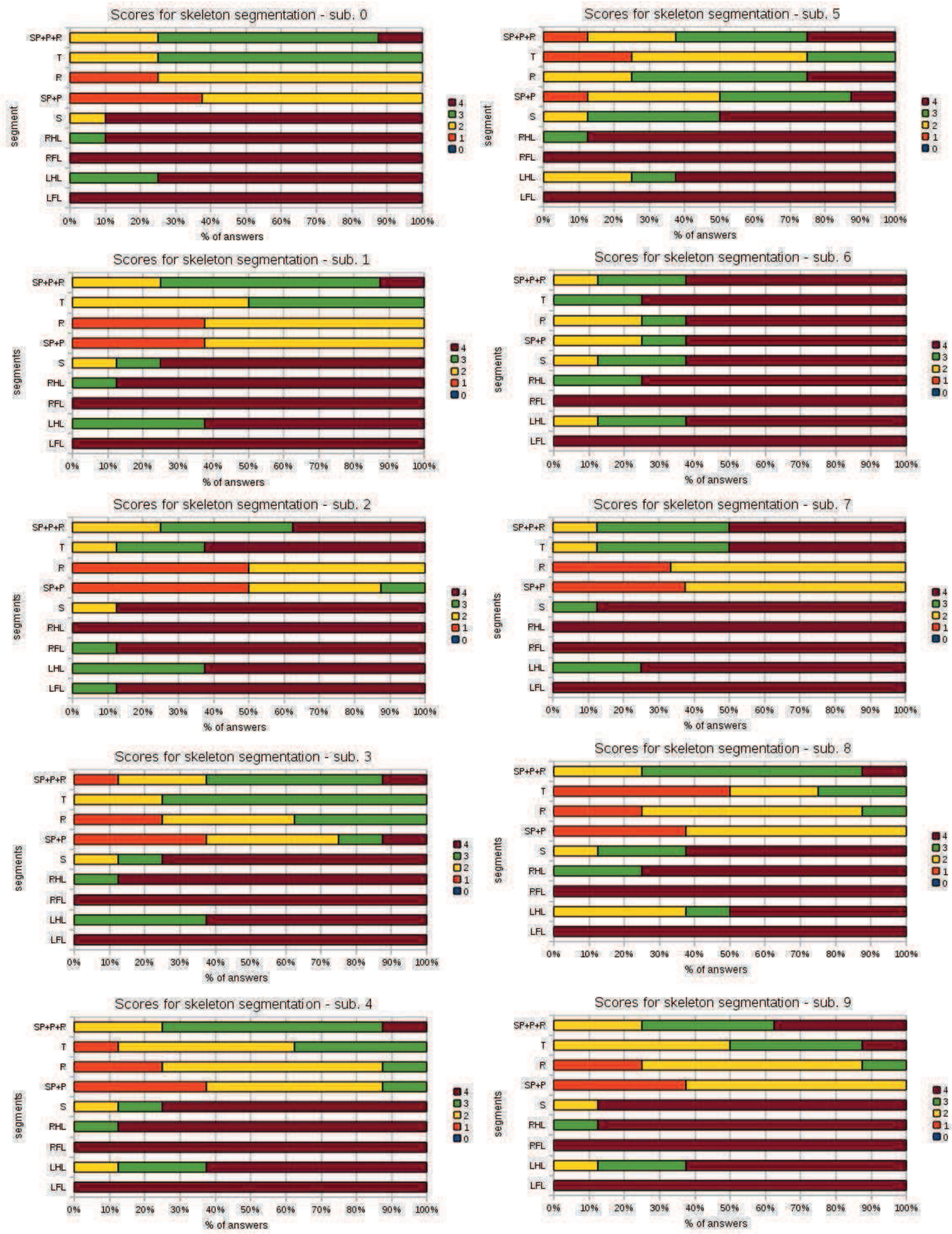

Figure C.3: Summary of the Scores of the skeleton segmentation in subparts with the automatic segmentation workflow, as described in Section 4.3.2. LFL=left forelimb; lhl=left hindlimb; RFL=right forelimb; RHL=right hindlimb; SK=skull; SP+P=spine+pelvis; RC=ribcage; T=tail; SP+P+RC=spine+pelvis+ribcage.

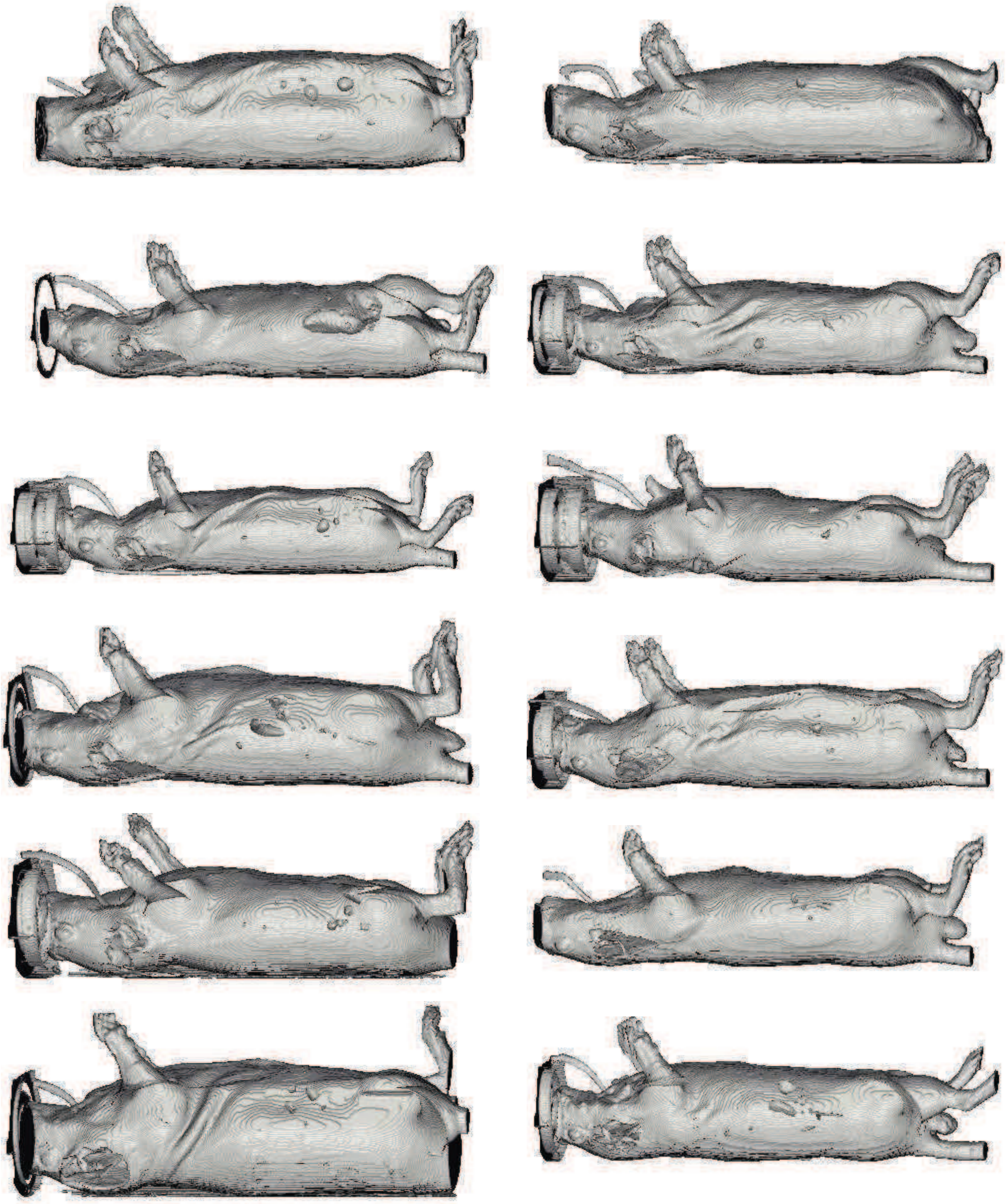

Figure C.4: Representation of the skin segmented with the automatic segmentation workflow, from 12 individuals.

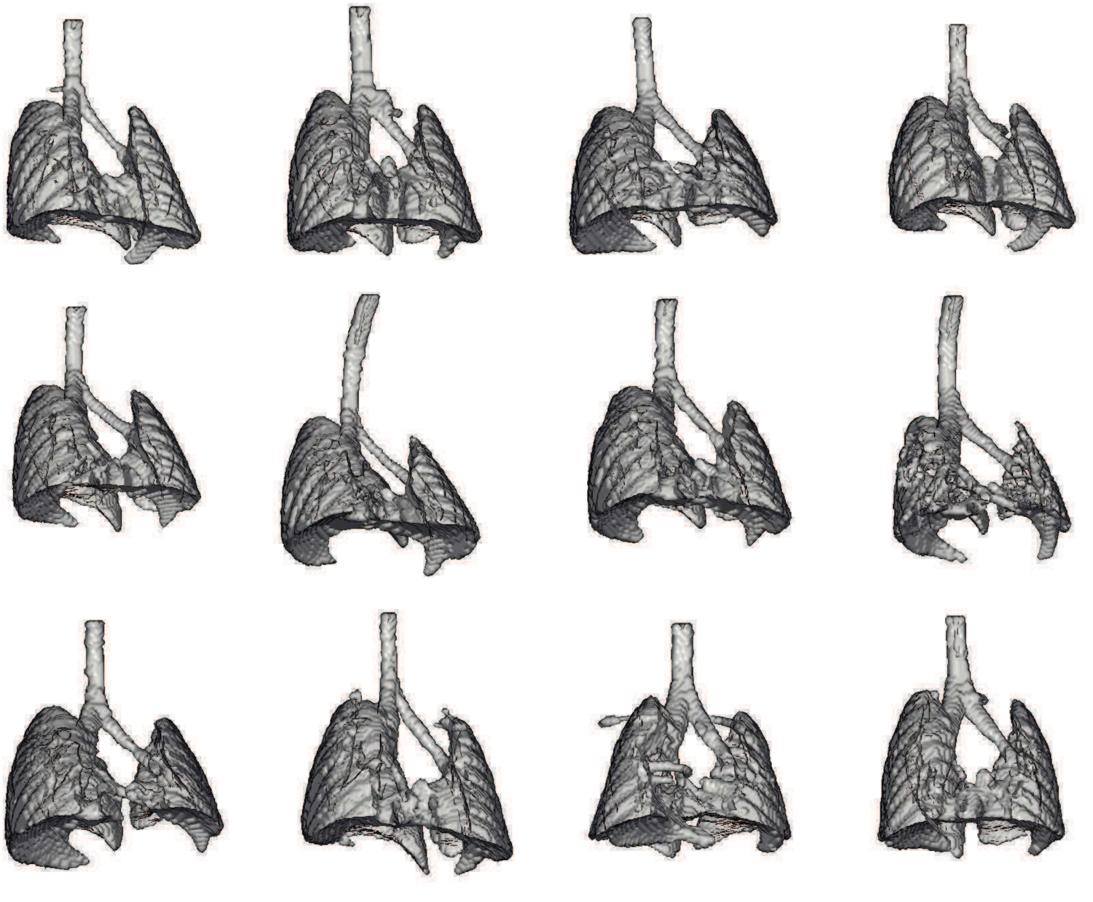

Figure C.5: Representation of the lungs segmented with the automatic segmentation workflow, from 12 individuals.

Appendix D: Segmentation of high contrast tissues from limited angle micro-CT images

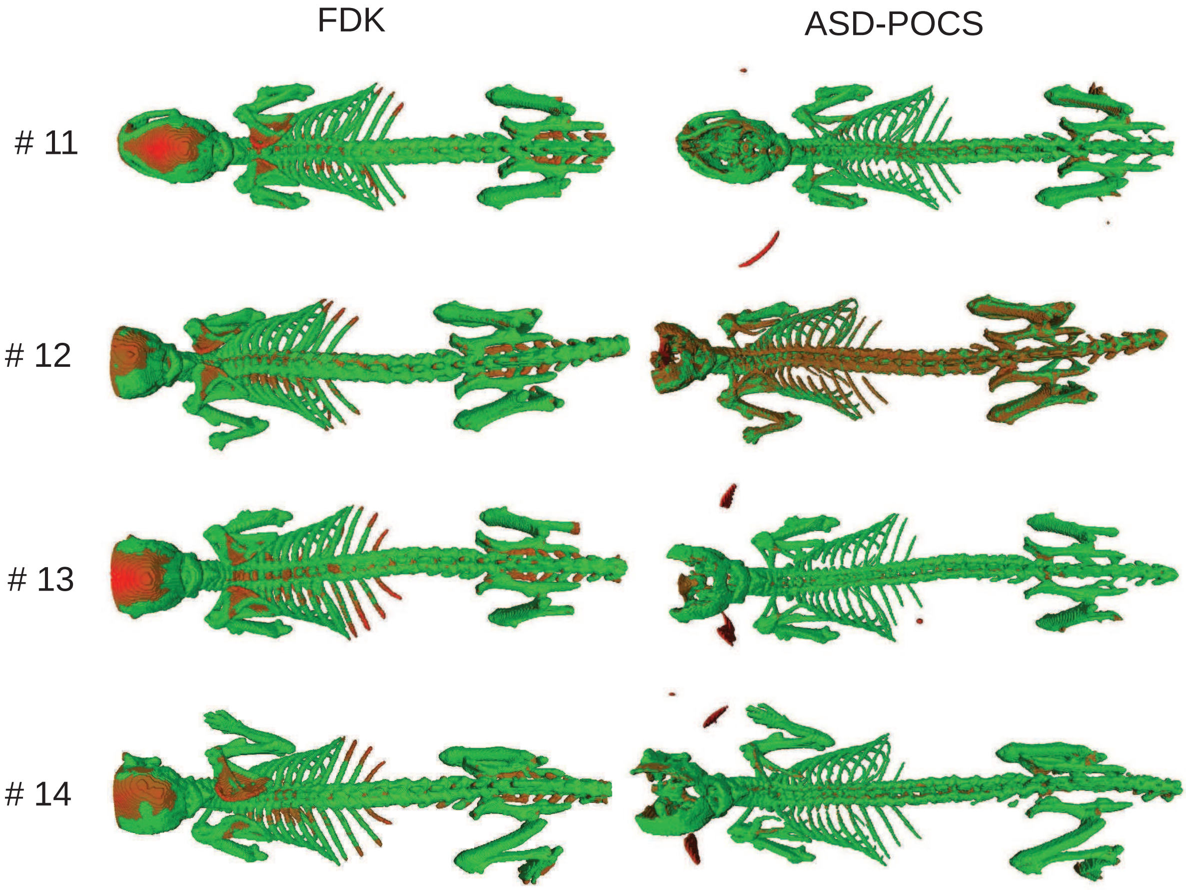

Figure D.1: Representation of the skeleton segmented with the automatic segmentation workflow, from 12 individuals (top view).

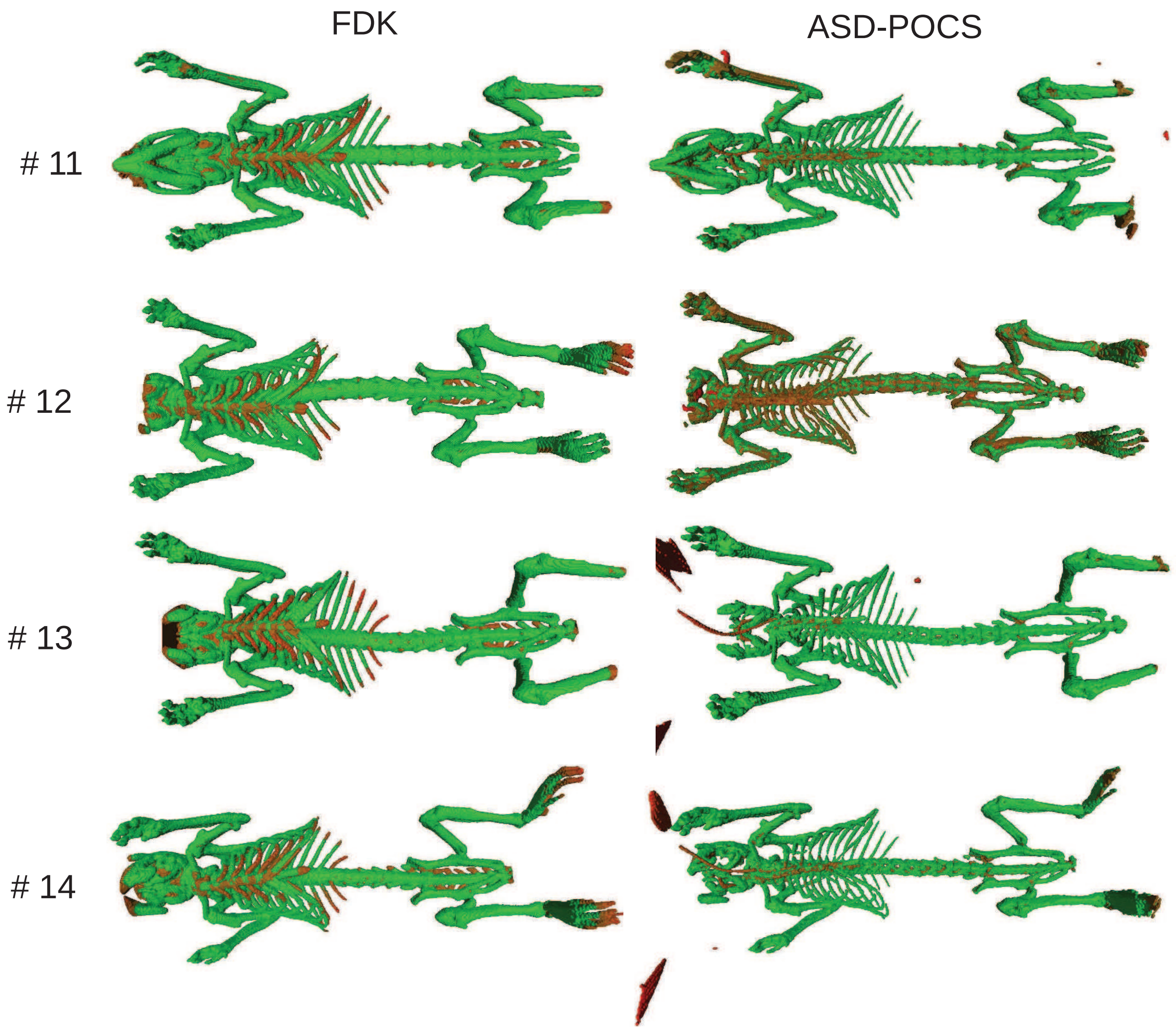

Figure D.2: Representation of the skeleton segmented with the automatic segmentation workflow, from 12 individuals (bottom view).

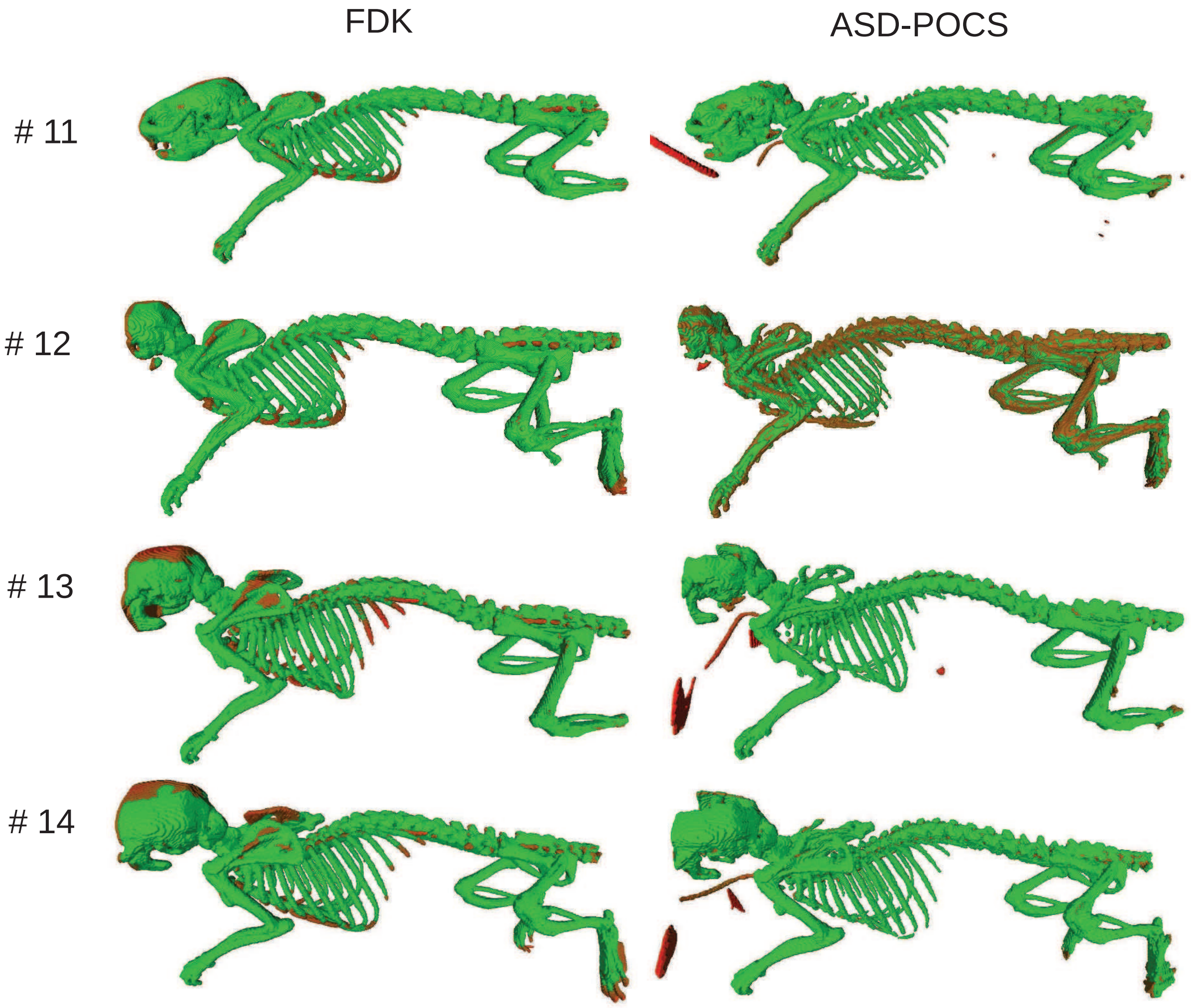

Figure D.3: Representation of the skeleton segmented with the automatic segmentation workflow, from 12 individuals (side view).

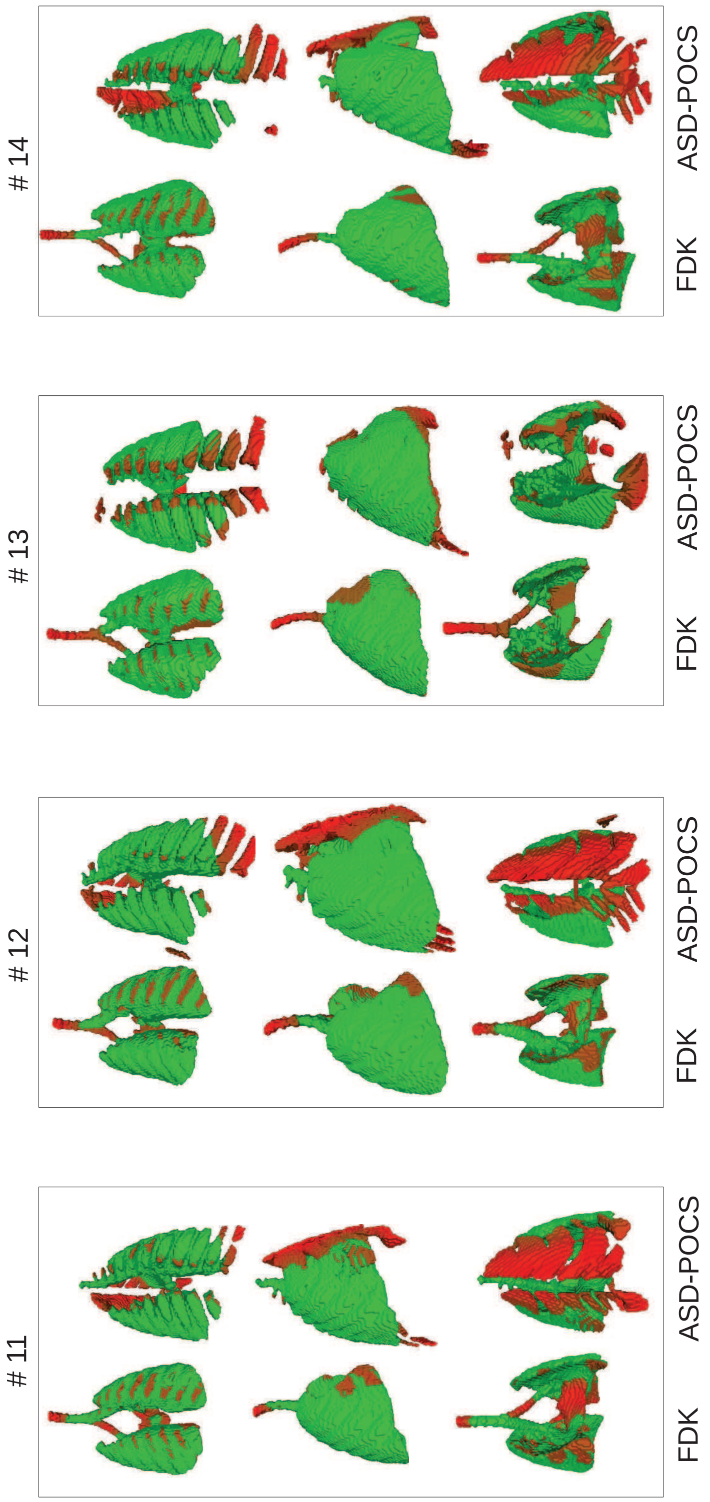

Figure D.4: Representation of the lungs segmented with the automatic segmentation workflow, from 12 individuals.

Appendix E: Statistical atlas

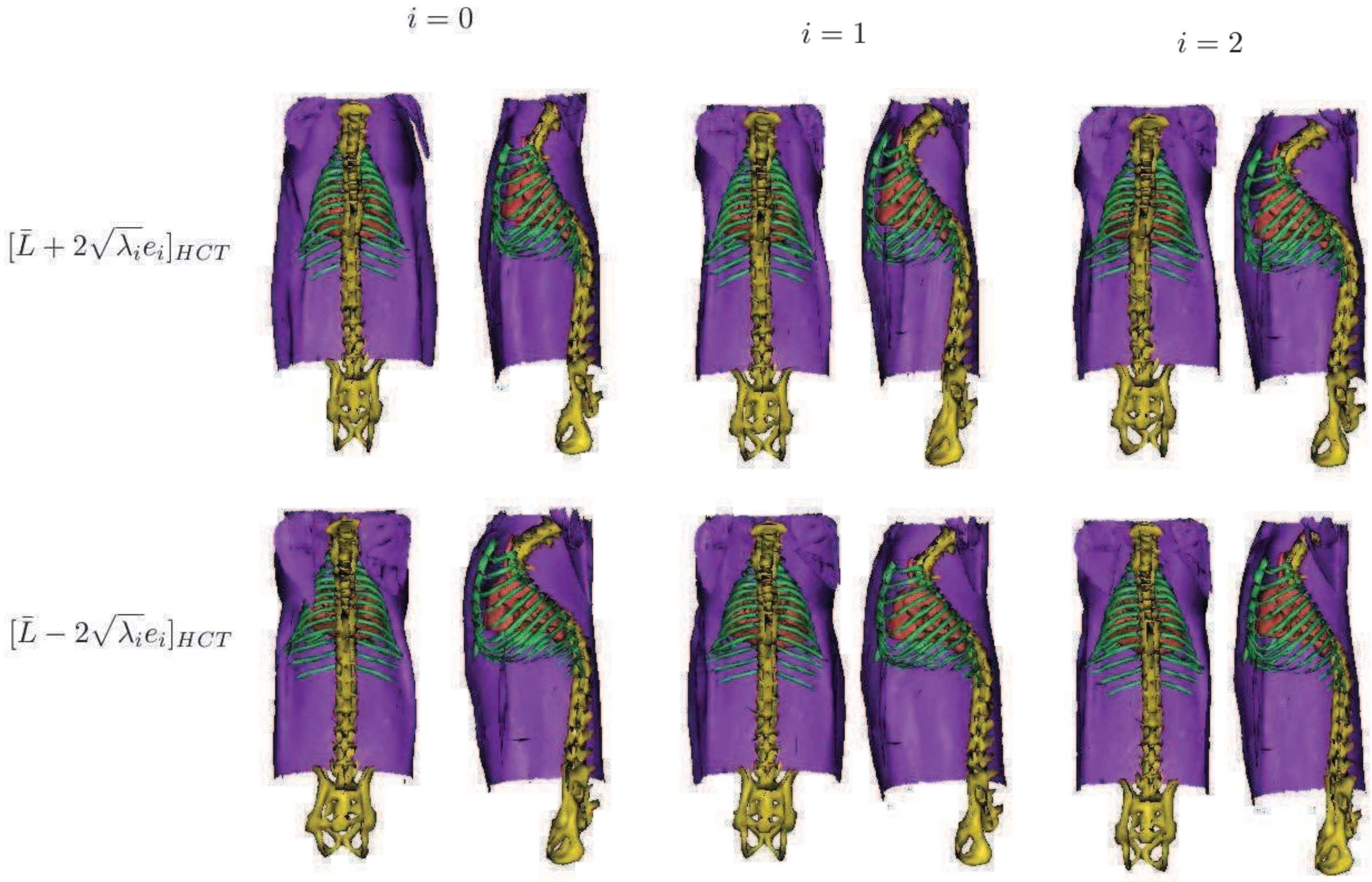

Figure E.1: First three variation modes of the statistical shape model for the High Contrast Tissues.

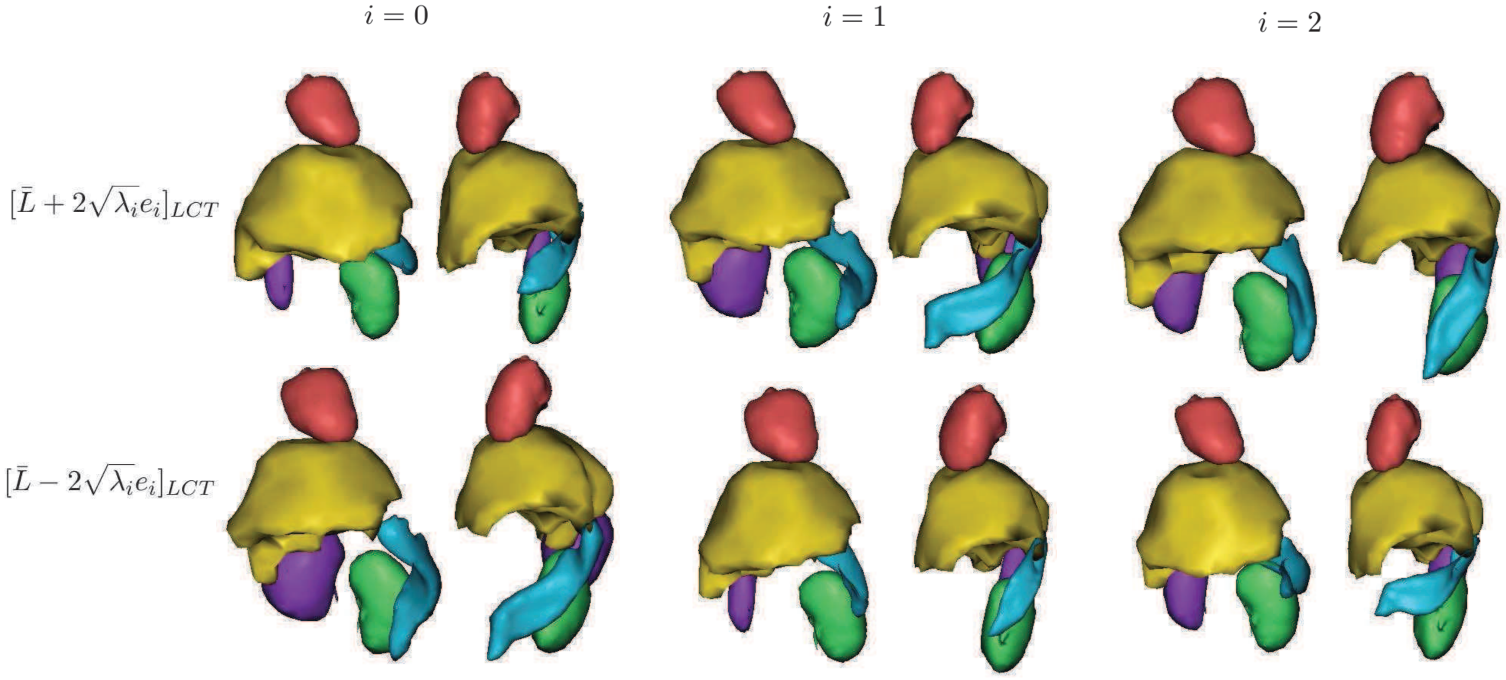

Figure E.2: First three variation modes of the statistical shape model for the Low Contrast Tissues.

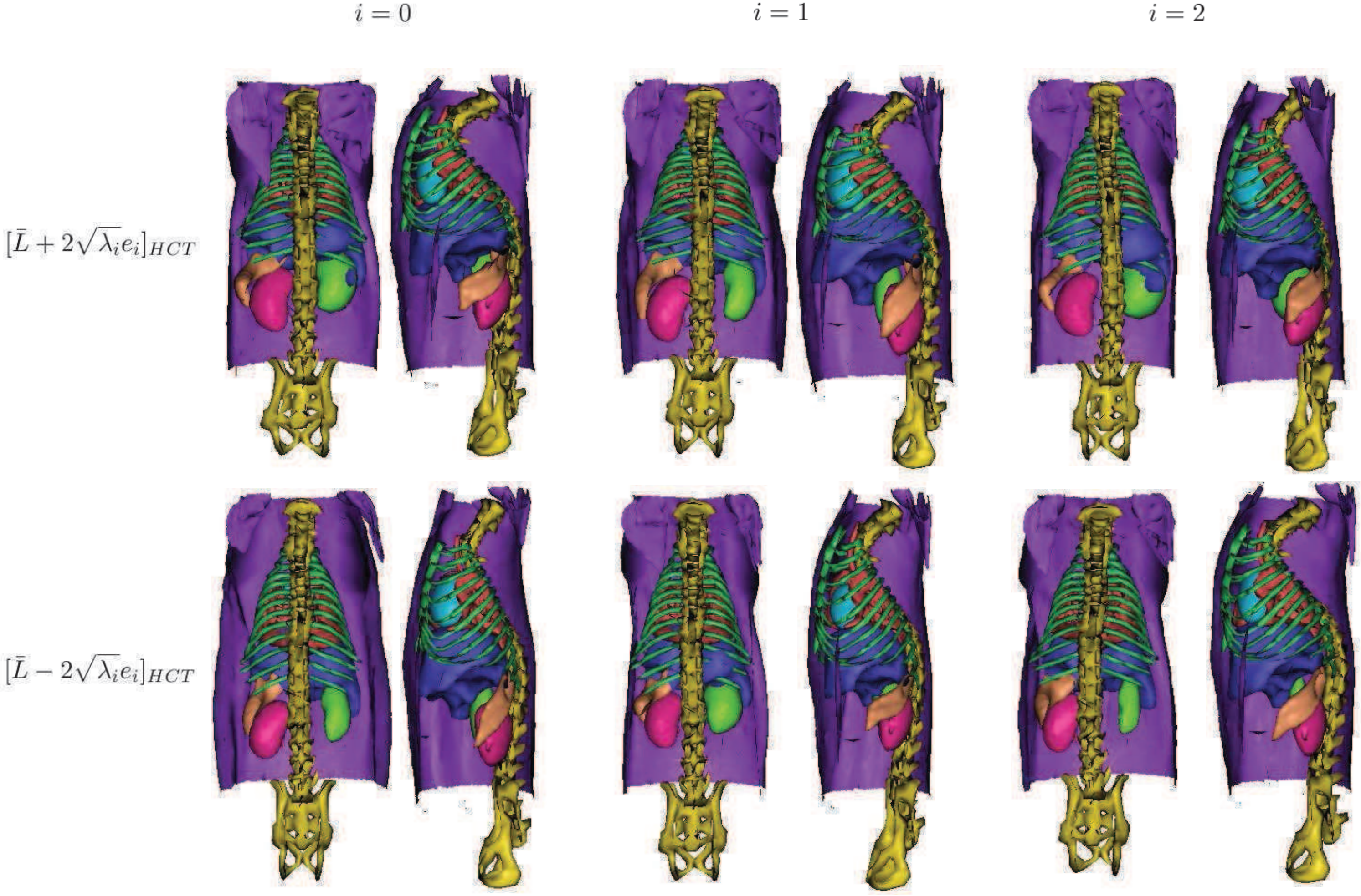

Figure E.3: Result of the Conditional Gaussian Model for the first three variation modes of the statistical shape model of the High Contrast Tissues.

Appendix F: Registration of the Statistical Atlas

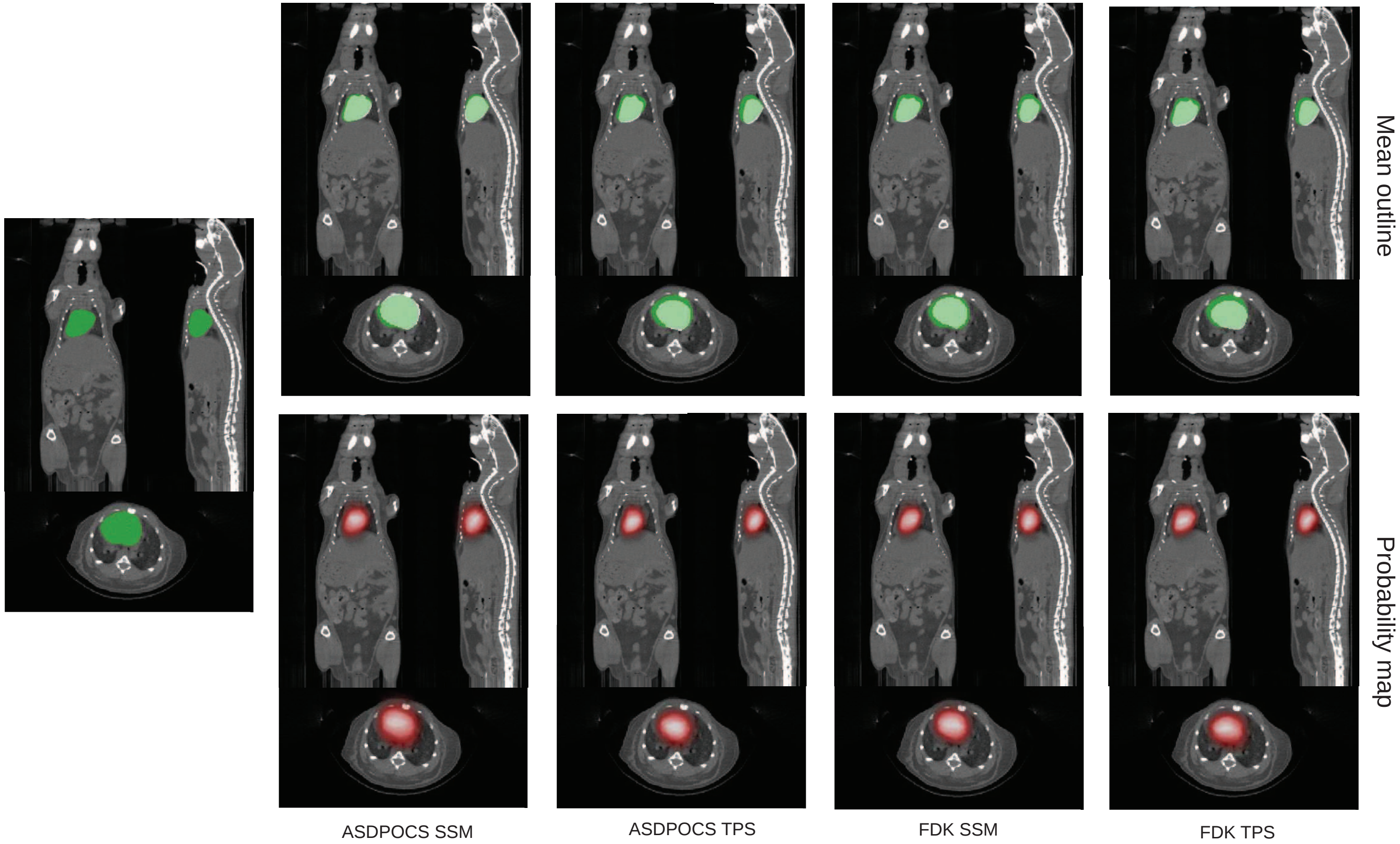

Figure F.1: Mean outline (top row) and probability map (bottom row) of the heart for one individual, determined by the automatic segmentation workflow. The most left image represents the manual segmentation. The green region represents the manual segmentation result while the mean outlines enclose the regions in white. In the probability maps, brighter voxels mean a higher probability.

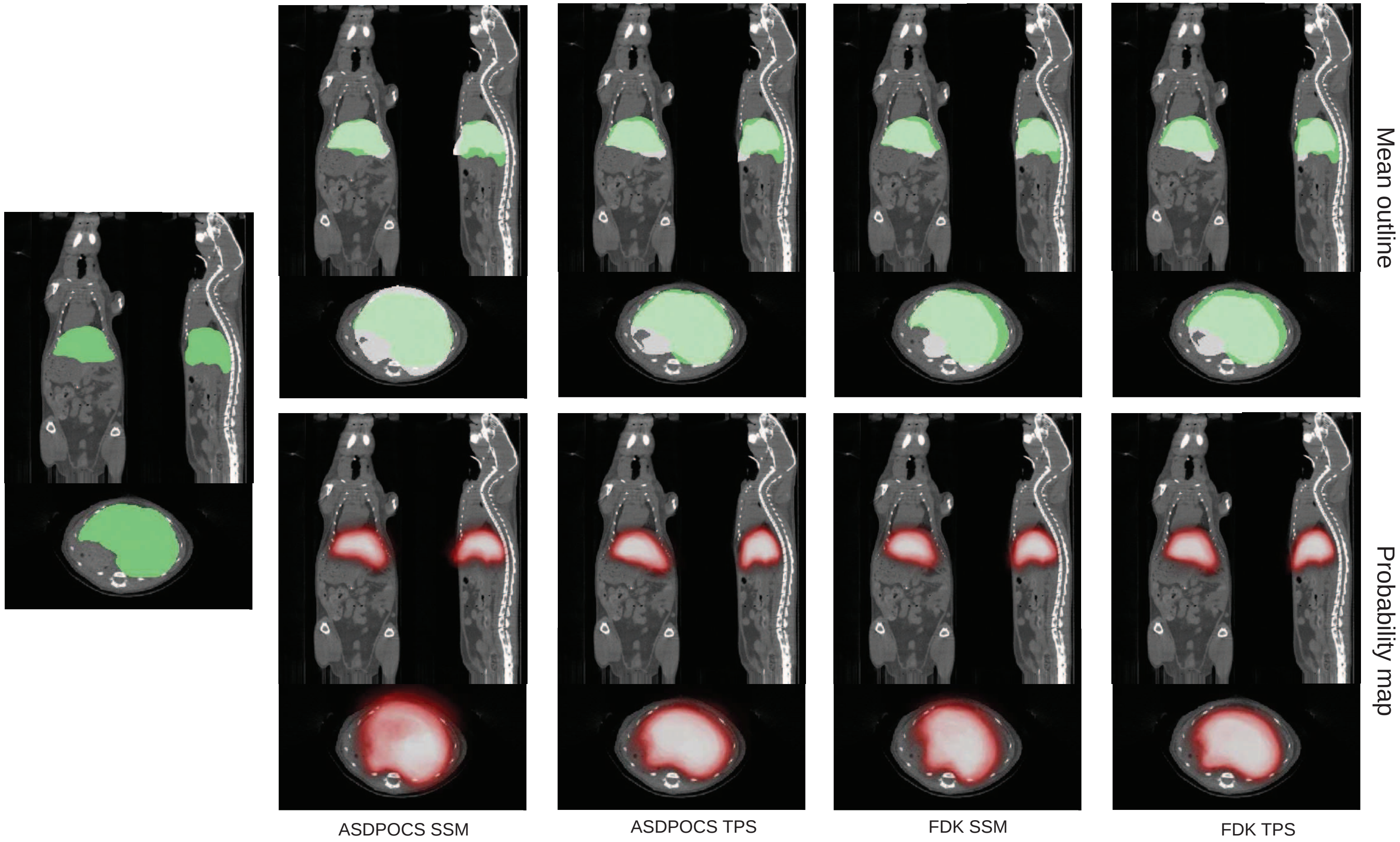

Figure F.2: Mean outline (top row) and probability map (bottom row) of the liver for one individual, determined by the automatic segmentation workflow. The most left image represents the manual segmentation. The green region represents the manual segmentation result while the mean outlines enclose the regions in white. In the probability maps, brighter voxels mean a higher probability.

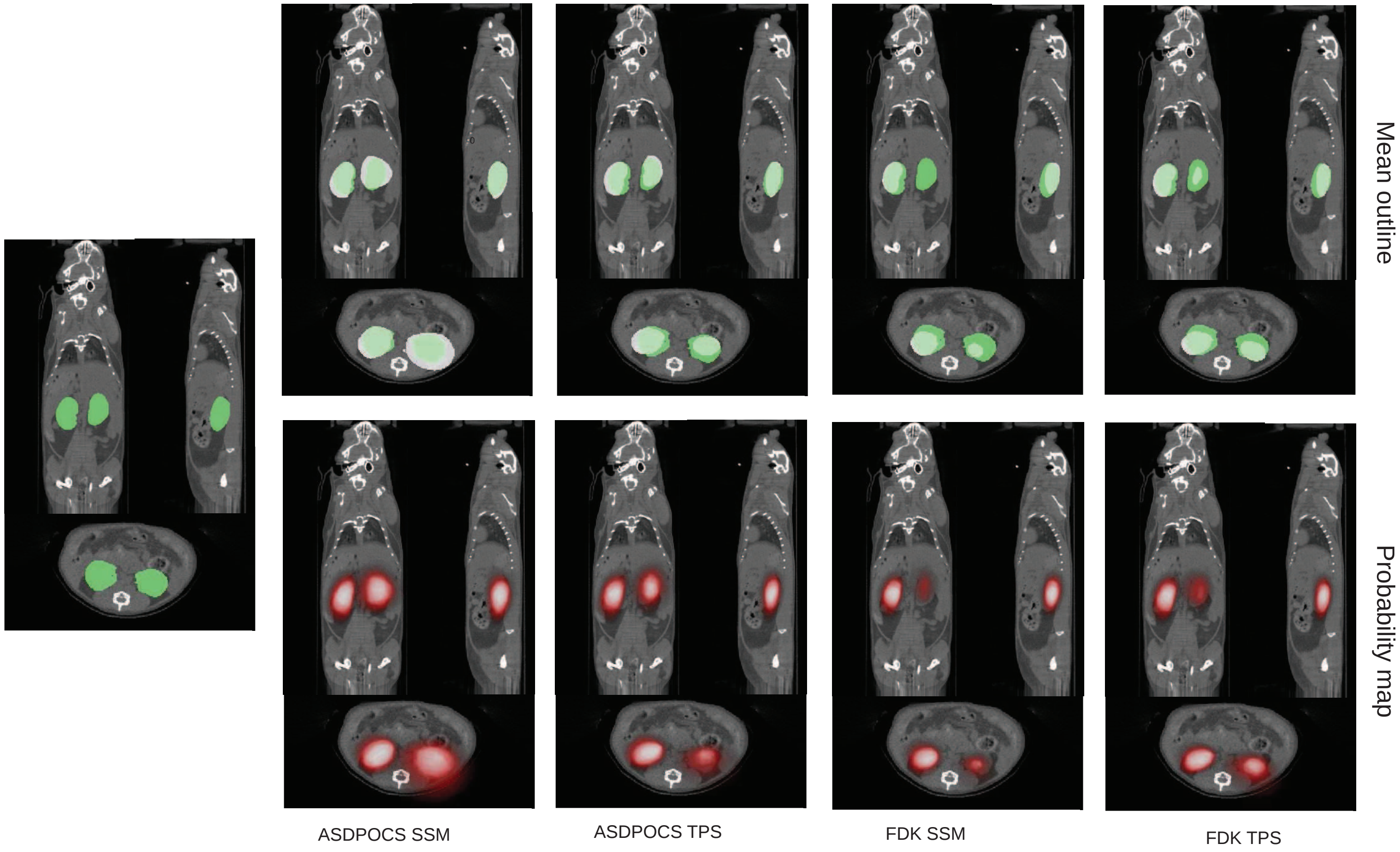

Figure F.3: Mean outline (top row) and probability map (bottom row) of the kidneys for one individual, determined by the automatic segmentation workflow. The most left image represents the manual segmentation. The green region represents the manual segmentation result while the mean outlines enclose the regions in white. In the probability maps, brighter voxels mean a higher probability.

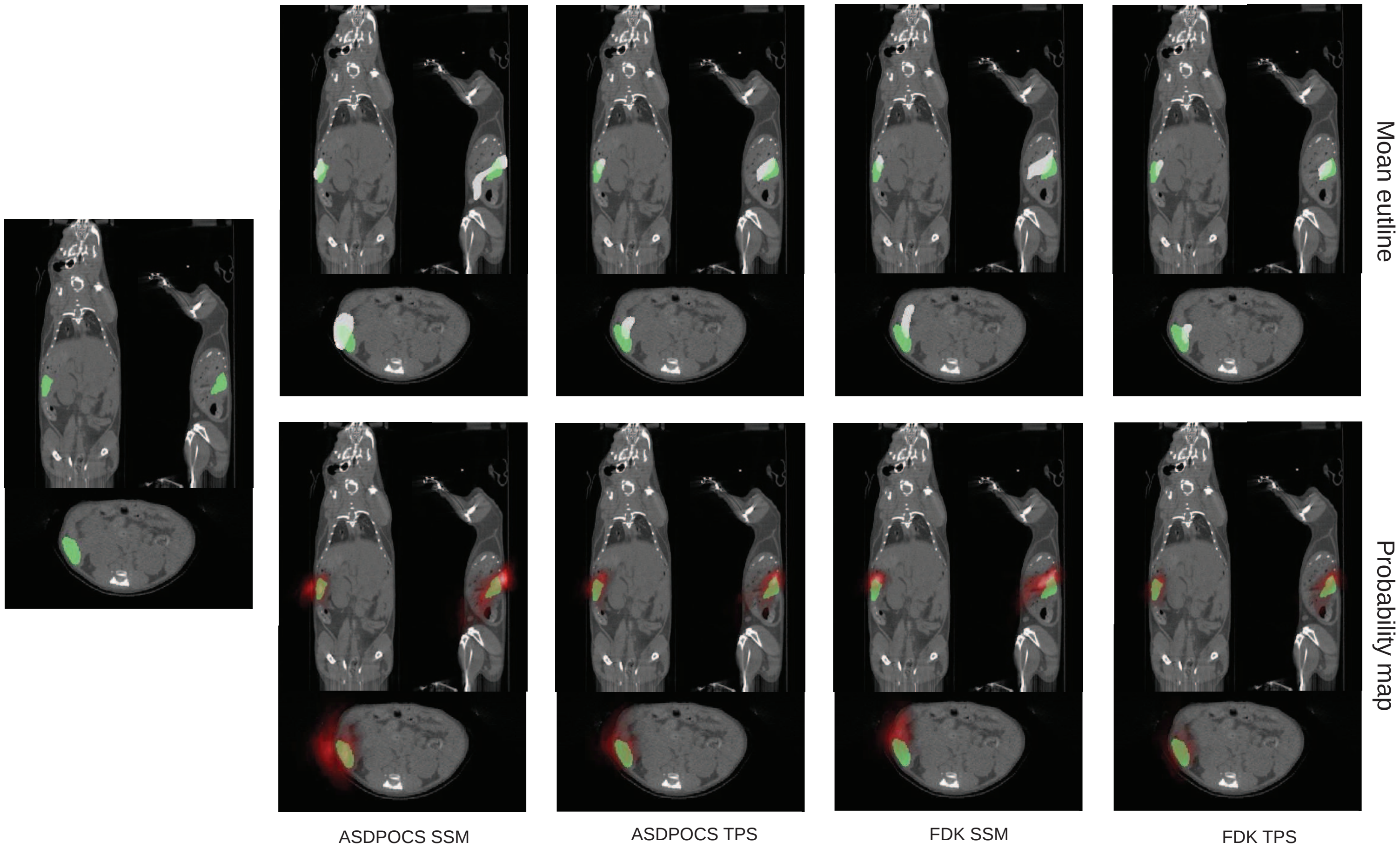

Figure F.4: Mean outline (top row) and probability map (bottom row) of the spleen for one individual, determined by the automatic segmentation workflow. The most left image represents the manual segmentation. The green region represents the manual segmentation result while the mean outlines enclose the regions in white. In the probability maps, brighter voxels mean a higher probability.

Appendix G : Algorithms for the registration of point sets

Any registration task involves a *model* object registered on a *target* object, through the association of some of their features. All the registration tasks performed in this work are geometric registration processes and the geometrical primitives they match are points of the euclidean space. Let the model be a set of N_m points, denoted $P^m = \{p_0^m, p_1^m, ..., p_{N_m-1}^m\}$, and let the target be a set of N_t points, denoted $P^t = \{p_0^t, p_1^t, ..., p_{N_t-1}^t\}$. Translations and rotations between P_m and P_t are denoted t and R, respectively, where t is a vector and R is a rotation matrix. The *optimal* transformation – in the sense that it minimizes some optimization problem – is denoted t^* if it is a translation, R^* if it is a rotation. Each of the algorithms is summarized in this appendix. In the following, DoF stands for *Degree of Freedom*.

Iterative Closest Point

- Abbreviation : ICP
- Correspondances : one-to-one with rejection
- Type of transform : global, rigid – 6 DoF – or affine – 9 DoF.
- Function to minimize : sum of squared distances between couples of closest points
- Significative characteristics : iterative

Iterative Closest Point [Besl and McKay, 1992] has become one of the reference algorithms for rigid point matching[119]. This algorithm iteratively minimizes the mean squared distance between couples of closest points in the model and target point sets, by finding the optimal transformation between them. The algorithm is initialized, then iteration k – the index k is omitted for simplicity, except when it is necessary for understanding – consists in the following steps:

1. Compute of the closest points between the model and the target – each point of the model is associated to its closest point in the target, by the application

$$c(p_i^m) = p_k^t \text{ such as } p_k^t = \underset{j \in \{0,...,N_t\}}{\operatorname{argmin}} d(p_i^m, p_j^t) \tag{1}$$

---

[119] ICP was performed using the function implemented in trimesh2 [Rusinkiewicz, 2013]

$d(\cdot,\cdot)$ being the euclidean distance for two points $a(x_a, y_a, z_a)$ and $b(x_b, y_b, z_b)$:

$$d(a,b) = \|b-a\| = \sqrt{(x_b - x_a)^2 + (y_b - y_a)^2 + (z_b - z_a)^2}. \tag{2}$$

The set of points minimizing the distance to each point of the model is denoted

$$P^c = \{c(p_0^m), c(p_1^m), ..., c(p_{N_m}^m)\}. \tag{3}$$

For simplicity, $d(p_i^m, p_k^t)$ will be denoted equivalently $d(p_i^m, P^t)$. Points can be optionally rejected when the point-to-point distance exceeds a threshold.

2. Compute of the optimal transformations to minimize the mean square distance. Firstly, apply the translations $\bar{p^m}$ and $\bar{p^t}$, respectively, to match the isobarycenter of each point set and the origin. The resulting point sets are denoted, respectively, $P^{m'}$,$P^{c'}$. Then, minimize the sum of squares

$$d_k = D(P^{m'}, P^{c'}) = \frac{1}{N_m}\sum_{i=0}^{N_m} \|p_i^{c'} - R^* p_i^{m'} + t^*\|_2^2. \tag{4}$$

This can be typically done using a Singular Value Decomposition (SVD) of the cross-covariance matrix $W = P^{c'}(P^{m'})^T = U\Sigma V^T$, where U and V are 3×3 unitary matrices, and Σ is a diagonal matrix which diagonal values are the singluar values of W. In this formalism, the optimal rotation is given by:

$$R^* = UV^T. \tag{5}$$

and the optimal translation is given by:

$$T^* = \bar{p^t} - \bar{p^m}. \tag{6}$$

3. Transform the model point set with R^* and T^*;

4. Stop if $\|d_k - d_{k-1}\| < \epsilon \ / \ \epsilon \in \mathbb{R}^{+*}$;

In its affine form, the algorithm aims at minimizing

$$d_k = D(P^{m'}, P^{c'}) = \frac{1}{N_m}\sum_{i=0}^{N_m} \|p_i^{c'} - A^* p_i^{m'} + t^*\|_2^2 \tag{7}$$

at each iteration, where $A^* = S^* R^*$ with S^* the optimal scaling matrix. The scaling matrix S^* can be determined, for example, by computing the Principal Component Analysis of each point set and attributing a scaling factor to each axis by the ratio of its eigenvalues in the target and model point set, respectively. Other approaches include the derivation of a closed form for the optimal affinity matrix A^* as proposed in [Du et al., 2008].

In this work, the ICP implemented in the trimesh2 library [Rusinkiewicz, 2013] was used.

Generalized Procrustes Analysis

- Abbreviation : GPA

- Correspondances : one-to-one
- Type of transform : global, rigid – 6 DoF
- Function to minimize : sum of squared distances between couples of closest points
- Significative characteristics : one-pass

Generalizes Procrustes Analysis[120] consists in casting a set of shapes into the same reference frame, and applying transformation to each to get rid of orientation and size variability. GPA constitutes a standard algorithm in Statistical Shape Analysis [Bookstein, 1997a] and is typically realized by the following steps:

1. the barycenters of the point sets are matched to the origin of the cartesian reference frame;
2. for each point set : the sum of squared distance between each point and the barycenter is normalized;
3. the optimal rotation matching the point sets is calculated using e.g. SVD in a similar manner as in step 2 of the ICP algorithm.
4. the optimal rotation matching the point sets is applied to the model.

In this work, the TPS-RPM algorithm was implemented using the Eigen library [Guennebaud et al., 2010].

Thin Plate Spline – Robust Point Matching

- Abbreviation : TPS-RPM
- Correspondances : softassign
- Type of transform : [global, affine – 9 DoF] + [Thin Plate Spline : local, radial basis function]
- Function to minimize : the squared distance between the target point set and the transformed model point set, under the softassign constraint and a smoothness constraint.
- Significative characteristics : iterative

The use of thin-plate spline in geometric morphometrics has been introduced by Bookstein in [Bookstein, 1989]. The transformation is defined as:

$$f(p_i^m, d, w) = p_i^m d + \phi(p_i^m) w \tag{8}$$

where ϕ is the $1 \times N_m$ vector defined from the TPS kernel as:

$$\phi_j(p_i^m) = \|p_j^t - p_i^m\| \tag{9}$$

---

[120] GPA was named after the ancient Greek mythological figure, Procrustes ($\Pi\rho o\kappa\rho o\upsilon\sigma\tau\eta\varsigma$), who stretched or cut off the legs of people so that they fit an iron bed. He was killed by Theseus.

and d is the vector describing the affine transform.

The Robust Point Matching algorithm, proposed by Chui and Rangarajan in [Chui and Rangarajan, 2003], aims at establishing correspondence between points through a softassign process and a non-rigid registration based on simulated annealing. The softassign step aims at building a matrix $M = (m_{ij})_{(N_m+1)\times(N_t+1)}$, which rows and columns are normalized to 1. The matrix defined by the first N_m lines and N_t columns of M establishes correspondences between the points. The last line and column stand for the outliers in both point set. At each annealing iteration, the matrix M undergoes an iterative normalization of its lines and columns. In this sense, it *softassigns* a set of points of the target to each point of the model, i.e. the constraint of one-to-one correspondence is relaxed, conversely to ICP and GPA.

Initialization is performed by setting the iteration index $k = 0$, the temperature $T = T_0$, the annealing factor $r \in \mathbb{R}^{+*}$ and the transform to identity. The algorithm basically executes the following steps at each iteration:

1. The matrix M is initialized with

$$\forall\ (i,j) \in \{0,...,N_m\} \times \{0,...,N_t\}\ :\ m_{ij} = \frac{1}{T} e^{-\frac{(f(p_i^m)-p_j^t)^T (f(p_i^m)-p_j^t)}{2T}}. \tag{10}$$

2. The outlier columns are initialized with

$$\forall\ (i) \in \{0,...,N_m\}\ :\ m_{iN_t} = \frac{1}{T_0} e^{-\frac{(f(p_i^m)-g_t)^T (f(p_i^m)-g_t)}{2T_0}} \tag{11}$$

   and

$$\forall\ (j) \in \{0,...,N_t\}\ :\ m_{N_m j} = \frac{1}{T_0} e^{-\frac{(g_m-p_j^t)^T (g_m-p_j^t)}{2T_0}} \tag{12}$$

   where g_m and g_t are the centers of the outlier centers in the model and in the target point sets.

3. The lines and columns of M are iteratively normalized to 1.

4. The transformation is updated by computing the parameters d and w as described in [Chui and Rangarajan, 2003].

5. The transformation is applied to the model point set.

6. The temperature is decreased by setting : $T^{k+1} = rT^k$.

In this work, the TPS-RPM algorithm was implemented using the Eigen library [Guennebaud et al., 2010]. To account for the variability of the results depending on the point sets to be registered, e.g. because of outliers, the algorithm includes the following parameters:

- the initial temperature T_0 regulating the influence of each points on the others, depending on the distance between them;

- the cooling rate r regulating the decrease of T at each iteration;

- two scalars λ_1 and λ_2 regulating the relative importance of the affine transformation and the thin plate spline deformation.

. Moreover, the number of iterations has to be chosen – it can be fixed based on the temperature when $|T - T_0|$ goes below a certain threshold. The tuning of these parameters is problematic and in practice they are chosen arbitrarily.

Nonrigid registration based on a Gaussian Mixture Model

- Abbreviation : GMMREG
- Correspondances : softassign
- Type of transform : [global, affine – 9 DoF] + [Thin Plate Spline : local, radial basis function]
- Function to minimize : sum of squared distance between gaussian mixtures and minimization of the TPS bending energy.
- Significative characteristics : iterative.

Introduced by Jian and Vemuri in [Bing and Vemuri, 2011], this nonrigid registration algorithm models explicitly the point sets as mixtures of Gaussian distributions. Three-dimensional Gaussian distributions are built using the point position as the mean μ_i and assuming that the Gaussian distributions have isotropic covariance modeled by the covariance matrix Σ_i proportional to the identity matrix. A Gaussian density distribution is associated to each of the K point of index i:

$$p_i \sim N(\mu_i, \Sigma_i) \tag{13}$$

and the density distribution is noted $\phi_i(\mathrm{x}|\mu_i, \Sigma_i)$. The probability density function is explicitly defined by:

$$p(\mathrm{x}) = \sum_{i=1}^{K} w_i \phi_i(\mathrm{x}|\mu_i, \Sigma_i). \tag{14}$$

Practically, the weights w_i are assumed to be the same over the point set.

The algorithm finds the optimal transformation minimizing the $\mathbf{L}_2$ norm between the Gaussian mixtures, for which a closed form can be derived. An optimal rigid or affine transformation can be determined from the closed form of the $\mathbf{L}_2$ norm. Then, Conjugate Gradient minimization of a cost function based on the thin-plate spline deformation makes it possible to realize the non-rigid registration.

In this work, the implementation proposed on the webpage [Bing and Vemuri, 2005] was used.

Appendix H : Sample for the construction of the Statistical Shape Models

ID	animal	bunch	acquisition date	age (weeks)	gender	mass (g)
8	16	109	31/01/14	20	♀	48
11	20	109	03/02/14	21	♀	48
13	15	97	04/02/14	38	♀	42.5
14	13	97	06/02/14	38	♀	36
15	3	123	10/02/14	8	♀	28.8
19	7	123	11/02/14	8	♀	29.7
20	8	123	11/02/14	8	♀	29.8
22	11	123	11/02/14	8	♂	35
23	12	123	14/02/14	8	♂	28
28	17	123	18/02/14	9	♂	40
29	18	123	18/02/14	9	♂	40
31	20	123	18/02/14	9	♂	40

Table H.1: Sample of the ICR strain population used to build the Statistical Shape Model

ID	animal	bunch	acquisition date	age (weeks)	gender	mass (g)
32	11	151	27/11/14	18	♀	33
33	12	151	27/11/14	18	♀	33
34	13	151	01/12/14	19	♀	33
35	14	151	01/12/14	19	♀	35
36	16	151	01/12/14	19	♀	35

Table H.2: Sample of the ICR strain population used for the validation study.

References

References

[Abdi and Williams, 2010] Abdi, H. and Williams, L. J. (2010). Principal component analysis. *Wiley Interdisciplinary Reviews - Computational Statistics*, 2(4):433–459.

[Ahn et al., 2008] Ahn, S., Chaudhari, A. J., Darvas, F., and A, C. (2008). Fast iterative image reconstruction methods for fully 3D multispectral bioluminescence tomography. *Physics in Medicine and Biology*, 53:3921–3942.

[Alexandrakis et al., 2005] Alexandrakis, G., Rannou, F. R., and Chatziioannou, A. F. (2005). Tomographic bioluminescence imaging by use of a combined optical-PET (OPET) system: a computer simulation feasibility study. *Physics in Medicine and Biology*, 50(17):4225.

[Allard et al., 2007] Allard, M., Côté, D., Davidson, L., Dazai, J., and Henkelman, R. M. (2007). Combined magnetic resonance and bioluminescence imaging of live mice. *Journal of Biomedical Optics*, 12(3):034018.

[Allied Control Council, 1949] Allied Control Council (1949). volume 2 of *Trials of War Criminals before the Nuremberg Military Tribunals under Control Council Law*, pages 181–182.

[Andersson-Engels et al., 1997] Andersson-Engels, S., af Klinteberg, C., Svanberg, K., and Svanberg, S. (1997). In vivo fluorescence imaging for tissue diagnostics. *Physics in Medicine and Biology*, 42(5):815.

[Arbeláez and Cohen, 2003] Arbeláez, P. A. and Cohen, L. D. (2003). Path variation and image segmentation. In Rangarajan, A., Figueiredo, M. A. T., and Zerubia, J., editors, *EMMCVPR*, volume 2683 of *Lecture Notes in Computer Science*, pages 246–260. Springer.

[Arridge et al., 2000] Arridge, S. R., Dehghani, H., Schweiger, M., and Okada, E. (2000). The finite element model for the propagation of light in scattering media: a direct method for domains with nonscattering regions. *Medical Physics*, 27(1):252–64.

[Artaechevarria et al., 2009] Artaechevarria, X., Perez-Martin, D., Ceresa, M., de Biurrun, G., Blanco, D., Montuenga, L., van Ginneken, B., Ortiz-de Solorzano, C., and Munoz-Barrutia, A. (2009). Airway segmentation and analysis for the study of mouse models of lung disease using micro-ct. *Physics in Medicine and Biology*, 54(22):7009.

[Aykac et al., 2005] Aykac, D., Price, J., and Wall, J. (2005). 3d segmentation of the mouse spleen in microct via active contours. In *Nuclear Science Symposium Conference Record, 2005 IEEE*, volume 3, pages 4 pp.–1545.

[Badea et al., 1998] Badea, C., Kolitsi, Z., and Pallikarakis, N. (1998). A wavelet-based method for removal of out-of-plane structures in digital tomosynthesis. *Computerized Medical Imaging and Graphics*, 22(4):309–15.

[Baiker et al., 2010] Baiker, M., Milles, J., Dijkstra, J., Henning, T. D., Weber, A. W., Que, I., Kaijzel, E. L., Löwik, C. W. G. M., Reiber, J. H. C., and Lelieveldt, B. P. F. (2010). Atlas-based whole-body segmentation of mice from low-contrast Micro-CT data. *Medical Image Analysis*, 14(6):723–737.

[Baiker et al., 2011] Baiker, M., Staring, M., Löwik, C., Reiber, J., and Lelieveldt, B. (2011). Automated Registration of Whole-Body Follow-Up MicroCT Data of Mice. In Fichtinger, G., Martel, A., and Peters, T., editors, *Medical Image Computing and Computer-Assisted Intervention - MICCAI 2011*, volume 6892 of *Lecture Notes in Computer Science*, pages 516–523. Springer Berlin Heidelberg.

[Basevi et al., 2013] Basevi, H. R. a., Guggenheim, J. a., Dehghani, H., and Styles, I. B. (2013). Simultaneous multiple view high resolution surface geometry acquisition using structured light and mirrors. *Optics Express*, 21(6):7222–39.

[Bentley, 1975] Bentley, J. L. (1975). Multidimensional binary search trees used for associative searching. *Communications of the ACM*, 18(9):509–517.

[Besl and McKay, 1992] Besl, P. J. and McKay, N. D. (1992). A method for registration of 3-D shapes. *IEEE Transactions on Pattern Analysis and Machine Intelligence*, 14(2):239–256.

[Bian et al., 2010] Bian, J., Siewerdsen, J. H., Han, X., Sidky, E. Y., Prince, J. L., Pelizzari, C. A., and Pan, X. (2010). Evaluation of sparse-view reconstruction from flat-panel-detector cone-beam CT. *Physics in Medicine and Biology*, 55:6575–6599.

[Bing and Vemuri, 2005] Bing, J. and Vemuri, B. C. (2005). gmmreg - http://code.google.com/p/gmmreg/.

[Bing and Vemuri, 2011] Bing, J. and Vemuri, B. C. (2011). Robust Point Set Registration Using Gaussian Mixture Models. *IEEE Transactions on Pattern Analysis and Machine Intelligence*, 33(8):1633–1645.

[BiospaceLab, 2014] BiospaceLab (2014). Biospace Lab (Paris, France) - http://www.biospacelab.com/.

[Bloquel et al., 2006] Bloquel, C., Trollet, C., Pradines, E., Seguin, J., Scherman, D., and Bureau, M. (2006). Optical imaging of luminescence for in vivo quantification of gene electrotransfer in mouse muscle and knee. *BMC Biotechnology*, 6(1):16.

[Boll et al., 2011] Boll, H., Nittka, S., Doyon, F., Neumaier, M., Marx, A., Kramer, M., Groden, C., and Brockmann, M. A. (2011). Micro-ct based experimental liver imaging using a nanoparticulate contrast agent: A longitudinal study in mice. *PLoS ONE*, 6(9):e25692.

[Bookstein, 1989] Bookstein, F. L. (1989). Principal warps: thin-plate splines and the decomposition of deformations. *IEEE Transactions on Pattern Analysis and Machine Intelligence*, 11(6):567–585.

[Bookstein, 1997a] Bookstein, F. L. (1997a). Landmark methods for forms without landmarks: morphometrics of group differences in outline shape. *Medical Image Analysis*, 1(3):225–243.

[Bookstein, 1997b] Bookstein, F. L. (1997b). Shape and the Information in Medical Images: A Decade of the Morphometric Synthesis. *Computer Vision and Image Understanding*, 66(2):97–118.

[Brasse et al.,] Brasse, D., Loreille, G., Carvou, N., Ostrowska, K., Cuscito, P., and Maitrejean, S. Cerenkov Luminescence imaging on the PhotonIMAGER system - biodistribution of the beta emitting radiotracer 32P. *www.biospacelab.com*.

[Brooksby et al., 2003] Brooksby, B., Dehghani, H., Pogue, B., and Paulsen, K. (2003). Near-infrared (nir) tomography breast image reconstruction with a priori structural information from mri: algorithm development for reconstructing heterogeneities. *IEEE Journal of Selected Topics in Quantum Electronics*, 9(2):199–209.

[Bruno and Svoronos, 2005] Bruno, T. and Svoronos, P. (2005). *CRC Handbook of Fundamental Spectroscopic Correlation Charts*. CRC Press.

[Cairns and Wolf, 1990] Cairns, B. and Wolf, E. (1990). Comparison of the born and the rytov approximations for scattering on quasi-homogeneous media. *Optics Communications*, 74(5):284 – 289.

[Candès and Wakin, 2008] Candès, E. and Wakin, M. (2008). An introduction to compressive sampling. *Signal Processing Magazine, IEEE*, 25(2):21–30.

[Candès et al., 2006a] Candès, E. J., Romberg, J., and Tao, T. (2006a). Robust uncertainty principles: Exact signal reconstruction from highly incomplete frequency information. *IEEE Transactions on Information Theory*, 52(2):489–509.

[Candès et al., 2006b] Candès, E. J., Romberg, J. K., and Tao, T. (2006b). Stable signal recovery from incomplete and inaccurate measurements. *Communications on Pure and Applied Mathematics*, 59(8):1207–1223.

[CGAL, 2013] CGAL (2013). CGAL v4.2 - https://www.cgal.org/.

[Chaudhari et al., 2005] Chaudhari, A. J., Darvas, F., Bading, J. R., Moats, R. A., Conti, P. S., Smith, D. J., Cherry, S. R., and Leahy, R. M. (2005). Hyperspectral and multispectral bioluminescence optical tomography for small animal imaging. *Physics in Medicine and Biology*, 50(23):5421.

[Chen and Earner, 2004] Chen, P. and Earner, K. (2004). Three-dimensional multi-resolution statistical reconstruction for tomosynthesis. In *Biomedical Imaging: Nano to Macro, 2004. IEEE International Symposium on*, pages 559–562 Vol. 1.

[Chin and Dyer, 1986] Chin, R. T. and Dyer, C. R. (1986). Model-based recognition in robot vision. *ACM Computing Surveys*, 18:67–108.

[Chishima et al., 1997] Chishima, T., Miyagi, Y., Li, L., Tan, Y., Baranov, E., Yang, M., Shimada, H., Moossa, A., and Hoffman, R. (1997). Use of histoculture and green fluorescent protein to visualize tumor cell host interaction. *In Vitro Cellular and Developmental Biology - Animal*, 33(10):745–747.

[Cho et al., 2009] Cho, J., Douraghy, A., Olma, S., Liu, K., Chen, Y., Shen, C., Silverman, R., van Dam, R., and Chatziioannou, A. F. (2009). Čerenkov radiation imaging as a method for quantitative measurements of beta particles in a microfluidic chip. In *2008 IEEE Nuclear Science Symposium Conference Record*, pages 4510–4515. IEEE.

[Chui and Rangarajan, 2003] Chui, H. and Rangarajan, A. (2003). A new point matching algorithm for non-rigid registration. *Computer Vision and Image Understanding*, 89(2-3):114–141.

[Clark et al., 2012] Clark, D., Badea, A., Liu, Y., Johnson, G. A., and Badea, C. T. (2012). Registration-based segmentation of murine 4d cardiac micro-ct data using symmetric normalization. *Physics in Medicine and Biology*, 57(19):6125.

[Comley, 2011] Comley, J. (2011). In Vivo Preclinical Imaging. Drug Discovery World.

[Cong et al., 2010] Cong, A., Cong, W., Lu, Y., Santago, P., Chatziioannou, A., and Wang, G. (2010). Differential evolution approach for regularized bioluminescence tomography. *IEEE Transactions on Biomedical Engineering*, 57(9):2229–38.

[Contag et al., 1995] Contag et al. (1995). Photonic detection of bacterial pathogens in living hosts. *Molecular Microbiology*, 18.

[Cook, 1965] Cook, M. (1965). *The anatomy of the laboratory mouse*. Academic Press.

[Cootes et al., 1995] Cootes, T., Taylor, C., Cooper, D., and Graham, J. (1995). Active shape models-their training and application. *Computer Vision and Image Understanding*, 61(1):38 – 59.

[Cuingnet et al., 2012] Cuingnet, R., Prevost, R., Lesage, D., Cohen, L., Mory, B., and Ardon, R. (2012). Automatic detection and segmentation of kidneys in 3d ct images using random forests. In Ayache, N., Delingette, H., Golland, P., and Mori, K., editors, *MICCAI 2012*, volume 7512 of *Lecture Notes in Computer Science*, pages 66–74. Springer Berlin Heidelberg.

[Dale et al., 1985] Dale, S., Edholm, P. E., Hellstrom, L. G., and Larsson, S. (1985). Ectomography-a tomographic method for gamma camera imaging. *Physics in Medicine and Biology*, 30(11):1237.

[Davison, 2003] Davison, A. C. (2003). *Statistical Models*. Cambridge Press.

[Defrise et al., 2011] Defrise, M., Vanhove, C., and Liu, X. (2011). An algorithm for total variation regularization in high-dimensional linear problems. *Inverse Problems*, 27(6):065002.

[Delacroix et al., 2002] Delacroix, D., Guerre, J. P., Leblanc, P., and Hickman, C. (2002). Radionuclide and radiation protection data handbook 2nd edition (2002). *Radiation Protection Dosimetry*, 98(1):9–168.

[Di et al., 2014] Di, L.-Z., Couture, V., Leblanc, E., Alinejad, Y., Beaudoin, J.-F., Lecomte, R., Berthod, F., Faucheux, N., Balg, F., and Grenier, G. (2014). A Longitudinal Low Dose microCT Analysis of Bone Healing in Mice: A Pilot Study. *Advances in Orthopedics*.

[Dice, 1945] Dice, L. R. (1945). Measures of the Amount of Ecologic Association Between Species. *Ecology*, 26(3):297–302.

[Dobbins and Godfrey, 2003] Dobbins, J. T. and Godfrey, D. J. (2003). Digital x-ray tomosynthesis: current state of the art and clinical potential. *Physics in Medicine and Biology*, 48:R65–R106.

[Dogdas et al., 2007] Dogdas, B., Stout, D., Chatziioannou, A. F., and Leahy, R. M. (2007). Digimouse: a 3D whole body mouse atlas from CT and cryosection data. *Physics in Medicine and Biology*, 52(3):577.

[Donoho, 2006] Donoho, D. (2006). Compressed sensing. *IEEE Transactions on Information Theory*, 52(4):1289–1306.

[Du et al., 2008] Du, S., Zheng, N., Meng, G., and Yuan, Z. (2008). Affine registration of point sets using icp and ica. *IEEE Signal Processing Letters*, 15:689–692.

[EFPIA, 2013] EFPIA (2013). The pharmaceutical industry in figures.

[Ehling et al., 2014] Ehling, J., Theek, B., Gremse, F., Baetke, S., MÃ¶ckel, D., Maynard, J., Ricketts, S.-A., GrÃŒll, H., Neeman, M., Knuechel, R., Lederle, W., Kiessling, F., and Lammers, T. (2014). Micro-ct imaging of tumor angiogenesis: Quantitative measures describing micromorphology and vascularization. *The American Journal of Pathology*, 184(2):431 – 441.

[Eklund et al., 2013] Eklund, A., Dufort, P., Forsberg, D., and LaConte, S. (2013). Medical image processing on the GPU - past, present and future. *Medical Image Analysis*, 17:1073–1094.

[Elliott and Dover, 1982] Elliott, J. C. and Dover, S. D. (1982). X-ray microtomography. *Journal of Microscopy*, 126(2):211–213.

[Emes et al., 2003] Emes, R. D., Goodstadt, L., Winter, E. E., and Ponting, C. P. (2003). Comparison of the genomes of human and mouse lays the foundatino of genome zoology. *Human Molecular Genetics*.

[European Commission, 2013] European Commission (2013). Seventh report on the statistics on the number of animals used for experimental and other scientific purposes in the member states of the european union.

[European Society of Radiology, 2013] European Society of Radiology (2013). The Story of Radiology, Vol.2.

[Fahrig et al., 1997] Fahrig, R., Fox, a. J., Lownie, S., and Holdsworth, D. W. (1997). Use of a C-arm system to generate true three-dimensional computed rotational angiograms: preliminary in vitro and in vivo results. *American Journal of Neuroradiology*, 18(8):1507–14.

[Fechteler et al., 2007] Fechteler, P., Eisert, P., and Rurainsky, J. (2007). Fast and high resolution 3d face scanning. In *Image Processing, 2007. ICIP 2007. IEEE International Conference on*, volume 3, pages 81–84.

[Feldkamp et al., 1989] Feldkamp, L., Jesion, G., and Kubinski, D. (1989). Fundamental aspects of micro-ct in cone-beam geometry. In Thompson, D. and Chimenti, D., editors, *Review of Progress in Quantitative Nondestructive Evaluation*, pages 381–388. Springer US.

[Feldkamp et al., 1984] Feldkamp, L. A., Davis, L. C., and Kress, J. W. (1984). Practical cone-beam algorithm. *Journal of the Optical Society of America*, 1(6):612–619.

[Fiebig et al., 2012] Fiebig, T., Boll, H., Figueiredo, G., Kerl, H. U., Nittka, S., Groden, C., Kramer, M., and Brockmann, M. A. (2012). Three-dimensional *In Vivo* imaging of the murine liver: A micro-computed tomography-based anatomical study. *PLoS ONE*, 7(2):e31179.

[Fischler and Elschlager, 1973] Fischler, M. A. and Elschlager, R. (1973). The representation and matching of pictorial structures. *IEEE Transactions on Computers*, C-22(1):67–92.

[Franco, 2013] Franco, N. H. (2013). Animal experiments in biomedical research: A historical perspective. *Animals*, 3(1):238–273.

[Frank and Tamm, 1937] Frank, I. and Tamm, I. (1937). Coherent visible radiation of fast electrons passing through matter. In Bolotovskii, B., Frenkel, V., and Peierls, R., editors, *Selected Papers*, pages 29–35. Springer Berlin Heidelberg.

[Fu et al., 2010] Fu, J., Jiang, B., and Li, B. (2010). Large field of view computed laminography with the asymmetric rotational scanning geometry. *Science China Technological Sciences*, 53(8):2261–2271.

[Golzio et al., 2004] Golzio, M., Rols, M. P., Gabriel, B., and Teissie, J. (2004). Optical imaging of in vivo gene expression: a critical assessment of the methodology and associated technologies. *Gene Therapy*, 11(S1):S85–S91.

[Gomi et al., 2011] Gomi, T., Hirano, H., Nakajima, M., and Umeda, T. (2011). X-ray digital linear tomosynthesis imaging. *J. Biomedical Science and Engineering*, (4):443–453.

[Gondrom and Schröpfer, 1999] Gondrom, S. and Schröpfer, S. (1999). Digital computed laminography and tomosynthesis - functional principles and industrial applications. In DGZfP, editor, *International Symposium on Computed Tomography and Image Processing for Industrial Radiology*.

[Goshtasby et al., 2003] Goshtasby, A., Staib, L., Studholme, C., and Terzopoulos, D. (2003). Nonrigid image registration: Guest editors' introduction. *Computer Vision and Image Understanding*, 89(2-3):109–113.

[Guennebaud et al., 2010] Guennebaud, G., Jacob, B., et al. (2010). Eigen v3. http://eigen.tuxfamily.org.

[Guggenheim et al., 2013] Guggenheim, J. A., Basevi, H. R. A., Styles, I. B., Frampton, J., and Dehghani, H. (2013). Bioluminescence tomography improves quantitative accuracy for pre-clinical imaging. In *Proceedings of SPIE*, volume 8799, pages 87990G–87990G–6.

[Guven et al., 2005] Guven, M., Yazici, B., Intes, X., and Chance, B. (2005). Diffuse optical tomography with a priori anatomical information. *Physics in Medicine and Biology*, 50(12):2837.

[Habold et al., 2010] Habold, C., Blanc, S., and Brasse, D. (2010). Microcomputed tomography: an accurate and low-cost method to assess body composition in small mammals. *International Journal of Body Composition Research*, 8(1):31–35.

[Habold et al., 2011] Habold, C., Momken, I., Ouadi, A., Bekaert, V., and Brasse, D. (2011). Effect of prior treatment with resveratrol on density and structure of rat long bones under tail-suspension. *Journal of Bone and Mineral Metabolism*, 29:15–22.

[Hagelshuher et al., 2009] Hagelshuher, I. et al. (2009). Luminescent imaging technology as an opportunity to reduce and refine animal experiments: Light at the end of the tunnel? *altex*, 26.

[Halliday et al., 2010] Halliday, D., Resnick, R., and Walker, J. (2010). *Fundamentals of Physics*. John Wiley & Sons.

[Hamamatsu, a] Hamamatsu. http://www.hamamatsu.com/jp/en/L9181-02.html.

[Hamamatsu, b] Hamamatsu. http://www.hamamatsu.com/jp/en/product/alpha/F/4158/C7942CA-22/index.html.

[Hamamatsu, 2013] Hamamatsu (2013). Mcp and mcp assembly selection guide.

[Han et al., 2011] Han, X., Bian, J., Eaker, D. R., Kline, T. L., Sidky, E. Y., and Pan, X. (2011). Algorihtm-Enabled Low-Dose Micro-CT Imaging. *IEEE Transactions on Medical Imaging*, 30:606–620.

[Hartwell et al., 2010] Hartwell, L., Hood, L., Goldberg, M., Reynolds, A., and Silver, L. (2010). *Genetics: From Genes to Genomes*. McGraw-Hill Education.

[Heckel et al., 2011] Heckel, F., Konrad, O., Hahn, H. K., and Peitgen, H.-O. (2011). Interactive 3d medical image segmentation with energy-minimizing implicit functions. *Computers and Graphics*, 35(2):275 – 287.

[Heckel et al., 2014] Heckel, F., Moltz, J. H., Meine, H., Geisler, B., Kießling, A., D'Anastasi, M., dos Santos, D. P., Theruvath, A. J., and Hahn, H. K. (2014). On the evaluation of segmentation editing tools. *Journal of Medical Imaging*, 1(3):034005.

[Heimann and Meinzer, 2009] Heimann, T. and Meinzer, H.-P. (2009). Statistical shape models for 3D medical image segmentation: A review. *Medical Image Analysis*, 13(4):543–563.

[Heimann et al., 2007] Heimann, T., peter Meinzer, H., and Wolf, I. (2007). A statistical deformable model for the segmentation of liver ct volumes. In *MICCAI Workshop on 3D segmentation in the Clinic - A Grand Challenge*.

[Heimann et al., 2009] Heimann, T., van Ginneken, B., Styner, M., Arzhaeva, Y., Aurich, V., Bauer, C., Beck, A., Becker, C., Beichel, R., Bekes, G., Bello, F., Binnig, G., Bischof, H., Bornik, A., Cashman, P., Chi, Y., Cordova, A., Dawant, B., Fidrich, M., Furst, J., Furukawa, D., Grenacher, L., Hornegger, J., Kainmuller, D., Kitney, R., Kobatake, H., Lamecker, H., Lange, T., Lee, J., Lennon, B., Li, R., Li, S., Meinzer, H.-P., Nemeth, G., Raicu, D., Rau, A.-M., van Rikxoort, E., Rousson, M., Rusko, L., Saddi, K., Schmidt, G., Seghers, D., Shimizu, A., Slagmolen, P., Sorantin, E., Soza, G., Susomboon, R., Waite, J., Wimmer, A., and Wolf, I. (2009). Comparison and evaluation of methods for liver segmentation from ct datasets. *IEEE Transactions on Medical Imaging*, 28(8):1251–1265.

[Heimann et al., 2006] Heimann, T., Wolf, I., and Meinzer, H.-P. (2006). Optimal landmark distributions for statistical shape model construction. In *Proceedings of SPIE on Medical Imaging: Image Processing*, volume 6144, pages 518–528.

[Herman, 1979] Herman, G. T. (1979). Correction for beam hardening in computed tomography. *Physics in Medicine and Biology*, 24(1):81.

[Herman and Davidi, 2008] Herman, G. T. and Davidi, R. (2008). On Image Reconstruction from a Small Number of Projections. *Inverse Problems*, 24.

[Heusser et al., 2012] Heusser, T., Brehm, M., Sawall, S., and Kachelriess, M. (2012). CT data completion based on prior scans. *2012 IEEE Nuclear Science Symposium Conference Record*, pages 2969–2976.

[http://www.htstec.com/,] http://www.htstec.com/.

[Hu et al., 2001] Hu, S., Hoffman, E. A., and Reinhardt, J. M. (2001). Automatic lung segmentation for accurate quantitation of volumetric x-ray ct images. *IEEE Transactions on Medical Imaging*, 20:490–498.

[Hu et al., 2010] Hu, Z., Liang, J., Yang, W., Fan, W., Li, C., Ma, X., Chen, X., Ma, X., Li, X., Qu, X., Wang, J., Cao, F., and Tian, J. (2010). Experimental Cerenkov luminescence tomography of the mouse model with SPECT imaging validation. *Optics Express*, 18(24):24441–24450.

[Huber et al., 2013] Huber, M., Pauluhn, A., Culhane, J., Timothy, J., Wilhelm, K., and Zehnder, A. (2013). *Observing Photons in Space: A Guide to Experimental Space Astronomy*. ISSI Scientific Report Series. Springer.

[Iglesias and de Bruijne, 2007] Iglesias, J. E. and de Bruijne, M. (2007). Semiautomatic segmentation of vertebrae in lateral x-rays using a conditional shape model. *Academic Radiology*, 14(10):1156–65.

[Ikawa et al., 1995] Ikawa, M. et al. (1995). Green fluorescent protein as a marker in transgenic mice. *Development Grownth and Differentiation*, 37:455–459.

[IPHC, 2014] IPHC (2014). Institut Pluridisciplinaire Hubert Curien (Strasbourg, France) - http://www.iphc.cnrs.fr/.

[itk SNAP, 2005] itk SNAP (2005). http://www.itksnap.org/pmwiki/pmwiki.php.

[J. L. Prince, 1990] J. L. Prince, A. S. W. (1990). Constrained sinogram restoration for limited-angle tomography. *Optical Engineering*, 29(5):535–544.

[Jackson et al., 1972] Jackson, D. A., Symons, R. H., and Berg, P. (1972). Biochemical method for inserting new genetic information into dna of simian virus 40: Circular sv40 dna molecules containing lambda phage genes and the galactose operon of escherichia coli. *Proceedings of the National Academy of Sciences*, 69(10):2904–2909.

[Jackson, 1991] Jackson, J. E. (1991). *A user's guide to principal components*. Wiley series in probability and mathematical statistics. Wiley, New York.

[Jadvar and Parker, 2005] Jadvar, H. and Parker, J. (2005). *Clinical PET and PET/CT*. Springer.

[Jaenisch and Mintz, 1974] Jaenisch, R. and Mintz, B. (1974). Simian virus 40 dna sequences in dna of healthy adult mice derived from preimplantation blastocysts injected with viral dna. *Proceedings of the National Academy of Science*, 4(71):1250–1254.

[Jamieson et al., 2007] Jamieson, T., Bakhshi, R., Petrova, D., Pocock, R., Imani, M., and Seifalian, A. M. (2007). Biological applications of quantum dots. *Biomaterials*, 28(31):4717 – 4732.

[Jaszczak, 2006] Jaszczak, R. J. (2006). The early years of single photon emission computed tomography (spect): an anthology of selected reminiscences. *Physics in Medicine and Biology*, 51(13):R99.

[Jelley, 1958] Jelley, J. V. (1958). *Čerenkov radiation and its applications*. Pergamon Press, Inc., London.

[Jensen et al., 2008] Jensen, M., Jorgensen, J., Binderup, T., and Kjaer, A. (2008). Tumor volume in subcutaneous mouse xenografts measured by microct is more accurate and reproducible than determined by 18f-fdg-micropet or external caliper. *BMC Medical Imaging*, 8(1):16.

[Jerri, 1977] Jerri, A. (1977). The shannon sampling theorem:its various extensions and applications: A tutorial review. *Proceedings of the IEEE*, 65(11):1565–1596.

[Johnson, 2007] Johnson, A. (2007). Imaging techniques for small animal imaging models of pulmonary disease: Micro-ct. *Toxicologic Pathology*, 35.

[Johnson et al., 2011] Johnson, L. C., Johnson, R. W., Munoz, S. A., Mundy, G. R., Peterson, T. E., and Sterling, J. A. (2011). Longitudinal live animal micro-ct allows for quantitative analysis of tumor-induced bone destruction. *Bone*, 48(1):141 – 151.

[Joshi et al., 2010] Joshi, A. A., Chaudhari, A. J., Li, C., Dutta, J., Cherry, S. R., Shattuck, D. W., Toga, A. W., and Leahy, R. M. (2010). DigiWarp: a method for deformable mouse atlas warping to surface topographic data. *Physics in Medicine and Biology*, 55(20):6197.

[Jouanna et al., 2012] Jouanna, J., Van Der Eijk, P., and Allies, N. (2012). *Greek Medicine from Hippocrates to Galen: Selected Papers*. Studies in Ancient Medicine. Brill.

[Judex et al., 2010] Judex, S., Luu, Y. K., Ozcivici, E., Adler, B., Lublinsky, S., and Rubin, C. T. (2010). Quantification of adiposity in small rodents using micro-CT. *Methods*, 50:14–19.

[Kaczmarz, 1937] Kaczmarz, S. (1937). Angenäherte Auflösung von Systemen linearer Gleichungen. *Bulletin International de l'Académie Polonaise des Sciences et des Lettres*, 35:355–357.

[Kak and Slaney, 1988] Kak, A. and Slaney, M. (1988). *Principles of Computerized Tomographic Imaging*. IEEE Press.

[Kalogerakis et al., 2010] Kalogerakis, E., Hertzmann, A., and Singh, K. (2010). Learning 3D Mesh Segmentation and Labeling. *ACM Transactions on Graphics*, 29(3).

[Kalukin and Sankaran, 1997] Kalukin, A. R. and Sankaran, V. (1997). Three-Dimensional Visualization of Multilayered Assemblies Using X-Ray Laminography. In *IEEE Transactions on Components, Packaging and Manufacturing Technology*, volume 20, pages 361–366.

[Kang et al., 2003] Kang, Y., Engelke, K., and Kalender, W. (2003). A new accurate and precise 3-d segmentation method for skeletal structures in volumetric ct data. *IEEE Transactions on Medical Imaging*, 22(5):586–598.

[Kim et al., 2008] Kim, H. W., Cai, Q.-Y., Jun, H. Y., Chon, K. S., Park, S. H., Byun, S. J., Lee, M. S., Oh, J. M., Kim, H. S., and Yoon, K.-H. (2008). Micro-ct imaging with a hepatocyte-selective contrast agent for detecting liver metastasis in living mice. *Academic Radiology*, 15(10):1282 – 1290.

[Kostomitsopoulos and Djurasevic, 2010] Kostomitsopoulos, N. and Djurasevic, S. (2010). The ethical justification for the use of animals in biomedical research. *Archives of Biological Science Belgrade*, 62(3):781–787.

[Koubar et al., 2011] Koubar, K., Vintache, D., El Bitar, Z., Laquerriere, P., and Brasse, D. (2011). Analytical Simulation of a Micro-CT System.

[Kudo and Saito, 1991] Kudo, H. and Saito, T. (1991). Sinogram recovery with the method of convex projections for limited-data reconstruction in computed tomography. *Journal of the Optical Society of America*, 8(7):1148–1160.

[Kuo et al., 2007] Kuo, C., Coquoz, O., Troy, T. L., Xu, H., and Rice, B. W. (2007). Three-dimensional reconstruction of in vivo bioluminescent sources based on multispectral imaging. *Journal of Biomedical Optics*, 12(2):24007–24012.

[Lakowicz, 2006] Lakowicz, J. R. (2006). *Principles of Fluorescence Spectroscopy*. Springer, third edition.

[Lasser et al., 2008] Lasser, T., Soubret, A., Ripoll, J., and Ntziachristos, V. (2008). Surface reconstruction for free-space 360° fluorescence molecular tomography and the effects of animal motion. *Medical Imaging, IEEE Transactions on*, 27(2):188–194.

[Lauritsch and Bruder,] Lauritsch, G. and Bruder, H. Head Phantom – http://www.imp.uni-erlangen.de/forbild/deutsch/results/head/head.html.

[Leblond et al., 2010] Leblond, F., Davis, S. C., Valdés, P. a., and Pogue, B. W. (2010). Pre-clinical whole-body fluorescence imaging: Review of instruments, methods and applications. *Journal of Photochemistry and Photobiology B.*, 98(1):77–94.

[Lee et al., 2012] Lee, H., Xing, L., Davidi, R., Li, R., Qian, J., and Lee, R. (2012). Improved compressed sensing-based cone-beam ct reconstruction using adaptive prior image constraints. *Physics in Medicine and Biology*, 57(8):2287.

[Levakhina et al., 2011] Levakhina, Y. M., Duschka, R. L., Barkhausen, J., and Buzug, T. M. (2011). Digital Tomosynthesis of Hands using Simultaneous Algebraic Reconstruction Technique with Distance Driven Projector. pages 167–170.

[Levakhina et al., 2013] Levakhina, Y. M., Mueller, J., Duschka, R. L., Vogt, F., Barkhausen, J., and Buzug, T. M. (2013). Weighted simultaneous algebraic reconstruction technique for tomosynthesis imaging of objects with high-attenuation features. *Medical Physics*, 40(3):–.

[Li et al., 2003] Li, A., Miller, E. L., Kilmer, M. E., Brukilacchio, T. J., Chaves, T., Stott, J., Zhang, Q., Wu, T., Chorlton, M., Moore, R. H., Kopans, D. B., and Boas, D. a. (2003). Tomographic optical breast imaging guided by three-dimensional mammography. *Applied Optics*, 42(25):5181–90.

[Li et al., 2010] Li, C., Mitchell, G. S., and Cherry, S. R. (2010). Cerenkov luminescence tomography for small-animal imaging. *Optics Letters*, 35(7):1109–1111.

[Li et al., 2009] Li, C., Mitchell, G. S., Dutta, J., Ahn, S., Leahy, R. M., and Cherry, S. R. (2009). A three-dimensional multispectral fluorescence optical tomography imaging system for small animals based on a conical mirror design. *Optics Express*, 17(9):7571–7585.

[Li et al., 2004] Li, H., Tian, J., Zhu, F., Cong, W., Wang, L. V., Hoffman, E. A., and Wang, G. (2004). A mouse optical simulation environment (MOSE) to investigate bioluminescent phenomena in the living mouse with the Monte Carlo method. *Acad Radiol*, 11:1029–1038.

[Li et al., 2008] Li, X., Yankeelov, T. E., Peterson, T. E., Gore, J. C., and Dawant, B. M. (2008). Automatic nonrigid registration of whole body CT mice images. *Medical Physics*, 35(4):1507–1520.

[Li et al., 2012] Li, Y., Chen, Y., Hu, Y., Oukili, A., Luo, L., Chen, W., and Toumoulin, C. (2012). Strategy of computed tomography sinogram inpainting based on sinusoid-like curve decomposition and eigenvector-guided interpolation. *Journal of the Optical Society of America A*, 29(1):153–63.

[Liu et al., 2010] Liu, K., Lu, Y., Tian, J., Qin, C., Yang, X., Zhu, S., Yang, X., Gao, Q., and Han, D. (2010). Evaluation of the simplified spherical harmonics approximation in bioluminescence tomography through heterogeneous mouse models. *Optics Express*, 18(20):20988–1002.

[Liu et al., 2008] Liu, L., Raber, D., Nopachai, D., Commean, P., Sinacore, D., Prior, F., Pless, R., and Ju, T. (2008). Interactive separation of segmented bones in ct volumes using graph cut. In Metaxas, D., Axel, L., Fichtinger, G., and Szakely, G., editors, *MICCAI 2008*, volume 5241 of *Lecture Notes in Computer Science*, pages 296–304. Springer Berlin Heidelberg.

[Lorensen and Cline, 1987] Lorensen, W. E. and Cline, H. E. (1987). Marching cubes: A high resolution 3D surface construction algorithm. *SIGGRAPH Comput. Graph.*, 21(4):163–169.

[Lu et al., 2010] Lu, X., Sun, Y., and Bai, G. (2010). Adaptive wavelet-Galerkin methods for limited angle tomography. *Image and Vision Computing*, 28:696–703.

[Lu et al., 2011] Lu, X., Sun, Y., and Yuan, Y. (2011). Optimization for limited angle tomography in medical image processing. *Patt. Rec.*, 44:2427–2435.

[Lu et al., 2009] Lu, Y., Zhang, X., Douraghy, A., and Stout, D. (2009). Source reconstruction for spectrally-resolved bioluminescence tomography with sparse a priori information. *Optics Express*, 17(10):377–382.

[Luke, 1999] Luke, H. (1999). The origins of the sampling theorem. *Communications Magazine, IEEE*, 37(4):106–108.

[Maisl et al., 2010] Maisl, M., Porsch, F., and Schorr, C. (2010). Computed laminography for X-ray inspection of lightweight constructions. In *Proceedings of the International Symposium on NDT in Aerospace*.

[Malicka et al., 2003] Malicka, J., Gryczynski, I., Geddes, C. D., and Lakowicz, J. R. (2003). Metal-enhanced emission from indocyanine green: a new approach to in vivo imaging. *Journal of Biomedical Optics*, 8(3):472–478.

[Mandelbrojt and Schwartz, 1965] Mandelbrojt, S. and Schwartz, L. (1965). Jacques hadamard (1865 - 1963). *Bulletin of the American Mathematical Society*, 71(1):107–129.

[Marchadier et al., 2011] Marchadier, A., Vidal, C., Tafani, J.-P., Ordureau, S., Lédée, R., and Léger, C. (2011). Quantitative CT imaging for adipose tissue analysis in mouse model of obesity. In *SPIE Medical Imaging 2011*, Orlando, United States.

[Masters, 2010] Masters, B. R. (2010). The development of fluorescence microscopy. *Encyclopedia of Life Science – www.els.net*.

[meshlab, 2005] meshlab (2005). http://meshlab.sourceforge.net/.

[Metzler et al., 2003] Metzler, S., Bowsher, J., and Jaszczak, R. (2003). Geometrical similarities of the orlov and tuy sampling criteria and a numerical algorithm for assessing sampling completeness. *IEEE Transactions on Nuclear Science*, 50(5):1550–1555.

[Mharib et al., 2011] Mharib, A. M., Ramli, A. R., Mashohor, S., and Mahmood, R. B. (2011). Survey on liver CT image segmentation methods. *Artificial Intelligence Review*, 37(2):83–95.

[Michalet et al., 2005] Michalet, X., Pinaud, F. F., Bentolila, L. A., Tsay, J. M., Doose, S., Li, J. J., Iyer, G., and Weiss, S. (2005). Peptide-coated semiconductor nanocrystals for biomedical applications. volume 5704, pages 57–68.

[Missimer et al., 2004] Missimer, J., Madi, Z., Honer, M., Keller, C., Schubiger, A., and Ametamey, S.-M. (2004). Performance evaluation of the 16-module quad-hidac small animal pet camera. *Physics in Medicine and Biology*, 49(10):2069.

[Mitteroecker and Gunz, 2009] Mitteroecker, P. and Gunz, P. (2009). Advances in Geometric Morphometrics. *Journal of Evolutionary Biology*, 36(2):235–247.

[Momey et al., 2011] Momey, F., Denis, L., Mennessier, C., Thiebaut, E., Becker, J.-M., and Desbat, L. (2011). A new representation and projection model for tomography, based on separable b-splines. In *Nuclear Science Symposium and Medical Imaging Conference (NSS/MIC), 2011 IEEE*, pages 2602–2609.

[Mourning et al., 2010] Mourning, C., Nykl, S., Xu, H., Chelberg, D. M., and Liu, J. (2010). Gpu acceleration of robust point matching. In Bebis, G., Boyle, R. D., Parvin, B., Koracin, D., Chung, R., Hammoud, R. I., Hussain, M., Tan, K.-H., Crawfis, R., Thalmann, D., Kao, D., and Avila, L., editors, *ISVC (3)*, volume 6455 of *Lecture Notes in Computer Science*, pages 417–426. Springer.

[Myronenko and Song, 2009] Myronenko, A. and Song, X. (2009). Point Set and Registration: Coherent Point Drift. *IEEE Transactions on Pattern Analysis and Machine Intelligence*, 32(12).

[National Institute of Standards and Technology, 2015] National Institute of Standards and Technology (2015). http://www.nist.gov/pml/data/xcom/index.cfm.

[Natterer, 2008] Natterer, F. (2008). X-ray tomography. In Bonilla, L., editor, *Inverse Problems and Imaging*, volume 1943 of *Lecture Notes in Mathematics*, pages 17–34. Springer Berlin Heidelberg.

[Natterer and Wübbeling, 2001] Natterer, F. and Wübbeling, F. (2001). *Mathematical Methods in Image Reconstruction*. Mathematical Modeling and Computation. Society for Industrial and Applied Mathematics (SIAM, 3600 Market Street, Floor 6, Philadelphia, PA 19104).

[Naylor, 1999] Naylor, L. (1999). Reporter gene technology: the future looks bright. *Biochemical Pharmacology*, 58(5):749–757.

[Nealen et al., 2006] Nealen, A., Igarashi, T., Sorkine, O., and Alexa, M. (2006). Laplacian mesh optimization. In *Proceedings of the 4th International Conference on Computer Graphics and Interactive Techniques in Australasia and Southeast Asia*, GRAPHITE '06, pages 381–389, New York, NY, USA. ACM.

[Nguyen and Lee, 2010] Nguyen, V. G. and Lee, S. J. (2010). Image reconstruction from limited-view projections by convex nonquadratic spline regularization. *Optical Engineering*, 49.

[Ntziachristos, 2006] Ntziachristos, V. (2006). Fluorescence Molecular Imaging. *Annual Review of Biomedical Engineering*, 8:1–33.

[Oliveira et al., 2009] Oliveira, J. P., Bioucas-Dias, J. M., and Figueiredo, M. A. (2009). Adaptive total variation image deblurring: A majorization/minimization approach. *Signal Processing*, 89(9):1683 – 1693.

[OpenMP Architecture Review Board, 2008] OpenMP Architecture Review Board (2008). OpenMP application program interface version 3.0 – http://www.openmp.org/mp-documents/spec30.pdf.

[Ordas et al., 2007] Ordas, S., Oubel, E., Leta, R., Carreras, F., and Frangi, A. F. (2007). A statistical shape model of the heart and its application to model-based segmentation. In *Proceedings of SPIE*, volume 6511, pages 65111K–65111K–11.

[Pan et al., 2009] Pan, X., E. Y. Sidky, and Vannier, M. (2009). Why do commercial CT scanners still employ traditional, filtererd back-projection for image reconstruction? *Inverse Problems*, 25.

[Park et al., 2003] Park, H., Bland, P. H., and Meyer, C. R. (2003). Construction of an abdominal probabilistic atlas and its application in segmentation. *IEEE Transactions on Medical Imaging*, 22(4):483–492.

[Paroo et al., 2004] Paroo, Z., Bollinger, R. a., Braasch, D. a., Richer, E., Corey, D. R., Antich, P. P., and Mason, R. P. (2004). Validating bioluminescence imaging as a high-throughput, quantitative modality for assessing tumor burden. *Molecular Imaging*, 3(2):117–24.

[Patterson et al., 1991] Patterson, M., Wilson, B., and Wyman, D. (1991). The propagation of optical radiation in tissue i. models of radiation transport and their application. *Lasers in Medical Science*, 6(2):155–168.

[Pekar and Patterson, 2010] Pekar, J. and Patterson, M. S. (2010). Multispectral bioluminescence tomography: Simulations and phantom studies with a priori x-ray ct spatial priors. In *Biomedical Optics and 3-D Imaging*, page BMB8. Optical Society of America.

[Persson et al., 2001] Persson, M., Bone, D., and Elmqvist, H. (2001). Total variation norm for three-dimensional iterative reconstruction in limited view angle tomography. *Physics in Medicine and Biology*, 46:853–866.

[Price et al., 2006] Price, J., Aykac, D., and Wall, J. (2006). A 3d level sets method for segmenting the mouse spleen and follicles in volumetric microct images. In *Engineering in Medicine and Biology Society, 2006. EMBS '06. 28th Annual International Conference of the IEEE*, pages 2332–2336.

[Prince and Willsky, 1993] Prince, J. L. and Willsky, A. S. (1993). Hierarchical Reconstruction Using Geometry and Sinogram Restoration. *IEEE Transactions on Image Processing*, 2(3):401–416.

[Prince, 2012] Prince, S. J. D. (2012). *Computer Vision: Models, Learning, and Inference.* Cambridge University Press, New York, NY, USA, 1st edition.

[Rantala et al., 2006] Rantala, M., Vanska, S., Jarvenpaa, S., Kalke, M., Lassas, M., Moberg, J., and Siltanen, S. (2006). Wavelet-based reconstruction for limited-angle X-ray tomography. *IEEE Transactions on Medical Imaging*, 25(2):210–217.

[Reiser et al., 2009] Reiser, I., Bian, J., Nishikawa, R. M., Sidky, E. Y., and Pan, X. (2009). Comparison of reconstruction algorithms for digital breast tomosynthesis. In *Fully3D Conference Proceedings*.

[Remy and Michnick, 2006] Remy, I. and Michnick, S. W. (2006). A highly sensitive protein-protein interaction assay based on gaussia luciferase. *Nature Methods*, 3:977–979.

[Ritschl et al., 2011] Ritschl, L., Bergner, F., Fleischmann, C., and Kachelriess, M. (2011). Improved total variation-based ct image reconstruction applied to clinical data. *Physics in Medicine and Biology*, 56(6):1545.

[Ritschl et al., 2015] Ritschl, L., Kuntz, J., and Kachelries, M. (2015). The rotate-plus-shift c-arm trajectory: complete ct data with limited angular rotation. In *Proceedings of SPIE*, volume 9412, pages 941221–941221–4.

[Robertson et al., 2009] Robertson, R., Germanos, M. S., Li, C., Mitchell, G. S., Cherry, S. R., and Silva, M. D. (2009). Optical imaging of Cerenkov light generation from positron-emitting radiotracers. *Physics in Medicine and Biology*, 54(16):N355–65.

[Rokhlin et al., 2009] Rokhlin, V., Szlam, A., and Tygert, M. (2009). A randomized algorithm for principal component analysis. *SIAM Journal on Matrix Analysis and Applications*, 31(3):1100–1124.

[Rothe et al., 2015] Rothe, J. H., Rudolph, I., Rohwer, N., Kupitz, D., Gregor-Mamoudou, B., Derlin, T., Furth, C., Amthauer, H., Brenner, W., Buchert, R., Cramer, T., and Apostolova, I. (2015). Time course of contrast enhancement by micro-ct with dedicated contrast agents in normal mice and mice with hepatocellular carcinoma: Comparison of one iodinated and two nanoparticle-based agents. *Academic Radiology*, 22(2):169 – 178.

[Roura et al., 2013] Roura, S., Galvez-Monton, C., and Bayes-Genis, A. (2013). Bioluminescence imaging: a shining future for cardiac regeneration. *Journal of Cellular and Molecular Medicine*.

[Rusinkiewicz, 2013] Rusinkiewicz, S. (2013). trimesh2 v 2.12 - http://gfx.cs.princeton.edu/proj/trimesh2/.

[Rusu et al., 2013] Rusu, M., Bloch, B. N., Jaffe, C. C., Rofsky, N. M., Genega, E. M., Feleppa, E., Lenkinski, R. E., and Madabhushi, A. (2013). Statistical 3D Prostate Imaging Atlas Construction via Anatomically Constrained Registration. *Proceedings of SPIE*, 8669.

[Saeed et al., 2008] Saeed, Z., Guilbault, C., Sanctis, J. B. D., Henri, J., Marion, D., St-Arnaud, R., and Radzioch, D. (2008). Fenretinide prevents the development of osteoporosis in cftr-ko mice. *Journal of Cystic Fibrosis*, 7(3):222 – 230.

[Sahiner and Yagle, 1993] Sahiner, B. and Yagle, A. (1993). Limited angle tomography using wavelets. In *IEEE Conference Record – Nuclear Science Symposium and Medical Imaging Conference*, pages 1912–1916 vol.3.

[Savai et al., 2009] Savai, R., Langheinrich, A. C., Schermuly, R. T., Pullamsetti, S. S., Dumitrascu, R., Traupe, H., Rau, W. S., Seeger, W., Grimminger, F., and Banat, G. A. (2009). Evaluation of angiogenesis using micro-computed tomography in a xenograft mouse model of lung cancer. *Neoplasia*, 11(1):48 – 56.

[Schäfer et al., 2012] Schäfer, D., Meyer, C., Bullens, R., Saalbach, A., and Eshuis, P. (2012). Limited Angle C-Arm Tomography and Segmentation for Guidance of Atrial Fibrillation Ablation Procedures. In Ayache, N., Delingette, H., Golland, P., and Mori, K., editors, *MICCAI (1)*, volume 7510 of *Lecture Notes in Computer Science*, pages 634–641. Springer.

[Schleif, 1993] Schleif, R. F. (1993). *Genetics and molecular biology /.* The John Hopkins University Press,, 2nd ed. edition.

[Schofer and others., 2007] Schofer, S. and others. (2007). A microct-based method for the measurement of pulmonary compliance in healthy and bleomycin-exposed mice. *Experimental Lung Research*, 33(3-4):169–183.

[Segars and Tsui, 2009] Segars, W. P. and Tsui, B. (2009). MCAT to XCAT: The Evolution of 4-D Computerized Phantoms for Imaging Research. *Proceedings of IEEE*, 97(12):1954–1968.

[Segars et al., 2004] Segars, W. P., Tsui, B., Frey, E., Johnson, G. A., and Berr, S. (2004). Development of a 4D Digital Mouse Phantom for Molecular Imaging Research. *Molecular Imaging and Biology*.

[Serageldin, 2013] Serageldin, I. (2013). Ancient alexandria and the dawn of medical science. *Global Cardiology Science and Practice*, 47.

[Shaner et al., 2005] Shaner, N. C., Steinbach, P. A., and Tsien, R. Y. (2005). A guide to choosing fluorescent proteins. *Nature Methodsods*, 2(12):905–909.

[Sharma et al., 2013] Sharma, G., Agarwala, A., and Bhattacharya, B. (2013). Technical note: A fast parallel gauss jordan algorithm for matrix inversion using cuda. *Comput. Struct.*, 128:31–37.

[Sheikh et al., 2010] Sheikh, A. Y., van der Bogt, K. E., Doyle, T. C., Sheikh, M. K., Ransohoff, K. J., Ali, Z. A., Palmer, O. P., Robbins, R. C., Fischbein, M. P., and Wu, J. C. (2010). Micro-CT for Characterization of Murine CV Disease Models. *JACC: Cardiovascular Imaging*, 3(7):783–785.

[Shen and Wang, 2010] Shen, H. and Wang, G. (2010). A tetrahedron-based inhomogeneous Monte Carlo optical simulator. *Physics in Medicine and Biology*, 55(4):947–62.

[Shen et al., 2006] Shen, L., Saykin, A. J., Chung, M. K., Huang, H., Ford, J., Makedon, F., Mchugh, T. L., and Rhodes, C. H. (2006). Morphometric analysis of genetic variation in hippocampal shape in mild cognitive impairment: Role of an il-6 promoter polymorphism. In *In Life Science Society Computational Systems Bioinformatics Conference*.

[Shi et al., 2013] Shi, B., Xie, S., Berryman, D., List, E., and Liu, J. (2013). Robust separation of visceral and subcutaneous adipose tissues in micro-ct of mice. In *Engineering in Medicine and Biology Society (EMBC), 2013 35th Annual International Conference of the IEEE*, pages 2312–2315.

[Shimomura and Saiga, 1962] Shimomura, O., J. F. H. and Saiga, Y. (1962). Extraction, purification and properties of aequorin, a bioluminescent protein from the luminous hydromedusan, aequorea. *Journal of Cellular and Comparative Physiology*, 59:223–239.

[Shultis and Faw, 2010] Shultis, J. and Faw, R. (2010). *Fundamentals of Nuclear Science and Engineering Second Edition.* CRC Press.

[Sidky and Pan, 2008] Sidky, E. and Pan, X. (2008). Image reconstruction in circular cone-beam computed tomography by constrained, total-variation minimization. *Physics in Medicine and Biology*, 53:4777–4807.

[Sidky et al., 2011] Sidky, E. Y., Duchin, Y., Pan, X., and Ullberg, C. (2011). A constrained, total-variation minimization algorithm for low-intensity x-ray CT. *Medical Physics*, 38 Suppl 1(2011):S117.

[Sidky et al., 2009a] Sidky, E. Y., Kao, C.-m., and Pan, X. (2009a). Accurate image reconstruction from few-views and limited angle data in divergent-beam CT. *Journal of X-Ray Science and Technology*, 14:119–139.

[Sidky et al., 2009b] Sidky, E. Y., Pan, X., Reiser, I. S., Nishikawa, R. M., Moore, R. H., and Kopans, D. B. (2009b). Enhanced imaging of microcalcifications in digital breast tomosynthesis through improved image-reconstruction algorithms. *Medical Physics*, 36(11):4920.

[Soler et al., 2001] Soler, L., Delingette, H., Malandain, G., Montagnat, J., Ayache, N., Koehl, C., Dourthe, O., Malassagne, B., Smith, M., Mutter, D., and Marescaux, J. (2001). Fully automatic anatomical, pathological, and functional segmentation from CT scans for hepatic surgery. *Computer Aided Surgery*, 6(3):131–42.

[Spinelli et al., 2010] Spinelli, A. E., D'Ambrosio, D., Calderan, L., Marengo, M., Sbarbati, A., and Boschi, F. (2010). Cerenkov radiation allows in vivo optical imaging of positron emitting radiotracers. *Physics in Medicine and Biology*, 55(2):483.

[Spinelli et al., 2011] Spinelli, A. E., Kuo, C., Rice, B. W., Calandrino, R., Marzola, P., Sbarbati, A., and Boschi, F. (2011). Multispectral Cerenkov luminescence tomography for small animal optical imaging. *Optics Express*, 19(13):12605–12618.

[Subach et al., 2011] Subach, O. M., Cranfill, P. J., Davidson, M. W., and Verkhusha, V. V. (2011). An enhanced monomeric blue fluorescent protein with the high chemical stability of the chromophore. *PLoS ONE*, 6(12):e28674.

[Taylor, 1998] Taylor, S. A. (1998). CCD and CMOS Imaging Array Technologies : Technology Review. Technical report, Xerox Limited.

[Thoyer-Rozat and Moussard, 1953] Thoyer-Rozat and Moussard (1953).

[Townsend, 2008] Townsend, D. W. (2008). Multimodality imaging of structure and function. *Physics in Medicine and Biology*, 53(4):R1.

[van der Have et al., 2009] van der Have, F., Vastenhouw, B., Ramakers, R. M., Branderhorst, W., Krah, J. O., Ji, C., Staelens, S. G., and Beekman, F. J. (2009). U-SPECT-II: An Ultra-High-Resolution Device for Molecular Small-Animal Imaging. *Journal of Nuclear Medicine*, 50(4):599–605.

[Van Haver et al., 2014] Van Haver, A., MAHIEU, P., Claessens, T., Li, H., Pattyn, C., Verdonk, P., and Audenaert, E. (2014). A statistical shape model of trochlear dysplasia of the knee. *The Knee*.

[Verhoeven, 1993] Verhoeven, D. (1993). Limited-data computed tomography algorithms for the physical sciences. *Applied Optics*, 32(20):3736–54.

[Vintache et al., 2010] Vintache, D., Humbert, B., and Brasse, D. (2010). Iterative reconstruction for transmission tomography on GPU using Nvidia CUDA. *Tsinghua Science and Technology*, 15(1):11–16.

[Walpole et al., 2012] Walpole, S., Prieto-Merino, D., Edwards, P., Cleland, J., Stevens, G., and Roberts, I. (2012). The weight of nations: an estimation of adult human biomass. *BMC Public Health*, 12(1):439.

[Wang et al., 2006] Wang, G., Cong, W., Durairaj, K., Qian, X., Shen, H., Sinn, P., Hoffman, E., McLennan, G., and Henry, M. (2006). In vivo mouse studies with bioluminescence tomography. *Optics Express*, 14(17):7801–7809.

[Wang et al., 2012a] Wang, H., Stout, D., and Chatziioannou, A. (2012a). Mouse Atlas Registration with Non-tomographic Imaging Modalitie : a Pilot Study Based on Simulation. *Molecular Imaging and Biology*, 14(4):408–419.

[Wang et al., 2012b] Wang, H., Stout, D. B., and Chatziioannou, A. F. (2012b). Estimation of mouse organ locations through registration of a statistical mouse atlas with micro-CT images. *IEEE Transactions on Medical Imaging*, 31(1):88–102.

[Wang et al., 2012c] Wang, H., Stout, D. B., Taschereau, R., Gu, Z., Vu, N. T., Prout, D. L., and Chatziioannou, A. F. (2012c). MARS: a mouse atlas registration system based on a planar x-ray projector and an optical camera. *Physics in Medicine and Biology*, 57(19):6063.

[Wathen et al., 2013] Wathen, C. A., Foje, N., Avermaete, T. v., Miramontes, B., Chapaman, S. E., Sasser, T. A., Kannan, R., Gerstler, S., and Leevy, W. M. (2013). In vivo x-ray computed tomographic imaging of soft tissue with native, intravenous, or oral contrast. *Sensors*, 13(6):6957–6980.

[Watson and Crick, 1953] Watson, J. D. and Crick, F. H. C. (1953). Molecular Structure of Nucleic Acids: A Structure for Deoxyribose Nucleic Acid. *Nature*, 171(4356):737–738.

[Wiens, 2013] Wiens, V. (2013). Volumetric segmentation of complex bone structures from medical imaging data using reeb graphs. In *Central European Seminar on Computer Graphics for Students (CSCG'2013)*, pages 113–120.

[Williams et al., 2008] Williams, M., Judy, P., More, M., Harvey, J., Majewski, S., Proffitt, J., McKisson, J., Stolin, A., Kross, B., Stewart, A., Bullard, E., Kankaria, M., and Janer, R. (2008). Tomographic dual modality breast scanner. In Krupinski, E., editor, *Digital Mammography*, volume 5116 of *Lecture Notes in Computer Science*, pages 99–107. Springer Berlin Heidelberg.

[World Medical Association, 1964] World Medical Association (1964). Declaration of Helsinki – http://www.wma.net/en/30publications/10policies/b3/17c.pdf.

[Wu et al., 2009] Wu, C., Murtha, P. E., and Jaramaz, B. (2009). Femur statistical atlas construction based on two-level 3D non-rigid registration. *Computer Aided Surgery*, 14(4-6):83–99.

[www.etymonline.com, 2015] www.etymonline.com (2015).

[www.nobelprize.org, 2015] www.nobelprize.org (2015).

[Xiao et al., 2010] Xiao, M., Soh, J., Pastor, O. M., Schmidt, E. J., Hallgrimsson, B., and Sensen, C. W. (2010). Building generic anatomical models using virtual model cutting and iterative registration. *BMC Medical Imaging*, 10:5.

[Yang et al., 2000] Yang, M., Baranov, E., Jiang, P., Sun, F. X., Li, X. M., Li, L., Hasegawa, S., Bouvet, M., Al-Tuwaijri, M., Chishima, T., Shimada, H., Moossa, A. R., Penman, S., and Hoffman, R. M. (2000). Whole-body optical imaging of green fluorescent protein-expressing tumors and metastases. *Proceedings of the National Academy of Sciences*, 97(3):1206–1211.

[Yau and Wong, 1996] Yau, S. F. and Wong, S. H. (1996). A linear sinogram extrapolator for limited angle tomography. In *Proceedings of ICSP*, pages 386–389.

[Zagorchev et al., 2010] Zagorchev, L. et al. (2010). Micro Computed Tomography for Vascular Exploration. *Journal of Angiogenesis Research*, 2.

[Zhang et al., 2011a] Zhang, H., Bao, Q., Vu, N., Silverman, R., Taschereau, R., Berry-Pusey, B., Douraghy, A., Rannou, F., Stout, D., and Chatziioannou, A. (2011a). Performance evaluation of petbox: A low cost bench top preclinical pet scanner. *Molecular Imaging and Biology*, 13(5):949–961.

[Zhang et al., 2006] Zhang, Y., Chan, H.-P., Sahiner, B., Wei, J., Goodsitt, M. M., Hadjiiski, L. M., Ge, J., and Zhou, C. (2006). A comparative study of limited-angle cone-beam reconstruction methods for breast tomosynthesis. *Med. Phys.*, 33(10):3781–3795.

[Zhang et al., 2011b] Zhang, Y., Hong, H., and Cai, W. (2011b). Pet tracers based on zirconium-89. *Curr Radiopharm.*, 2(4):131–139.

[Zheng et al., 2007] Zheng, Y., Barbu, A., Georgescu, B., Scheuering, M., and Comaniciu, D. (2007). Fast automatic heart chamber segmentation from 3d ct data using marginal space learning and steerable features. In *Proceedings of IEEE 11th International Conference on Computer Vision (ICCV)*, pages 1–8.

[Zhong et al., 2013] Zhong, H., Zheng, Y., Funka-Lea, G., and Vega-Higuera, F. (2013). Automatic heart isolation in 3d ct images. In Menze, B., Langs, G., Lu, L., Montillo, A., Tu, Z., and Criminisi, A., editors, *Medical Computer Vision. Recognition Techniques and Applications in Medical Imaging*, volume 7766 of *Lecture Notes in Computer Science*, pages 165–180. Springer Berlin Heidelberg.

[Zhong et al., 2011] Zhong, J., Tian, J., Yang, X., and Qin, C. (2011). Whole-Body Cerenkov Luminescence Tomography with the Finite Element SP3 Method. *Annals of Biomedical Engineering*, 39(6):1728–1735.

[Zhou et al., 2008] Zhou, L., Yazici, B., and Ntziachristos, V. (2008). Fluorescence molecular-tomography reconstruction with a priori anatomical information. In *Proceedings of SPIE*, volume 6868, pages 68680O–68680O–11.

[Zhou et al., 2004] Zhou, X., Hara, T., Fujita, H., Yokoyama, R., Kiryu, T., and Hoshi, H. (2004). Automated segmentations of skin, soft-tissue, and skeleton, from torso ct images. In *Proceedings of SPIE*, volume 5370, pages 1634–1639.

[Zhu et al., 2006] Zhu, L., Bennett, N. R., and Fahrig, R. (2006). Scatter correction method for x-ray ct using primary modulation: Theory and preliminary results. *IEEE Transactions on Medical Imaging*, 25(12):1573–1587.